
THE UNIVERSITY *of* EDINBURGH

# Bayesian estimation of resistivities from seismic velocities

**Dieter Werthmüller**

Thesis presented for the degree

**Doctor of Philosophy**


THE UNIVERSITY
*of* EDINBURGH

School of GeoSciences

2013

# Bayesian estimation of resistivities from seismic velocities

## Bayesian methodology for the determination of background resistivities from seismic velocities

**Ph.D. Thesis**
01/10/2010–30/09/2013

Submission 30/09/2013
Viva Voce 17/12/2013
Final Version 30/01/2014

University of Edinburgh
School of GeoSciences

**Dieter Werthmüller**
Dieter@Werthmuller.org

B.Sc. Earth Sciences 2007
*ETH Zürich*

M.Sc. Applied Geophysics 2009
*TU Delft, ETH Zürich, RWTH Aachen*

**Supervisors**

**Prof. Anton Ziolkowski**
PGS and Royal Academy of Engineering
Research Professor of Petroleum Geoscience

**Dr. David Wright**

# Abstract

I address the problem of finding a background model for the estimation of resistivities in the earth from controlled-source electromagnetic (CSEM) data by using seismic data and well logs as constraints. Estimation of resistivities is normally done by trial-and-error, in a process called "inversion", by finding a model of the earth whose responses match the data to within an acceptable error; what comes out of the inversion is what is put into the model by the geophysicist: it does not come out of the data directly. The premise underlying this thesis is that an earth model can be found that satisfies not only the CSEM data but also the seismic data and any well logs. I present a methodology to determine background resistivities from seismic velocities using rock physics, structural constraints, and depth trends. The physical parameters of the seismic wave equation are different from those in the electromagnetic diffusion equation, so there is no direct link between the governing equations. I therefore use a Bayesian framework to incorporate not only the errors in the data and our limited knowledge of the rock parameters, but also the uncertainty of our chosen and calibrated velocity-to-resistivity transform. To test the methodology I use a well log from the North Sea Harding South oil and gas field to calibrate the transform, and apply it to seismic velocities of the nearby Harding Central oil and gas field. I also use short-offset CSEM inversions to estimate the electric anisotropy and to improve the shallow part of the resistivity model, where there is no well control. Three-dimensional modelling of this resistivity model predicts the acquired CSEM data within the estimated uncertainty. This methodology makes it possible to estimate background resistivities from seismic velocities, well logs, and other available geophysical and geological data. Subsequent CSEM surveys can then focus on finding resistive anomalies relative to this background model; these are, potentially, hydrocarbon-bearing formations.

# Lay summary

I address the problem of finding a background model for the estimation of resistivities in the earth from controlled-source electromagnetic (CSEM) data by using seismic data and well logs as guidance. Estimation of resistivities is normally done by trial-and-error, in a process called "inversion", by finding a model of the earth whose responses match the data to within an acceptable error; what comes out of the inversion is what is put into the model by the geophysicist: it does not come out of the data directly. The premise underlying this thesis is that an earth model can be found that satisfies not only the CSEM data but also the seismic data and any well logs. I present a methodology to determine background resistivities from seismic velocities using rock physics, horizons from seismic data, and depth trends. The physical parameters in the seismic theory are different from those in the electromagnetic theory, so there is no direct link between the governing equations. I carry out an uncertainty analysis to include not only the errors in the data and our limited knowledge of the rock parameters, but also the uncertainty of our chosen and calibrated velocity-to-resistivity transform. To test the methodology I use a well log from the North Sea Harding South oil and gas field to calibrate the transform, and apply it to seismic velocities of the nearby Harding Central oil and gas field. I also use CSEM processing tools to estimate the electric anisotropy and to improve the shallow part of the resistivity model, where there is no well control. Three-dimensional modelling of this resistivity model predicts the measured CSEM data within the estimated uncertainty. This methodology makes it possible to estimate background resistivities from seismic velocities, well logs, and other available geophysical and geological data. Subsequent CSEM surveys can then focus on finding resistive anomalies relative to this background model; these are, potentially, oil and gas reservoirs.

# Declaration

I declare that this thesis has been composed solely by myself and that it has not been submitted, either in whole or in part, in any previous application for a degree. Except where otherwise acknowledged, the work presented is entirely my own.

Dieter Werthmüller
September 2013

8

# Acknowledgment

It is a pleasure to thank those who made this thesis possible. I owe my deepest gratitude to my supervisors Anton Ziolkowski and David Wright for offering me this Ph.D. project. They always had an open door to discuss my project and guide me through my thesis, and they taught me a great deal regarding electromagnetic responses, signal processing, and the scientific method in general.

My thanks go to PGS for funding this project and giving me access to both MTEM data and forward modelling and inversion codes. I would specifically like to thank John Linfoot and his group in Edinburgh for providing the possibility to work regularly in their office, which led to many good discussions, and Allan McKay and his group in Oslo for the great time and good inputs during the three months I spent in Oslo in 2012. I also thank BP for providing seismic data and well log data.

I would like to express my gratitude to Jinsong Chen (Berkeley Lab), Thomas Dickens (ExxonMobil), and Folke Engelmark (PGS) for their very quick and helpful responses to my queries.

A great cheers to all my fellow students, colleagues and staff here in the School of GeoSciences, who made these three years a great pleasure.

Most importantly I would like to thank Liliana for undertaking this adventure with me, and both my family and her family for their support and understanding of our plans.

# Contents

# List of Figures

# List of Tables

# Symbols and Abbreviations

## Symbols

SI and SI-derived units are used throughout the thesis as specified in the following list. The guidelines for correct use of the International System of Units (SI) can be found at the Bureau International des Poids et Mesures, http://www.bipm.org/en/si (current: 8th edition, 2006, http://www.bipm.org/utils/common/pdf/si_brochure_8_en.pdf).

These variables are repeatedly used for various purposes: $x, y, z, i, n, N, p, K, \eta, \theta, \tau$; similarly the functions $g$ and $h$. I list only the most common subscripts.

| Symbol | Description | Units |
|---|---|---|
| $a$ | **Acceleration** | $\mathrm{m/s^2}$ |
| $\varphi$ | **Angle** | rad |
| $K$ | **Bulk modulus** | GPa |
| | Subscripts **f**, **s**, and **m** for fluid fraction, solid fraction, and matrix (dry modulus). | |
| $\zeta$ | **Cementation exponent** | – |
| $\varrho$ | **Density** | $\mathrm{g/cm^3}$ |
| | Subscripts **f** and **s** for fluid fraction and solid fraction. | |
| $d$ | **Depth** | km |
| $u$ | **Displacement** | m |
| $E$ | **Electric field** | V/m |
| $\varepsilon$ | **Electrical permittivity** | F/m |
| | $\varepsilon_0$ Free space electrical permittivity, $\varepsilon_0 \approx 8.854 \times 10^{-12}$ F/m . | |
| $\epsilon$ | **Error** | – |
| $F$ | **Force** | N |
| $\Xi$ | **Forward model** | – |
| $q_\mathrm{f}$ | **Free charge density** (linear) | C/m |
| $f, \omega$ | **Frequency** | |
| | $f$ Frequency | Hz |
| | $\omega$ Angular frequency, $\omega = 2\pi f$ . | rad/s |

| Symbol | Description | Units |
|---|---|---|
| $\hat{}$ | **Hat** Denotes change of domain from time to frequency. | |
| $j$ | **Imaginary unit**, $j = \sqrt{-1}$ . | – |
| $\kappa$ | **Krief exponent** | – |
| $B$ | **Magnetic field** | T |
| $\mu$ | **Magnetic permeability** | H/m |
| | $\mu_0$ Free space magnetic permeability, $\mu_0 = 4\pi \times 10^{-7}$ H/m. | |
| $m$ | **Mass** | kg |
| $M$ | **Molality** | mol/kg |
| $\mathcal{V}$ | **MTEM: measured voltage response** | V |
| $\mathcal{S}$ | **MTEM: system response** | $\mathrm{A\,m^2}$ |
| $\mathcal{G}$ | **MTEM: earth response** | |
| | $\mathcal{G}^{\mathrm{S}}$ Step response (SR) | $\Omega/\mathrm{m^2}$ |
| | $\mathcal{G}^{\mathrm{I}}$ Impulse response (IR) | $\Omega/(\mathrm{m^2\,s})$ |
| $\mathcal{N}$ | **MTEM: uncorrelated noise** | V |
| $\mathcal{I}$ | **MTEM: measured input current** | A |
| $\phi$ | **Porosity** | – |
| $\rho$ | **Resistivity** | $\Omega\,\mathrm{m}$ |
| | Subscripts **f** and **s** for fluid and solid fraction; subscripts **v** and **h** for vertical and horizontal resistivity. | |
| | $\rho_{\mathrm{m}}$ (Geometric) Mean resistivity, $\rho_{\mathrm{m}} = \sqrt{\rho_{\mathrm{v}}\rho_{\mathrm{h}}}$ . | |
| $r$ | **Radius** | m |
| $\lambda$ | **Resistivity anisotropy**, $\lambda = \sqrt{\frac{\rho_{\mathrm{v}}}{\rho_{\mathrm{h}}}}$ . | – |
| $S$ | Fluid **Saturation** | – |
| | Subscripts **w**, **o**, and **g** for water, oil, and gas saturation. | |
| $\alpha, \beta$ | **Shape and rate parameter in gamma distribution** | – |
| $G$ | **Shear modulus** | GPa |
| | Subscripts **f**, **s**, and **m** for fluid fraction, solid fraction, and matrix (dry modulus). | |
| $k$ | **Stiffness** | N/m |
| $T$ | **Temperature** | °C |
| $t$ | **Time** | s |
| $\psi$ | **Tortuosity factor** | – |
| $v$ | **Velocity** | km/s |
| | Without subscripts it generally stands for P-wave velocity; subscripts **P** and **S** for P-wave and S-wave velocity; subscripts **f** and **s** for fluid and solid fraction. | |

## Functions

### Dirac delta function

$$\delta(t) = 0 \quad \text{if} \quad t \neq 0 \quad \text{and} \quad \int_{-\infty}^{\infty} \delta(t)\,\mathrm{d}t = 1$$

### Fourier transform pair

$$\hat{g}(\omega) = \int_{-\infty}^{\infty} g(t) \exp(-j\omega t)\,\mathrm{d}t$$

$$g(t) = \frac{1}{2\pi} \int_{-\infty}^{\infty} \hat{g}(\omega) \exp(j\omega t)\,\mathrm{d}\omega$$

### Convolution

$$g(t) * h(t) = \int_{-\infty}^{\infty} g(\tau) h(t-\tau)\,\mathrm{d}\tau = \hat{g}(\omega)\hat{h}(\omega)$$

### Error function and complementary error function

$$\mathrm{erf}(x) = \frac{2}{\sqrt{\pi}} \int_0^x \exp\left(-t^2\right)\,\mathrm{d}t$$

$$\mathrm{erfc}(x) = 1 - \mathrm{erf}(x)$$

### Gamma function and gamma distribution

$$f(x) = \frac{\beta^\alpha x^{\alpha-1}}{\Gamma(\alpha)} \exp\left(-\beta x\right) \ , \quad x \geq 0, \quad \alpha, \beta > 0$$

$$\Gamma(x) = \int_0^\infty y^{x-1} \exp(-y)\,\mathrm{d}y$$

## Abbreviations

| | |
|---|---|
| AVA | amplitude variation with angle of incidence |
| CSEM | controlled-source electromagnetic |
| CMP | common midpoint |
| DC | direct current |
| EM | electromagnetic |
| FEM | frequency-domain CSEM |
| GOC | gas-oil contact |
| GPR | ground-penetrating radar |

| | |
|---|---|
| HED | horizontal electric dipole |
| IR | impulse response |
| KDE | kernel density estimation |
| MD | measured depth |
| MT | magnetotelluric |
| MCMC | Markov chain Monte Carlo |
| MTEM | multi-transient electromagnetic |
| NMO | normal moveout |
| NRMSD | normalised root mean square difference |
| OWC | oil-water contact |
| pdf | probability density function |
| PRBS | pseudo-random binary sequence |
| SBL | seabed logging |
| SR | step response |
| TEM | time-domain CSEM |
| TI | transverse isotropy |
| TVDSS | true vertical depth below sea surface |
| UKCS | United Kingdom continental shelf |
| VTI | vertical transverse isotropy |

## Societies

| | |
|---|---|
| EAGE | European Association of Geoscientists & Engineers |
| EGU | European Geosciences Union |
| SEG | Society of Exploration Geophysicists |

## Companies

Companies are solely named by their abbreviations in the thesis.

| | |
|---|---|
| AGO | AGA Geomarine Operations LLC |
| AOA | AOA Geophysics Inc |
| BP | BP plc |
| Britoil | Britoil plc |
| EMGS | ElectroMagnetic GeoServices ASA |
| ExxonMobil | ExxonMobil Corporation |
| Mærsk | Mærsk A/S |
| MTEM | MTEM Ltd |
| OHM | Offshore Hydrocarbon Mapping Ltd |
| PGS | Petroleum Geo-Services ASA |
| RSI | Rock Solid Images plc |
| Schlumberger | Schlumberger Ltd |
| Statoil | Statoil ASA |
| TAQA | Abu Dhabi National Energy Company, PJSC |

# Thesis

# 1

# Introduction

**The purpose of computing is insight, not numbers.**

*Richard Wesley Hamming (1915–1998)*
*Mathematician*

## 1.1 Review

Hydrocarbons are a diminishing resource that is becoming harder to detect. The estimate of our reserves is possibly the biggest uncertainty, but it is a fact that oil companies are finding it harder to discover economically viable resources; the big elephant fields have been discovered.

Hydrocarbons have been used by humans for thousands of years. First they were discovered directly by observing oil seeps at the earth's surface, or gas bubbles rising to the sea surface. But it was not until the second half of the 19th century that the modern era of hydrocarbon exploration and exploitation started. The early, shallow findings were usually exploited with a more or less regular grid of wells. The new industry, arguably launched with the first oil well in the United States of America drilled roughly 20 m deep by Colonel Edwin Drake in 1859, replaced overnight the then massive whale hunting industry. (Whale oil is obtained by boiling strips of whale blubber.) The direct discovery method was replaced by the geologist who studied outcrops and tried to predict, by downward projection of the geology observed at outcrops, possible structural hydrocarbon traps such as anticlines or salt domes. These structural highs were then drilled with so-called wildcats, to see whether or not there was any oil in them. The geologists were joined by the geophysicists in the early 20th century, who used geophysical methods to gain insights into the subsurface, such as seismic reflection, gravity measurements, and well logging.

The seismic method proved so successful that it has become the single most important exploration tool, especially in the marine environment. Massive improvements in seismic acquisition, seismic processing, and in computing power improved quality and quantity of seismic data and enables us today to walk virtually along subsurface horizons as if we would be really there. The rate of water-wet wells, so-called dry wells that produce no or not an economical amount of hydrocarbons, is despite all these improvements about 40 %. Figure 1.1 shows the percentage of water-wet wells compared to successful oil and gas wells in the U.S. from 1973 to 2010. The ratios stagnated during the 1970s and 1980s, but 3D seismic acquisition brought improvements. However, still roughly four out of ten exploration wells are water-wet. One reason is that the big, shallow fields have been discovered. But another reason is the limitation of the seismic method. As good as seismic surveys are in delineating structures, they are often ambiguous or misleading in discriminating between different pore fluids (often because of noise in the data). The seismic signal is almost the same if a potential reservoir is filled with oil or brine, as can be seen in Figure 1.2: seismic P-wave velocity does almost not change if brine is replaced by oil in a potential reservoir. But resistivity is very sensitive to

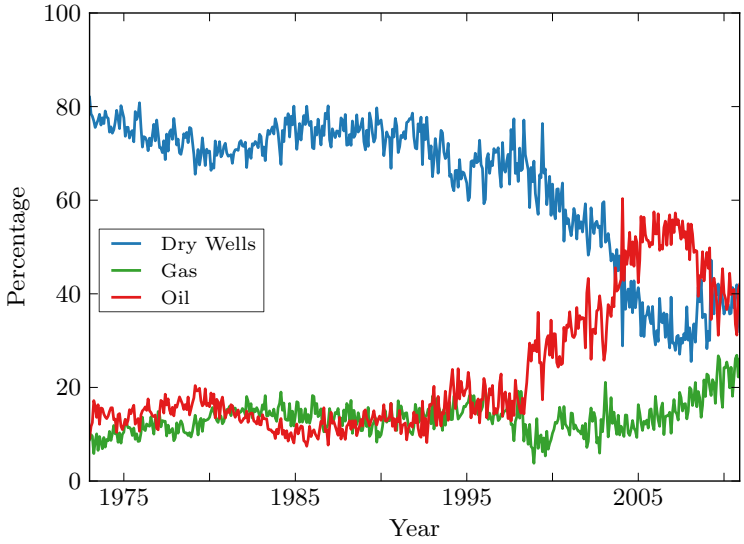


**Figure 1.1:** U.S. exploration drilling success rates. In blue the percentage of water-wet holes, and in green and in red the percentages of successful drillings into gas and oil targets, respectively (source: U.S. Energy Information Administration).

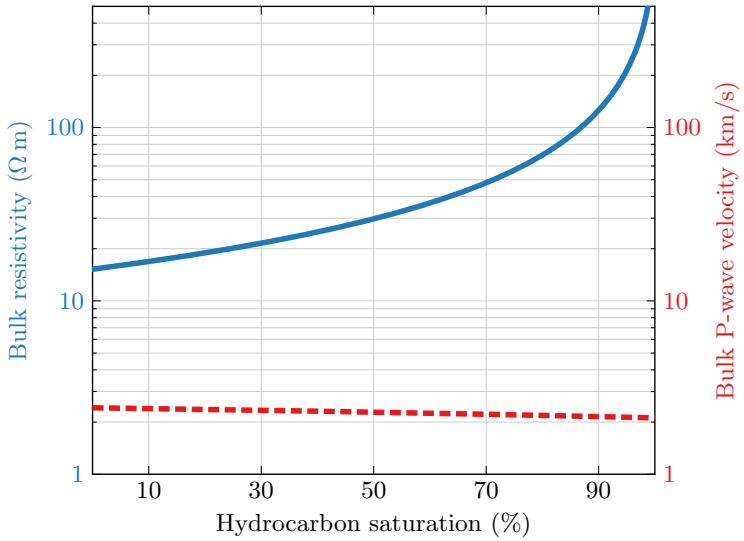


**Figure 1.2:** Influence of hydrocarbon saturation on bulk P-wave velocity (dashed red) and bulk resistivity (solid blue) in a typical sandstone reservoir. Velocity varies only by a few per cent, whereas resistivity changes more than an order of magnitude. See Chapter 3 for detailed information.

these changes, and changes by more than an order of magnitude. The seismic method is better in detecting gas, which yields high amplitudes, so-called bright spots. But even sub-commercial quantities of gas result in bright spots; resistivity can help to distinguish sub-commercial quantities from commercial quantities.

Electromagnetic (EM) methods have been around in hydrocarbon exploration since

the beginning of the 20th century, when Conrad and Marcel Schlumberger began to measure resistivities in wells (which was the start of Schlumberger, today the biggest oil service company). The very first year of the journal *Geophysics*, a publication by the Society of Exploration Geophysicists (SEG), saw a contribution from EM by Statham (1936), entitled "Electric earth transients in geophysical prospecting", who states in the first sentence of his abstract: "A suddenly applied electric current is passed through the earth by means of spaced electrodes", very much what is still done today in EM surveys.

EM surveys were rapidly adopted by the mining industry for the search for conducting sulfides and ore bodies, mainly onshore. It is hence not surprisingly that it was the SEG Mining Committee that initiated the publication of "Electromagnetic methods in applied geophysics" (Nabighian, 1988, 1991), a two-volume book of the state of the art in EM. The targeted audience was mainly the mining industry, but with petroleum, groundwater, and civil engineering in mind as well.

Talking about the controlled-source electromagnetic (CSEM) method we have to consider two different approaches and two different environments. First, there is land and marine CSEM. Second, we have time-domain CSEM (TEM), and frequency-domain CSEM (FEM). The former uses a finite source signal, for instance a pseudo-random binary sequence (PRBS) (Ziolkowski et al., 2011), and measures the transient change of the received signal (a PRBS was already used by (Duncan et al., 1980), but as an infinite sequence and hence FEM). The latter has a continuous source signal, and measures the amplitude and phase for certain frequencies, usually a centre frequency and a few odd harmonics. The two methods are in theory equal, as one can get one from the other through a Fourier transform. However, because of limitations in acquisition and noise this is in reality not possible. The transient signal in TEM can contain the full frequency spectrum (depending on the source signal), which has therefore a clear advantage over FEM. The advantage of TEM is also stressed by Chave et al. (1991), who state that "transient will replace frequency", or by Nekut and Spies (1989), who give a good overview with the title "Petroleum exploration using controlled-source electromagnetic methods". They also mention the power of joint analysis including EM data. The expectation for TEM led to a special section of *Geophysics* in 1984, Nabighian (1984).

The potential of CSEM for mapping was recognised as early as Bannister (1968), who used CSEM to measure the electrical conductivity of the seabed in shallow water. Chave and Cox (1982) tested different source configurations and the results favoured the horizontal electric dipole (HED) for detecting thin resistive layers, which is the standard source configuration today. "An introduction to marine CSEM methods for

hydrocarbon exploration" by Constable and Srnka (2007), but also Edwards (2005) and Ziolkowski and Wright (2012), give an excellent overview of the history and basic theory of marine CSEM. Constable (2010) concludes that CSEM is now well established in the industry, thanks to its sensitivity to resistive feature. And although CSEM has less resolution than seismic data, it has better resolution than potential field methods such as magnetic surveys or gravity surveys. Marine CSEM measurements started in the early 20th century, albeit related to military research in the area of submarines. Academics started to use FEM and TEM in the 1970s for the study of the lithosphere in deep water (e.g. Cox et al., 1986; Edwards et al., 1984; Edwards and Chave, 1986; Cheesman et al., 1987).

The first successful tests of marine CSEM for hydrocarbon exploration were performed west of Africa between 2000 and 2002 (Ellingsrud et al., 2002; Eidesmo et al., 2013; Srnka et al., 2006) in various experiments carried out collaboratively between academia and industry (Scripps Institution of Oceanography, Southampton University, ExxonMobil, Statoil, AOA). This success marked the start of a shift from academia to industry, which shortly resulted in three commercial companies within a year: EMGS was launched by Norwegian oil company Statoil, OHM was a spin-out of Southampton University, England, and AGO was a spin-off of AOA, United States of America. OHM was acquired by EMGS in 2011, and AGO was acquired by Schlumberger in 2004, who later ceased CSEM acquisition. All these companies use FEM, with a stationary receiver-grid on the sea-floor, and a moving source.

From land EM emerged another CSEM method, the multi-transient electromagnetic (MTEM) method, Wright et al. (2002); Ziolkowski et al. (2007). MTEM was founded in 2004 as a spin-out of University of Edinburgh, Scotland, and acquired in 2007 by Norwegian oil service company PGS. A marine MTEM survey consists of an array of receivers laid on the sea-floor, and a source laid on the sea-floor too. The source is moved from shot-point to shot-point, and laid down for the time of acquisition. However, PGS has since reworked their system, and they now offer a fully-towed CSEM system, analogous to marine seismic acquisition.

The advantage of CSEM over the seismic method is its sensitivity to thin, resistive layers, such as hydrocarbon reservoirs. EM propagation is usually described as diffusion, but sometimes also as waves. Løseth et al. (2006) discuss this ambiguity theoretically, with the conclusion that EM propagation can be called diffusion or wave propagation. They state that one has to keep in mind that diffusion in EM field propagation does not include random motion that is often linked with diffusion. And similarly, if described as waves, one has to keep in mind the high dispersion and strong attenuation of these waves.

**Table 1.1:** Physical properties of geophysical exploration methods (adapted from Ziolkowski and Engelmark, 2009). There is no physical property in common in seismic surveying and EM surveying.

| Technique & Theory | Physical Properties | |
|---|---|---|
| **Gravity** | Density | $\varrho$ |
| Newton's law of gravitation | | |
| Laplace's equation | | |
| **Seismics** | Density | $\varrho$ |
| Wave equation: | Bulk modulus | $K$ |
| Hooke's law | Shear modulus | $G$ |
| Newton's laws of mechanics | | |
| **Magnetotellurics** | Magnetic permeability | $\mu$ |
| Laplace's equation | | |
| **Electromagnetics** | Magnetic permeability | $\mu$ |
| Maxwell's equations | Electrical resistivity | $\rho$ |
| | Electrical permittivity | $\varepsilon$ |

There is no theory that allows resistivities to be extracted directly from EM data, in the way we can extract seismic P-wave velocity out of seismic data by lining up the arrivals of adjacent seismic traces (for instance in normal moveout (NMO) corrections or migration). Instead, an initial, made-up resistivity model is adjusted until its calculated electromagnetic response fits the data. This process of iterative forward modelling is termed inversion. But it is important to note that nothing is done to the data in an inversion scheme. The non-uniqueness of CSEM data – several resistivity models fit the data equally well – is a big problem. It is generally solved by assuming the simplest (or smoothest) model. In any case, modelling is a very important part of CSEM analysis. This was recognised very early on, and even before the launch of the marine CSEM industry a book regarding 3D EM modelling was published by the SEG, Oristaglio and Spies (1999). Due to the high computational costs of 3D modelling, 1D modelling and inversions are still very common, but 2.5D and 3D are slowly becoming the standard.

On one side there is the high resolution data of seismic surveying, but sometimes without great sensitivity to pore fluids, and on the other side the sensitivity to resistive layers from CSEM surveys, but with poor resolution. It is therefore desirable to combine these two types of data. Unfortunately, seismic and EM data share no common physical parameters, as Ziolkowski and Engelmark (2009) point out, see Table 1.1. Gravity data and seismic data both depend on the density of the rocks in the subsurface, and they can successfully be analysed together (e.g. Ursin et al., 2003; Lelièvre et al., 2012). But there is no such fundamental link between CSEM data and seismic data.

In summary, Figure 1.1 shows why we would like to improve our understanding of the subsurface, Figure 1.2 explains why CSEM data are the right addition to seismic data, and Table 1.1 reveals why this task is not straightforward.

The usual approach is to apply rock physics to link the two different data sets for a joint inversion (Hoversten et al., 2006), or use the gradient of the two kinds of data sets to align structural similarities in the cross-gradient method (Gallardo and Meju, 2007; Hu et al., 2009). There exists a large variety of rock-physics models, theoretical and empirical, which are usually calibrated to a certain geological setting. Carcione et al. (2007) give an overview of the variety of different models. The interest in joint inversion has also led to new developments of cross-properties (Han et al., 2011) and refinements for existing relations (Engelmark, 2010). Any uncertainty in the input parameters or in the models introduces unwanted bias to a joint inversion; this effect was investigated by Chen and Dickens (2009).

Most of these research results work in the parameter space, where the goal is to get a model of porosity and fluid saturations mainly within the reservoir. Nobody tried to get a resistivity model from seismic data and subsequently verified it by comparing its resulting CSEM responses with acquired data. And there has certainly been no joint analysis using MTEM data.

## 1.2 Claim

The purpose of my thesis is to establish, test, and verify a workflow to estimate background resistivities from seismic velocities, and use these resistivities to predict CSEM responses. Using additional data for the analysis of CSEM data is not fundamentally new, as the afore mentioned examples have shown. Srnka et al. (2006), for instance, present a 3D resistivity model that is "developed by iterative 3D modelling guided by the 3D seismic data (background), log data from wells (...), and the full frequency-offset spectrum of the CSEM data", but they do not explain this guidance at all.

I derive background resistivities that are consistent with the known seismic velocities, which are the best and most detailed information of the local area. More detailed but very sparse are well logs, which I use for calibration and verification. I develop a velocity-to-resistivity transform which is achieved by using rock-physics relations to transform velocities into porosities, and porosities into resistivities. Rock properties such as pore-fluid resistivity or bulk and shear moduli are generally a function of depth (i.e. temperature, pressure) and of lithology. I capture these depth-dependences by including depth-trends into the rock-physics transform, and further include structural

constraints from seismic horizons. I calibrate this transform with a well log, and then apply it to an adjacent field, where I check the calibration with available well logs from that field. Uncertainty is ubiquitous in geophysics. An important part of the transform is to estimate the involved uncertainty. Every rock-physics model, theoretical or empirical, is in error, not just because of errors of measurement, but also because there is no physical link between seismic velocities and resistivities (Table 1.1). It is therefore important to estimate the error of the transform, which includes the error of the rock-physics model, the error of the estimated rock parameters, and the data error. Many of the uncertainties are not well known and have to be estimated. It is therefore necessary to use a Bayesian framework, which allows parameters to be expressed as probability distributions rather than fixed values. I apply the method of Chen and Dickens (2009) to assess the uncertainty of the transform. This yields resistivities in the form of a probability density function (pdf) instead of a deterministic value, for any point in the subsurface. This is particularly useful for feasibility studies, where one is interested in the likelihood that a potential reservoir can be detected with a CSEM survey.

The background resistivity model gained in this way has some weaknesses. First, that outside well coverage the control is insufficient. Theoretically, depending on for instance the chosen depth trends, any resistivity range could be created outside the well-controlled area. Of course this is not what happens, as one wants to achieve a realistic model and hence makes sensible assumptions. However, there is no control how good these assumptions are. Second, the calculated resistivities represent primarily horizontal resistivities. This is because the calibration well is a nearly vertical well, which mainly measures horizontal resistivities (Chemali et al., 1983). The calibration of the model therefore yields horizontal resistivities. I use short offset 1D modelling to test and improve the shallow part of the background model. Short offsets are only sensitive to the shallow subsurface. The shallow subsurface at the Harding oil and gas field in the North Sea consists of relatively flat sedimentary layers, permitting a 1D earth assumption. I use step and impulse response inversions to define the anisotropy value, and invert the impulse responses to improve the shallow section of my background resistivity model.

The last part is 3D modelling and comparison to real data. I carry out a feasibility study with my detailed background resistivity model, and predict the acquired CSEM data. As I have uncertainty estimates, I can do this for the most likely case, but also for lower and upper error bounds. Finally, I compare these modelled data with the measured data. This comparison shows that this workflow is able to predict CSEM responses fairly accurately; the acquired responses are generally within plus and minus one standard deviation of the predicted responses.

The novelty of my approach is twofold: First, I combine many methods: rock physics, depth trends, structural information, uncertainty analysis, and using seismic horizons, seismic velocities, and well data for calibration and control. Second, I use MTEM data to improve my background model outside the well coverage, and get an estimate of anisotropy. Finally, I compare this 3D background model to the MTEM data. Such CSEM predictions are useful for feasibility studies, survey planning, and acquisition quality control (QC), if seismic data are at hand before acquisition. These predictions can help to interpret the acquired data and serve as starting model and constraints in inversions. The presented workflow is a guide. It has to be adjusted for the field of interest, and it can be scaled up or down, depending on available data at hand. It is another example of today's awareness of the importance of the interplay between geophysicists, geologists, and petrophysicists in any exploration project.

To make research results reproducible is important for their credibility (e.g. Fomel and Claerbout, 2009). Every result, every figure, and the thesis itself can be reproduced, and I created an extensive manual for the corresponding `Python` codes.

## 1.3 Agenda

Following this introduction is a discussion of seismic data and CSEM data in Chapter 2. Seismic velocities can be extracted directly from seismic data, an advantage that sets the seismic method above all other geophysical methods. It is the only method where the geophysical property can be extracted directly from the physical measurements. But its sometimes poor discrimination of pore fluids requires the incorporation of additional methods, for instance EM measurements. The chapter also contains an overview of previous research, on which the foundation of this thesis are partly built. An important part of the presented workflow is rock physics and its uncertainty, on which I elaborate in Chapter 3, where I also introduce the Bayesian framework. The workflow is applied to acquired data from the North Sea Harding field, which I introduce in Chapter 4. It is followed by the velocity-to-resistivity transform in Chapter 5, where I apply the derived rock-physics transform including the Bayesian uncertainty analysis to the Harding field to get a background resistivity model. This chapter was published in Werthmüller et al. (2013a), and is re-printed here with minor stylistic changes. However, parts of the publication that fit better into other chapters have been moved accordingly.

I then improve and test my derived resistivity background model in the two following chapters with the measured EM responses from the Harding field. In Chapter 6 I use one-dimensional modelling to improve the shallow part of the model and get an estimate of the anisotropy. The shallow part has to be improved because I lack well control in this

section. I have to get an estimate of anisotropy because the well logs represent horizontal resistivity. Three-dimensional modelling with the final background model in Chapter 7 yields the best estimate of the Harding field, and I compare these synthetic responses with the measured data. A 3D feasibility study reveals that the Harding reservoir is at the edge of being detectable by CSEM. However, the responses calculated from the updated background resistivity model predict the acquired data very accurately. I draw my discussion and conclusions in Chapter 8, where I also consider other work published since I started my thesis, hence other approaches that have evolved in parallel. I discuss the steps that work very well and can easily be implemented, but also the steps that have to be handled with care. Furthermore I emphasise once more the advantages and limitations of my approach.

The appendix contains a variety of interesting things that do not fit into the main body of work. I put complementary theory into Appendix A; theory that is not necessary to follow my thesis, but helps to understand it fully and is necessary to reproduce my results. In Appendix B I look into what I coined extrema analysis, where I attempt to use the arrival time of the peaks of MTEM impulse responses and apply ray theory to them. The last appendix, Appendix C, contains some explanations regarding reproducibility, data, and software. The results from the entire project, including this thesis and every figure, can be reproduced. The necessary `Python` codes come with an extensive manual. However, most data and some (crucial) software is proprietary, but I point to free- and open-source alternatives, and freely available data.

Chapter 5 is a published paper (Werthmüller et al., 2013a), as mentioned before, but the publication contains also bits of other chapters. I gave additionally oral presentations of the progress of my research at the European Association of Geoscientists & Engineers (EAGE) conference 2012 (Werthmüller et al., 2012b) and the SEG conference 2012 (Werthmüller et al., 2012a), and a poster presentation at the European Geosciences Union (EGU) conference 2013 (Werthmüller et al., 2013b). Parts of Chapters 4, 6, and 7 have been submitted to the journal *Interpretation* by the SEG, for a special topic issue regarding "Interpretation and integration of CSEM data".

■

# 2

# Seismic data and CSEM data

**It is essential to the possibility of induction that we shall be prepared for occasional wrong decisions.**

*Harold Jeffreys (1891–1989)*
*Statistician and Geophysicist*

---

Seismic data obey the wave equation and seismic velocities can be determined directly from the data by lining up arrivals. Controlled-source electromagnetic (CSEM) data obey the diffusion equation and there are no distinct arrivals to line up from which resistivities may be estimated. This advantage makes the results from seismic data more trustworthy when it comes to subsurface properties, and it is therefore desirable to link seismic data with CSEM data in order to enhance the interpretation of the latter. But the physical parameters of the seismic wave equation are different from those in the electromagnetic diffusion equation, which means that there is no direct link between the governing equations. In this chapter I review the approaches others have taken to combine these two different data sets and explain how my approach differs. Using a Bayesian approach to estimate a detailed resistivity model that is in agreement with seismic velocity and well logs significantly reduces the bias from constraints applied in standard CSEM inversions. More importantly, these estimated resistivities can be used to model CSEM responses which can be directly compared with acquired CSEM data.

---

## 2.1 The advantage of the seismic method

Seismic data acquisition and processing is the main geophysical tool in hydrocarbon exploration and has been for decades. In the marine case, a source is towed behind a vessel, emitting an acoustic wave. This wave propagates through the water and the subsurface, and its reflections and refractions are recorded at various receivers, which are also towed behind the vessel. In the land case, sources and receivers are placed on the surface. An exhaustive description of seismic data processing, inversion and interpretation is given in Yilmaz (2001).

Seismic data are acquired to reveal the structure of the subsurface. In order to do so one needs to know the seismic velocities. This is where the seismic reflection method has a unique advantage over all other geophysical methods, which is one of the reasons why it is the standard tool for exploration. It is possible to extract this physical property, velocity, directly from the data by aligning arrivals in the data, measured at different distances from the source. Normal moveout (NMO) is the most obvious example of this, as shown in Figure 2.1. Figure 2.1a shows a schematic seismic layout, with a source at position $x_0$, and receivers at positions -$x_1, \ldots, x_6$. Their corresponding rays are also shown, indicating the path from the source to the receivers via reflection from a horizontal boundary at depth $d$. The boundary is a change in acoustic impedance, which is the product of seismic velocity and density. The measured signals at the receivers are

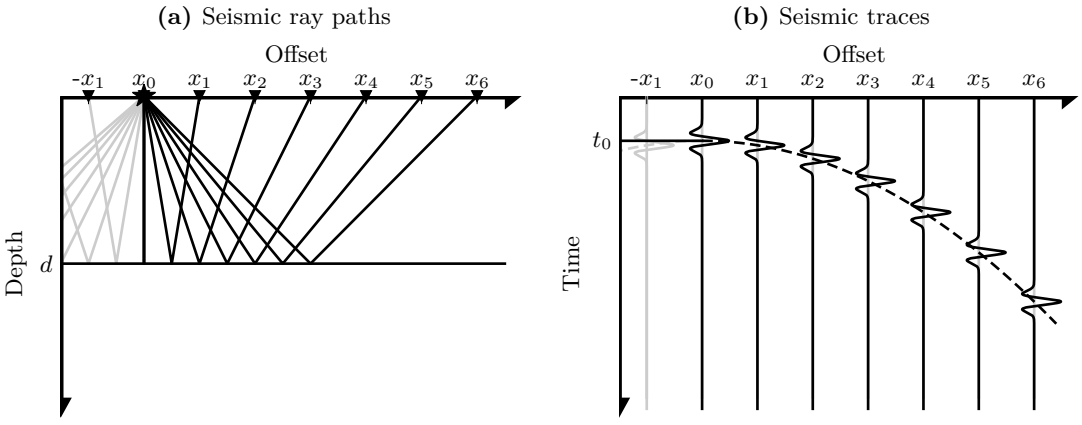


**Figure 2.1:** The advantage of seismic exploration: (a) shows one shot point with several receivers, and their corresponding ray paths which are reflected on a horizontal layer boundary. (b) shows their corresponding traces with their corresponding normal-moveout curve. These arrivals will only line-up for the correct velocity.

shown in Figure 2.1b, where the wavelets show a typical NMO curve, described by

$$t^2(x) = t^2(0) + \frac{x^2}{v^2} \ , \tag{2.1}$$

where $t(0) = 2d/v$, the normal-incidence two-way traveltime, $t(x)$ is traveltime, $x$ is offset, and $v$ the velocity. The arrivals will line up only for the correct velocity. Hence shifting the data around reveals the velocity of the layer above the boundary. It not only reveals the velocity, but also the horizon at depth $d$.

NMO correction is one processing tool. But aligning arrivals occurs also in migration, which is like inversion, an iterative process, where the data is moved according to a velocity model. Reflectors will only collapse if the velocity model is correct, otherwise the velocities have to be adjusted (because the arrivals do not line up but produce, for instance, "smiles"). Nevertheless, the seismic exploration method has weaknesses too. One weakness is the restricted illumination as measurements are taken from one side only, the surface. This is a general problem of non-intrusive geophysical methods. Another, more seismic-specific limitation is the weak sensitivity to changes in pore fluids: seismic velocities of oil and brine are very similar (see Chapter 3 for more details).

It is desirable to combine different geophysical methods to gain a better understanding of the subsurface physical properties. CSEM has become a complement to seismic data acquisition in the last decade, mainly due to its sensitivity to resistivity, and hence its ability to distinguish between conductive brine and resistive hydrocarbons. But the CSEM method lacks the ability of direct extraction of the physical property, resistivity, from the data. The interpretation of CSEM data is done by either special ways of displaying the data, for instance subtracting an estimated background response from the responses, or by inversion, which is another term for iterative forward modelling. In this process, one assumes an initial model or guess, calculates its response at the same source-receiver locations as the measured data, calculates the misfit between this response and the measured data, and adjusts the model in order to minimise the difference between the synthetic and the measured data, the error. The resulting resistivity model tends to depend a lot on the choice of starting model, the definition of the error, the criteria when this error is small enough, and the rules on adjusting this initial guess. The measured CSEM data are never modified during this process, only the assumed model changes. Sometimes, mainly in the land case, the real data are even multiplied by some "fudge factors" to make them match the synthetic data more closely. This is called "static shift" (e.g. Linfoot et al., 2007).

Choosing a starting model and defining rules on how to update a model leaves lots of room for ambiguity, a problem that is exacerbated by the non-uniqueness of CSEM

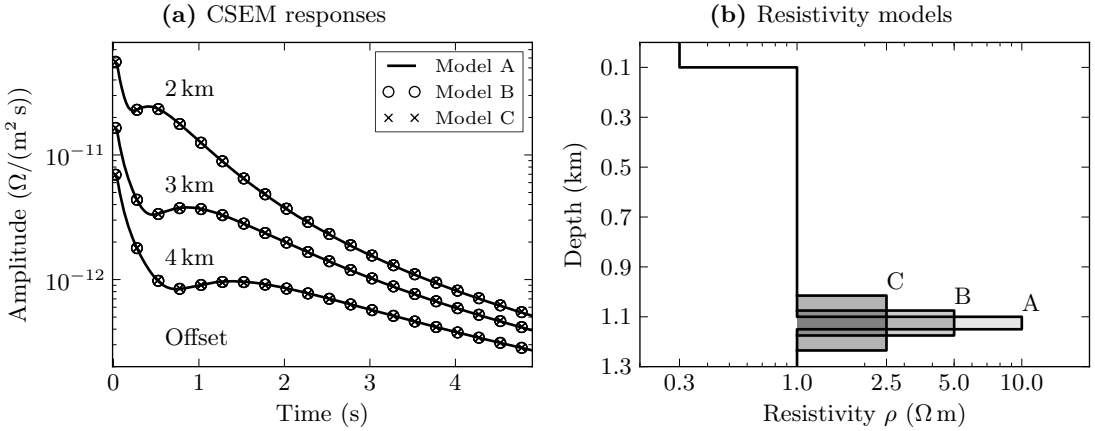


**Figure 2.2:** (a) responses from three resistivity models given in (b) for offsets of 2, 3, and 4 km. In general, an infinite number of resistivity model fit a CSEM response. Constraints are therefore a requirement for the interpretation of CSEM responses. Usually, an initial model is only adjusted minimal to fit the data. A good and accurate initial model is therefore crucial.

methods, as shown in Figure 2.2. Three CSEM responses at offsets of 2, 3, and 4 km are shown in (a), and as can be seen, they are basically identical, but originate from three different isotropic models, which are shown in (b). One could define an infinite number of models which would result in the same response in 1D as shown, and even more models could be found in 3D. (Having responses from multiple offsets decreases the non-uniqueness to some extent; however, taking anisotropy into account increases it again.) Combining the non-uniqueness with the shortcomings in CSEM processing shows that the initial model has to be close to the true model, otherwise the inversion will find a model that fits the data but has very little to do with reality. This is why we would like to combine seismic data and CSEM data. The combination of seismic data and CSEM data is unfortunately not straightforward. To see this, we have to look at the underlying theories of these two methods.

The general wave equation, which describes the propagation of sound and light, and for instance also the movement of water waves, is given by

$$\nabla^2 u = \frac{1}{v^2} \frac{\partial^2 u}{\partial_t^2} \ . \tag{2.2}$$

It describes the displacement $u$ as a function of position and time, where $v$ is the speed of the wave (e.g. Riley et al., 2006). For the seismic method it describes the P-wave with the assumption of a linear and isotropic medium, neglecting gravity and velocity gradients, and the speed of the wave is given by $v_\mathrm{P} = \sqrt{(K + 4G/3)/\varrho}$ ; $K$, $G$ are the bulk and shear moduli, respectively, and $\varrho$ the density of the rock.

The wave equation can be derived from Hooke's law and Newton's second law of motion. Hooke's law states that stress is proportional to strain, or in other words, the displacement $u$ is proportional to the applied force $F$,

$$F = ku \ , \tag{2.3}$$

where $k$ is the stiffness of the body (N/m).

Newton's second law of motion states that the acceleration $a$ is directly proportional to the used force $F$,

$$F = ma = m\frac{\partial^2 u}{\partial t^2} \ , \tag{2.4}$$

where $m$ is the mass of the body.

The electromagnetic (EM) wave equation, which is a damped wave equation, can be derived from Maxwell's equations for linear media inside matter (in differential form, following Griffiths (1999)),

$$\nabla \cdot E = \frac{q_\mathrm{f}}{\varepsilon} \ , \qquad \text{Gauss's law,} \tag{2.5}$$

$$\nabla \cdot B = 0 \ , \qquad \text{Gauss' law for magnetism,} \tag{2.6}$$

$$\nabla \times E = -\frac{\partial B}{\partial t} \ , \qquad \text{Faraday's law of induction,} \tag{2.7}$$

$$\nabla \times B = \frac{\mu E}{\rho} + \mu\varepsilon\frac{\partial E}{\partial t} \ , \qquad \text{Modified Ampère's law ,} \tag{2.8}$$

where $q_\mathrm{f}$ is the free charge density. The free charge dissipates almost immediately in conductive media, and we can assume therefore that

$$\nabla \cdot E = 0 \ . \tag{2.9}$$

By taking the curl of Equation 2.7,

$$\nabla \times (\nabla \times E) = \nabla \times \left(-\frac{\partial B}{\partial t}\right) \quad \Rightarrow \quad \nabla (\nabla \cdot E) - \nabla^2 E = -\frac{\partial}{\partial t}(\nabla \times B) \ , \tag{2.10}$$

and inserting Equations 2.9 and 2.8, we get

$$\nabla^2 E = \mu\varepsilon\frac{\partial^2 E}{\partial_t^2} + \frac{\mu}{\rho}\frac{\partial E}{\partial_t} \ , \tag{2.11}$$

where $E$ is the electric field, and $\mu, \varepsilon, \rho$ are the magnetic permeability, electrical permittivity, and electrical resistivity, respectively. The second term on the right-hand side is the loss-term. In a "perfect" resistor, such as a vacuum, where resistivity is infinite,

this term vanishes, and the equation becomes the wave equation that describes the propagation of light in vacuum (Equation 2.2 with $v = 1/\sqrt{\mu_0 \varepsilon_0}$, which is the speed of light).

Transforming Equation 2.11 into the frequency domain results in

$$\nabla^2 \hat{E} = -\omega^2 \mu \varepsilon \hat{E} - j\omega \frac{\mu}{\rho} \hat{E} \ , \tag{2.12}$$

where the hat denotes frequency domain. This notation reveals the frequency dependence: with the low frequencies used in CSEM measurements (less than 10 Hz),

$$\omega \ll \frac{1}{\rho \varepsilon} \ , \tag{2.13}$$

and the first term on the right-hand side in Equation 2.12 (and therefore also in Equation 2.11) vanishes. This is why it is sometimes referred to as a diffusion equation rather than a wave equation when speaking about EM (for a discussion see Løseth et al., 2006).

Even though the underlying theories of seismic wave propagation and EM wave propagation look mathematically similar, they share no physical property. The seismic wave is a function of the density and the elastic moduli of the rock. The EM wave is a function of magnetic permeability, electrical resistivity, and electrical permittivity of the rock. The two equations are not linked directly.

The exception of the discussed advantage of the seismic method over all other geophysical methods is ground-penetrating radar (GPR), often also called geo-radar or ground-probing radar, which has some of the same advantages as reflection seismology, even though it is an EM method. However, GPR uses very high-frequency pulses (about 0.1 - 1.5 GHz), with the result that the first term in Equation 2.11 is large enough to have wave propagation. But GPR can only penetrate centimeters to metres into the ground because of the loss term, which is still present. Because GPR utilises EM waves instead of acoustic waves, the reflections result from boundaries with different dielectric constants, instead of different acoustic impedances.

## 2.2 Approaches to combine seismic data with EM data

A simple and commonly used way to combine these two data types is to analyse them jointly after processing each data set independently; usually the CSEM inversion result is displayed on top of a seismic section, which allows an interpreter to get a better idea of the complete picture. However, the data are only combined in the display, it is not a

link between the two data sets. There are two ways to truly tackle the lacking physical link between seismic and CSEM data: structural constraints and parameter constraints. Structural constraints make use of seismic boundaries or structural similarities between the two data sets. Parameter constraints make use of rock physics to bridge the gap of the non-existent link in the physics; I treat rock physics in more detail in Chapter 3. Both constraints can be exploited in different ways, and often a combination of the two is used. I summarise in the following some common approaches, which have been published prior to this project.

### Structural constraints

The straightforward approach to include a structural constraint is to take the finished interpretation of a seismic section and extract a structural model for the subsurface. This model can be used to define the layer boundaries of either a starting model for an inversion of CSEM data, or as constraints therein. The inversion of EM data will then yield the resistivity of the layers defined by this seismic interpretation. Jegen et al. (2009) present a study where they jointly invert magnetotelluric (MT) and gravity data, using seismic data as "a priori constraints". They extract layer boundaries from seismic data, and use them to define the layers of the starting model for the joint inversion, hence structural constraints. But they also apply parameter constraints by calculating starting resistivities from seismic data, using linear relationships derived from well logs. They claim that this approach improves the final result, specifically in revealing the top and bottom of a thick basalt layer. They also conclude with one of the big issues I see in these joint methods, the relative weighting of the two data sets. Although this joint inversion was done with MT and gravity data, it heavily depends on the relative weight given to these two data sets, even though their resolution is much more alike than seismic data and CSEM data.

Another structural constraint is the cross-gradient method, which assumes that the trends for both velocity and resistivity are similar. Meju et al. (2003) report their findings on "evidence for correlation of electrical resistivity and seismic velocity in heterogeneous near-surface materials". They follow up on their findings in Gallardo and Meju (2007), where they present a joint 2D cross-gradient imaging method, using MT and seismic traveltime data, but it is equally applicable to CSEM and seismic reflection data. The main idea behind their approach is that if seismic velocities change, resistivities should change too, either in the same direction or in the opposite direction. And if seismic velocities stay constant, resistivities should stay constant too, and vice versa. The method consists of three steps. (1) each data set should simultaneously minimise its cost function in its own linearised inversion scheme. (2) the MT and

seismic models should be structurally identical. In mathematical terms, this is ensured by setting the cross-gradient to zero,

$$\nabla \boldsymbol{\Xi}_{\mathrm{MT}}(x, y, z) \times \nabla \boldsymbol{\Xi}_{\mathrm{S}}(x, y, z) = 0 \ , \tag{2.14}$$

where $\Xi_{\mathrm{MT}}$ and $\Xi_{\mathrm{S}}$ are the modelled data for MT and seismic traveltime, respectively. They state that the major convenience for a purely geometrical approach is the total independence of any correlation that may exist between the parameter themselves. (3), the models should be as simple as necessary to fit the data, a general assumption in inversion schemes, known as Occam's razor. They conclude that the cross-gradient technique can be successfully adapted to the problem of joint 2D inversion of collocated MT and seismic data from measurements at different spatial scales, and that it leads to models that are in better structural accordance and closer to the reality than those derived from separate inversion of MT and seismic data.

The cross-gradient method is applied for instance by Hu et al. (2009) for joint inversion of CSEM and seismic data in an iterative manner. (1) one inversion routine for every data set is carried out individually. (2) the cross-gradient of the updated P-wave velocities and the updated resistivities is taken, and a second inversion routine is carried out for the resistivities. (3) the cross-gradient of the updated resistivities with the P-wave velocities is taken and a second inversion routine is carried out for the P-wave velocities. If the cost-function does not match any stopping criteria, steps (2) and (3) are repeated.

### Parameter constraints

Another way of linking seismic data and CSEM data is by using rock physics. Rock physics is defined by Sheriff (2002) as the *Study of rock properties and their interrelation based on rock, core, or log samples. Also called petrophysics.* In the combination of seismic and CSEM data, rock physics can be used to transform seismic velocities and electric resistivities to other rock properties, for instance porosity or fluid saturation.

One way to combine the two data sets is to include them both in the same cost function, the function which is to be minimised in an inversion scheme. Viriglio et al. (2010) use this approach for a simultaneous joint inversion of seismic and MT data in a complex sub-salt case. For this they include in the cost function the residuals and the constraints of the individual domains, and several interdomain constraints, which is where rock physics is used. They claim that the joint inversion improves the quality of the seismic migration and reduces uncertainty in the inversion. This method of joint inversion with a single cost function is straightforward to implement. The difficulties with it, however,

are twofold: the weighting of the two individual data sets, and the accuracy of the link between the two.

The most common application of the joint analysis of seismic and CSEM data is the estimation of reservoir parameters. The estimation is quite often carried out in a Bayesian framework (e.g., Chen et al., 2007). Hoversten et al. (2006) present a 1D joint-inversion algorithm to estimate reservoir parameters using both seismic amplitude variation with angle of incidence (AVA) data and CSEM data. They emphasise that AVA can distinguish if there is gas or not, but fails to distinguish between commercial and noncommercial gas accumulations. Resistivity is, on the other hand, insensitive to small quantities of hydrocarbons, but is sensitive when a substantial quantity of hydrocarbons is present. The reservoir is parameterised by porosity $\phi$, and by fluid saturations $S_w$, $S_\mathrm{g}$, and $S_\mathrm{o}$ for water, gas, and oil, respectively. The AVA model is further parameterised for a zone above the reservoir by seismic pressure and shear wave velocities $v_\mathrm{P}$ and $v_\mathrm{S}$ and density $\varrho$. The CSEM model is parameterised for the whole overburden and underburden by the electrical resistivities $\rho$. Layer thicknesses and pore pressure in the target could be inversion parameters too. They solve the inversion as a nonlinear least-squares problem, where they use the first spatial derivatives of the model parameters as regularisation matrix. They admit that the benefits of jointly inverting AVA and CSEM data are more striking in synthetic data than with real data. However, they show that combined inversion does result in values which are closer to the logged ones for $S_\mathrm{g}, S_\mathrm{o}$ and porosity, but $S_\mathrm{g}$ is resolved better with CSEM inversion only.

Hou et al. (2006) build on the same work, but they use a stochastic inversion in a Bayesian framework instead of a linearised inversion. They state that the advantage of the stochastic approach is that the outcome is not a single deterministic value, but a probability density function (pdf), which is useful for a rigorous evaluation of uncertainty and its consequences.

The effects of uncertainty in this approach is analysed in detail by Chen and Dickens (2009), who investigate the likely bias caused by linking two non-related geophysical parameters with a rock-physics model. They state that joint inversions may produce misleading results if the biases in rock-physics models and their corresponding parameters are unknown. This is mainly due to the nonlinear and non-unique relationship between geophysical and reservoir parameters. The right choice of rock-physics model is therefore crucial, and even then they might introduce uncertainty and biases. For the chosen rock-physics model (the model is parameterised similar to the one by Hoversten et al. (2006)) they derive a joint posterior pdf in a Bayesian framework and explore it by using Markov chain Monte Carlo (MCMC) sampling. They do the same analysis not just for uncertainties in rock-physics models, but also for uncertainties in rock-physics

model parameters themselves. They state that this distinction between uncertainty in rock-physics models and uncertainty in rock-physics model parameters is rarely made, but that the actual uncertainty is the sum of both. I adapt their approach to build my Bayesian framework in Chapter 3, and apply it in Chapter 5.

### Commercial investigations

Given the limitation of CSEM data on its own, there is a great incentive for companies that build their business on CSEM data or use CSEM data for exploration to invest a lot to explore the possibilities of joint analysis of seismic and CSEM data. However, not a lot of these results are published, and if so, then they are in case-study focused journals like *The Leading Edge* or *First Break*, where the emphasis is on showing results rather than on the methodology and the theory behind it.

ExxonMobil acknowledges in Srnka et al. (2006) that CSEM has considerable value when integrated carefully with other geoscientific information. They show an example of a resistivity model that was developed by iterative 3D modelling guided by the 3D seismic data (background), log data from wells, and CSEM data. But that is all they reveal.

Statoil and EMGS use 3D seismic data, well logs, and rock physics to derive background resistivities in order to calculate the effect of $CO_2$ injection to CSEM data in a synthetic study (Norman et al., 2008). In a similar study they use seismic data, well logs and rock physics to predict horizontal resistivities, and compare these to CSEM inversion results (Brevik et al., 2009). (Although the main purpose of this acquisition was to show the advantages and disadvantages of different acquisition forms such as dense versus sparse receiver grid or 2D versus 3D acquisition.)

OHM and RSI use well logs, seismic data and CSEM data for feasibility studies and gas estimation (Walls and Shu, 2008; Harris et al., 2009). They conclude that seismic data on its own cannot distinguish between a non-commercial low case saturation of 30 % and a gas-filled case saturation of 100 %, whereas a careful joint inversion of seismic and CSEM data, calibrated with well logs, is able to.

PGS emphasises the problem of the non-existent physical link between seismic and CSEM data (Ziolkowski and Engelmark, 2009), and shows the rock-physics way to overcome it (Engelmark, 2010), by also emphasizing the importance of resistivity background modelling.

### Resolution and coverage issues

The non-existent physical link is not the only problem in combining seismic data with EM data. Another issue is the difference in data resolution. Due to the diffusive behaviour and the low frequencies used in CSEM, usually less than a few hertz, the resolution of CSEM data is very low. Seismic data yield sharp layer boundaries, whereas EM inversion usually results in a blurred image (unless it is constrained); the resolution of the seismic data is probably more than a magnitude higher than that of EM data.

Newman and Commer (2010) present a roadmap to a joint-inversion approach using the Laplace-Fourier domain for the seismic data; the Laplace-Fourier domain approach for seismic data is based on Shin and Cha (2009). The transform acts principally as a low-pass filter, changing the seismic wave field from propagation to diffusion. The cost of this process is that high-frequency information, such as sharp layer boundaries, is lost. The advantage is, that the seismic data and EM data have the same resolution, which puts them on equal footing in a joint inversion. This might indeed lower the problem of weighting in a joint inversion. For the actual inversion they use the cross-gradient approach, as described earlier.

Another issue of geophysical data analysis is coverage, as mentioned before. We usually probe the subsurface non-intrusively from the surface, which yields a poor illumination and raises the issue of non-uniqueness. Crosswell studies have a slightly better illumination, where the sources and receivers are placed in wells which results in an improved, but very local, coverage. Hoversten et al. (2003), for instance, combine seismic and EM data to predict changes in water saturation, pressure, and $CO_2$/oil ratio during $CO_2$ flooding of a reservoir. For this they create a very detailed rock-physics model using a sweep of log measurements. Crosswell studies are able to yield much more detail than joint analysis of seismic and CSEM data on an exploration scale. However, they are more suited for monitoring than for exploration.

## 2.3 My approach

The research presented above involves, in one way or another, the inversion of CSEM data. One way is to use seismic data to derive structural constraints or starting models for the CSEM inversion, and another way is to invert seismic data and CSEM data separately for reservoir parameters, and then combine or constrain the results in the reservoir parameter space.

The drawback of structural constraints is that seismic boundaries (changes in acoustic impedance) are not necessarily the same as resistivity boundaries, and this constraint

biases the inversion. The same applies for cross-gradient models, where we assume that one property changes if the other does, which is not necessarily true. Parameter constraints are biased by the accuracy of the chosen rock-physics model, and often by the weighting of the different data sets. This is why the Bayesian approach is the right approach for this problem: there is a lot of prior information and uncertainties that have to be taken into account.

My approach differs in that it is not a primary goal to invert CSEM data, and I am, at this point, not directly interested in porosity or fluid saturations either. The idea is to use the available knowledge, seismic data and well logs, to derive a detailed resistivity model and calculate its CSEM responses. These responses, together with the estimated uncertainty, should be accurate enough so that they can be compared directly with the responses from subsequent CSEM acquisitions. Any deviation between the acquired and the predicted responses is a resistivity anomaly that can be interpreted with the given geological setting.

Even though the primary goal is not inversion, the result can be used in inversions too. The resistivity model can be used as a starting model, or as a fixed background model. More importantly, the resulting pdfs can be used to constrain the background in a stochastic inversion. Using the complete pdfs will significantly reduce the bias due to the non existing physical link between the two data sets.

## Summary

Seismic data have an advantage over all other geophysical methods, because one can extract a physical property directly from the data by aligning arrivals. Furthermore, the resolution of seismic data is superior to the resolution of CSEM data. It is therefore desirable to combine these two methods in order to get a better understanding of the properties of the subsurface. But this is not an easy task, as there is no common physical parameter in the underlying theories of the two methods. The topic is of high interest, and I have summarised published research on this topic. I approach the problem from a different angle, as I intend to predict CSEM responses from seismic data without an inversion. Using a Bayesian framework allows me to incorporate all available knowledge of the area, and estimate the involved uncertainty. The resulting pdfs can then be used to calculate the range of possible CSEM responses and to interpret the acquired CSEM data.

■

# 3

# Rock physics and its uncertainty

**The true logic of this world is in the calculus of probabilities.**

*James Clerk Maxwell (1831–1879)*
*Physicist*

Seismic wave propagation and electromagnetic wave propagation share no physical property, but rock physics can be used to link the two empirically or with theoretical models. I review and compare the most common rock-physics transforms to get bulk resistivity out of bulk P-wave velocity either directly or via porosity. These transforms are not a real, physical link, and it is therefore crucial to asses the uncertainty of the resulting resistivities. I apply a Bayesian approach to include the uncertainty of the transforms and the involved rock-physics parameters. This results in resistivities in the form of probability density functions, which provide an idea of the most likely resistivity values, given the available data and knowledge.

## 3.1 Bridging the non-existent link

In Chapter 2 (Seismic data and CSEM data) I make two main points. First, we cannot, as of today, extract resistivity directly from controlled-source electromagnetic (CSEM) data, in the same way that we can extract velocities directly from seismic data by lining up arrivals. Second, there is no physical link between CSEM and seismic data, but it is desirable to link these two methods in order to improve our understanding of the subsurface. CSEM data are, in contrast to seismic data, very sensitive to resistivity variations. A combined analysis of these two data sets can therefore help to determine whether a potential hydrocarbon reservoir is filled with resistive hydrocarbon or with conductive brine.

Figure 3.1 highlights the difference in sensitivity of P-wave velocity (dashed red) and electrical resistivity (solid blue) to hydrocarbon saturation. If hydrocarbons replace brine, resistivity values change more than an order of magnitude, whereas velocity values vary only by a few per cent. For the diagram I set porosity to 40 %, and mixed the fluid properties successively from 100 % brine to 0 % brine; the rock parameters are listed in Table 3.1. In this simple example I used the arithmetic mean of the oil and brine properties to calculate the fluid bulk modulus and density, and the harmonic mean to calculate the fluid resistivity, hence the arithmetic mean for the corresponding conductivities. I used the Gassmann model to calculate bulk velocity, and the self-similar model to calculate bulk resistivity (see Chapter 5 for more details regarding the Gassmann and self-similar models). A very similar and often cited figure was published by Wilt and Alumbaugh (Figure 1b, 1998), where they plot laboratory measurements from a sandstone core rather than rock-physics relations. The conclusion is the same for laboratory measurements as for the shown theoretical model.

Rock physics is generally used to bridge this gap, the non-existent link between geophysical observations and the physical properties of the rocks. In the case of P-wave velocities and electrical resistivities this is usually done in two steps: First, velocities are transformed into porosities, and second, porosities are transformed into resistivities. But direct relations exist as well. Direct models are always empirical models (as there is no physical link), whereas for the two-step approach both empirical and theoretical

**Table 3.1:** Material properties used in Figure 3.1, see Symbols and Abbreviations for units (from Carcione et al., 2007, Table 1).

| $\rho_s$ | $\rho_{oil}$ | $\rho_{brine}$ | $K_s$ | $K_{oil}$ | $K_{brine}$ | $G_s$ | $\varrho_s$ | $\varrho_{oil}$ | $\varrho_{brine}$ |
|---|---|---|---|---|---|---|---|---|---|
| $10^{-3}$ | $10^{-5}$ | 2.5 | 39 | 0.57 | 2.25 | 40 | 2.65 | 0.7 | 1 |

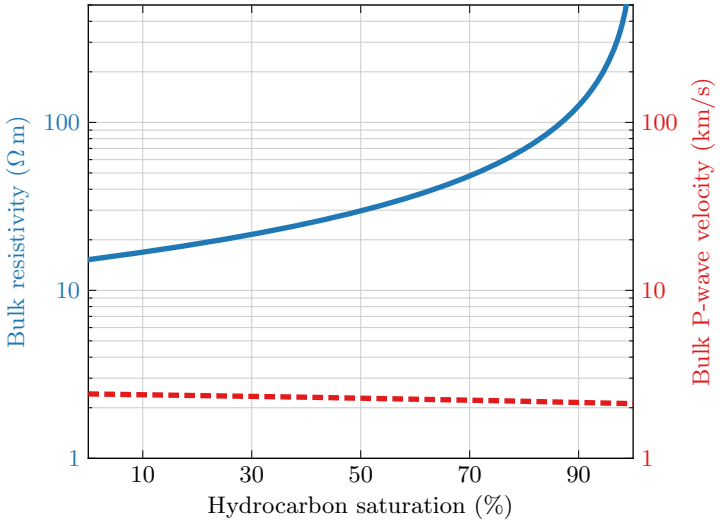


**Figure 3.1:** Influence of hydrocarbon saturation to bulk P-wave velocity (dashed red) and bulk resistivity (solid blue) in a typical sandstone reservoir. Velocity varies only by a few per cent, whereas resistivity changes more than an order of magnitude.

models exists. However, in doing so we have to carefully assess the uncertainty, because it is not a true physical link, but either a theoretical or an empirical relationship.

In this chapter I show the principle idea of rock-physics transforms, and list the most common ones. The focus here is on simple models with few parameters, in order to demonstrate a simple workflow to obtain CSEM responses from seismic data. The rock-physics transform is one component of that workflow, which can be exchanged with a more complex model if necessary. These transforms generally have to be calibrated to a specific regime, such as pressure and temperature. I then explain the uncertainty analysis that I apply to these rock-physics models, which I do in a Bayesian framework. My workflow is used to obtain a background resistivity model (because I assume brine saturated pores for the rock-physics transforms) from seismic velocities using a combination of rock physics, structural constraints (in the form of depth trends and seismic horizons), and uncertainty analysis. I demonstrate the application of the workflow in Chapter 5 with data from the North Sea Harding field.

## 3.2 Rock-physics transforms

Rock-physics transforms can be used to build a relation between two unrelated rock properties, such as P-wave velocity $v_P$ and resistivity $\rho$,

$$\rho = g_1(v_P) \ , \tag{3.1}$$

where $g_1$ is an empirical relation. In the case of resistivity and P-wave velocity this is usually, but not always, done via porosity (e.g. Carcione et al., 2007): velocity is transformed into porosity, and porosity is transformed into resistivity,

$$\phi = g_2(v_\mathrm{P}) \ , \qquad \rho = g_3(\phi) = g_3\left[g_2(v_\mathrm{P})\right] \ . \tag{3.2}$$

Here, $g_2$ and $g_3$ are either empirical or theoretical relations. Empirical transforms are derived from curve fitting of extensive (laboratory or well log) measurements. Theoretical relations are based upon the specification of the properties of the individual constituents, their volume fractions, and their geometrical arrangement. A special case of theoretical relations are bounds, which yield theoretical upper and lower limits without the need to specify the geometry. They represent the upper and lower limit of all possible geometries.

Most relations in the literature include conductivity, not resistivity. However, we are interested in resistive bodies rather than conductive bodies in the exploration of hydrocarbons. I therefore express all my equations in terms of resistivities.

Rock-physics models assume some knowledge of the subsurface in addition to the P-wave velocities gained from well logs or seismic processing. This additional information may come from well logs, laboratory measurements on core samples, the literature, or from experience. The most frequently used ones are the P-wave velocity of the pore fluid and of the grains (solid fraction), $v_\mathrm{f}$ and $v_\mathrm{s}$ respectively, and the resistivities of the pore fluid and the grains, $\rho_\mathrm{f}$ and $\rho_\mathrm{s}$. Furthermore, the density of the pore fluid and of the grains, $\varrho_\mathrm{f}$ and $\varrho_\mathrm{s}$ respectively; the bulk density of the saturated rock is then given by

$$\varrho = (1-\phi)\varrho_\mathrm{s} + \phi\varrho_\mathrm{f} \ , \tag{3.3}$$

where $\phi$ is porosity. If the densities of the rock and its constituents are known, the porosity can be determined by,

$$\phi = \frac{\varrho - \varrho_\mathrm{s}}{\varrho_\mathrm{f} - \varrho_\mathrm{s}} \ . \tag{3.4}$$

Some relations make use of the bulk modulus and the shear modulus of the rock, $K$ and $G$. These models require the bulk modulus of the pore fluid and the grains, $K_\mathrm{f}$ and $K_\mathrm{s}$, and the shear modulus of the grains, $G_\mathrm{s}$ (the fluid shear modulus $G_\mathrm{f}$ is zero). The P-wave velocity is defined with these moduli as

$$v = \sqrt{\frac{K + 4G/3}{\varrho}} \ . \tag{3.5}$$

Some models require the moduli for the dry rock, $K_\mathrm{m}$ and $G_\mathrm{m}$, which are the characteristics of the bulk rock with its matrix structure, but without pore fluid or gas. These properties are obviously not in-situ properties of a rock, but come from laboratory measurements.

### Mixture theories

Rocks are generally inhomogeneous materials, a mixture of different minerals and voids filled with pore fluids. All components of a rock have different physical properties. Rock-physics mixture theories try to estimate the property of a rock from its individual components, e.g. the P-wave velocity of a rock from the P-wave velocities of its minerals and pore fluids. Mixture models are averages between the different constituents. The simplest of these models are the arithmetic mean (AM), the geometric mean (GM), and the harmonic mean (HM):

$$x = \sum_{i=1}^{n} p_i x_i \qquad \Rightarrow \qquad x = \phi x_\mathrm{f} + (1-\phi) x_\mathrm{s} \qquad \text{AM}, \tag{3.6}$$

$$x = \prod_{i=1}^{n} x_i^{p_i} \qquad \Rightarrow \qquad x = x_\mathrm{f}^{\phi} x_\mathrm{s}^{(1-\phi)} \qquad \text{GM}, \tag{3.7}$$

$$x = \left( \sum_{i=1}^{n} \frac{p_i}{x_i} \right)^{-1} \qquad \Rightarrow \qquad x = \left( \frac{\phi}{x_\mathrm{f}} + \frac{1-\phi}{x_\mathrm{s}} \right)^{-1} \qquad \text{HM}. \tag{3.8}$$

Here, $x$ is the quantity to average, and $p$ is the volume fraction. I consider solely a solid fraction and a fluid fraction, hence $n = 2$ for $x_\mathrm{f}$ and $x_\mathrm{s}$, where $x$ can be either P-wave velocity or resistivity. For positive numbers the inequality between these means is AM $\geq$ GM $\geq$ HM. It is insightful to notice that the harmonic mean is the inverse of the arithmetic mean and vice versa. This means that, for example, the arithmetic mean of resistivities is the same as the harmonic mean of the respective conductivities, or the arithmetic mean of the velocities is the same as the harmonic mean of the respective slownesses.

Figure 3.2 illustrates the idea of averaging. (a) shows the simplest model of a rock, uniform circular grains, just touching the four closest neighbours. In this (2D) case the porosity is $\phi = 1 - \pi/4 \approx 21.5\,\%$. The two simplest theoretical models to calculate the bulk properties are (b) the arithmetic mean, and (c) the harmonic mean. They correspond to two separate fractions, one pure solid and one pure liquid, arranged in series or in parallel, respectively. A good introduction to mixture theories is given by Berryman (1995). Carcione et al. (2007) give a nice overview of velocity-to-resistivity

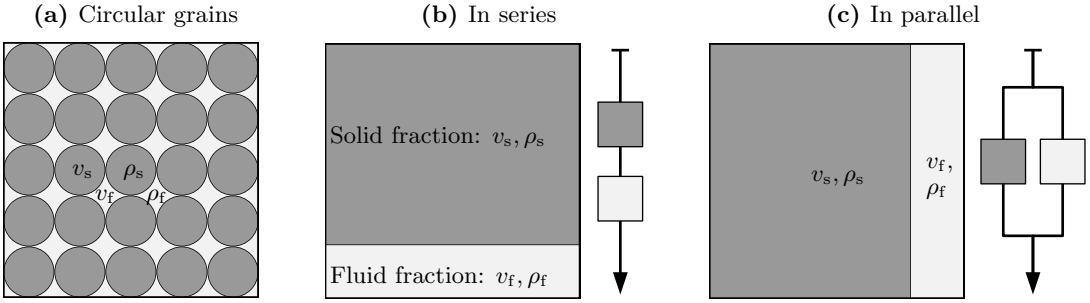


**Figure 3.2:** The idea of averaging to obtain bulk properties: (a) shows the simplest rock model (in 2D), aligned circular grains; this rock has porosity of $\phi = 1 - \pi/4 \approx 21.5\,\%$. The simplest averages correspond to two completely separate fractions in series (b) and in parallel (c).

cross-property relations. An extensive introduction to rock-physics is given by *The Rock Physics Handbook: Tools for Seismic Analysis of Porous Media*, Mavko et al. (2009).

## Porosity from velocity

I am interested in obtaining resistivities from velocities. Mixing models, however, generally derive velocity as a function of porosity and the velocities of the solid and the fluid phases. Some models can easily be rearranged, others have to be calculated iteratively. I list both of them, if there is an easy relation for porosity as a function of velocity.

The simplest models are the averages, as described previously. The harmonic mean of the solid and fluid P-wave velocities is known as the *Wyllie equation* (Wyllie et al., 1956), also called the *time-average equation*,

$$v = \left(\frac{\phi}{v_f} + \frac{1-\phi}{v_s}\right)^{-1}, \qquad \phi = \frac{v_f}{v}\left(\frac{v - v_s}{v_f - v_s}\right). \tag{3.9}$$

The *Raymer equations* are a set of empirical relations for different ranges of porosity, given by Raymer et al. (1980). The relation for porosities $\phi < 37\,\%$ is given by a modified version of the arithmetic mean,

$$v = (1-\phi)^2 v_s + \phi v_f, \qquad \phi = \frac{-\sqrt{4v_s(v - v_f) + v_f^2} + 2v_s - v_f}{2v_s}. \tag{3.10}$$

There are many more empirical relations than the Wyllie and Raymer equations just shown, Gardner et al. (e.g. 1974); Castagna et al. (e.g. 1985); Han et al. (e.g. 1986). However, these are equations which take other parameters, such as clay content or effective pressure, into account. They often contain three or more constants which are

found by curve fitting. Wyllie and Raymer, on the other hand, provide simple relations in terms of the velocity only.

The *Acoustic Formation Factor equation (AFF)* by Raiga-Clemenceau et al. (1988) provides a simple relation in terms of $v_s$ only,

$$v = (1-\phi)^{\zeta} v_s \ , \qquad \phi = 1 - \left(\frac{v}{v_s}\right)^{1/\zeta} \ . \tag{3.11}$$

The ratio $v/v_s$ is termed *acoustic formation factor*, and $\zeta$ is the cementation exponent. Issler (1992) suggests $\zeta = 2.19$ and $v_s = 4.5\,\mathrm{km/s}$; that is why the AFF model is sometimes referred to as the Issler model (e.g. Engelmark, 2010). (Note the similarities with the later described Archie equation.) The AFF is a simpler version of the Raymer equation given in Equation 3.10, neglecting the velocity of the fluid fraction.

The *Hashin-Shtrikman bounds* provide a measure of the bulk and shear moduli without specifying the shape of the grains. Hashin and Shtrikman (1963) derive their bounds from mixture models of the elastic moduli, rather than of the velocities. These bounds define the upper and lower bounds of the physically possible values of these moduli, and hence of velocity. Following Berryman (1995) for two constituents (fluid and solid) yields

$$K^- = \left(\frac{\phi}{K_f} + \frac{1-\phi}{K_s}\right)^{-1} \ , \tag{3.12}$$

$$K^+ = \left(\frac{1-\phi}{K_s + \frac{4}{3}G_s} + \frac{\phi}{K_f + \frac{4}{3}G_s}\right)^{-1} - \frac{4}{3}G_s \ , \tag{3.13}$$

for the bulk moduli, and

$$G^- = 0 \ , \tag{3.14}$$

$$G^+ = \left(\frac{1-\phi}{G_s + \eta} + \frac{\phi}{\eta}\right)^{-1} - \eta \ , \qquad \eta = \frac{G_s}{6}\left(\frac{9K_s + 8G_s}{K_s + 2G_s}\right) \ , \tag{3.15}$$

for the shear moduli. The Hashin-Shtrikman bounds yield, together with Equation 3.5 and the bulk density, the porosity for a given P-wave velocity in an iterative manner.

### Porosity to Resistivity

Mixture theories usually describe resistivity as a function of the different constituents and their volume fraction. I provide the relations also to yield porosity, if a non-iterative solution exists.

*Archie's law* is an empirical relationship given by

$$\rho = \psi \rho_\mathrm{f} \phi^{-\zeta} \ , \qquad \phi = \left( \psi \frac{\rho_\mathrm{f}}{\rho} \right)^{1/\zeta} \ , \tag{3.16}$$

where $\zeta$ is the cementation exponent, and $\psi$ is termed the tortuosity factor. Archie (1942) found this relationship empirically by analyzing resistivity measurements in the laboratory. He examined clean reservoir sandstones, and Archie's law hence holds for shale-free, porous sandstones, where $\zeta$ is close to 2, and $\psi$ is 1. The tortuosity factor is often (mis-)used to make Archie's law work for shaley sandstones. (The ratio $\rho/\rho_\mathrm{f}$ is termed *resistivity formation factor*. Note the similarities to the above described AFF equation.)

The *Hermance model* is an adaptation of Archie's law. It takes the resistivity of the grains into account with the harmonic mean,

$$\rho = \left( \frac{\phi^\zeta}{\rho_\mathrm{f}} + \frac{1-\phi^\zeta}{\rho_\mathrm{s}} \right)^{-1} \ , \qquad \phi = \left[ \frac{\rho_\mathrm{f}}{\rho} \left( \frac{\rho - \rho_\mathrm{s}}{\rho_\mathrm{f} - \rho_\mathrm{s}} \right) \right]^{1/\zeta} \ . \tag{3.17}$$

The only difference between Hermance (1979) and the harmonic mean is the cementation exponent $\zeta$, which weights the solid fraction higher than the fluid fraction. Similar models are the *Glover model* (Glover et al., 2000) and the *Complex Refractive Index Method CRIM* (Schön, 1996). They just differ by the exponents for porosity and resistivity values.

The *Hashin-Shtrikman bounds* provide upper and lower limits if the geometry is not specified (Hashin and Shtrikman, 1963). For the case of two constituents (solid and fluid) they are given by Berryman (1995),

$$\left.\begin{aligned} \rho^- &= \left[ \left( \frac{(1-\phi)\rho_\mathrm{f}\rho_\mathrm{s}}{\rho_\mathrm{f} + 2\rho_\mathrm{s}} + \frac{\phi\rho_\mathrm{f}}{3} \right)^{-1} - \frac{2}{\rho_\mathrm{f}} \right]^{-1} \\ \phi^- &= \left( \frac{\rho - \rho_\mathrm{s}}{\rho_\mathrm{f} - \rho_\mathrm{s}} \right) \left( \frac{3\rho_\mathrm{f}}{2\rho + \rho_\mathrm{f}} \right) \end{aligned} \right\} \quad \text{lower bound, and} \tag{3.18}$$

$$\left.\begin{aligned} \rho^+ &= \left[ \left( \frac{(1-\phi)\rho_\mathrm{s}}{3} + \frac{\phi\rho_\mathrm{f}\rho_\mathrm{s}}{2\rho_\mathrm{f} + \rho_\mathrm{s}} \right)^{-1} - \frac{2}{\rho_\mathrm{s}} \right]^{-1} \\ \phi^+ &= \left( \frac{\rho - \rho_\mathrm{s}}{\rho_\mathrm{f} - \rho_\mathrm{s}} \right) \left( \frac{2\rho_\mathrm{f} + \rho_\mathrm{s}}{2\rho + \rho_\mathrm{s}} \right) \end{aligned} \right\} \quad \text{upper bound.} \tag{3.19}$$

These bounds are true if $\rho_\mathrm{f} < \rho_\mathrm{s}$, which is generally the case if conductive brines are in the pores. The bounds are reversed if $\rho_\mathrm{s} < \rho_\mathrm{f}$, and the upper bound becomes the lower, and vice versa. Other elastic bounds are, amongst others, Kuster Töksov (which

are the same as Hashin-Shtrikman in the case of two components), or Voigt-Reuss.

### Resistivity from velocity

To gain resistivities from velocities, any combination of the presented velocity-to-porosity models and porosity-to-resistivity models yields, in principle, a velocity-to-resistivity transform.

An often cited model that calculates resistivity directly from velocity, without porosity as the connecting parameter, but with a depth dependence is the *Faust equation* (Faust, 1953), given by

$$\rho = \frac{\rho_\mathrm{f}}{d}\left(\frac{v}{2.289}\right)^6 , \tag{3.20}$$

where $d$ is depth in km. The reason it is frequently used is, besides the simplicity, its depth trend, which often makes it work fairly well.

Figure 3.3 shows examples of these rock-physics transforms: (a) the Wyllie and AFF models for velocity to porosity, (b) the Archie and Hermance models for porosity to resistivity, and (c) the Wyllie/Hermance combination and the Faust model for velocity to resistivity. The figure also indicates some characteristics and possible pitfalls of these transforms. An important point is that theoretical models have the logical assumption that velocity equals $v_\mathrm{s}$ if porosity is 0 %, and equals $v_\mathrm{f}$ if porosity is 100 %; a similar argument applies to resistivity. The models therefore go from the solid properties (0 % porosity, no fluids) to the fluid properties (100 % porosity, only fluids), as indicated by the blue dots. This is not true for the empirical models, indicated by the red dots. This means for instance that if the velocity-to-porosity transform yields a very low porosity, the Archie model would result in unrealistically high resistivities. (From Equation 3.16 it can be seen that $\rho_\mathrm{Archie} \to \infty$ for $\phi \to 0$.) The grey area in (c) indicates where the intermediate porosity would be higher than 45 %. This is why the intermediate porosities should always be restricted or observed, as the resulting resistivities might look absolutely reasonable, while the porosities used for them may not be realistic.

More figures showing these velocity-to-porosity, porosity-to-resistivity, and velocity-to-resistivity transforms are shown in Chapter 5, where Table 5.1 lists also the rock parameters used for Figure 3.3.

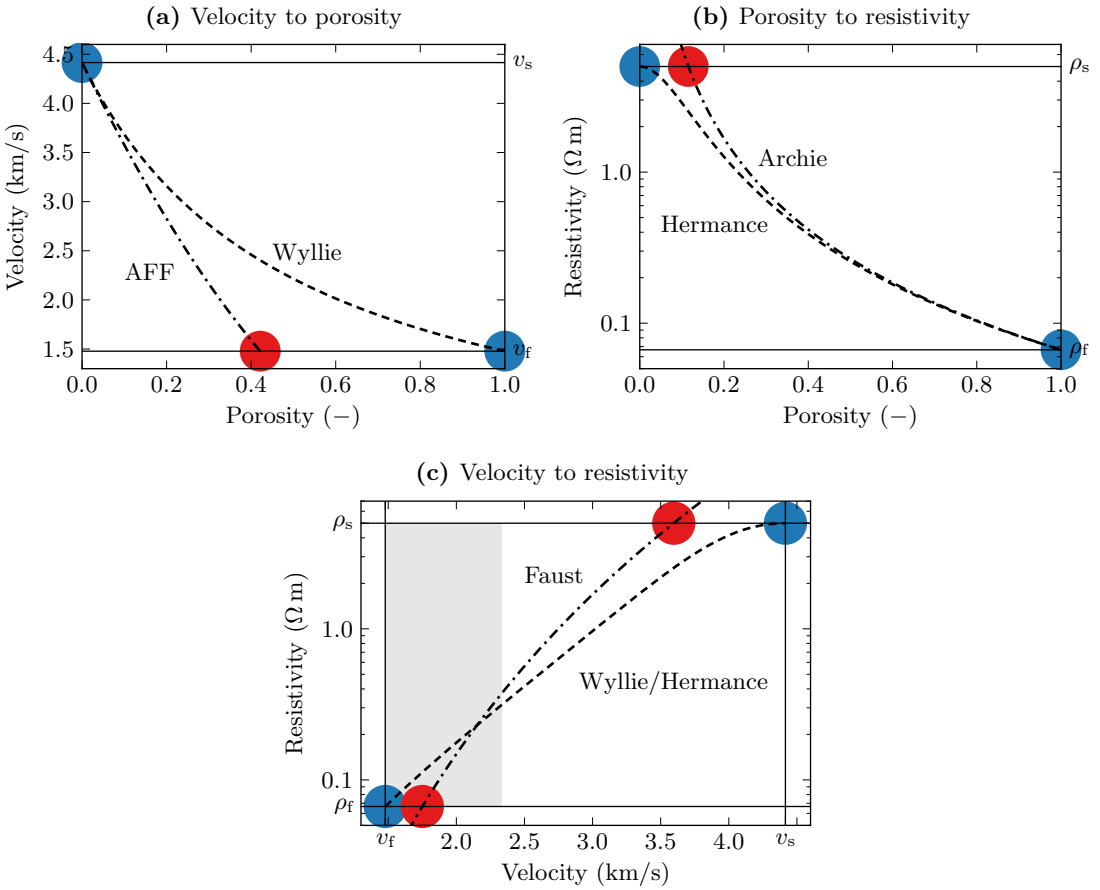


**Figure 3.3:** Rock-physics transforms. (a) velocity to porosity with Wyllie and AFF, (b) porosity to resistivity with Archie and Hermance, and (c) velocity to resistivity with Wyllie/Hermance and Faust. The grey shaded area in (c) indicates where the intermediate porosity of the Wyllie/Hermance model is above 45 %. (Parameters listed in Table 5.1.)

## 3.3 Uncertainty

Uncertainty is ubiquitous in geophysics. Our measured data have errors. Our model of the Earth is always an idealised and simplified one. Also, as in the case of seismic and electromagnetic (EM) data acquisition, we often try to image the subsurface from the surface alone. The illumination is therefore solely from one side, which leaves us generally with a non-unique problem. (Compare this with computed tomography, CT scan, in medical imaging. It applies the same underlying theory of wave propagation, but has the advantage of 360° illumination, which results in very sharp, detailed images.)

Probability is the mathematical tool to quantify uncertainty. The vast number of unknowns, which is usually overcome with experience and guesses, is what makes Bayesian probability (also called probability of causes or inverse probability) an ideal tool for

geophysics. The father of Bayesian probability, Thomas Bayes, thought of including our understanding and knowledge of uncertainty into our calculations. His idea was posthumously published by Richard Price (Bayes and Price, 1763), and it was Laplace (1774) who put it on a sound mathematical foundation,

$$h(x|y) = \frac{h(y|x)h(x)}{h(y)} \qquad \Rightarrow \qquad \text{posterior} = \frac{\text{likelihood} \cdot \text{prior}}{\text{normalization}} \ , \tag{3.21}$$

where x is the model (or outcome) and y is the data vector. The posterior $h(x|y)$ is the probability of the outcome $x$ given data $y$. The likelihood of data $y$ given the model $x$ is described by $h(y|x)$, and the prior $h(x)$ describes our knowledge of the model independently of the data. Bayesian theory states that the posterior is proportional to the likelihood times the prior. The normalization $h(y)$, a constant, ensures that the probability of all possible outcomes sums up to one. The strength in this equation is that if new data are available, the old posterior becomes the new prior information, and the model can be updated with the new information.

The total probability of all possible outcomes $\mathbf{x}$ is then given by

$$h(\mathbf{x}|y) = \frac{h(y|\mathbf{x})h(\mathbf{x})}{\sum_i h(y|x_i)h(x_i)} \ . \tag{3.22}$$

Note that the likelihood is a function of the data, whereas the posterior is a function of the parameters. In contrast to frequentist probability, where only measured data are included into the statistics, Bayesian probability allows us to input parameters as random variables of a probability density function (pdf). An example: Instead of saying that a parameter has the discrete value of 10, one can describe it as a stochastic variable of a uniform distribution between 0.9 and 1.1, hence 10 $\pm$10 %. Or one can describe it as a stochastic variable of a normal distribution with mean equal to 10, and a certain variance. In Bayesian statistics, $z = 10$ represents our best knowledge or estimate of the variable $z$, and we express our best estimate of the associated uncertainty with the characteristics of a probability distribution.

The theory of Bayes was almost forgotten several times, despite the many application areas where decisions have to be made with very little or no data at all at hand, mainly due to the attacks by believers in frequentist probability. A very readable review of Bayes, rather historical than mathematical, is given in *The theory that would not die* by McGrayne (2011), where she states that "*It was a geophysicist, Harold Jeffreys, who almost singlehandedly kept Bayes alive during the anti-Bayesian onslaught of the 1930s and 1940s*". This shows that Bayes' theory has been used in geophysics for a long time. This is possibly not very surprising, given the large number of uncertainties involved in geophysics and the often limited amount of data available. Jeffreys famous

book *Theory of probability* (Jeffreys, 1983, first published in 1939) was revised and translated into modern mathematics by Christian et al. (2009). A good introduction to Bayesian probability and Markov chains with regards to geophysics is given in Sen and Stoffa (1995, Chapter 1), and the short note by Tarantola (2006) is worthwhile reading.

### Uncertainty in rock-physics transforms

Estimating the uncertainty is essential, in any case but especially in velocity-to-resistivity transforms, as there is no physical link between velocity and resistivity. This means that not only do the involved parameters have a certain error, but the rock-physics model itself is erroneous. Chen and Dickens (2009) propose a Bayesian workflow, which I adapt here for my problem. They use rock-physics transforms to go from resistivities and from elastic bulk and shear moduli into the parameter space, e.g. porosity or water saturation, where they use different ways to assess the uncertainties of the different transforms. I treat the velocity-to-resistivity transform as one model, regardless of whether it consists of two cascaded models or one direct model. This model has a certain uncertainty, which I describe with a gamma distribution. A gamma distribution is well suited for one-sided distributions $[0, \infty]$, and is defined as

$$g(\rho_\mathrm{m}) \;=\; \frac{\beta^\alpha \rho_\mathrm{m}^{\alpha-1}}{\Gamma(\alpha)} \exp\left(-\beta\rho_\mathrm{m}\right) \;, \quad \rho_\mathrm{m} \geq 0, \quad \alpha, \beta > 0 \;, \tag{3.23}$$

for the model resistivity $\rho_\mathrm{m}$. It is characterised by the shape parameter $\alpha$ and the rate parameter $\beta$. (The gamma distribution is sometimes given in terms of $k$ and $\theta$, where $k = \alpha$ is the shape parameter, and $\theta = 1/\beta$ is termed the scale parameter. See e.g. section 1.3.6.6.11 of the *NIST/SEMATECH e-Handbook of Statistical Methods*, `http://www.itl.nist.gov/div898/handbook/eda/section3/eda366b.htm` [accessed 3 June 2013].) The mean and variance are given by $\alpha/\beta$ and $\alpha/\beta^2$, respectively. The gamma function $\Gamma$ is defined as

$$\Gamma(\alpha) = \int_0^\infty y^{\alpha-1} \exp(-y)\,\mathrm{d}y \;, \tag{3.24}$$

as given in Olver et al. (2010a, Equation 5.2.1).

Chen and Dickens (2009) propose to define the shape parameter as a function of our estimated error $\epsilon$ of the rock-physics transform, and the rate parameter as a function of the error and the outcome of the rock-physics model,

$$\alpha = \frac{1}{\epsilon^2} \;, \qquad \beta = \frac{\alpha - 1}{\rho_\mathrm{rp}} \;, \tag{3.25}$$

where $\rho_{\mathrm{rp}}$ is the resulting resistivity from the transform.

Remember that the outcome of the rock-physics model is a function of the rock-physics parameters. In the case of the Faust model, for instance, we can describe $\rho_{\mathrm{rp}}$ as

$$\rho_{\mathrm{rp}} = h(v, \rho_{\mathrm{f}}) \ . \tag{3.26}$$

I defined these parameters, $v, \rho_{\mathrm{f}}$, as distributions rather than scalar values, including the best knowledge and estimate of the uncertainty. So in order to get the pdf of the resulting resistivity, including parameter and model uncertainty, we have to integrate over the whole parameter space,

$$g(\rho) = \int g(\rho_{\mathrm{m}}|\mathbf{p}) g(\mathbf{p}) \, \mathrm{d}\mathbf{p} \ , \tag{3.27}$$

where $\mathbf{p}$ contains all parameter distributions. Note that this yields a multi-dimensional integral if more than one parameter distribution is involved.

### Calculating the probability density function

The multi-dimensional integral in Equation 3.27 (the dimensionality depends on the number of parameters described as pdf), which includes the calculation of the gamma distribution in Equation 3.24, cannot be calculated numerically with existing standard computers, due to numerical underflow and machine precision. Another way of evaluating the integral is to sample it with a Markov chain Monte Carlo (MCMC) sampler. Monte Carlo integration samples an integral with random values, and calculates the integral from the ratio of samples that fall within the integral and the ones that are outside the integral. For a sufficiently large number of random calculations, Monte Carlo integration approximates the true value according to Bernoulli's *Law of Large Numbers* (e.g. Bolthausen and Wüthrich, 2013), which says that the average of a sufficiently large number of trials approximates the expected value. For example, if you throw a die many times, the average will approximate 3.5.

Monte Carlo integration can take a long time, and sophisticated algorithms exist to speed it up. One of them is MCMC. The numbers are not random in a Markov chain, but the next set of parameters depends only on the present set of numbers, and has no knowledge of previous ones. Some of the well known MCMC methods are the Metropolis-Hastings algorithm and the Gibbs sampler. I use `PyMC`, a `Python` package, for the MCMC sampling, described in Patil et al. (2010) (see also Appendix C.3). The default Markov transition in `PyMC` is a Metropolis-Hasting walk.

Figures 3.4 and 3.5 show a simple example of the approach, using the Faust model

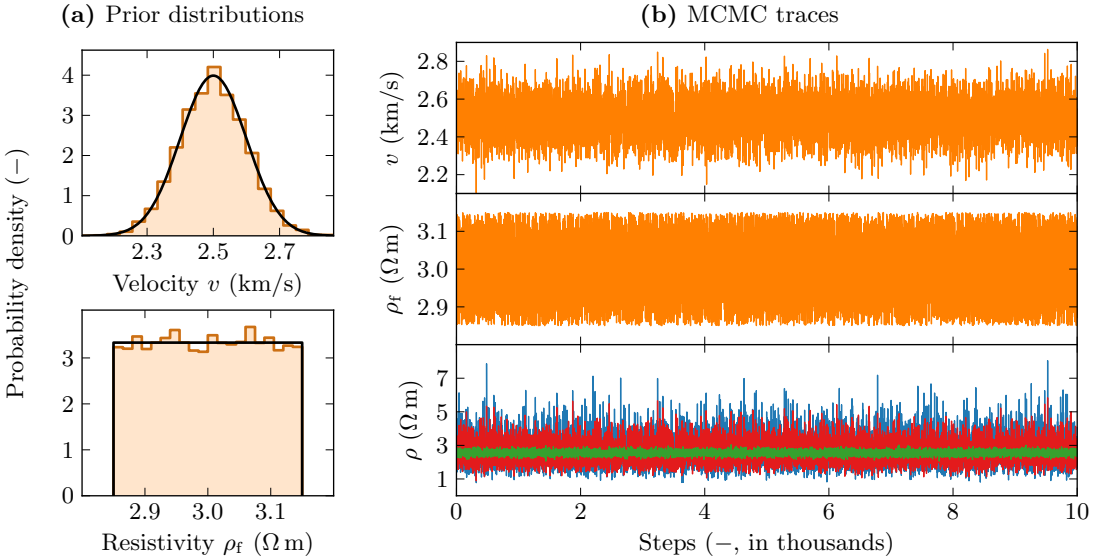


**Figure 3.4:** (a) prior sampling of normal distributed P-wave velocity and uniform distributed brine resistivity. (b) MCMC traces of the prior sampling of $v$ and $\rho_f$ (orange) and of the posterior sampling of the model uncertainty $\rho_m$ (green), the parameter uncertainty (the combined error propagation of the orange traces) $\rho_{rp}$ (red), and the total uncertainty $\rho$ (blue).

as given in Equation 3.20. The two model parameters are the P-wave velocity $v$ and the brine resistivity $\rho_f$, depth is $d = 2\,\text{km}$. In this example I describe the velocity as a normal distribution with mean $= 2.5\,\text{km/s}$ and variance of $0.01\,\text{km}^2/\text{s}^2$, and the brine resistivity as a uniform distribution from $2.85\,\Omega\,\text{m}$ to $3.15\,\Omega\,\text{m}$, or $3\,\Omega\,\text{m} \pm 5\,\%$. The uniform distribution says that we simply do not know if $\rho_f = 3\,\Omega\,\text{m}$, or a bit higher or a bit lower, it does not give any preference, only a range. The normal distribution says that we think $v = 2.5\,\text{km/s}$, it might be a bit more or less, but with decreasing probability. (In Chapter 5 I estimate the velocity distribution from the well data.) The model uncertainty is set to $\epsilon = 5\,\%$. (Chen and Dickens (2009) use in their uncertainty analysis 1 %, 3 %, and 5 % to show the influence of the error; I use 5 % for the model and the parameter uncertainties throughout my thesis to develop my workflow, however, more accurate estimates could be used if available.) I calculate 10 000 samples with `PyMC`. Figure 3.4a shows the analytical pdfs in black, and the histograms of the samples in orange for velocity $v$ (top) and fluid resistivity $\rho_f$ (bottom). Note that the histograms are normalised: the area under them equals one. These figures would look slightly different for each run, as it is a stochastic method. Figure 3.4b shows in orange the traces of velocity $v$ and fluid resistivity $\rho_f$, which nicely show the randomness of the draws. The lowest plot shows, overlapped, the traces of: the final resistivity (blue); the resistivity if only the parameter uncertainty is taken into account (red, which is basically the error propagation from the orange traces); and the resistivity if only the model uncertainty,

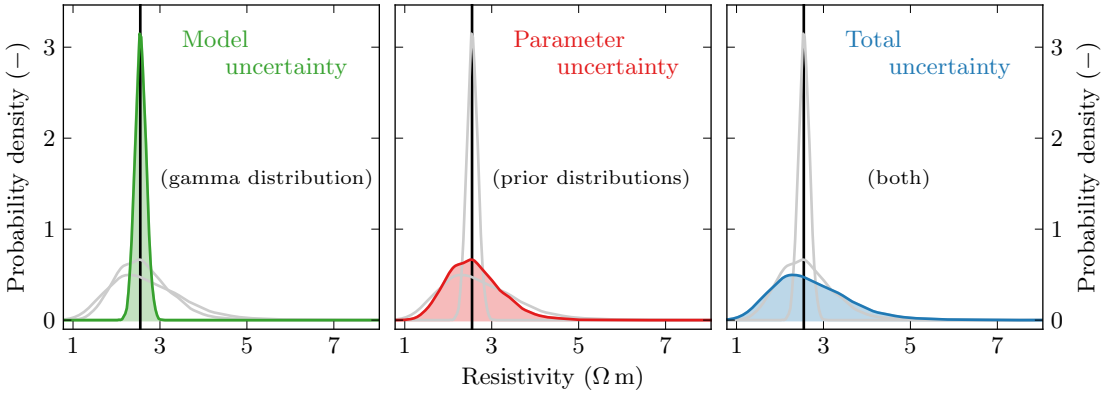


**Figure 3.5:** Example of the Bayesian model using MCMC with 10 000 samples; in green the model uncertainty, in red the parameter uncertainty (error propagation), and in blue the combined uncertainty. The deterministic value is indicated by the vertical black line.

here the gamma distribution, is taken into account (green). The colours correspond to the pdfs in Figure 3.5, in which the black vertical lines indicate the deterministic outcome of the Faust equation. In other words: The green pdf shows the error of the model, where the uncertainty is described as a gamma distribution (Equation 3.23), $\rho_\mathrm{m}$ is the deterministic value from the Faust model (Equation 3.20), and $\epsilon = 5\,\%$; the red pdf shows the error propagation of the prior distributions (orange in Figure 3.4) through the Faust model; the blue model shows the distribution if both uncertainties are taken into account. (The pdfs are estimated using a kernel density estimation (KDE), see Appendix A.) In this example it appears that parameter uncertainty has a bigger influence than model uncertainty, but this depends on the model, the defined priors, and the associated errors.

A real data example is shown in Chapter 5: Compare the velocity prior in Figure 3.4a with Figure 5.7, the model, parameter, and combined uncertainties in Figure 3.5 with Figure 5.4, and see Figure 5.9 for an idea how this compares to the measured well data distribution.

## Summary

Rock physics can be used to bridge the non-existent link between seismic P-wave velocity and electrical resistivity. Usually, but not always, this involves two steps, one from velocity to porosity, and one from porosity to resistivity. Many different models exist, both theoretical and empirical, and it is up to personal preference and proper calibration as to which one to choose. I show more plots of velocity-to-resistivity transforms in Chapter 5, where I apply the whole workflow to the North Sea Harding data. It is important to assess the uncertainty involved in this transform. The uncertainty arises both from errors in the rock-physics parameters and from the transform itself. The Bayesian framework is an ideal tool for the main purpose of this thesis, to present a simple methodology, that can be extended if more knowledge of the uncertainties involved is available. It can also easily be extended when more information is available, or adapted to suit other models.

■

# 4

# North Sea Harding field

**In theory, there is no difference between theory and practice.**
**But, in practice, there is.**

*Johannes Lambertus Adriana van de Snepscheut (1953–1994)*
*Computer scientist*

The North Sea Harding field is an Eocene oil and gas field, discovered in 1987. Oil production started in 1996. There is an abundance of seismic data and well logs for the mature Harding field. Two controlled-source electromagnetic (CSEM) surveys were carried out over Harding Central in 2007 and 2008 for a successful repeatability experiment. I summarise in this chapter the history and geology of the Harding field, and introduce the seismic, CSEM, and well data that are used in subsequent chapters.

## 4.1 History and geology of the Harding field

The North Sea Harding field is a gas and oil field in Block 9/23b on the United Kingdom continental shelf (UKCS), 320 km northeast of Aberdeen in the Central North Sea close to the Norwegian sector, as outlined in Figure 4.1; Quadrant 9 is marked in blue, and the median line, defining the economic sectors, is given in black. The field is named after David Harding, BP UK operations chief executive during field appraisal. The history of Block 9/23b is twofold. It was awarded in the third licensing round in 1970, but the western part (9/23b) was abandoned after three unsuccessful wells. Block 9/23b was again awarded in 1985 in the ninth UKCS licensing round to Britoil (now BP). The Harding field was discovered in February 1987 in a water depth of roughly 110 m, at a depth below seabed of about 1580 metres in the Eocene, and sanctioned as the *Forth field* in 1992 and renamed in 1993. Production started in April 1996, and peaked in 1998 with roughly 100 000 barrels per day (0.16 $m^3$/s). The oil produced at Harding is exported in tankers as the crude is heavy and naphthenic, and therefore of lower value than the crude in the North Sea pipelines. As of 2003, Harding had 15 production wells, three water injection wells, and one gas injection well.

The Harding complex consists of the two main fields, Harding Central and Harding South, the two fields used in this work, and four smaller satellite fields, Harding North, Harding Northeast, Harding Southeast and Harding Deep South, the naming following the geographical distribution of the fields. Gas produced during oil production is re-injected into the reservoir (there is no export of gas). BP and its Harding partner

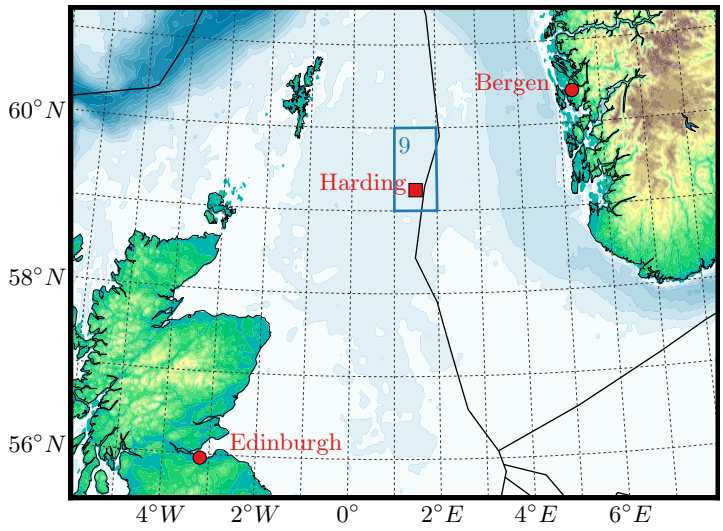


**Figure 4.1:** Location of the North Sea Harding field. Quadrant 9 is outlined in blue, and the median line, which defines the economic sectors, in black.

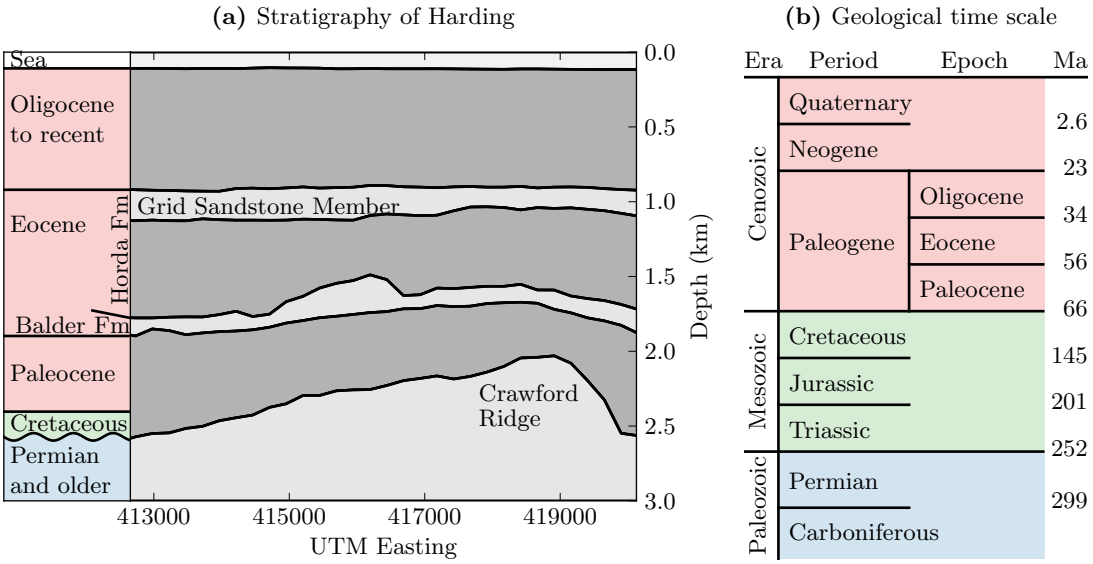


**Figure 4.2:** In (a) is the stratigraphy of Harding, outlined with the seismic horizons. The Harding reservoir is the mound in the Balder Formation in the middle of the figure. The geological time scale covering the times of interest is shown in (b).

Mærsk planned a gas blow-down after oil production. However, this project was put on hold due to the low gas price. BP announced in November 2012 that they sold a package of Central North Sea oil and gas fields, including the Harding field, to TAQA for 1.058 billion USD (BP, 2012). The acquisition was completed on 1 June 2013, according to TAQA, and they expect "to add 20 000 barrels of oil equivalent per day (1.4 GJ/s) of production" (TAQA, 2013) to its portfolio thanks to the acquisition. Technical details of the field are provided in the asset portfolio of the Harding field (BP, 2003).

## Geology

Figure 4.2 shows the simplified stratigraphy of Harding in (a), where the seismic horizons are used to delineate the stratigraphy. The Harding field lies on the western flank of the Crawford Ridge, which is a Paleozoic high that separates the Viking Graben from the Bruce-Beryl Embayment, and lies just below the base-Cretaceous unconformity. Comparing it with the geological time scale in (b) it can be seen that in the base-Cretaceous unconformity over 100 million years of sediments are missing. The upwards movement of the Crawford Ridge must have happened sometimes in the early Eocene, as the Grid Sandstone member is hardly affected by it, in contrast to the Balder Formation. The Cretaceous at Harding is only a thin cover over Permian and older strata.

Most reservoirs in the Central and Northern North Sea, a mature oil province, lie within

the syn-rift and pre-rift formations of Jurassic and Triassic age. However, Harding belongs to post-rift reservoirs within Tertiary sediments, where the reservoirs lie within the late Paleocene and early Eocene. These Tertiary accumulations are massive sands of the Eocene Balder Formation, which lie within the shales in the Balder Formation. The Balder acts therefore as reservoir (massive sands) and as seal (shales). The two main fields, Harding Central and Harding South, are both in the Balder Formation, which is at Harding a broad compactional anticline over the Crawford Ridge. The first discovery in the Balder Formation was 1967 the Balder field in the Norwegian sector. The Harding field is a typical example of a large mounded geometry in the Cenozoic basin floor sequences of the Northern North Sea (other examples are the Gryphon and the Balder fields, Erratt et al., 2010). Harding belongs, together with the Alba, Gryphon, and Maclure fields, to the significant post-Paleocene discoveries in the UKCS.

These massive sands, deposited by mass-flow processes, are clean and well-sorted. The trap type is mainly of stratigraphic nature, with some structural closing to the west. There was significant post-depositional deformation of the sand bodies, which resulted in complex injection structures on both well core scale and seismic scale. All six Harding fields are Tertiary, but not all in the same formation: Harding Central, Harding South, and Harding Northeast are in the Balder Formation, Harding Southeast and Harding Deep South (renamed Morrone) are in the Sele Formation below the Balder Formation, and Harding North is in the so-called Frigg Formation equivalent, just above the Balder Formation. The principal source rock is the Upper Jurassic Kimmeridge Clay formation, with bio-degradation within the reservoir.

The Harding reservoir itself is characterised by exceptional reservoir quality such us up to 35 % porosity and permeability in excess of 10 $(\mu\text{m})^2$ (10 darcys). The oil is a heavy acid crude, with a gas cap of almost pure methane. Estimated volumes are almost 30 million tonnes of oil (221.8 million barrels) and 7.64 billions cubic metre gas. A lot of the historical and geological information is from Beckly et al. (2003), who describe the Harding field in great detail. Useful information regarding the Paleocene and Eocene reservoirs of the Central and Northern North Sea in general and of Harding in particular can also be found in *The Millennium Atlas: Petroleum Geology of the Central and Northern North Sea* (Evans et al., 2003).

A note regarding the term *Tertiary*: Tertiary is a deprecated geological period of the Cenozoic Era. One should use Paleogene and Neogene instead, see Figure 4.2b. The Harding fields are in the modern terminology all within the Paleogene. However, the term Tertiary is well known and still widely used, not least in the petroleum industry.

## Data

Figure 4.3 is an outline of Harding Central and Harding South, together with all the data used in this thesis. The shape of the oil fields is delineated by the initial oil-water contact (OWC). The seismic velocities map (black outline) covers the bigger area, followed by the seismic horizons map (purple outline); the three horizons do not cover exactly the same area, but close enough to be outlined together. The black circles mark the wells that penetrate the reservoir, and the white circle marks the water-wet well. Multi-transient electromagnetic (MTEM) data were acquired along two lines. Line 1 is shown in blue and line 2 is shown in red. The two short black lines perpendicular to the MTEM survey mark the *start and the end of the MTEM line*. These two points were the planned direction for the MTEM acquisition, and they cover nicely the area where there is a good common midpoint (CMP) coverage (see Figure 4.5b). These two points are consistently used throughout this work to mark the MTEM line. The figure shows that the data coverage from the seismic data does not cover the whole area where there are MTEM sources and receivers placed. These outlines are the limitations in 3D modelling for, for example, the bathymetry, or the extent in which background

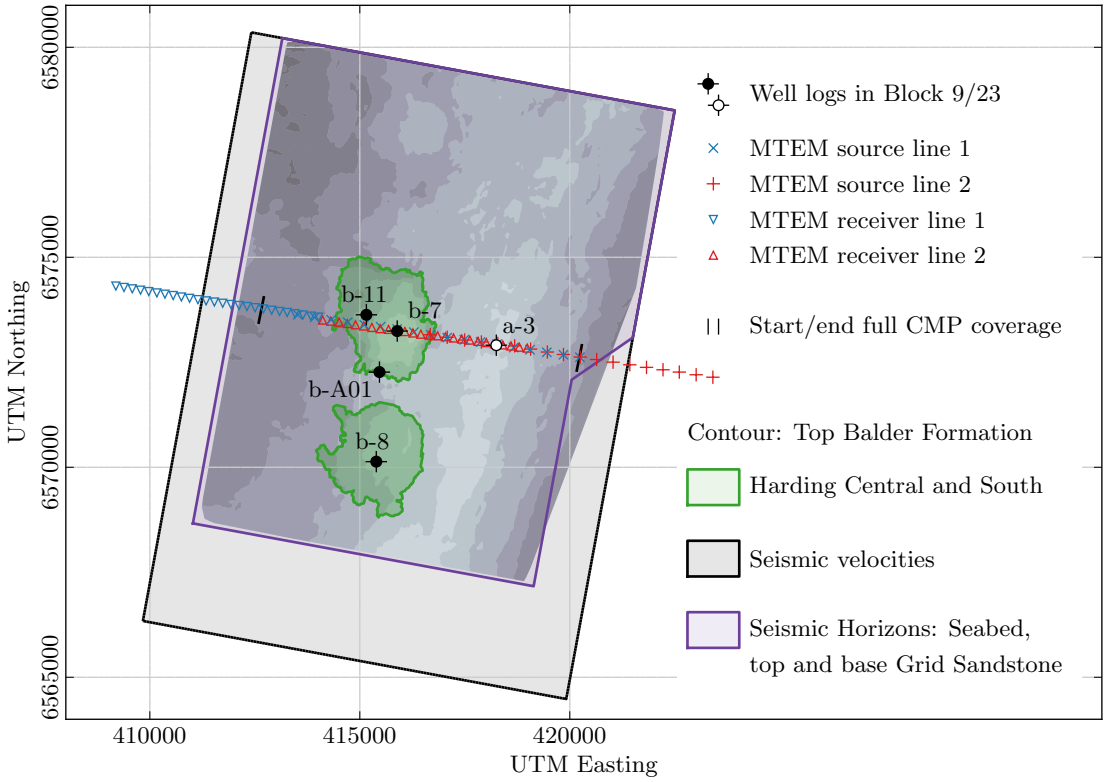


**Figure 4.3:** Outline of the data used in this study in the Harding field: seismic velocities and seismic horizons, MTEM data, and well logs. The outline of Harding Central and Harding South is the original OWC.

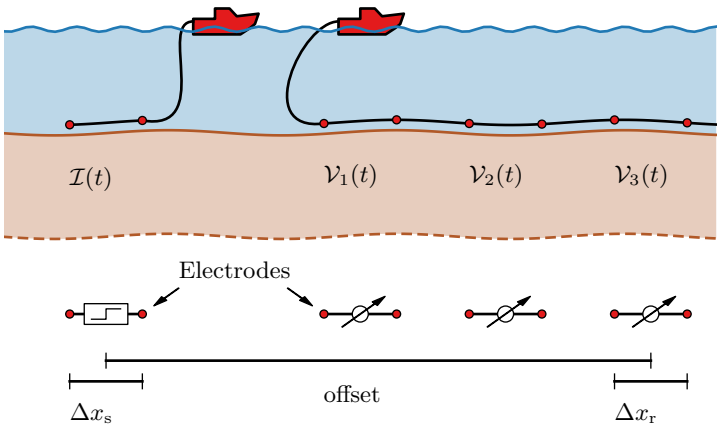


**Figure 4.4:** MTEM method. One vessel is towing the source, and the other the receiver cable. Both source and receiver are put down on the seabed for the measurement.

resistivities can be calculated in general.

## 4.2 MTEM data

PGS acquired two CSEM surveys over Harding, 2007 and 2008, repeating the same survey line which ties with wells 9/23b-7 and 9/23a-3, see Figure 4.3. The acquisition was part of a collaborative research project between PGS (formerly MTEM), BP, and the UK Department for Business, Innovation and Skills (formerly the UK Department of Trade and Industry). The aim was to demonstrate the repeatability of the MTEM method, and Ziolkowski et al. (2010) showed that the responses have in average a very low normalised root mean square difference (NRMSD) of 3.9 % (NRMSD is defined in detail in Appendix A). In this thesis I use the 2007 data.

The CSEM surveys over Harding used the old MTEM layout. PGS has replaced it in the meantime with their developed towed CSEM system. The old MTEM system involved two vessels, as shown in Figure 4.4. One vessel is towing the receiver cable, and the other is towing the source. During acquisition, both source and receiver rest on the seabed (hence no movement). In each survey at Harding there were two lines shot. One line means that the receiver cable was laid down, and the source moves consecutively from one shot point to the next. All source and receiver positions for the two acquisition lines are show in Figure 4.5a, and the corresponding CMP versus depth plot is shown in Figure 4.5b.

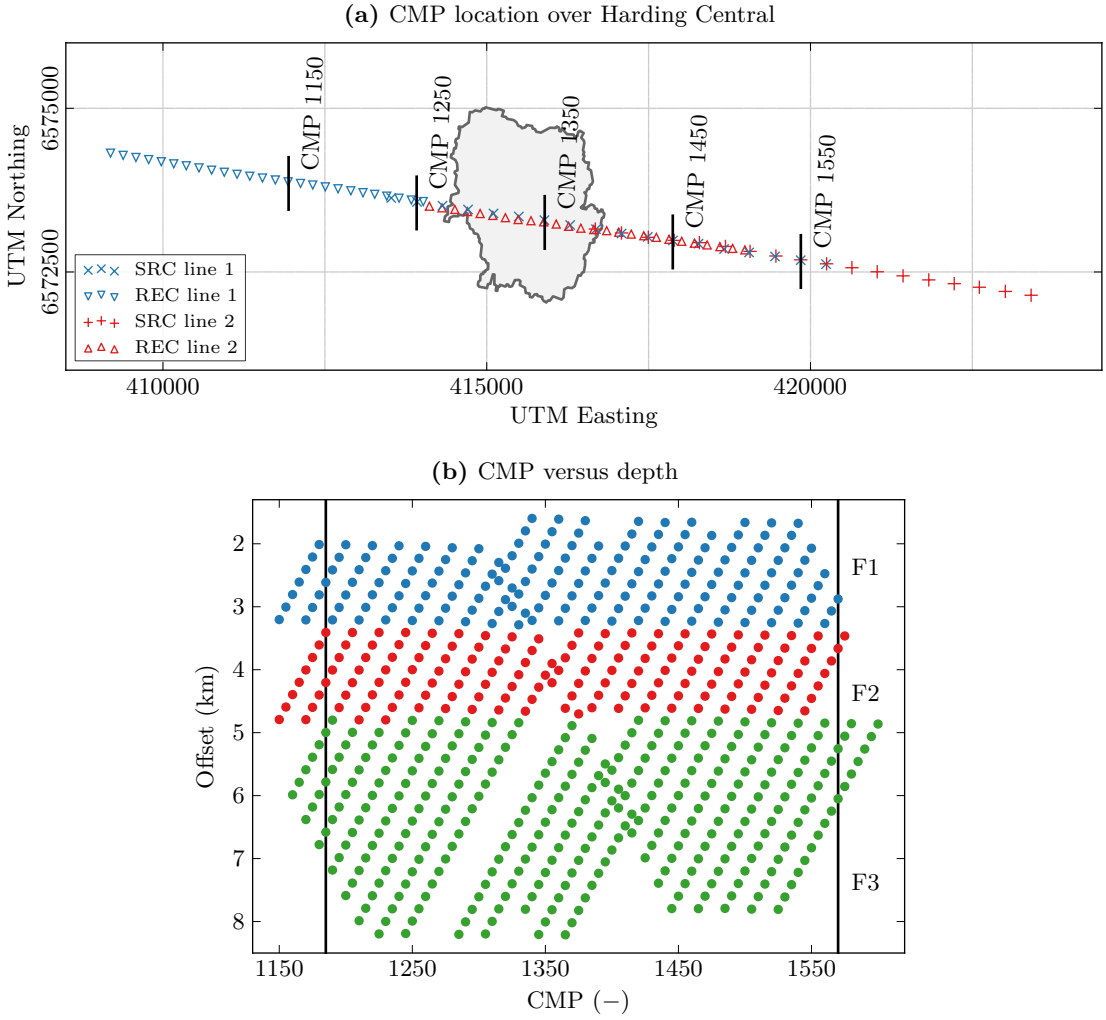


**Figure 4.5:** CMP position over Harding (a) and CMP versus depth (b). The different offsets for the three frequency bands are plotted in blue, red, and green, respectively, in (b).

The MTEM method is extensively described in Wright et al. (2002, 2005); Ziolkowski et al. (2007); Ziolkowski and Wright (2012), and the layout is shown in Figure 4.4. In the MTEM method a time-varying current, e.g. a step function or a pseudo-random binary sequence (PRBS), is injected between two source electrodes and is measured and recorded; the source signal used at Harding was a PRBS. The resulting time-varying voltage between two receivers is measured at the same time. Briefly, the MTEM method can be described by following Ziolkowski et al. (2007, Appendix A). The measured voltage $\mathcal{V}(t)$ at the receiver is given by

$$\mathcal{V}(t) = \mathcal{S}(t) * \mathcal{G}^{\mathrm{I}}(t) + \mathcal{N}(t) \ , \tag{4.1}$$

where $\mathcal{S}(t)$ is the system response, the convolution of the input current $\mathcal{I}(t)$ with the

measured response of the recording system, $*$ denotes convolution, $\mathcal{G}^{\mathrm{I}}(t)$ is the unknown impulse response of the Earth, and $\mathcal{N}(t)$ is the uncorrelated noise. As with the data, the above equation has been normalised by source and receiver length $\Delta x_{\mathrm{s}}$ and $\Delta x_{\mathrm{r}}$; the source strength is normalised through the deconvolution.

We would like to know the earth response $\mathcal{G}^{\mathrm{I}}(t)$, having measured $\mathcal{V}(t)$ and $\mathcal{S}(t)$. Unfortunately, $\mathcal{S}(t)$ is not close to an impulse $\delta(t)$, so the convolution $\mathcal{S}(t) * \mathcal{G}^{\mathrm{I}}(t)$ is not close to the impulse response. Transforming Equation 4.1 into the frequency domain we get

$$\hat{\mathcal{V}}(\omega) = \hat{\mathcal{S}}(\omega) * \hat{\mathcal{G}}^{\mathrm{I}}(\omega) + \hat{\mathcal{N}}(\omega) \ , \tag{4.2}$$

where the hat marks the change in domain from time to frequency. The convolution in time domain becomes a multiplication in frequency domain, which allows us to remove the source signal $\hat{\mathcal{S}}(\omega)$ from the measured voltage $\hat{\mathcal{V}}(\omega)$ with a simple division. We get the earth response then by transforming it back to the time domain. Due to real data limitations (noise), these steps require a band-limited, zero-phase filter in the form of a Gaussian (see Appendix A). This nine-point filter causes non-causal arrivals for four time steps before zero. This filter has therefore to be applied to synthetic data as well, in order to compare the two.

In Harding the source length was 400 m and its strength 600 A, and the receiver length 200 m. However, the data have been deconvolved and the responses are normalised by source and receiver length, so all plotted responses in this thesis correspond to source and receiver length of 1 m, and source strength of 1 A. The source signal in the Harding acquisition was a PRBS; Ziolkowski et al. (2011) compared the PRBS with the standard square wave function. Three frequency bands were chosen for the acquisition, which leads to three different time-sampling steps in the final data. Frequency band one (F1) was used up to 3.4 km offset and sampled at 40 Hz (time sampling $\Delta t = 0.025$ s). Band two (F2) was used between 3.4 km and 4.8 km offset, sampled at 10 Hz ($\Delta t = 0.1$ s), and band three (F3) was used for offsets greater than 4.8 km, and used 5 Hz ($\Delta t = 0.2$ s).

The acquisition at Harding suffered from strong magnetotelluric (MT) noise, and spatially correlated noise reduction methods were developed and applied to the data, see Ziolkowski and Wright (2008). Figure 4.6 shows three examples of MTEM responses before and after noise removal at an offset of roughly 4.6 km for three different source-receiver pairs (CMPs 1255, 1275, and 1365). Impulse responses are characterised by an impulse, which falls of and approaches zero for late times. This is not the case in these noisy Harding responses, as the example responses (solid lines) show. The improvement

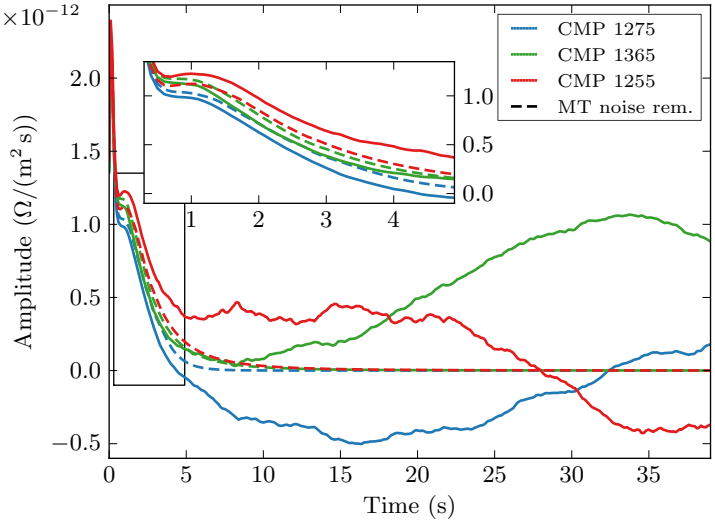


**Figure 4.6:** MT noise (correlated noise) removal. Solid lines are measured responses, dashed lines are the corresponding ones after noise removal. Inset is a zoom-in to the times we are most interested in.

of the responses becomes obvious by looking at the noise removed responses (dashed lines), as the responses approach zero for late times.

## 4.3 Seismic data

Seismic surveys were shot repeatedly over the Harding area; the Harding reservoir shows a large fluid response on the seismic data, mainly due to reduction in density from the thick gas cap. The discovery Well 9/23b-7 was drilled based on 2D seismic data from 1984. Additional 2D seismic data were acquired in 1986 and 1988. 3D seismic surveys were carried out in 1990, 2000, 2002, 2005 (2000 and later were time-lapse acquisitions), and entire datasets were repeatedly re-processed. This means that there is over 20 years of experience with seismic data in the Harding area, from at least seven different surveys. And there is a huge range of well logs available to tie the seismic data. This gives us a lot of confidence regarding the accuracy of the models (velocities, horizons) resulting from seismic processing.

Figure 4.3 outlines the available data coverage for this study. The black outline is the area of the velocity cube from the 3D acquisition of 2005, which has a resolution of 250 metres by 250 metres horizontally, and 20 metres vertically. The seismic horizons used have (almost) the same shape, as outlined in purple. Its resolution is irregular, but about a factor of 20 denser than the resolution of the velocity cube. The seabed horizon is used for the bathymetry in the 3D modelling, see Chapter 7. The top and

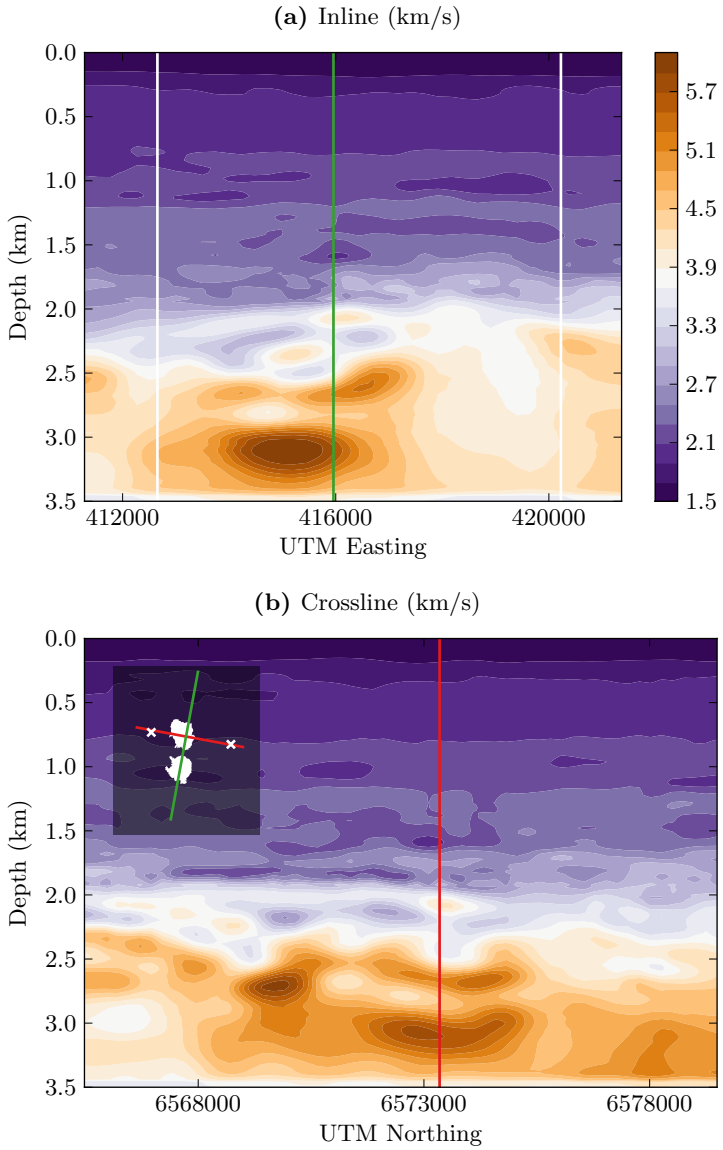


**Figure 4.7:** Inline and crossline of the seismic velocity cube. The inline (a) is roughly along the CSEM survey, the crossline (b) crosses Harding Central and Harding South, as shown in the little map in (b).

base Grid Sandstone horizons are used as a structural constraint in the rock-physics modelling, as explained in Chapter 5.

Figure 4.7 shows an inline section and a crossline section of the velocity cube. The inline (a) crosses Harding Central east-west, and the crossline (b) crosses Harding Central and South north-south, see the little map in (b). The two white lines (crosses in the map) mark the start and end of the full CSEM coverage, as shown in Figure 4.3, and the green and red lines mark the crossing of the other line. I use an interpolated vertical section along the CSEM survey line for the rock-physics modelling in Chapter 5, rather

than an inline.

P-wave velocities start at slightly less than 1.5 km/s for sea water, and reach 6 km/s towards the Cretaceous and Permian formations. The velocity model shows that the Harding area is horizontally very smooth (almost 1D) in the shallower part, and it is only at depths greater than 2 km that the lateral changes become important (which is below the Harding field).

## 4.4 Well data

There are more than a hundred wells in the Harding area, drilled between 1971 (exploration wildcat Well 9/23-1, completed 15 September 1971) to present (e.g. sidetrack Well 9/23b-A32Z, completed 26 April 2013). I chose five wells for this study (of which four are vertical exploration and appraisal wells), whose locations are shown in Figure 4.3. Well 9/23b-7 and Well 9/23a-3 are along the CSEM-line (the CSEM survey was planned to intersect these two wells), the first one on the Harding Central target and the second one off target. Well 9/23b-11 is a near-by well on the target, and Well 9/23b-8 is a well from Harding South. All these wells are relatively old wells, drilled between 1981 and 1989, and basically vertical. 9/23b-A01 is an example of a more recent well (1996), which has good log coverage also in the shallow section. It is nearly vertical down to target depth, and runs horizontally within the reservoir.

I provide in the following a very brief description of each well, together with a figure showing the well data itself. (All five resistivity logs are also shown side-by-side in Figure 5.10.) For the study I use the velocity (which comes from the sonic log), and the resistivity (from the deep resistivity log; the deep resistivity measurement penetrates the deepest of the various resistivity logs, and is very narrowly focused, yielding horizontal resistivity, see Chemali et al. (1983)). The gamma ray log is plotted additionally. The logs are shown as a function of true vertical depth below sea surface (TVDSS) for the section where both velocity and resistivity logs are available. The light grey lines show the original data, and the dark grey lines show the cleaned original data, where outliers are removed. Outliers might result from casing problems or casing changes, sample extractions, or measurement tool problems. The black line is a smoothed curve of the cleared log, using a Hann function (a standard smoothing window function) of length 320; depth resolution of the logs is 0.5 ft (0.3048 m), the smoothing window is hence $320 \times 0.5\,\text{ft} \approx 48.8\,\text{m}$. The smoothing is partly done to resemble more the resolution we have from the seismic velocity cube and the CSEM data. I use the above-mentioned logs together with the composite logs to clean the log data, and also to split every well into rough sections of the two lithologies, shale and sandstone. The cross-plots

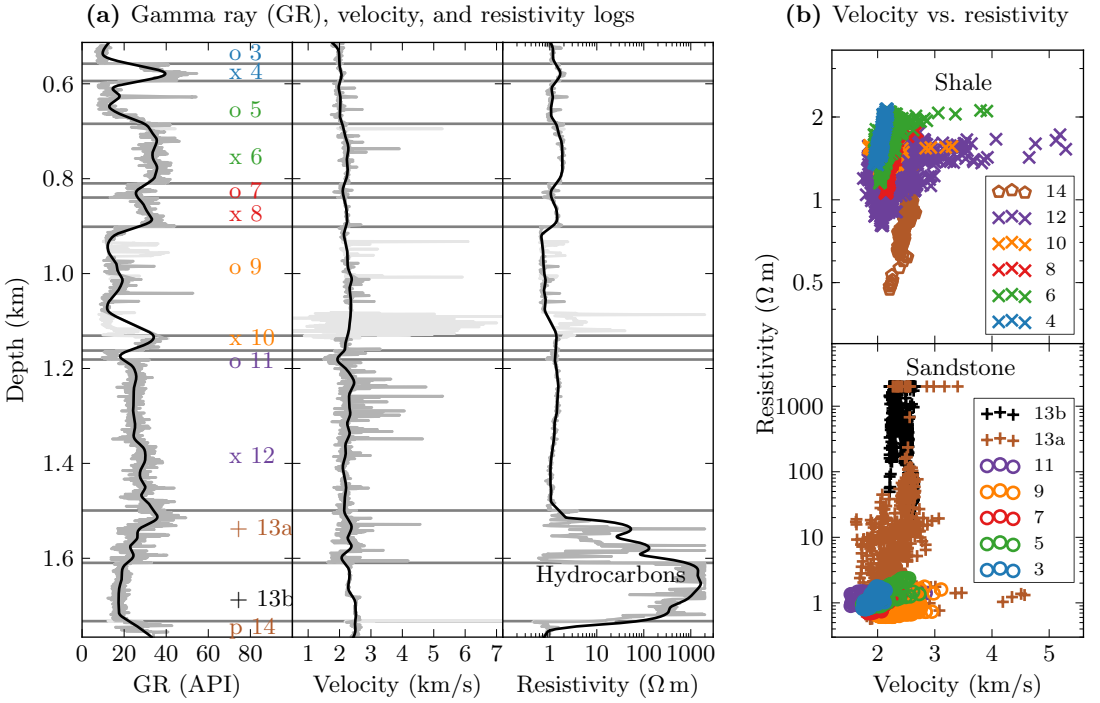


**Figure 4.8:** Well 9/23b-7. In (a) the three logs gamma ray, velocity, and resistivity, and in (b) the cross-plots velocity versus resistivity for the different sandstone and shale sections. Sandstone sections 13a and 13b are the hydrocarbon bearing ones.

of velocity versus resistivity for these sections indicate the relationship between the two, and they also show the depth dependence. Rock physics takes advantage of these relationships, see Chapters 3 and 5. Note that not all data are shown in the cross-plots of velocity versus resistivity. Some *edge-effect* data are removed sometimes. With edge-effect I mean data in the transition between shaley and sandy sections, which would blur the whole plot and mask the cleaner shale and sandstone section. For an in-depth introduction into well logging I recommend the book *Well Logging for Earth Scientists* by Ellis and Singer (2007).

## Well 9/23b-7

Well 9/23b-7 is the abandoned vertical oil and gas discovery well, completed 15 January 1987, in a water depth of 111.3 m. Useful samples for both resistivity and velocity range from 502.1 m TVDSS to 1765.7 m TVDSS. Top Balder is at 1515.2 m TVDSS, top Sele at 1764.9 m TVDSS. Gas-oil contact (GOC) is at 1676.3 m TVDSS. Section 14 consists of tuff.

Figure 4.9 shows the data from Well 9/23b-7 as in Figure 4.8b, but without the samples

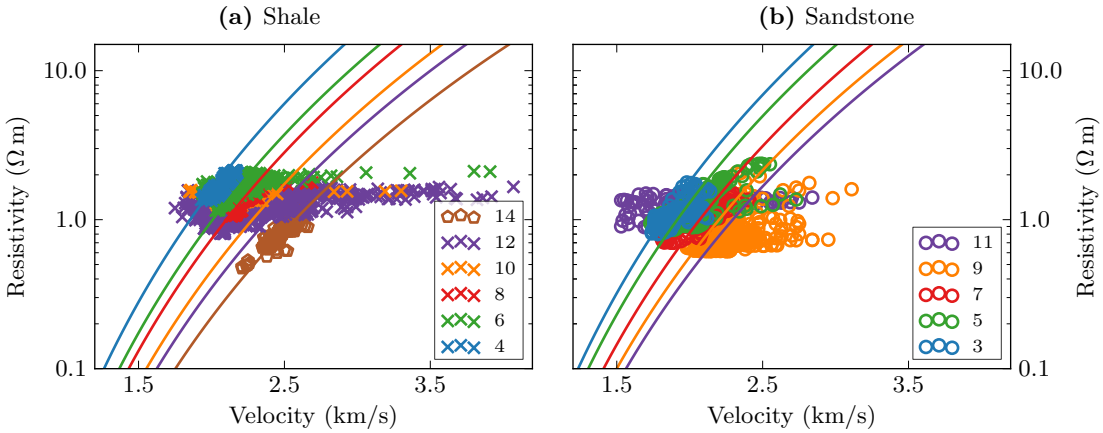


**Figure 4.9:** Data from Well 9/23b-7 (without hydrocarbon bearing layers 13a and 13b) together with the Faust model; In (a) for the shale sections and in (b) for the sandstone sections. The empirical Faust model is often a simple and good approximation. (The Faust equation is described in Chapter 3.)

from the hydrocarbon bearing layers (13a and 13b). The data are plotted together with different realisations of the Faust equation, as explained in Chapter 3, Equation 3.20. For the calculation I use for depth $d$ the depth of the midpoint of each layer (in km), and for the resistivity of the pore fluid $\rho_f$ I use a simple depth-trend given by $0.3+1/d$. This example links the theory in Chapter 3 with measured data from Harding. It shows that rock physics often means fitting a line (a curve) through a cloud; a theoretical model through the scatter of measured data. It also shows that the empirical Faust equation, with a simple depth-trend for the fluid resistivity, does overall a good job in predicting resistivity from velocity, but not always, as, for instance, the misfit of sandstone layer 11 shows. This is why each transform has to be calibrated with available data, what I do in Chapter 5.

### Well 9/23a-3

Well 9/23a-3 is a water-wet, abandoned vertical wildcat, completed 7 April 1981, most likely targeting the Crawford Ridge. Water depth is 113.4 m. Useful samples for both resistivity and velocity are from 1448.4 m TVDSS to 2156.6 m TVDSS. Top Balder is at 1644.1 m TVDSS, and top Permian (top Crawford Ridge) at 2074.2 m TVDSS.

### Well 9/23b-11

Well 9/23b-11 is an abandoned vertical well, completed 2 February 1989, in a water depth of 107.0 m. Top Balder is at 1658.7 m, top Sele at 1821.8 m, and the OWC is at

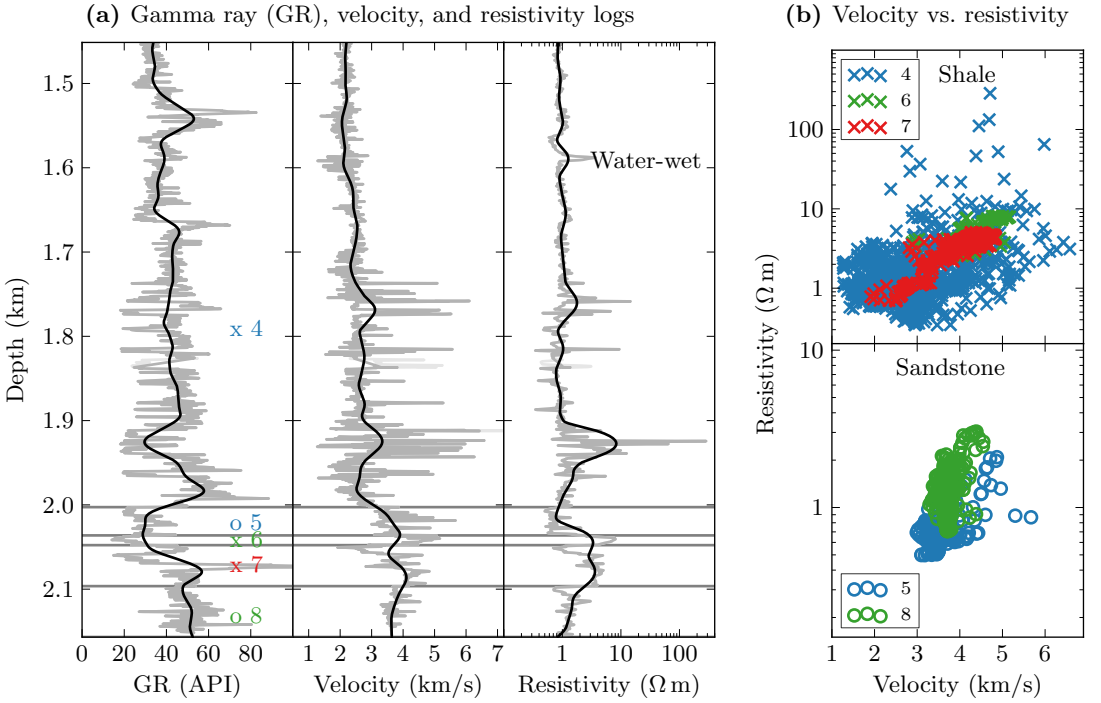


**Figure 4.10:** Water-wet Well 9/23a-3. In (a) the three logs gamma ray, velocity, and resistivity, and in (b) the cross-plots velocity versus resistivity for the different sandstone and shale sections.

1748.6 m.

## Well 9/23b-A01

Well 9/23b-A01 is an oil producer (horizontal development within the reservoir) with extensive logging, completed 13 April 1996; water depth is 109.7 m. Top Balder is at 1581.6 m TVDSS. Well 9/23b-A01 is a deviated well, unlike the other four wells I use. The plotted depth in Figure 4.12 is measured depth (MD) below sea surface (measured along the borehole and hence different from true depth if the well is not vertical), and not TVDSS. The well goes first almost vertically down to reservoir level, and then almost horizontal within the reservoir. The deviation in the section where both resistivity and velocity logs are available is only minor; the deviation is plotted in Figure 4.13.

## Well 9/23b-8

Well 9/23b-8 is an abandoned vertical oil and gas well, completed 26 February 1988; water depth is 112.8 m. It is the only considered well from Harding South, and I use

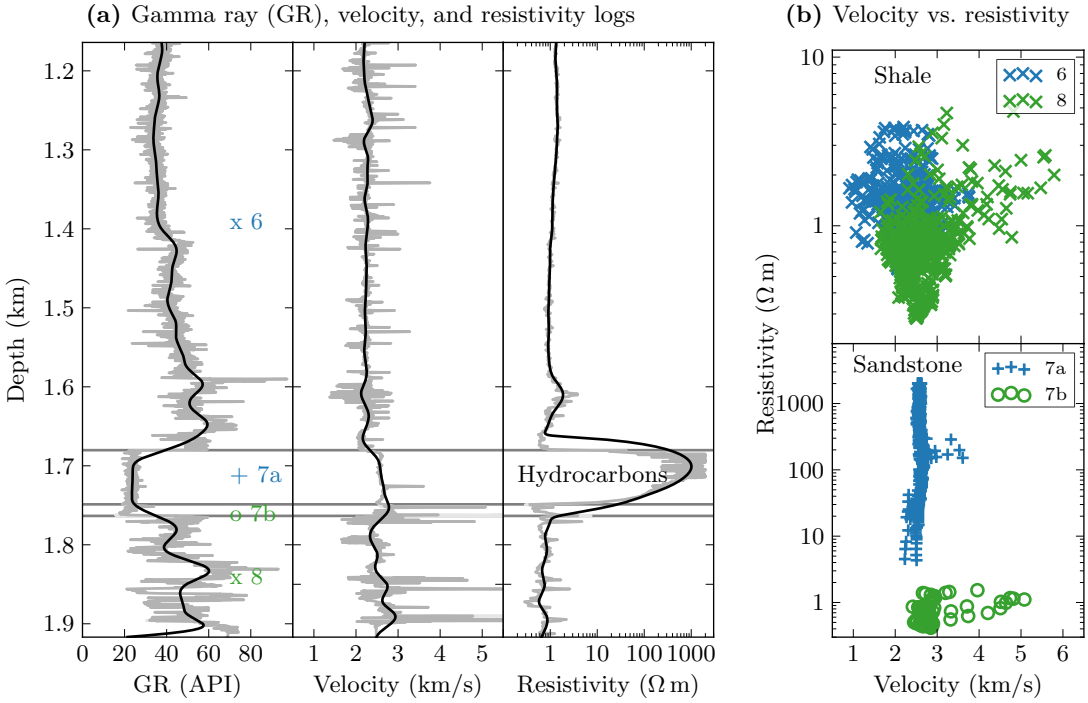


**Figure 4.11:** Well 9/23b-11. In (a) the three logs gamma ray, velocity, and resistivity, and in (b) the cross-plots velocity versus resistivity for the different sandstone and shale sections. The sands in section 7a are the hydrocarbon bearing ones.

this well for the calibration of my rock-physics transform in Chapter 5. Top Balder is at 1584.4 m, and top Sele at 1719.4 m. Figure 4.15 shows a comparison of the velocities from the well log measurement with the velocities resulting from seismic processing. The comparison shows that the two datasets agree very well.

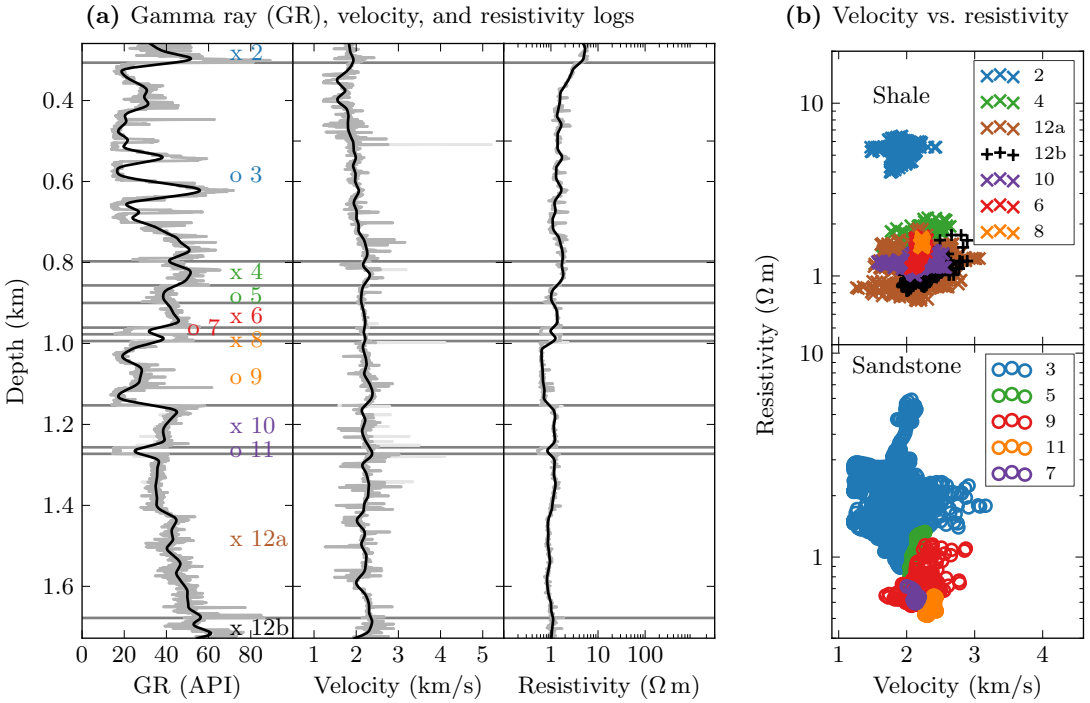


**Figure 4.12:** Well 9/23b-A01. In (a) the three logs gamma ray, velocity, and resistivity, and in (b) the cross-plots velocity versus resistivity for the different sandstone and shale sections. The well is not penetrating the reservoir in this part (the reservoir is deeper).

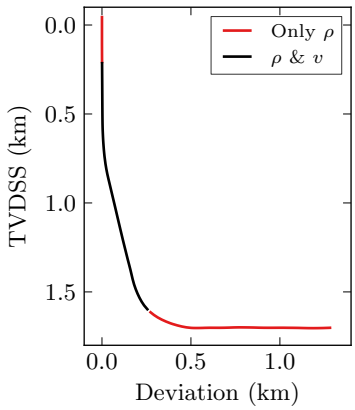


**Figure 4.13:** Deviation of Well 9/23b-A01, plotted with an aspect ratio of 1:1. The part where both resistivity and velocity measurements are available is mainly vertical. However, not as vertical as all the other used wells.

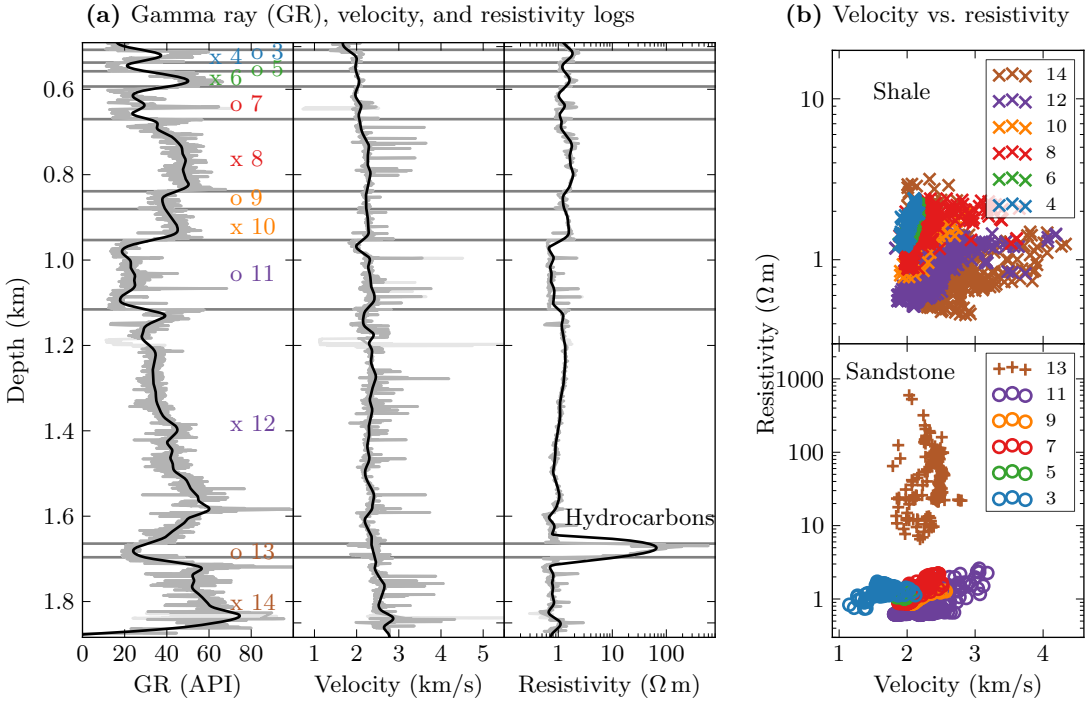


**Figure 4.14:** Well 9/23b-8. In (a) the three logs gamma ray, velocity, and resistivity, and in (b) the cross-plots velocity versus resistivity for the different sandstone and shale sections. The sands in layer 13 are the hydrocarbon bearing ones.

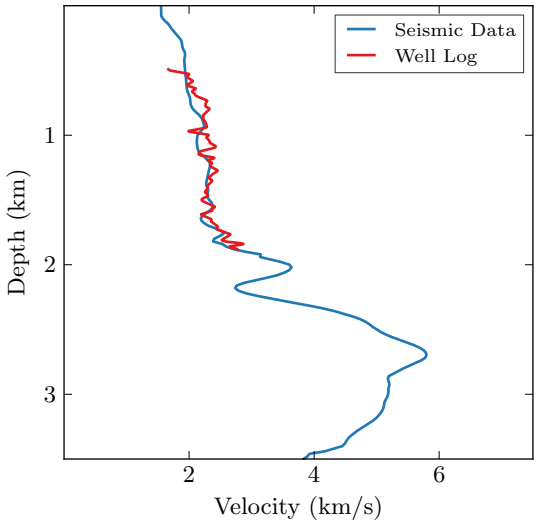


**Figure 4.15:** Comparison of velocities from the well log measurement (from the sonic log) with the velocities resulting from seismic data processing. The two datasets agree very well.

**Summary**

The North Sea Harding field is a mature oil and gas field in Paleogene formations. It was discovered in 1987 and has been in production since 1996. It has had regular 2D and 3D seismic acquisitions since the early 1980s, a big range of well logs, and two CSEM surveys in 2007 and 2008. A reservoir group in an oil company together with the geologists and geophysicists can make detailed models about such a mature oil field. For this thesis, only the velocity and the resistivity logs in five wells, the seismic velocities, three horizons, and one CSEM line are chosen to demonstrate a concept. This has several good reasons, besides limited man-power and knowledge. It allows control of the input and demonstrates more easily possible weaknesses of the workflow. Once the workflow is established, we can start to include more information. The Bayesian uncertainty analysis introduced in the previous chapter makes it easy to include all kind of additional data, together with their uncertainty.

■

# 5

# Velocity-to-resistivity transform

**Everything should be made as simple as possible,**
**but not simpler.**

*Albert Einstein (1879–1955)*
*Physicist*

I present a methodology to estimate resistivities from seismic velocities. I apply known methods, including rock physics, depth trends, structural information, and uncertainty analysis. The result is the range of background resistivity models that is consistent with the known seismic velocities. I show a successful example of the methodology with real data from the North Sea Harding field. These 2D or 3D background resistivity models yield a detailed insight into the background resistivity, and are a powerful tool for feasibility studies. They can also serve as starting models or constraints in (iterative) forward modelling of electromagnetic data for the determination of subsurface resistivities.

This chapter is published under the title *Background resistivity model from seismic velocities* in Werthmüller et al. (2013a), copyright 2013 SEG. I adjusted the original text, layout, and symbols to fit the style of the thesis, and moved the appendices to Chapter 3 and Appendix C.

## 5.1 Introduction

Seismic data and controlled-source electromagnetic (CSEM) data yield complementary information about the subsurface. Seismic data yield the depth structure and the velocity model. CSEM data provide insight into how the formations behave if an electric current is applied, which can be used to determine whether the pore fluids are conductive, for instance brine, or resistive, for instance hydrocarbons. Geophysicists process seismic data to get structural information and with it seismic velocities. Seismic velocities are derived from the data: they are the result of aligning seismic arrivals. This process of deriving a geophysical property directly from the data is not available to CSEM data, as discussed by Ziolkowski and Wright (2012). There is no theory for the direct extraction of resistivities from CSEM data. Instead, resistivities are determined using the process of iterative forward modelling, which is often termed inversion. In this process synthetic data are generated from an initial model (a guess) of the subsurface resistivities, often a uniform half-space. The misfit between the synthetic and the measured data is minimised by adjusting this starting model. A range of schemes exist for how the model should be varied; Occam's razor of the simplest solution that matches the data is often applied in CSEM (Constable et al., 1987). We do not alter the measured CSEM data in this process, only the model. That is, the resistivities are derived from modelling, and are not derived directly from the data.

It is therefore desirable to consult seismic velocities, if available, to gain a better understanding of the subsurface resistivities. However, getting from velocities to resistivities is not a trivial task, as the underlying theories of seismic wave propagation and CSEM wave propagation share no physical property, see Table 1.1 and Ziolkowski and Engelmark (2009). The theory of seismic surveying is based on the wave equation, and with it Hooke's law and Newton's second law of mechanics. These depend on the density and the elastic moduli of the rock, which define P-wave velocity and S-wave velocity. The theory of CSEM surveying, on the other hand, is based on Maxwell's equations, which depend on the magnetic permeability, the electrical resistivity, and the electrical permittivity of the rock.

The most obvious way to combine these two data is to extract the structures from the interpreted seismic data, and use them in (iterative) CSEM forward modelling (e.g. Harris et al., 2009). Another structural constraint is the cross-gradient method (e.g. Gallardo and Meju, 2007; Hu et al., 2009), where it is assumed that the resistivity changes if the velocity changes. A different approach is to replace the non-existent link with rock physics, usually, but not always, via porosity. Carcione et al. (2007) presented a nice overview of common relations. Engelmark (2010) emphasises the importance of

background (shale) modelling for CSEM inversions, and the depth dependence of rock-physics models.

Whatever the approach, the biggest problem remains: there is no physical link between velocity and resistivity. A change in velocity does not necessarily mean that there is a change in resistivity. That means that any of these methods can introduce unwanted bias. Chen and Dickens (2009) looked at the effects of uncertainty involved in the rock-physics model itself (intrinsic) and their parameters (extrinsic), and Kwon and Snieder (2011) showed that the uncertainty of the rock-physics parameter contributes more to the overall uncertainty than the uncertainty in the data itself. I discuss rock physics and its uncertainty in detail in Chapter 3.

The purpose of this work is to determine the range of resistivity models that is consistent with known seismic velocities. This is not fundamentally new: Constable and Srnka (2007), for instance, presented a 3D resistivity model that was "guided by 3D seismic data, well-log data (...), and the CSEM data", but without explaining this guidance at all. I bring together the work of many others, and include rock physics, depth trends, structural information, and uncertainty analysis. It is a workflow that can be adjusted to personal needs and preferences. I choose the Gassmann model to get from velocity to porosity, and the self-similar model to get from porosity to resistivity, both as presented in Carcione et al. (2007). Following Engelmark (2010), I use the dual-water model from Clavier et al. (1984) to get depth-dependent brine resistivity. Other parameters are either constant, or a linear function of depth. Finally I use Chen and Dickens (2009) to estimate the related uncertainty. The result is a transform that can be applied to seismic velocities to get background resistivities. Once a transform is calibrated it can be applied to the whole depth extent of seismic velocities without further interaction. Such a background model yields valuable information about the subsurface background resistivity distributions. It can be used for an integrated field analysis, for accurate CSEM feasibility studies, and provides a good model to generate synthetic CSEM responses.

This chapter is split into two parts. First, I explain the methodology, namely the rock-physics models, their depth dependence, and the uncertainty analysis; all symbols with their units are listed in Symbols and Abbreviations at the beginning. Second, I apply the theory to data from the North Sea Harding field (Beckly et al., 2003), where a successful CSEM repeatability experiment was carried out (Ziolkowski et al., 2010); see Chapter 4 for more information regarding Harding and the data. In this repeatability experiment, 1D inversion results were collated to form a 2D resistivity section. However, this result is not very detailed, and is mainly limited by the chosen layer thicknesses (taken from seismic structures). Furthermore, the 1D inversions resulted in

an unrealistically low resistivity contrast with target resistivity of approximately $5\,\Omega\,\mathrm{m}$, embedded in a background with resistivities of approximately $1-3.5\,\Omega\,\mathrm{m}$. To apply the theory, I calibrate my rock-physics model with a well log from Harding South, and apply it to seismic velocities at Harding Central. A comparison with well data from Harding Central shows that the well log resistivities fall within the error bounds of my predicted background resistivity model, which validates the accuracy of this approach. This approach yields a resistivity model, including uncertainties, assuming brine in the pore fluids. Any deviation in the CSEM data from this would be an indicator of the presence of hydrocarbons.

## 5.2 Velocity-to-resistivity transform

However tempting and desirable it is to analyze seismic data and CSEM data together, they do not share a common physical property, and hence cannot be linked by any law of physics. This absence of a physical link is usually overcome with rock physics. Rocks are generally inhomogeneous materials, a mixture of different minerals and pores filled with fluids. Petrophysical mixture theories try to estimate the property of a rock from its individual components, for example, the P-wave velocity of a rock from the P-wave velocities of its minerals and pore fluids. Hence rock-physics models are averages. The simplest ones use arithmetic and harmonic means. (The harmonic mean of $v_\mathrm{f}$ and $v_\mathrm{s}$ is known as the time-average or Wyllie equation, Wyllie et al. (1956).)

There are many different rock-physics models to relate velocity to porosity, and porosity to resistivity. Some are based on theoretical assumptions, e.g. geometry, such as the self-similar model, the Gassmann equation, or the Hashin-Shtrikman upper and lower bounds. Others are derived empirically, e.g. Archie or the Raymer equation. The simplest model of a rock is a model with two constituents, one being the minerals of the rock (the solid fraction), and the other the fluid which occupies the pore space. In this simple case the volume fraction of the fluid is the porosity of the rock, $\phi$, and the volume fraction of the grains is $1-\phi$.

A good introduction to mixture theories is given by Berryman (1995), and an overview of velocity-to-resistivity cross-property relations is given by Carcione et al. (2007) (which can be found in the *The Rock Physics Handbook* by Mavko et al. (2009)). All petrophysical models assume some knowledge of the subsurface in addition to the P-wave velocities gained from well logs or seismic processing. Additional information may come from well logs, from laboratory measurements on core samples, from the literature, or simply from experience.

Most relations in the literature include electric conductivity, not resistivity; conductivity is the reciprocal of resistivity. I am searching for resistive rather than conductive bodies in the exploration for hydrocarbons. I therefore express all equations in terms of resistivity. I list in the following sections the models I use later in my example. Any other relation that is mentioned or plotted can be found in Chapter 3. Symbols and Abbreviations are given at the beginning of the thesis, providing a complete list of variables, together with the applied units. The equations, as presented, assume isotropic, linear, elastic media.

### Velocity to porosity

The P-wave velocity in terms of bulk modulus $K$, shear modulus $G$, the densities of the solid and the fluid fraction $\varrho_\mathrm{s}$, and $\varrho_\mathrm{f}$, and porosity $\phi$ is given by,

$$v = \sqrt{\frac{K + 4G/3}{(1-\phi)\varrho_\mathrm{s} + \phi\varrho_\mathrm{f}}} \ . \tag{5.1}$$

I use the *Gassmann equation* to calculate the moduli: Gassmann (1951) derives equations for fluid substitution in porous, elastic media. The Gassmann bulk modulus $K_\mathrm{G}$, as given by Carcione et al. (2007), is

$$K_\mathrm{G} = \frac{K_\mathrm{s} - K_\mathrm{m} + \phi K_\mathrm{m}(K_\mathrm{s}/K_\mathrm{f} - 1)}{1 - \phi - K_\mathrm{m}/K_\mathrm{s} + \phi K_\mathrm{s}/K_\mathrm{f}} \ , \tag{5.2}$$

where $K_\mathrm{s}$ and $K_\mathrm{f}$ are the bulk moduli of the solid and the fluid fraction respectively. Krief's relations (Krief et al., 1990) are used to calculate the dry bulk and shear moduli, $K_\mathrm{m}$ and $G_\mathrm{m}$,

$$K_\mathrm{m} = K_\mathrm{s}(1-\phi)^{\kappa/(1-\phi)} \ , \tag{5.3}$$

$$G_\mathrm{m} = G_\mathrm{s}(1-\phi)^{\kappa/(1-\phi)} \ , \tag{5.4}$$

where $G_\mathrm{s}$ is the shear modulus of the solid fraction, and Krief et al. (1990) suggest that $\kappa = 3$. I refer to $\kappa$ as the Krief exponent. The Gassmann equation does not provide a way of calculating porosities directly from velocities. Equation 5.1 must be solved in an iterative way with $K_\mathrm{G}$ and $G_\mathrm{m}$ to calculate porosity from P-wave velocity.

Figure 5.1 shows the velocity-to-porosity transforms for the Gassmann equation, the Raymer equation, the acoustic formation factor (AFF), and the Hashin-Shtrikman bounds, for rock parameters as given in Table 5.1. The porosity range is from 0 % to 45 %. Note that the Raymer equation, in the form provided, is valid for porosities

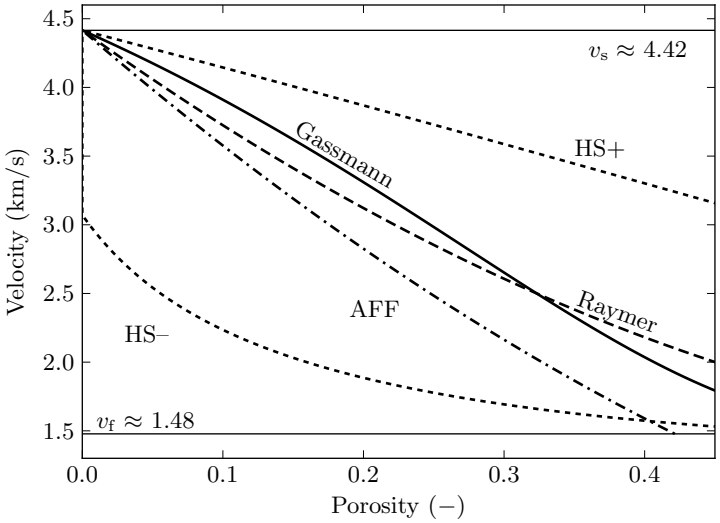


**Figure 5.1:** Different velocity-to-porosity transforms for $0 \leq \phi \leq 0.45$, and $v_f \leq v \leq v_s$. Note that AFF for the given parameters falls outside the Hashin-Shtrikman bounds for porosities higher than roughly 40 %.

lower than 37 %. All transforms are within the HS bounds, except the AFF for high porosities. It is important to realise that most relations have the realistic assumptions that porosity is 0 % if velocity is equals $v_s$, and 100 % if velocity is equals $v_f$.

The models do not differ significantly. Well data could be fitted by all of these models by calibrating (or adjusting) the rock parameters. The assessment of the uncertainty of a model therefore appears to be more important than the choice of model itself.

## Porosity to resistivity

The *self-similar model* from Sen et al. (1981) is based on the self-consistent effective medium theory (Bruggeman, 1935; Hanai, 1960). In this model, the resistivity $\rho$ is given by

$$\rho = \left(\frac{\rho - \rho_s}{\rho_f - \rho_s}\right)^{\zeta} \rho_f \phi^{-\zeta} \ , \tag{5.5}$$

**Table 5.1:** Material properties used in Figures 5.1 to 5.4, see Symbols and Abbreviations for units (from Carcione et al., 2007, Table 2, shale).

| $\rho_s$ | $\rho_f$ | $K_s$ | $K_f$ | $G_s$ | $\varrho_s$ | $\varrho_f$ |
|---|---|---|---|---|---|---|
| 5 | 0.067 | 25 | 2.25 | 20 | 2.65 | 1.03 |

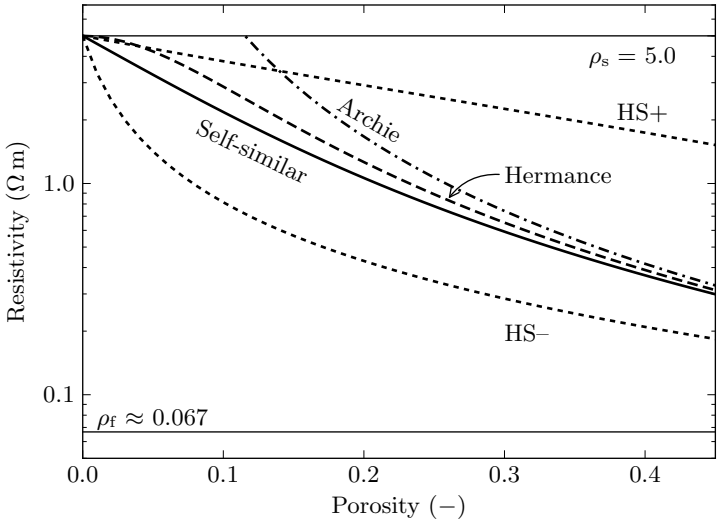


**Figure 5.2:** Different porosity-to-resistivity transforms for $0 \leq \phi \leq 0.45$, and $\rho_f \leq \rho \leq \rho_s$. These models differ mainly in the low porosity range. Archie is good for porous rocks, but yields $\rho \to \infty$ for $\phi \to 0$.

where $\rho_s$ and $\rho_f$ are the resistivities of the solid and the fluid fraction, respectively, $\phi$ is porosity, and $\zeta$ is the cementation exponent.

Sen et al. (1981) take the formation fluid as host to derive the relation, which has to be solved iteratively to yield resistivity, whereas a similar model by Bussian (1983) takes the rock as host. For two constituents, the results are the same. (Bussian additionally uses a binomial expansion to provide a direct solution for resistivity, with an approximate criterion for the validity.) The self-similar model reduces to the harmonic mean if $\zeta = 1$.

Figure 5.2 shows porosity-to-resistivity transforms, for the self-similar, Archie, and Hermance models, and upper and lower Hashin-Shtrikman bounds. All models are restricted to $\rho_f \leq \rho \leq \rho_s$; the Archie model would otherwise predict resistivities $\rho \to \infty$ for $\phi \to 0$. As in the case for velocity to porosity, the different porosity-to-resistivity models do not differ significantly, and it is up to personal preference and proper calibration.

### Velocity to resistivity

Figure 5.3 shows a choice of cross-property relations: the Gassmann equation combined with the self-similar model, the Raymer equation combined with the Hermance model, the Faust equation (with $d = 0.2\,\mathrm{km}$), and the Hashin-Shtrikman bounds. The bounds were calculated by combining the lower bound from velocity to porosity with the upper

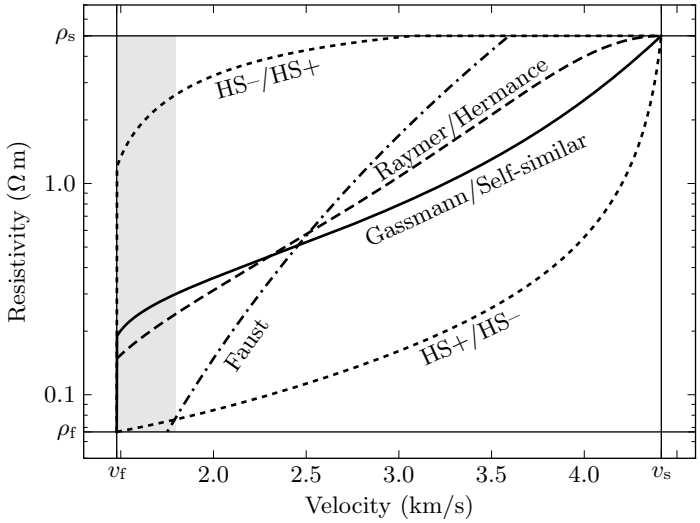


**Figure 5.3:** Different velocity-to-resistivity transforms for $v_f \leq v \leq v_s$, and $\rho_f \leq \rho \leq \rho_s$. The grey area marks the zone where the intermediate porosity would be greater than 45 % in the Gassmann model (as an example). Depth $d = 0.2$ km for Faust.

bound from porosity to resistivity, and vice versa. The grey area shows where the intermediate porosity is larger than 45 % in the Gassmann/self-similar transform. (The area would be similar for the Raymer/Hermance model; there is no intermediate porosity in the Faust equation.) The danger in cross-property relations is that one does not see the porosity in the middle, and it is a good idea to limit the possible porosity range, otherwise the resulting resistivity might look perfectly sensible when, in fact, it is nonsense.

I could have plotted any combination of the previous mentioned transforms. However, I am convinced that the choice of rock-physics model does not really matter, as they have to be calibrated to every case anyway. One only has to be careful with relations like Archie, Faust, and AFF. For example, the resistivity tends to infinity as the porosity tends to zero in Archie's equation. The other relations have similar pitfalls for extreme porosities.

## Depth dependence

A rock-physics model, as established in the previous section, provides a transform from seismic velocity to resistivity. Such a transform is usually calibrated with a set of data, often from well logs, as in my case, or from core samples. However, this transform then holds only for this particular environment. That is because rock properties (like velocity or resistivity) are a function of many parameters, such as pressure, temperature, wetability, residual oil and water saturations, shaliness, porosity and permeability.

I can ignore some of these parameters, such as wetability and residual oil and water saturations, as I am looking for a background model without any hydrocarbons. Others cannot be neglected, for instance temperature and pressure, which are functions of depth, as a first-order approximation. This depth dependence of the transform is one reason why the Faust equation, an empirically derived relation without a physical foundation, often works very well and is widely used, just like Archie in the case of porosity to resistivity.

To get a background resistivity model from seismic data it is desirable to have a transform that holds for the whole depth range; that is, a transform that can be applied to the seismic velocity cube as a whole. The simplest depth trend would be to calibrate the transform at a shallow and a deep part of the section, and establish a linear depth trend. Engelmark (2010) showed that the change of brine resistivity with changing temperature is likely to be the major influence. He successfully applied the dual-water model (Clavier et al., 1984) for the transform from porosity to resistivity. The dual-water model states that there are two kinds of resistivity in the rock, one from the pore water (ionic), and one from the clay-bound water (Cation Exchange Capacity CEC). The weight of these two resistivities is a function of the concentration of NaCl and of CEC. However, Engelmark (2010) got good results by using the pore water resistivity in the shallow, unconsolidated section solely, and the clay-bound water resistivity in the deeper, consolidated section solely. He uses Archie with the resistivity of sea water for the top 525 m, and Archie with the temperature-dependent clay-bound water resistivity from Waxman and Thomas (1974), as given in Dewan (1983, eq. 7.22),

$$\rho_\mathrm{f} = \left[6.8\left(1 + 0.0545\,T_0 - 1.127\times10^{-4}\,T_0^2\right)\right]^{-1} \quad , \tag{5.6}$$

where $T_0 = T - 25$, $\rho_\mathrm{f}$ is brine resistivity, and $T$ is Temperature in °C.

Instead of the resistivity of sea water, we can apply the model of Sen and Goode (1992, eq. 9), which provides temperature-dependent pore water resistivity, incorporating the molality (mol solute per kg solvent) of salt water:

$$\rho_\mathrm{f} = \left\{\left(5.6 + 0.27\,T - 1.5\times10^{-4}\,T^2\right)\,M - \frac{2.36 + 0.099\,T}{1.0 + 0.214\,M}\,M^{3/2}\right\}^{-1} \quad , \tag{5.7}$$

taken as the thermal gradient, this relationship provides basically nothing other than a depth dependent relation for the resistivity of the pore fluid.

There are other factors that influence a velocity-to-resistivity transform. One of these is resistivity anisotropy, which is known to have a big impact for multi-transient electromagnetic (MTEM) modelling (Werthmüller, 2009); I estimate the anisotropy in Chapter 6. The available well logs commonly measure horizontal conductivity. The procedure

presented here provides therefore an estimate of the available horizontal resistivities. If there is an anisotropy estimate from data, modelling, or experience, it can be incorporated into the final model. In any case, a slight resistivity anisotropy of $\lambda \approx 1.5$ might be more realistic than the isotropic assumption (where $\lambda$ is the square root of the ratio of vertical over horizontal resistivity, $\lambda = \sqrt{\rho_v/\rho_h}$). Overpressure affects velocity and resistivity differently, as can be seen in Eaton's pore pressure equations, Eaton (1975). It is another factor that could improve a velocity-to-resistivity transform, and which could be implemented in the framework presented here.

### Structural information

Seismic data provide more information than just seismic velocities. In fact, the main reason for acquiring seismic data is that they are particularly good at detecting elastic and acoustic impedance contrasts, which delineate geological structures in 3D. In addition to depth constraints, a velocity-to-resistivity transform can be improved by using different transforms for different lithologies, e.g. one model for shaley sections, and another model for sandstone sections.

## 5.3 Uncertainty

There exist many different rock-physics models to link seismic velocity to electric resistivity, as we have seen. Some of them use an intermediate variable, mostly porosity, others are a direct function. Whatever the choice of the rock-physics model, we gain a resistivity value derived from rock physics, $\rho_{\mathrm{rp}}$, which is a function of seismic P-wave velocity $v$ and other parameters,

$$\rho_{\mathrm{rp}} = h(v, \mathbf{p}) \ , \tag{5.8}$$

where the other parameters are here summarised by $\mathbf{p}$. In my example I use the relations given in Equations 5.1 to 5.5, hence I have relations in the form of

$$\rho_{\mathrm{rp}} = h_{\mathrm{s}}(\rho_{\mathrm{s}}, \rho_{\mathrm{f}}, \zeta, \phi) \ , \quad \text{where} \tag{5.9}$$

$$\phi = h_{\mathrm{G}}(K_{\mathrm{s}}, K_{\mathrm{f}}, G_{\mathrm{s}}, \varrho_{\mathrm{s}}, \varrho_{\mathrm{f}}, \kappa, v) \ . \tag{5.10}$$

Here $h_{\mathrm{s}}$ stands for the self-similar model and $h_{\mathrm{G}}$ for the Gassmann-based relations.

Using rock-physics modelling to get resistivities from seismic velocities introduces two kind of errors. The parameters in the model ($\rho_{\mathrm{s}}$, $\rho_{\mathrm{f}}$, $\zeta$, $K_{\mathrm{s}}$, $K_{\mathrm{f}}$, $G_{\mathrm{s}}$, $\varrho_{\mathrm{s}}$, $\varrho_{\mathrm{f}}$, $\kappa$, $v$) have errors, and the models ($h_{\mathrm{s}}$, $h_{\mathrm{G}}$) themselves have errors. These errors are likely to be bigger

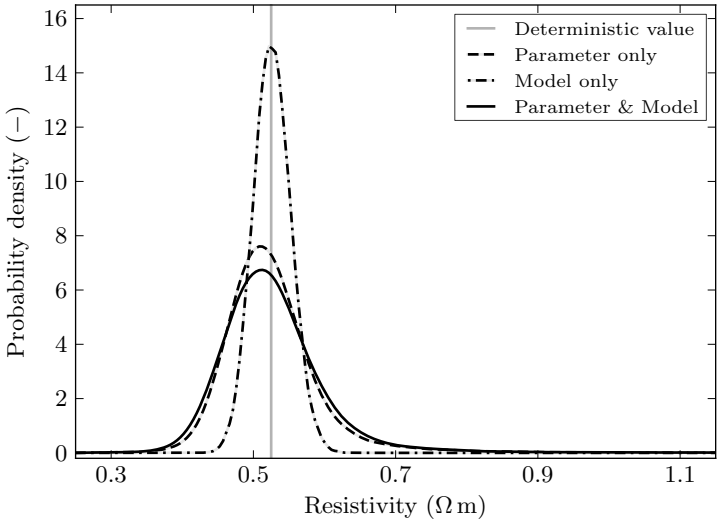


**Figure 5.4:** Example of the uncertainty analysis applied to the Gassmann/self-similar transform for velocity $v = 2.5\,\mathrm{km/s}$ and the parameters in Table 5.1. The applied error is 5 % for both the uncertainty of each parameter and of the model.

than the errors in the data themselves, as shown by Kwon and Snieder (2011). I adapt the methodology of Chen and Dickens (2009), who emphasised that both parameter uncertainty and model uncertainty have to be taken into account.

They describe the rock-physics model as a gamma distribution with error $\epsilon$,

$$g(\rho|v, \mathbf{p}) = \frac{\beta^\alpha \rho^{\alpha-1}}{\Gamma(\alpha)} \exp(-\beta\rho) \ , \tag{5.11}$$

where $\mathbf{p}$ is a vector containing all model parameters, the shape parameter $\alpha = 1/\epsilon^2$, and the scale parameter $\beta = (\alpha - 1)/\rho_{\mathrm{rp}}$. The parameters themselves are described as uniform distributions of a defined error around my best estimate. To get the probability density function (pdf) of the whole range of possible parameters, one has to integrate over all values,

$$g(\rho|v) = \int g(\rho|v, \mathbf{p}) g(\mathbf{p}|v) \, \mathrm{d}\mathbf{p} \ . \tag{5.12}$$

I use a Markov chain Monte Carlo (MCMC) sampler to calculate the distribution, as suggested by Chen and Dickens (2009) (for more details see Chapter 3). The result of this methodology is resistivity $\rho$ as a pdf for any given set of model parameters, instead of a single deterministic value $\rho_{\mathrm{rp}}$, as shown in Figure 5.4. The grey line shows the deterministic resistivity value resulting from the Gassmann/self-similar equation with the parameters given in Table 5.1 and velocity $v = 2.5\,\mathrm{km/s}$. The dashed curve shows the distribution if the model has no uncertainty, but with the parameters uniformly

distributed with a range of $\pm 5\,\%$. The dash-dotted curve shows the distribution if the parameters have no error, but the rock-physics model is a gamma distribution with $\epsilon = 0.05$. The solid curve finally shows the distribution if both uncertainties are taken into account. The parameter uncertainty is more important than the model uncertainty in this example. However, both contribute to the final pdf, and their relative contributions vary from case to case.

Even though a seismic section never displays an error bar, seismic data have errors too. To quantify the error in seismic data is difficult, and one would have to take into account acquisition and processing errors. In Figure 5.4 I assigned to the seismic velocities the same error as to all the other parameters. However, with the real data I estimate the uncertainty in seismic velocities from the data themselves, using the same well logs I use to calibrate my rock-physics model, which I show in the example section.

## 5.4 Example: The Harding field

My study area is the North Sea Harding field, operated by BP and Mærsk. The field is a medium-size oil and gas field at a depth of about 1.7 km; water depth is approximately 110 m. See Chapter 4 and Beckly et al. (2003) for a thorough description. Two CSEM surveys with a transient source signal were carried out in 2007 and 2008 in a successful MTEM repeatability experiment described by Ziolkowski et al. (2010). The MTEM method is described in Chapter 4 and Ziolkowski et al. (2007). The source dipole current signal in MTEM is a measured pseudo-random binary sequence (PRBS), which allows the impulse responses of the subsurface to be recovered from the measured receiver responses. The full spectrum of the earth response is recovered. Figure 5.5 shows the outline of Harding Central and Harding South, the location of the wells used and the CSEM acquisition line, which passes the discovery Well 9/23b-7, and the water-wet Well 9/23a-3. In this repeatability experiment, 1D inversion results were collated to form a 2D resistivity section, where the layer thicknesses were derived from the seismic data. The result is mainly constrained by these chosen layers. The resulting 1D models fit the CSEM data reasonably well, however, I do not know if they are realistic or not, due to the non-uniqueness of, specifically, 1D CSEM inversion.

First, I calibrate my rock-physics model with Well 9/23b-8 from Harding South. Second, I check this transform with the other well logs. Third, satisfied by this control, I apply this transform to a seismic velocity section along the CSEM-line to get a detailed model of the background resistivities. The result is a 2D background resistivity model. However, I can also apply the same transform to the whole seismic cube, in order to

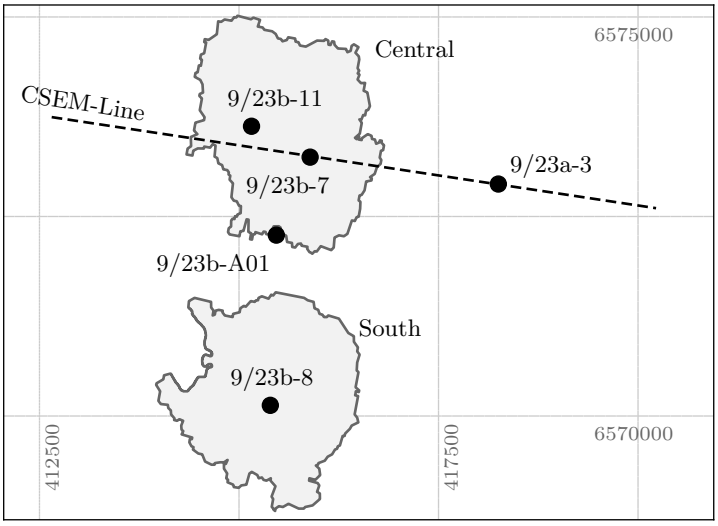


**Figure 5.5:** Location of Harding Central and Harding South, the CSEM survey outlines from 2007 and 2008, and the five wells I use in my example. Well 9/23b-8 is my calibration well. Wells 9/23b-7, 9/23b-11, 9/23b-A01, and 9/23a-3 are my control wells, where the ultimate one is off-target.

get a 3D background resistivity model of my area of interest. I do not do this here, as it does not add anything to the methodology described.

Figure 5.6 shows P-wave velocity versus resistivity from Well 9/23b-8 for relatively clean shale sections, colour-coded for different depth intervals. The depth-trend is clearly visible, with resistivities becoming smaller and velocities higher for deeper sections. The data indicate a weak relationship between velocity and resistivity. This relation is what I try to capture with the rock-physics transform from velocity to resistivity, incorporating the noticeable depth trend.

### Seismic velocity uncertainty

I assign my rock-physics model and all involved parameter errors as described in the first part of the chapter: the Gassmann/self-similar transform is described as a gamma distribution with an error of 5 %, and the parameters are uniformly distributed around my best estimate with an error of ±5 %. Exceptions to this are the seismic velocities. Seismic sections and seismic velocities usually come without a measure of the associated error. Errors in seismic velocities come from both acquisition and processing. It is, however, not an easy task to estimate this error. I use the well log data to get an estimate of the variability of seismic velocities. Figure 5.7 shows the velocity measurements of Well 9/23b-8, where the grey curve ($v$) is the original data, and the black curve ($\bar{v}$) is the original data smoothed using a Hann function over 320 samples ($\approx 48.8\,\mathrm{m}$). The

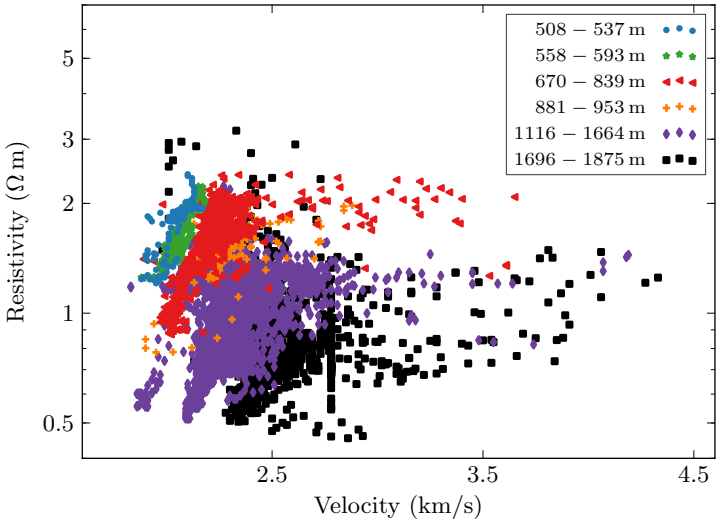


**Figure 5.6:** Velocity versus resistivity plot for some relatively clean shale sections in Well 9/23b-8. There seem to be a weak relationship between velocity and resistivity, which rock physics tries to predict. Note the depth trend, resistivity is generally decreasing and velocity is increasing with increasing depth.

smoothed curve reflects the expected resolution of CSEM data better than the 15 cm (0.5 ft) sampling of the well log. I now define my velocity distribution as the difference between the log values and the values of the smoothed log, $v(z) - \bar{v}(z)$. This method is a good measure for the variability of velocities, and the resulting distribution is thought to be wider than errors in seismic velocities resulting from acquisition and processing of seismic data. The resulting distribution is shown in Figure 5.7, where the pdf of this data distribution is found with a Gaussian kernel density estimation (KDE). This approach should be replaced with a better estimate of seismic velocity uncertainty, if it is available. The point is to estimate velocity uncertainty from the data.

## Calibration and depth trend

Figure 5.8 shows in plots (a) and (b) the original (grey) and smoothed (black) velocity and resistivity logs of my calibration Well 9/23b-8, and the mode and ±1 and ±2 standard deviations of my analysis in red, orange, and purple, respectively. I wanted the transform to be as simple as possible, yet be able to predict the whole depth range. One of the difficulties with rock-physics transforms is that they usually hold for only a very specific environment, for instance, for a specific depth range. The seismic velocities in Harding are between 1.5 and 3 km/s in the shallow part, but up to 6 km/s in the deeper part. I therefore model the bulk and shear moduli of the solid fraction as linear functions of depth, to allow velocities to increase with increasing depth: the bulk modulus is defined as $K_s = 10 + 15\,d$ GPa, and the shear modulus is defined as

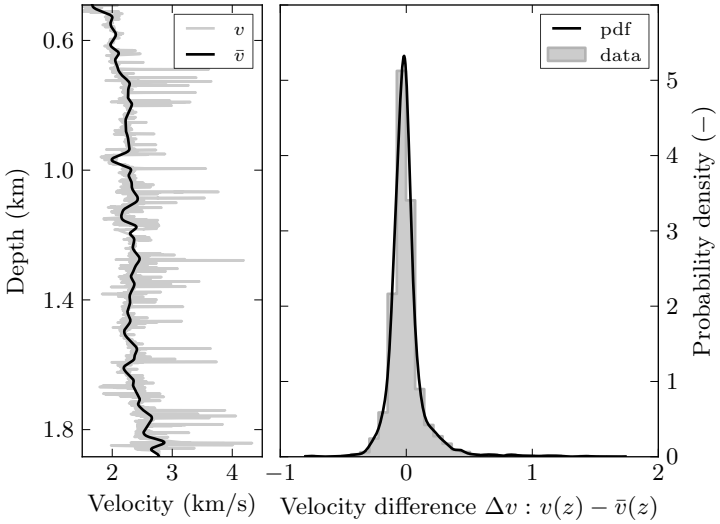


**Figure 5.7:** Velocity log of Well 9/23b-8. The grey curve ($v$) is the original log, and the black curve ($\bar{v}$) is smoothed with a Hann function over 320 samples. I estimate the P-wave velocity distribution from the well log data by taking the difference of the original and the smoothed data, $v(z) - \bar{v}(z)$.

$G_s = 5 + 13\,d\,\mathrm{GPa}$; $d$ is depth in km. Fixed parameters are the density of the solid fraction, $\varrho_s = 2.65\,\mathrm{g/cm^3}$, the density of the fluid fraction, $\varrho_f = 1.03\,\mathrm{g/cm^3}$, and the bulk modulus of the fluid fraction, $K_f = 2.25\,\mathrm{GPa}$. Following Engelmark (2010), I make the cementation exponent a function of porosity, $\zeta = 2.1 - \phi$, and I furthermore define the Krief exponent as a function of depth, $\kappa = 3.2 - 0.4\,d$. The resistivity of the solid fraction is given by $\rho_s = 3{+}10\,d\,\Omega\,\mathrm{m}$. The sum of the free water resistivity, Equation 5.6, and the bound water resistivity, Equation 5.7, yields in my case the best result for the fluid resistivity. However, Equation 5.6 yields unreasonable values for shallow depths (hence low temperatures). I therefore apply it from 350 m below mudline downwards, and keep it constant above.

I include an example of structural constraints in the form of the Grid sandstones, which are outlined from picked horizons in the seismic data. The same parameters are used for the Grid sandstones, except that $\kappa = 2.6$, and the fluid resistivity is given by the free water resistivity solely, as sands have no clay-bound water.

The plots (c), (d), and (e) in Figure 5.8 show all the depth-dependent values. This rock-physics transform is able to predict the resistivities for the whole depth range of the well log. However, the predictions are a bit too high for some shallow, sandy sections. These sand sections could be handled in the same way as I treat the Grid sandstones.

Figure 5.9 shows a *depth-snapshot* of the calibration of the transform for $d = 1.474\,\mathrm{km}$, together with the well data of $d \pm 50\,\mathrm{m}$. With the exception of some high velocity values,

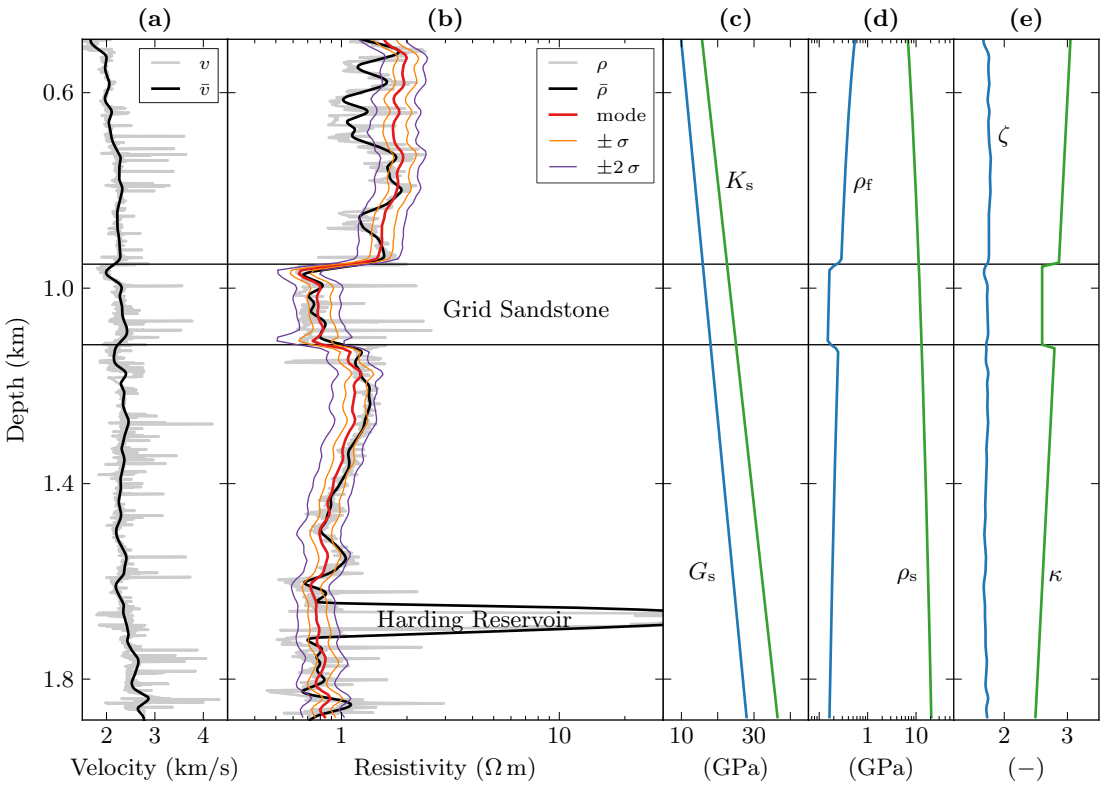


**Figure 5.8:** Velocity (a) and resistivity (b) log of Well 9/23b-8. The grey curve is the original log, the black curve is smoothed with a Hann function over 320 samples. The red curve is the mode of the pdfs from the uncertainty analysis using the Gassmann/self-similar velocity-to-resistivity relation. The orange and purple curves are $\pm\sigma$ and $\pm 2\sigma$, respectively. Plots (c), (d), and (e) show all depth-dependent parameters: $K_s, G_s, \rho_s, \rho_f, \zeta$, and $\kappa$.

resulting mostly from thin limestone layers, the mode of the uncertainty analysis $\pm 2\sigma$ includes all the well samples.

## Near-field scenario

I now use this calibration from Harding South and test it on a field nearby, Harding Central. I apply the rock-physics transform with the parameters as described before to the Harding Central velocity cube, and compare them first to well logs. Figure 5.10 shows the well logs, and the mode as well as $\pm 2\sigma$ of the resistivity calculated from the seismic velocities. The predicted resistivities match the well logs very accurately, except for the hydrocarbon-bearing formations (the Harding reservoir; the reservoir is below the log shown for Well 9/23b-A01, and Well 9/23a-3 is water wet). This is exactly what I want, as I am interested in a background resistivity model.

The result of my velocity-to-resistivity transform is shown in Figure 5.11; (a) shows the mode of my resistivity distributions, derived from the seismic velocities shown in

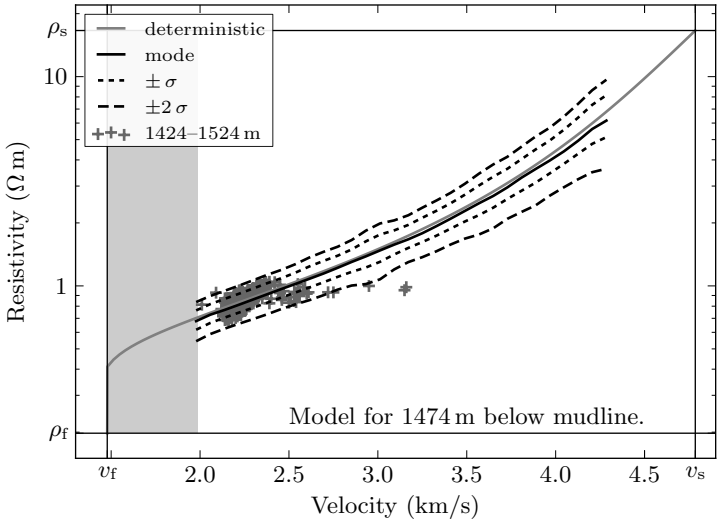


**Figure 5.9:** Comparison of the rock-physics model and uncertainty analysis with well data. The plotted well data are from within $1424-1524$ m depth of Well 9/23b-8. Depth is set to $d = 1.474$ km for the depth dependent parameters. The deterministic result of the transform is shown in grey, and the outcome of the uncertainty analysis in black. The well data are within $\pm 2\,\sigma$, except for some high velocity outliers originating from thin limestone layers.

(b). It is a vertical section through the velocity cube along the CSEM line from 2007 and 2008, including some major horizons, such as the Grid sandstones and the Balder formation, Well 9/23b-7, and the start and end points of these surveys. Subplots (c) and (d) show the mode plus and minus one standard deviation of the resistivity distributions. Applying the transform to the velocity cube instead of just a vertical section yields a 3D resistivity background model. Please note one limitation: The transform is calibrated using well log measurements from a vertical well, which measure mainly horizontal resistivity. These models therefore provide an estimate of horizontal resistivities. Reasonable anisotropy values have to be estimated independently of the approach presented here (see Chapter 6).

## 5.5 Discussion

I present a methodology to estimate the range of background resistivity models that is consistent with known seismic velocities. I apply and extend known methods. The approach employs depth-dependent petrophysical cross-property relations, and uncertainty analysis of both the data and the model. My near-field exploration example shows that this methodology yields a good estimate of background resistivities away from my control point, and hence provides an excellent additional data set, which can be used for integrated analysis, or as a starting point for a detailed CSEM feasibility study or

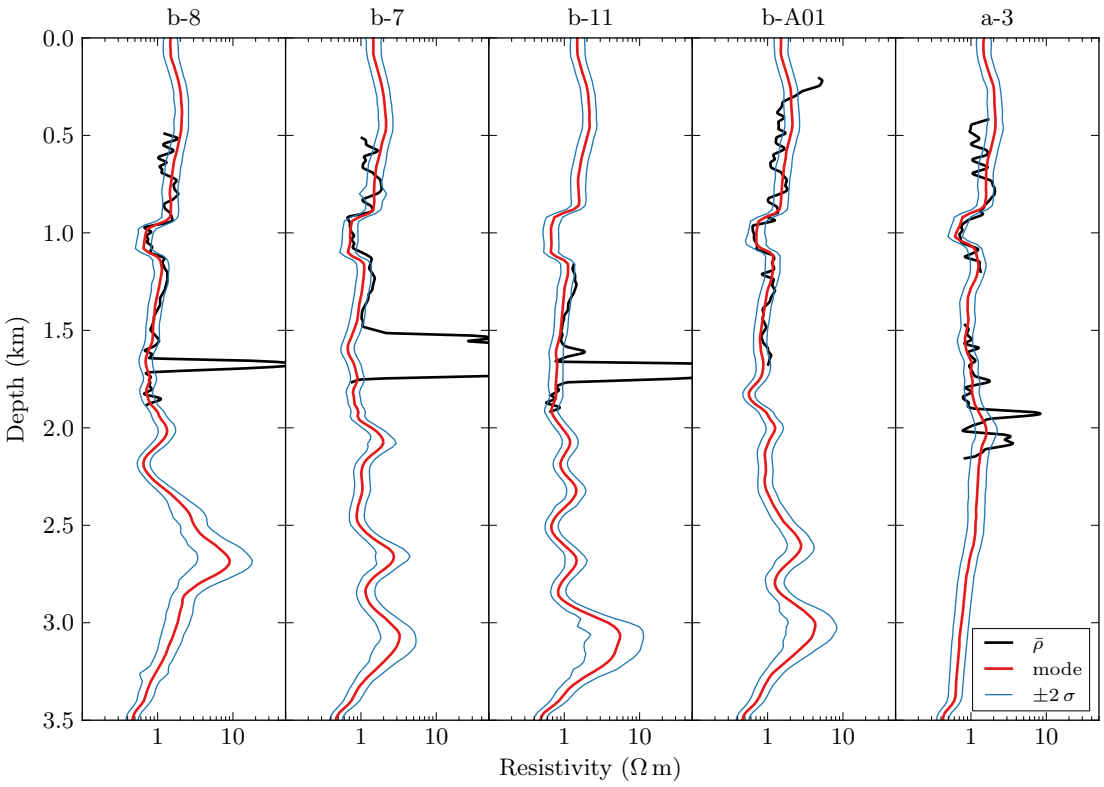


**Figure 5.10:** Well logs (grey) and the mode (black) and $\pm 2\,\sigma$ (dashed) of the resistivity predictions calculated using the seismic velocities. Well 9/23b-8 (leftmost) is the calibration well. The same transform applied to four wells on Harding Central shows a good match: most well measurements lie within $\pm 2\,\sigma$. High resistive, hydrocarbon-bearing formations are not predicted, as I assume brine-filled pores. Shallow, sandy sections are also poorly resolved, except for the Grid sandstones, which I explicitly incorporated into my model.

(iterative) forward modelling. Using a probability distribution instead of fixed values for the background model decreases the influence of unwanted bias that originates from the different physical properties of the seismic and CSEM methods. Additionally, the uncertainty estimates yield error bars to this data set, and the pdfs can be incorporated into weighting functions for 3D inversion schemes, where the background resistivities would be limited to these values.

This workflow needs fine tuning from case to case, as it is not always easy to find a single rock-physics model that fits a large depth range. Every part of the scheme is disputable, and other models might fit better in other cases; it is also a function of personal experience and preference. The Gassmann and the self-similar model are a choice out of many, as is the gamma distribution for the model uncertainty. The greater the knowledge of the present rock-physics parameters, the better are the estimates of their uncertainties. An individual uncertainty for each parameter might therefore be more sensible than my approach of assigning a range of 5 % to each of them. Similar

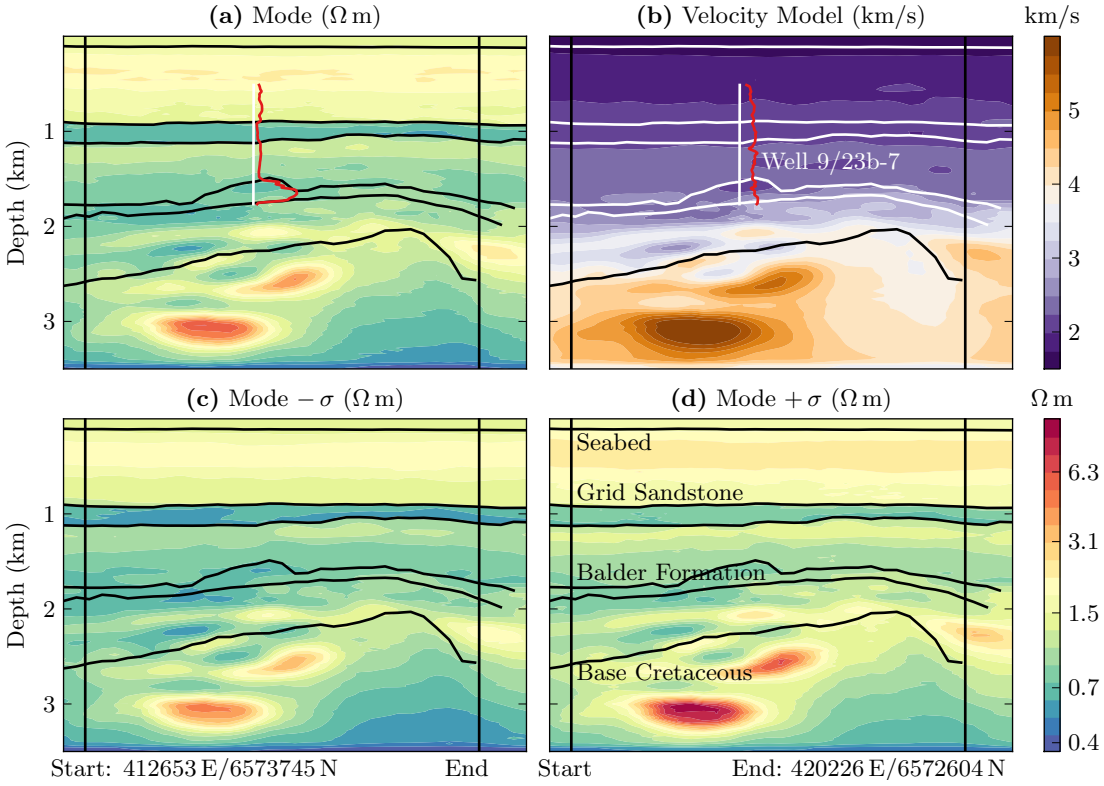


**Figure 5.11:** (a) is the mode of my background resistivity model, derived from the velocity model in (b); Well 9/23b-7 and some major formations are annotated. (c) and (d) are the mode with $-\sigma$ and $+\sigma$, respectively. These resistivities represent horizontal resistivities, as they are calibrated with a vertical well log, which mainly measures horizontal resistivities.

conclusions apply to the depth trend, where I could choose many more horizons, and include different rock-physics models for different lithologies in general. However, my approach was to be as simple as possible, yet as complex as necessary. The resulting background resistivity model is in any case a much better resistivity model than a uniform half-space (often used as a starting model in inversion), and is corroborated by the good match with the well logs. I have shown only a vertical section along the CSEM line. However, I can apply the transform to the entire velocity cube. This gives us the range of possible 3D background resistivity models of the whole area.

Having well log information for calibration is crucial. My example shows that this well log does not necessarily have to be from the field of interest, but from within the region of interest (from similar lithologies). The calibration issue remains a problem above and below the depths of available logs, where other information might help to improve the calibration. Furthermore, the calibration with well logs also limits us to predict horizontal resistivities. Reasonable anisotropy values have to be found independently of this approach.

## Summary

I derive a model of horizontal background resistivities from seismic velocities for the North Sea Harding Central field, where I apply rock physics, depth trends, and structural constraints. I use a well log from nearby field Harding South to calibrate the transform, and confirm it by applying it to well logs in Harding Central. Furthermore, I use a Bayesian framework to estimate the error in these resistivities resulting from the errors of the involved rock-physics parameters, rock-physics models, and the seismic data. This workflow results in a detailed background resistivity model that is in agreement with the seismic velocities and the well logs.

■

# 6

# One-dimensional modelling

**Essentially, all models are wrong,**
**but some are useful.**

*George Edward Pelham Box (1919–2013)*
*Mathematician*

Rock physics can be used to determine background resistivities from seismic velocities, using well logs for calibration. This method yields detailed background resistivity information, but suffers from two weaknesses: velocity-to-resistivity transform outside well control, and resistivity anisotropy. If controlled-source electromagnetic (CSEM) data are available, they can be used to improve this background resistivity model with fast 1D (iterative) forward modelling. In this chapter, I look first at the advantages and limitations of 1D modelling, and then use the concept of apparent anisotropy to estimate the anisotropy in the Harding area of the North Sea. I then use 1D inversions of the short-offset Harding data to determine the anisotropy, and to improve the horizontal resistivities of the shallow section of the background model. I finish with a note about the deep section, below well control.

I submitted parts of this chapter to the SEG journal *Interpretation* for a special section on *Interpretation and integration of CSEM data* in the August 2014 issue.

## 6.1 Improving the background resistivity model

Rock physics can be used to transform seismic velocities into porosities, and porosities into resistivities, with well logs used to calibrate the transforms. These transforms as well as the associated parameters contain errors, but we can estimate the resulting resistivity distribution. I derive in Chapter 5 in this manner a background resistivity model (called background model in this thesis) for Harding Central from seismic velocities, with the final result shown in Figure 5.11. I include structural information and depth trends into the rock-physics model, and estimate its uncertainty. I calibrate my transform with a well log from Harding South, and check the result with well logs from Harding Central. This background model predicts the well logs correctly, which shows that this model provides detailed knowledge of the subsurface resistivities. It is arguably the best continuous knowledge (as opposed to only discrete well log information) of our subsurface resistivities; unfortunately it applies only in the depth range where there is well control. Such a background model provides an additional data set, resistivity, in the absence of any CSEM data, which can be used for CSEM modelling and feasibility studies.

However, a model generated in this way has two weaknesses: there is a problem with accuracy outside well control, and there is no account of resistivity anisotropy (just termed anisotropy in this thesis). The model accuracy is limited outside the depth range where there is well control, as there is no measure to check the velocity-to-resistivity transform. The resistivities in this model represent horizontal resistivities, as the calibration was done with measurements made with conventional resistivity tools in vertical wells, measuring mainly horizontal resistivity (see Chapter 4). The transform provides no knowledge of the anisotropy.

Anisotropy describes the variation of a material property with direction. In an isotropic medium, a material property is a scalar. But in reality, a material property is a tensor. An often used simplification of this tensor is vertical transverse isotropy (VTI), where the property behaves differently in the horizontal and vertical directions. In this case, anisotropy is commonly defined as

$$\lambda = \sqrt{\frac{\rho_\mathrm{v}}{\rho_\mathrm{h}}}\,, \tag{6.1}$$

where $\rho_\mathrm{v}$ and $\rho_\mathrm{h}$ are vertical and horizontal resistivity respectively, and $\lambda$ is the anisotropy factor. This is a justifiable simplification for the geological case of horizontal sedimentary layers. The (geometric) mean resistivity $\rho_\mathrm{m}$ is the quantity measured by

the direct current (DC) method (e.g. Negi and Saraf, 1989, p. 28), and is given by

$$\rho_{\mathrm{m}} = \sqrt{\rho_{\mathrm{v}}\rho_{\mathrm{h}}} \ . \tag{6.2}$$

It is important to note that it is not sufficient to say "increasing anisotropy leads to ...", as this is ambiguous. It follows from Equations 6.1 and 6.2 that it needs two out of the four parameters $\rho_{\mathrm{h}}$, $\rho_{\mathrm{v}}$, $\rho_{\mathrm{m}}$, and $\lambda$ to define the system. A conclusion needs therefore to specify two parameters, for instance "increasing anisotropy and keeping the mean resistivity constant leads to ...". The relation between horizontal, mean, and vertical resistivity is more clearly seen when written

$$\lambda\rho_{\mathrm{h}} = \rho_{\mathrm{m}} = \frac{1}{\lambda}\rho_{\mathrm{v}} \ . \tag{6.3}$$

Anisotropy has a huge influence on electromagnetic (EM) responses. Maillet (1947), Bhattacharya and Patra (1968), and also Negi and Saraf (1989) discuss the theory and the effect of anisotropy in DC measurements (e.g. Wenner or Schlumberger arrays), Edwards et al. (1984) for CSEM, and Werthmüller (2009) shows the influence on multi-transient electromagnetic (MTEM) data. Ellis et al. (2009) conclude that the difference between log-derived resistivities and resistivities gained from CSEM measurements are mainly due to anisotropy.

In the case of Harding I have CSEM data which I can use to improve the derived background model in two ways in this chapter. First, I derive an estimate of anisotropy, and second, I improve the shallow part of the model, where we have no well control. I do not deal with the deeper part, where there is no well control. However, I show that the deeper part is not very relevant for the range of offsets where we have measurements, and with the expected anisotropy. Figure 6.1 shows in red two CSEM responses from the Harding acquisition with their corresponding 1D modelled responses from the background model, taken at the location of the common midpoint (CMP); the locations of the responses are indicated by the inset map (see Figure 6.14). The discrepancy between measured data and modelled data varies from response to response. Figure 6.1a shows a typical result, where the amplitudes of the measured data are higher than the modelled ones. Figure 6.1b is an example where the measured response falls within the error bounds, although close to the upper limit. Generally, the responses from the forward model are lower then the measured responses. This can be attributed to too low (mean) background resistivities, or to the wrong anisotropy, or, most likely, both.

I have to emphasise that this step differs in a very important way from the previous derivation of a background model. In Chapter 5 I derive a background model from seismic data and well logs. No CSEM measurements are used at any point. For a

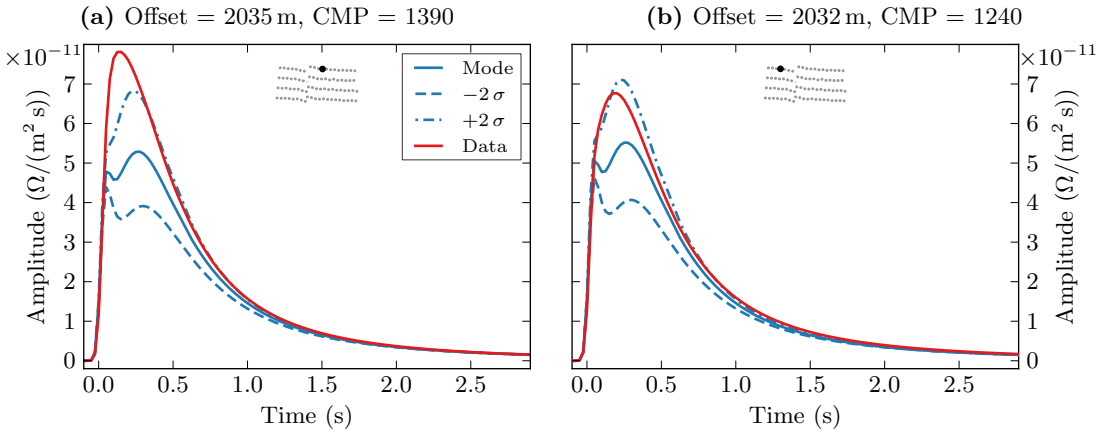


**Figure 6.1:** Two CSEM responses (red) and their corresponding 1D modelled responses from the background model. The resistivities at the corresponding CMPs were chosen for the modelling. (a) shows the usual case, were the modelled responses were too low. (b) is an example where the response lies within the error bounds, but close to the upper limit.

feasibility study prior to CSEM acquisition, a regional anisotropy factor should be used, or well measurements, or any other means to get an estimate of anisotropy. In this chapter I use CSEM data – hence measurements have already taken place – to improve this initial background model. The coverage of the CSEM data is very limited compared with the coverage of seismic data, so I have to extrapolate these adjustments to the extent of the background model. See Appendix C.3 for more information regarding the 1D forward modelling (`EX1D`) and inversion (`MTEM1D_INV`) codes used in this chapter.

All the results in this chapter are my own. However, two postgraduate projects used the background resistivity model for CSEM forward modelling and comparison to the measured data. Both projects provided interesting insights, which I have incorporated in my work. Yonas Brenner carried out his six weeks thesis project (M.Sc. in Petroleum Geoscience, Edinburgh University, Heriot-Watt University, and Newcastle University) in our group (July/August 2012). Yonas calculated various 1D forward models, and compared them with the measured data. Magdalena Escalas Oliver, at the time a third-year Ph.D. student at the University of Barcelona, Department of Geodynamics and Geophysics, Spain, spent three months in our research group (September to December 2012). She carried out 1D forward modelling of various offset ranges, and isotropic 1D inversions of the shallow part.

## 6.2 Advantages and limitations of one-dimensional modelling

Trying to model a 3D earth with a 1D model is a gross simplification, and most of the time simply wrong. This was recognised even before the new age of CSEM exploration, the Society of Exploration Geophysicists (SEG) published a book titled "Three-Dimensional Electromagnetics" in the late nineties (Oristaglio and Spies, 1999). However important it is to accurately model the subsurface in 3D, it is also computationally expensive. But it is without doubt one of the most important steps in the maturing process of the CSEM industry to move from 1D to 3D (iterative) forward modelling. For example: the Harding reservoir, as a 1D model, yielded a maximum target response of 76 % over background or more (PGS feasibility studies, internal documents) in feasibility studies. Modelled as a 3D reservoir embedded in an anisotropic background, the target is hardly detectable at all, see Chapter 7. Over-estimation of target responses is one pitfall of 1D modelling. Another is that multi-offset inversions often fail, because the earth is not 1D. Even a collation of various 1D inversion results does not yield the real 2D result either.

1D forward modelling has one major advantage; in addition to the benefit of being computationally cheap, it is simple. 1D modelling is very well understood and robust. It allows the sensitivity to different parameters to be investigated quickly. One of the simplifications in 1D modelling is water depth if the bathymetry is not flat. Figure 6.2a shows the influence of water depth for the simple model A in Figure 6.4 (representing simplified Harding), with water resistivity of $0.3\,\Omega\,\mathrm{m}$. Beneath the water layer is an anisotropic half-space with mean resistivity $1\,\Omega\,\mathrm{m}$, and $\lambda$ of 1.5. Water depth is 110 m (solid line) and $110\,\mathrm{m} \pm 10\,\%$ (dash-dotted line and dashed line, respectively). It shows that a 1D water layer can result in a significant error, if the water depth at source location is significantly different from the water depth at receiver location. However, it only affects the airwave. The responses are calculated for offsets of 3 km (blue), 5 km (red), and 7 km (green). The amplitudes are normalised by the maximum of the normal case (solid line) for each offset in this and the following figures. (This is only done for display purposes.)

Another parameter that is often not exactly known is water resistivity (which depends on the water salinity), both in 1D and 3D modelling. Figure 6.2b shows the influence of water resistivity. The model is the same as above, with water depth fixed at 110 m, and resistivity of $0.3\,\Omega\,\mathrm{m}$ (solid line) and $0.3\,\Omega\,\mathrm{m} \pm 10\,\%$ (dash-dotted line and dashed line, respectively), see model B in Figure 6.4. Note that the solid curves in the two plots are the same model. By comparing the two subplots of Figure 6.2 it can be seen that the effect of resistivity is very similar to the effect of varying water depth. As resistivity

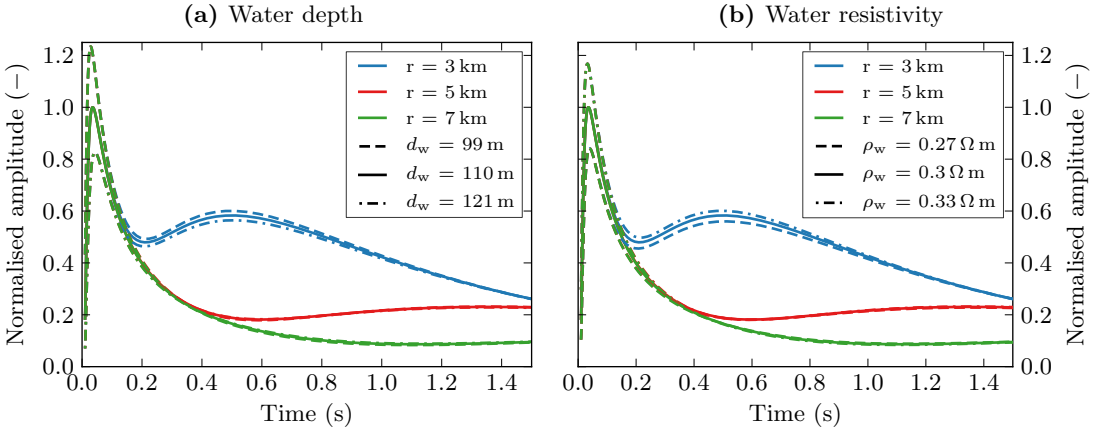


**Figure 6.2:** Influence of (a) water depth and (b) water resistivity. The solid responses are the same in both plots. The dashed responses show the influence of 10 % lower water depth and water resistivity, and the dashed-dotted responses show the influence of 10 % higher water depth and water resistivity. The models correspond to (a) A and (b) B in Figure 6.4.

decreases, the airwave is more attenuated by the water layer, which is essentially the same as increasing the water depth. Both affect the airwave only, and therefore short offsets more than long offsets. Whereas water depth is usually known very accurately, the importance of water resistivity is often neglected. For the Harding data the water depths are known, and bathymetry is relatively flat. The water resistivity was set to 0.3 Ω m in Ziolkowski et al. (2010), and the same assumption is used in this thesis.

Next I use similar models to investigate the sensitivity to the two biggest unknowns, anisotropy and the accuracy of the velocity-to-resistivity transform in the shallow part, where I have no well control. The solid line in Figure 6.3 shows the response for the same model as before ($d_w = 110$ m, $\rho_w = 0.3\,\Omega$ m, $\rho_m = 1.5\,\Omega$ m, $\lambda = 1.5$), where the dash-dotted and dashed models have anisotropies of $1.5 \pm 10$ %; see model C in Figure 6.4. The change in anisotropy only affects the airwave slightly, and the airwave is therefore not shown in order to show the effect on the earth response more clearly. However, over- or underestimating the anisotropy even by only 10 %, and by keeping the mean resistivity constant, has a big impact on the responses for all offsets.

The impact of incorrect shallow resistivities is simulated in Figure 6.5. The solid line in (a) shows the same model as above, but with an additional boundary at 390 m below mudline (500 m below sea-surface; below 500 m we have confidence from well logs). The mean resistivity of the first layer (0 m to 390 m below mudline), $\rho_m^1$, is 1.5 Ω m, where dash-dotted and dashed lines have $\rho_m^1 = 1.5\,\Omega\,\text{m} \pm 10$ %, see model D in Figure 6.4. Figure 6.5b shows the same, but with a subsurface anisotropy of $\lambda = 1$. The shallow subsurface has a bigger impact on short offsets than on long offsets, and is bigger with higher anisotropy, if the mean resistivity is kept constant. Figures 6.3 and 6.5

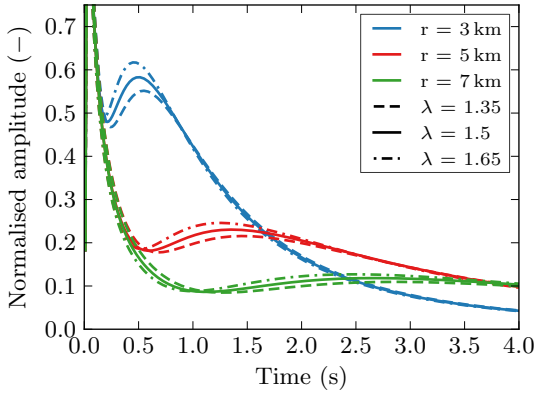


**Figure 6.3:** Sensitivity to anisotropy. Incorrect anisotropy affects responses at all offsets. Model corresponds to C in Figure 6.4.

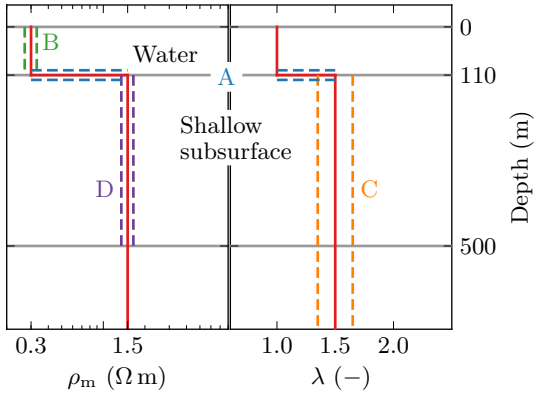


**Figure 6.4:** Standard model (red) for sensitivity tests, with changes (dashed lines) for Figures 6.2 (A & B), 6.3 (C), and 6.5 (D).

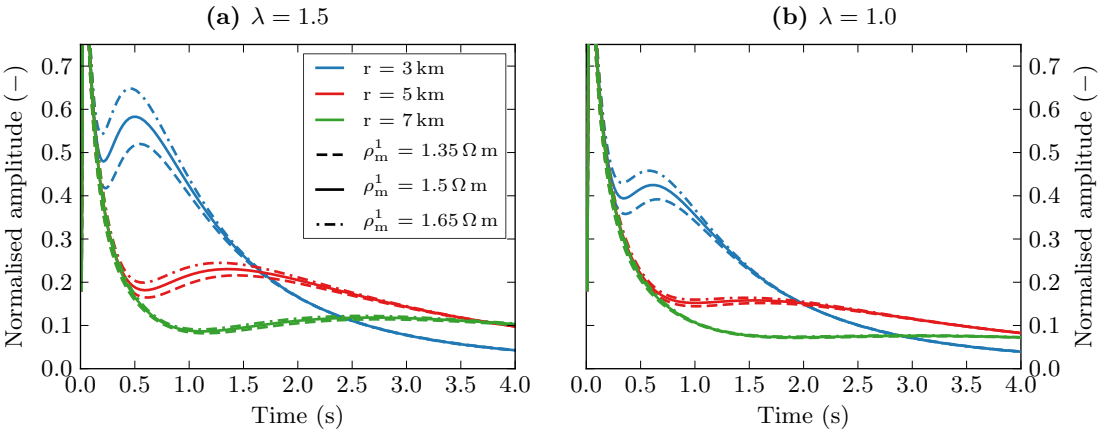


**Figure 6.5:** Sensitivity to shallow resistivity. (a) represents model D in Figure 6.4, and (b) is the same, but for an isotropic background. It shows that the shallow resistivity affects the short offsets much more then the long offsets. The effects are higher for higher anisotropy, if $\rho_m$ is kept constant.

show the importance of having a good estimate of anisotropy, and of improving the shallow resistivity. Note that in Figure 6.3 there is a cross-over: The airwave is higher if the anisotropy is lower (with constant mean resistivity), as it increases the horizontal resistivity. However, the earth response is smaller, as the vertical resistivity decreases. This is not the case in Figure 6.5, where the anisotropy is constant. In this case, the horizontal and vertical resistivities both increase or decrease, resulting in the response being higher or lower.

## 6.3 Apparent anisotropy

The concept of apparent resistivity is well known in DC measurements (e.g. Kaufmann and Keller, 1983, Chapter 5). Apparent resistivity is the resistivity of a half-space that yields the same DC value as a measurement of a more complex structure. The DC method measures the mean resistivity $\rho_\mathrm{m}$ (see Equation 6.2), but reveals no information regarding anisotropy. However, in transient measurements, such as MTEM, measured amplitudes at different times have different sensitivities to horizontal and vertical resistivities. In MTEM land responses, the late-time amplitude of the step response for $t \to \infty$ corresponds to the DC amplitude. Werthmüller (2009) uses this advantage to derive two methods for the determination of apparent anisotropy, which I briefly summarise here.

The analytical, anisotropic, inline time-domain step response (SR) and impulse response (IR) to an x-directed dipole source for a half-space and causal times are given by (Prof. Evert Slob, TU Delft, 2009, personal communication)

$$\mathcal{G}^\mathrm{S}(\rho_\mathrm{h}, \lambda) = \frac{\rho_\mathrm{h}}{2\pi r^3}\left[2\lambda + \operatorname{erf}\left(\frac{\tau_\mathrm{h}}{2}\right) - 2\lambda \operatorname{erf}\left(\frac{\tau_\mathrm{h}}{2\lambda}\right) + \frac{\tau_\mathrm{h}}{\sqrt{\pi}}\exp\left(-\frac{\tau_\mathrm{h}^2}{4\lambda^2}\right)\right] , \tag{6.4}$$

$$\mathcal{G}^\mathrm{I}(\rho_\mathrm{h}, \lambda) = \frac{\rho_\mathrm{h}}{2\pi r^3}\left[\delta(t) + \frac{\tau_\mathrm{h}}{2t\sqrt{\pi}}\left\{\left(\frac{\tau_\mathrm{h}^2}{2\lambda^2} + 1\right)\exp\left(-\frac{\tau_\mathrm{h}^2}{4\lambda^2}\right) - \exp\left(-\frac{\tau_\mathrm{h}^2}{4}\right)\right\}\right] , \tag{6.5}$$

where

$$\tau_\mathrm{h} = \sqrt{\frac{\mu_0 r^2}{\rho_\mathrm{h} t}} . \tag{6.6}$$

Here, $\mathcal{G}^\mathrm{S}$ and $\mathcal{G}^\mathrm{I}$ stand for SR and IR respectively, $\mu_0$ is the free space magnetic permeability, $r$ is offset (m), erf is the error function, and $\delta(t)$ is the Dirac delta function (see Symbols and Abbreviations).

Equations 6.4 and 6.5 reduce to the isotropic solutions for $\lambda = 1$, $\rho = \rho_\mathrm{h}$, and $\tau = \tau_\mathrm{h}$,

$$\mathcal{G}^\mathrm{S}(\rho) = \frac{\rho}{2\pi r^3}\left[2 - \operatorname{erf}\left(\frac{\tau}{2}\right) + \frac{\tau}{\sqrt{\pi}}\exp\left(-\frac{\tau^2}{4}\right)\right] , \tag{6.7}$$

as given by Weir (1980, Equation 6.13), and

$$\mathcal{G}^\mathrm{I}(\rho) = \frac{\rho}{2\pi r^3}\left[\delta(t) + \frac{\tau^3}{4t\sqrt{\pi}}\exp\left(-\frac{\tau^2}{4}\right)\right] , \tag{6.8}$$

as derived by Wilson (1997, Equation 5.38).

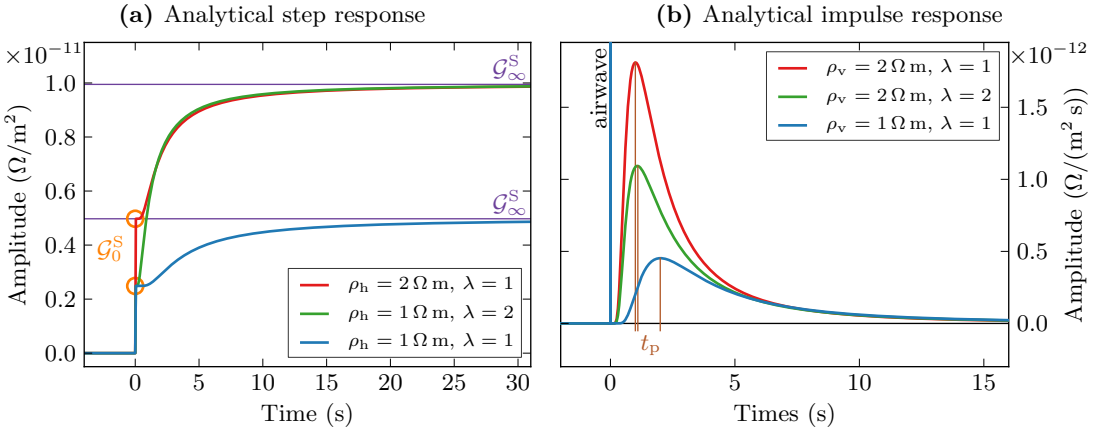


**Figure 6.6:** Analytical step (a) and impulse (b) responses for various half-space models. The characteristics used for the apparent anisotropy determination are annotated in orange ($\mathcal{G}^S_0$), purple ($\mathcal{G}^S_\infty$), and brown ($t_p$). Offset is 4 km.

By taking the limits of Equation 6.4 for times $t \to 0$ and $t \to \infty$, we obtain two characteristics of the step response, the step $\mathcal{G}^S_0$,

$$\lim_{t\to 0} \mathcal{G}^S(\rho_h, \lambda) = \mathcal{G}^S_0 = \frac{\rho_h}{2\pi r^3} \ , \tag{6.9}$$

and the DC amplitude $\mathcal{G}^S_\infty$,

$$\lim_{t\to \infty} \mathcal{G}^S(\rho_h, \lambda) = \mathcal{G}^S_\infty = \frac{\rho_h \lambda}{\pi r^3} \ . \tag{6.10}$$

Figure 6.6 shows analytical responses for Equations 6.4 and 6.5. Figure 6.6a shows step responses for half-spaces with $\rho_h = 2\,\Omega\,m$, $\lambda = 1$ (red), $\rho_h = 1\,\Omega\,m$, $\lambda = 2$ (green), and $\rho_h = 1\,\Omega\,m$, $\lambda = 1$ (blue); offset is 4 km. The characteristics $\mathcal{G}^S_0$ and $\mathcal{G}^S_\infty$ are indicated by the orange circles and the purple lines, respectively. These examples show that the initial step, the airwave, depends only on horizontal resistivity, and the late time responses are a function of the mean resistivity. Figure 6.6b shows impulse responses for half-spaces with $\rho_v = 2\,\Omega\,m$, $\lambda = 1$ (red), $\rho_v = 2\,\Omega\,m$, $\lambda = 2$ (green), and $\rho_v = 1\,\Omega\,m$, $\lambda = 1$ (blue). Impulse responses on land are characterised by an impulse at time $t = 0$ s, the airwave, followed by the earth response. The time of the peak $t_p$ of the earth response depends mainly, but not only, on the vertical resistivity, as indicated by the brown vertical lines.

The equivalent in MTEM to apparent resistivity from DC measurements follows from Equation 6.10,

$$\rho^a_a = \pi r^3 \mathcal{G}^S_\infty \ , \tag{6.11}$$

where the apparent resistivity means apparent mean resistivity. However, we can calculate an apparent anisotropy by combining the information from $\mathcal{G}_0^{\mathrm{S}}$ and $\mathcal{G}_\infty^{\mathrm{S}}$, termed airwave method (Hobbs and Werthmüller, 2010),

$$\lambda_{\mathrm{a}}^{\mathrm{a}} = \frac{\mathcal{G}_\infty^{\mathrm{S}}}{2\mathcal{G}_0^{\mathrm{S}}} \ , \tag{6.12}$$

where $\lambda_{\mathrm{a}}^{\mathrm{a}}$ stands for apparent anisotropy, airwave method.

The second method, the peak method (Hobbs and Werthmüller, 2011), uses $\mathcal{G}_\infty^{\mathrm{S}}$ together with the arrival time of the peak $t_{\mathrm{p}}$, the characteristic element of the impulse response. The peak method is an alternative if the step of measured data is not well defined. The peak arrival time is mainly a function of $\rho_{\mathrm{v}}$, but not only, as shown in Figure 6.6b. The arrival time in the isotropic case is found by taking the natural logarithm of both sides of Equation 6.8, differentiate it with respect to $t$, and set the result to zero, which yields (Ziolkowski et al., 2007, Appendix D)

$$t_{\mathrm{p}} = \frac{\mu_0 r^2}{10\rho} \ . \tag{6.13}$$

This relationship allows another way of calculating apparent resistivity,

$$\rho_{\mathrm{a}}^{\mathrm{p}} = \frac{\mu_0 r^2}{10 t_{\mathrm{p}}} \ . \tag{6.14}$$

Hobbs and Werthmüller (2011) did not find an equivalent $t_{\mathrm{p}}$ solution for the anisotropic case. However, they derived an empirical relation for the anisotropic case,

$$t'_{\mathrm{p}} = \frac{\mu_0 r^2}{9\rho_{\mathrm{v}} + \rho_{\mathrm{h}}} \ , \tag{6.15}$$

where the prime denotes that the relation is empirical. The relation shows that $\rho_{\mathrm{a}}^{\mathrm{p}}$ is dominated by the vertical resistivity. The apparent anisotropy is found by replacing $\rho_{\mathrm{v}}$ by $\lambda\rho_{\mathrm{m}}$, $\rho_{\mathrm{h}}$ by $\rho_{\mathrm{m}}/\lambda$, and solving for $\lambda$,

$$\lambda_{\mathrm{a}}^{\mathrm{p}} = \frac{\tau_{\mathrm{a}}^2 + \sqrt{\tau_{\mathrm{a}}^4 - 36}}{18} \ , \tag{6.16}$$

where

$$\tau_{\mathrm{a}} = \sqrt{\frac{\mu_0 r^2}{\rho_{\mathrm{a}}^{\mathrm{a}} t_{\mathrm{p}}}} \ . \tag{6.17}$$

For this, $\rho_{\mathrm{a}}^{\mathrm{a}}$ is used rather than $\rho_{\mathrm{a}}^{\mathrm{p}}$, as the latter is dominated by vertical resistivity.

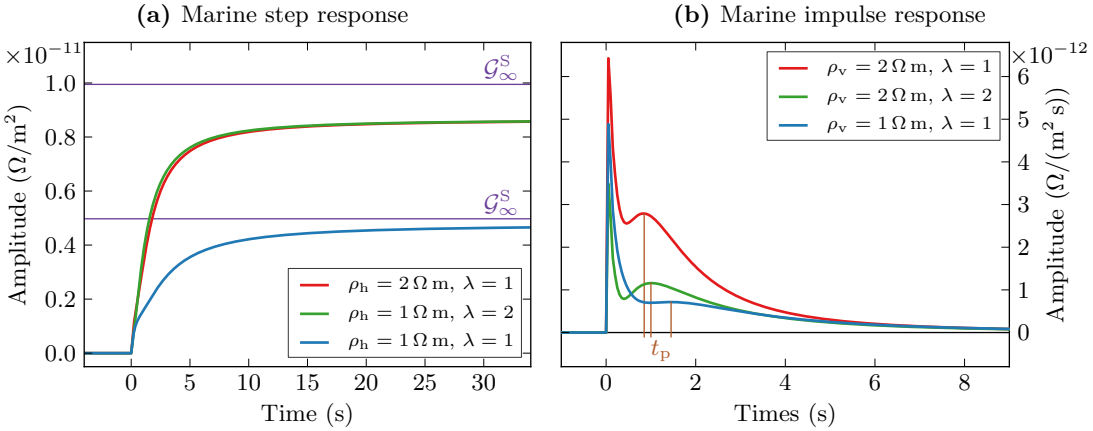


**Figure 6.7:** Marine step (a) and impulse (b) responses for various half-space models with an additional water layer of 110 m of resistivity $\rho_w = 0.3\,\Omega\,m$. Offset is 4 km, and source and receiver are on the seabed.

Apparent mean resistivity and apparent anisotropy do not yield real subsurface properties. But they can be used to estimate them. The two methods mentioned above were derived for land measurements. In the marine environment, the airwave is not a step in the step response and hence not an impulse at time zero in the impulse response. The airwave in a marine impulse response has a peak, usually before the earth response peak, and falls off thereafter, but remains part of the signal, as shown in Figure 6.7. The model of these responses is the same as in Figure 6.6, with the exception that a water layer is introduced of 110 m thickness with water resistivity of $0.3\,\Omega\,m$; offset is 4 km. It also reveals that the DC values are lower than in the land case, due to the damping effect of the water layer on the airwave. This will result in an underestimation of $\rho_a^a$. The arrival times of the peak are still mainly dependent on vertical resistivity, but less than in the land case. These effects are a function of water depth, but the figure is representative for the Harding area.

The airwave method cannot be used in the marine environment, because there is no step. But what are the effects if we apply the peak method to marine measurements? Figure 6.8a shows the apparent anisotropy curves for a half-space of $\rho_m = 20\,\Omega\,m$ and $\lambda = 1$ or 2 (HS in the legend), and including a target of $\rho_m = 500\,\Omega\,m$, 10 m thick at a depth of 500 m with the same anisotropies (TM in the legend). The result shows that the peak method yields the right anisotropy if the model is a half-space indeed, and that apparent anisotropy increases if the model is more complex. This is because a layered medium appears to be anisotropic to DC measurements, even if the layers themselves are isotropic.

Figure 6.8b shows the result for the same model, but with a 110 m thick water layer

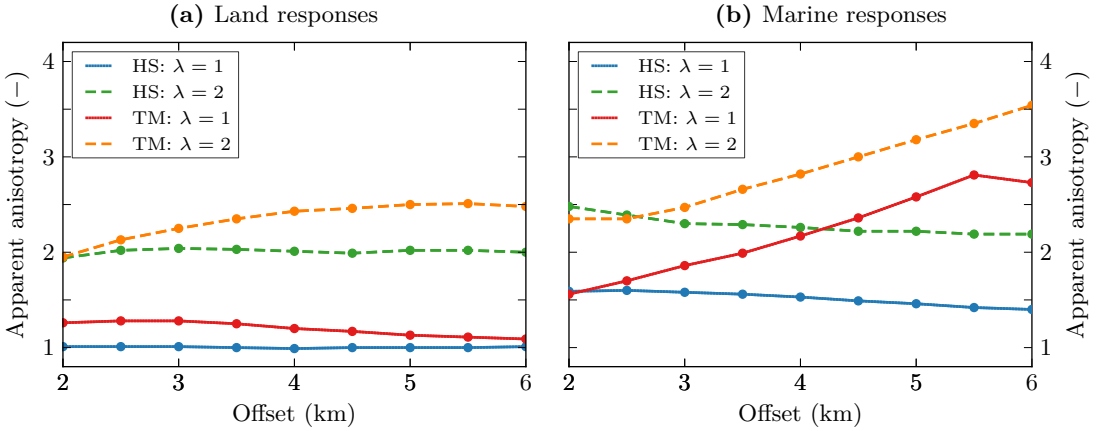


**Figure 6.8:** Synthetic apparent anisotropy determination for (a) land responses and (b) marine responses (models described in text). The result for marine responses generally overestimates the real anisotropy. However, different anisotropies are clearly distinguishable.

($\rho_w = 0.3\,\Omega\,m$), and resistivities of $\rho_m = 1\,\Omega\,m$ for the background, and $\rho_m = 100\,\Omega\,m$ for the target. The resulting apparent anisotropy values are higher than the corresponding anisotropy values in the land responses. One reason is that the airwave overlaps the earth response, shifting the arrival time of the peak to earlier times. This effect decreases with increasing offset, as the earth response arrives later, where the airwave becomes flatter and is therefore shifting the peak less. Another reason is that the water layer attenuates the airwave, which in turn lowers the DC value. However, the different cases are clearly distinguishable, but generally overestimated. We keep this in mind when interpreting apparent anisotropy values of Harding.

## Harding data

Figure 6.9 shows (a) apparent resistivity from the DC values (Equation 6.11), and (b) apparent resistivity from peak arrival times (Equation 6.14) for the Harding responses. Both plots show a fairly consistent distribution, which implies good data quality. The grey dots are values that yield unreasonable results, such as DC resistivities several orders of magnitude too high, due to a steady rise of the amplitudes (bad data). The peak arrival time for offsets greater than 7.5 km are sometimes not very well defined, as the overlap of the airwave with the relatively small earth response do not yield a peak with a unique maximum. This explains the patchy peak arrival times for large offsets. The difference of up to several $\Omega\,m$ in the two plots indicate that anisotropy is present, as $\rho_a^a$ represents $\rho_m$, but $\rho_a^p$ is dominated by the vertical resistivity.

Figure 6.10 shows the apparent anisotropy for the Harding responses, $\lambda_a^p$. Apparent

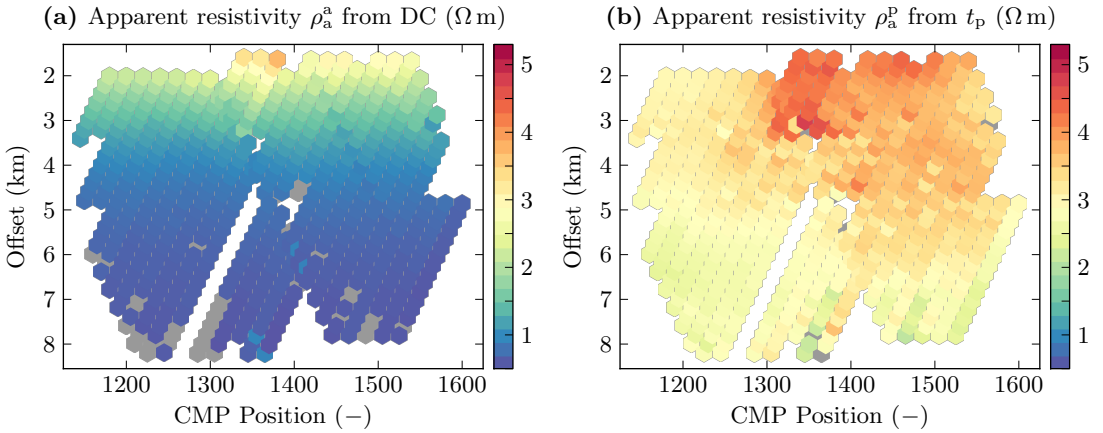


**Figure 6.9:** Apparent resistivities of the Harding area. In (a) the resistivities resulting from the DC values, and in (b) the values resulting from the peak arrival time for the Harding responses. Without anisotropy, these two plots would be the same. Grey dots represent removed values due to poor data quality.

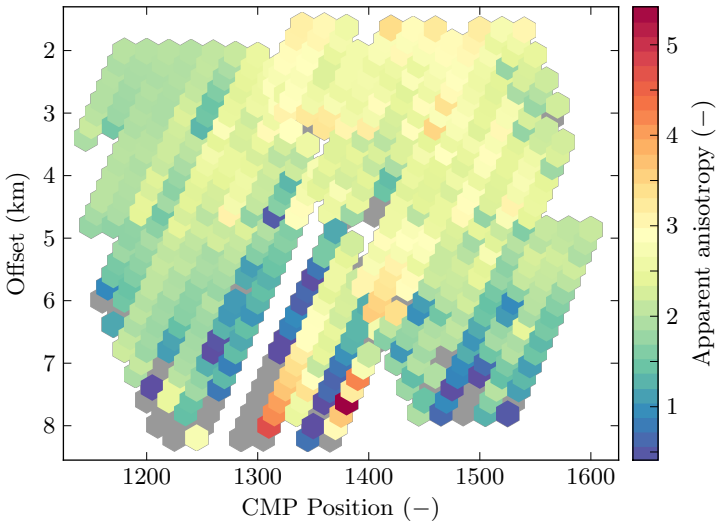


**Figure 6.10:** Apparent anisotropy for the Harding responses. Apparent anisotropy seems to decrease with increasing offset, which might be an effect of applying the peak method to marine data. Apparent anisotropy is up to more than three in the shallow section, which clearly shows that there is anisotropy present.

anisotropy seems to be decreasing with increasing offset, which is probably an effect of applying the peak method to marine data. Most of the apparent anisotropies in the shallower part lie somewhere between 2 and 3. This does indicate that there is anisotropy present in the Harding field, although the anisotropy will not be as high as these values, keeping the conclusions from Figure 6.9 in mind, namely that the methodology, applied to marine data, overestimates anisotropy.

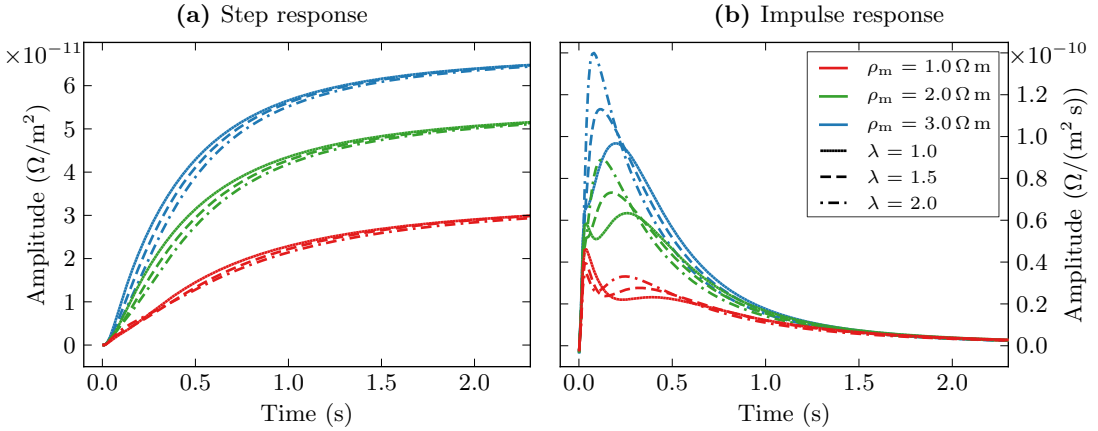


**Figure 6.11:** Influence of anisotropy to (a) step responses and (b) impulse responses, by keeping $\rho_m$ constant. The effect on the amplitudes seems to be bigger on impulse responses.

## 6.4 Anisotropy determination

Arguably the biggest unknown in my approach is anisotropy. Even more so, as my estimated resistivities are horizontal resistivities, so any increase in anisotropy will increase the total resistivity, see Equation 6.3. (The effect is hence stronger than the one shown in Figure 6.3, where $\rho_m$ was kept constant.) Here I try to estimate the overall VTI anisotropy of the subsurface. Note that this is still a bold simplification. It would have been more realistic to have $\rho_h$ and $\rho_v$ for every point in the subsurface, or even better the full tensor. However, a good estimate of a fixed anisotropy value is much better than assuming the (unlikely) case of isotropy, with $\lambda = 1.0$.

Figure 6.11 shows in (a) step responses and in (b) impulse responses for mean resistivities of $1\,\Omega\,m$, $2\,\Omega\,m$, and $3\,\Omega\,m$, each for anisotropies of 1.0, 1.5, and 2.0. Both responses clearly differ for different anisotropies. The late-time values stay the same; they go towards DC amplitude for the step responses, which is constant, as we keep $\rho_m$ constant, and towards zero for impulse responses. Comparing these two figures, it seems that the impulse response discriminates anisotropy better than the step response. That is, the relative amplitude changes are bigger in the impulse response than in the step response for varying values of anisotropy.

Typical 1D inversion results are shown in Figure 6.12 (location is indicated on inset map, compare with Figure 6.14), in (a) an isotropic inversion, and in (b) an inversion with anisotropy of $\lambda = 1.5$. The starting model (black) horizontal resistivities are the resistivities from the background model, and the inversion results of step and impulse responses are given in blue and red, respectively. The water depth is take from the seismic seabed horizon at the CMP location. (See Appendix C.3 for more details regarding

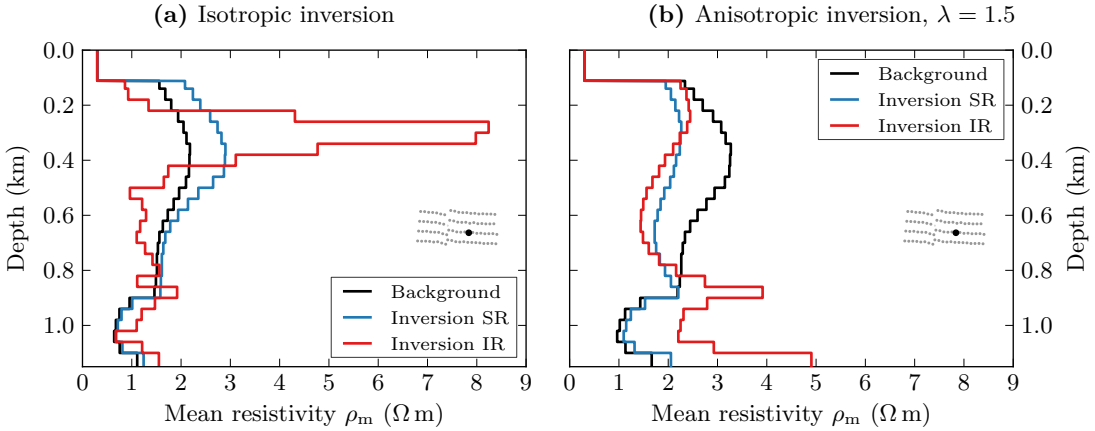


**Figure 6.12:** Typical inversion result of step response (SR) and impulse response (IR) for (a) the isotropic case and (b) with anisotropy $\lambda = 1.5$ . The starting model horizontal resistivity is from the background model. The anisotropic inversion results are much more alike than the isotropic ones. CMP is 1420, offset is 2442 m; corresponding final inversion responses are shown in Figure 6.13.

the inversion and inversion parameters.) The isotropic impulse response inversion result is very characteristic for an isotropic inversion of anisotropic data. It results in low resistivities at the very top, which yield the correct airwave (the airwave is a function of horizontal resistivity only). After this initial low resistivity, it is characterised by a highly resistive region, in order to compensate for the underestimated resistivities at the top. The step response inversion just adjusts resistivities a little, as it can more easily fit an isotropic inversion to anisotropic data. The transverse resistances (mean resistivity times thickness) between seabed and 820 m are in the isotropic inversion 1612 $\Omega\,m^2$ and 1786 $\Omega\,m^2$ for SR and IR, respectively, and in the anisotropic inversion 1415 $\Omega\,m^2$ and 1359 $\Omega\,m^2$ for SR and IR, respectively. Although the transverse resistance of the two results in the isotropic inversion are similar, the resistivities are distributed differently. In the anisotropic inversion, the resulting models look more alike (except for depths greater than roughly 800 m, where the sensitivity is low).

Figure 6.13 shows the corresponding final responses of the inversion results in Figure 6.12. The step response data (black) are compared with the final response of the step response inversion (blue), and with the forward modelled response of the model resulting from the impulse response inversion (red), and vice versa for the impulse response data. The result shows that the unrealistic spiky isotropic impulse response inversion result (low top resistivities, followed by high resistivities) yields a very good fit. The isotropic step response was not able to find a good fit. However, with $\lambda = 1.5$, both inversions yielded a reasonable fit to the data. This leads to the key idea of my anisotropy determination: The resulting models from inversions of step responses and

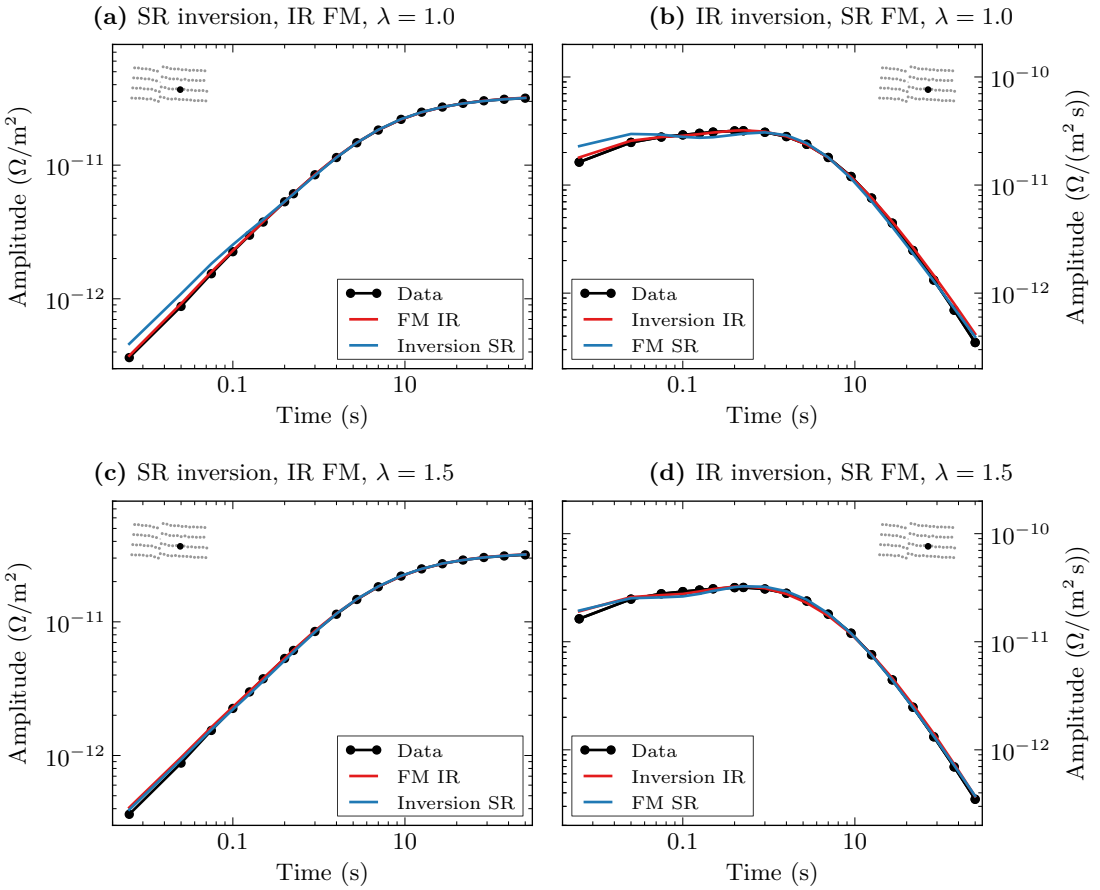


**Figure 6.13:** Isotropic versus anisotropic inversion: (a) & (c) show step response data (black) with the step response inversion result (blue) and the forward model of the impulse response inversion result (red). (b) & (d) show impulse response data (black) with impulse response inversion result (red) and the forward model of the step inversion result (blue). The achieved fit to the data is better in the anisotropic case. CMP is 1420, offset is 2442 m; corresponding final inversion models are shown in Figure 6.12.

impulse responses only agree (in the shallow part) and yield reasonable results if they are inverted with the right anisotropy.

Figure 6.14 shows the chosen offset-band for the anisotropy determination and the shallow resistivity improvements in the next section. The shortest four offsets, that span the whole CMP range, were chosen, so that there is one response for each CMP, 80 responses in total. It is for these short offsets, which are only sensitive to the shallow part, that we can assume a 1D earth. To find the best anisotropy values, 1D inversions were carried out for these selected offsets, for both impulse and step responses, where the starting model is always the background model at the corresponding CMP. For each model, 16 different inversions were carried out, for anisotropies $\lambda = 1.0, 1.1, \ldots, 2.4, 2.5$. The results are shown in Figure 6.15: The normalised root mean square difference

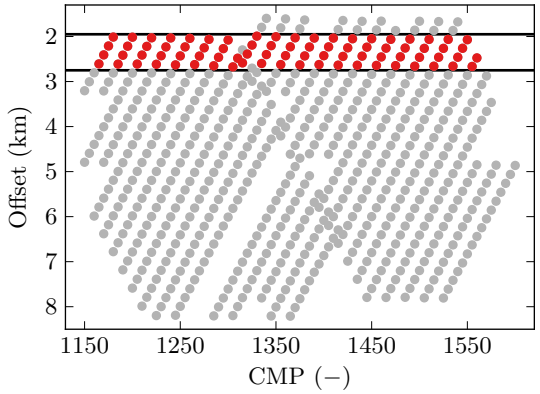


**Figure 6.14:** CMP-offset plot (see Chapter 4) with the chosen offsets for the anisotropy determination and the shallow resistivity improvements in the next section (red dots).

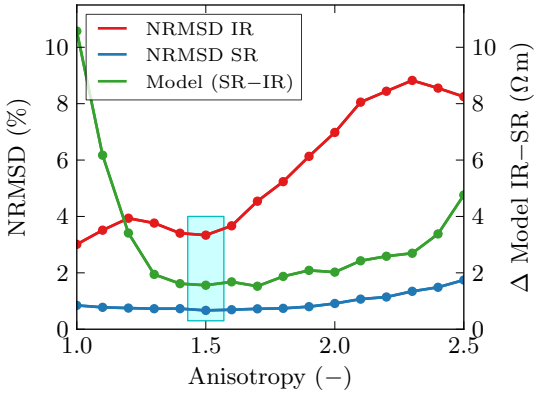


**Figure 6.15:** NRMSD from all impulse response inversions and step response inversions, and the difference of their resulting resistivity models. For $\lambda = 1.5$, both NRMSDs are relatively low, as well as the difference between the two models.

(NRMSD) (see Appendix A) is calculated between data and inversion responses, and the average NRMSD of all 80 responses is plotted as a function of anisotropy, for impulse response inversions in green, and step response inversions in blue. The NRMSD for the step response inversions are low and relatively constant, and only start to increase for anisotropy values higher than 2. The impulse response inversions show higher variability in NRMSD, with low values for anisotropies lower than about 1.7. The difference between the two resulting resistivity models is calculated by taking the mean of the absolute difference between them; the depth range considered is the top 300 m. This is the region that influences the airwave the most, and is hence mostly affected by anisotropy. The difference between the two models is high for low anisotropies, mainly reflecting what we have seen in Figure 6.12a. It rapidly decreases, and starts to increase again for anisotropies higher than about 1.7. From these three curves, it seems reasonable to assume an anisotropy value of $\lambda = 1.5$. To get an idea of NRMSD: the isotropic forward modelled IR from the isotropic SR model, the blue line in Figure 6.13b, has a NRMSD of 10.4. The red line in the same subplot has a NRMSD of 2.3.

Figure 6.16 shows the quality control of the inversions, in (b) for step responses, and in (a) for impulse responses. Generally, the impulse response inversions take a few iterations more, and the NRMSDs are higher, than the step response inversions. But the data looks overall pretty consistent, with a few exceptions.

Isotropic CSEM inversion often yield significantly higher resistivities than the resistivities measured in (horizontal) well logs. Ellis et al. (2009) investigated into this discrepancy, suggesting that anisotropy is the main driver behind this anomaly. They used vertical and deviated well logs from the North Sea Harding area and similar fields

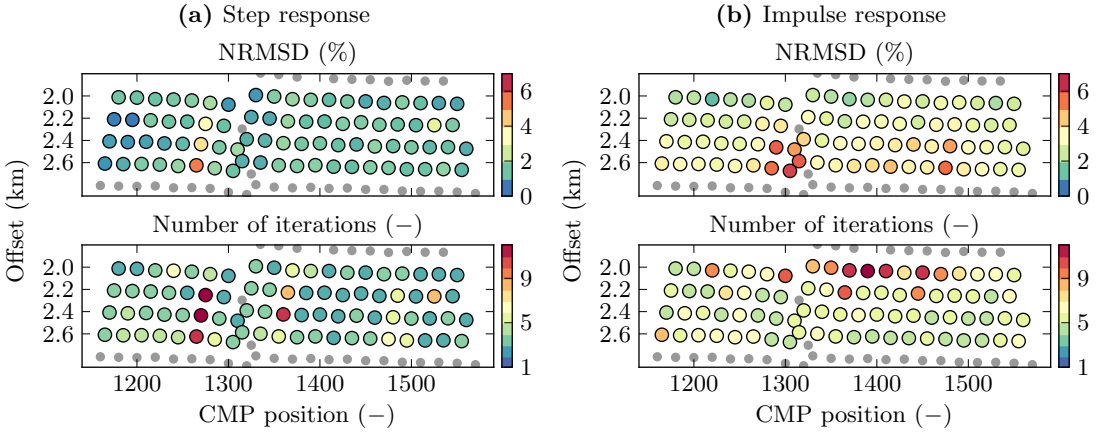


**Figure 6.16:** Quality control of the near-surface inversions, (a) for the step responses, and (b) for the impulse responses. The NRMSDs of impulse response inversions are generally higher than of step response inversions, and impulse response inversions take a few iterations more.

to estimate the anisotropy in the overburden sediments. Where the sandstones were almost isotropic, they found anisotropy values between roughly 1.4 and 1.6 for the shales. (They describe them as ratios $\rho_h : \rho_v$ from 1:1.9 to 1:2.6, which is equivalent with $\lambda \approx 1.4$ to 1.6.) Their findings are hence confirmed by the here presented anisotropy determination with near-surface inversions.

## 6.5 Improvement of the shallow part

The biggest unknown, anisotropy, is now known with $\lambda = 1.5$. The second step is to improve the shallow subsurface resistivities. For this, I use the inversion result for $\lambda = 1.5$ from the previous section.

The near-surface 1D inversion result is shown in Figure 6.17. The starting model from the background model is shown in (a), and (c) and (d) are the step response and impulse response inversion results, respectively; the colour bar applies to all three plots. It can be seen in (a) that there is not much variation in the top 700 m below mudline; the subsurface in this region is nearly 1D. Comparing (d) and (c) shows that the models from the two different inversions are similar. The resistivity values are cut if they go above 7 Ω m. Comparing these areas (dark red) with Figure 6.16, we can see that high resistivities occur where either the NRMSD is high, or the inversion was running for many iterations – when the inversion had problems to fit the data. The averages of the input, and of the impulse and step response inversion results, are shown in (b). I

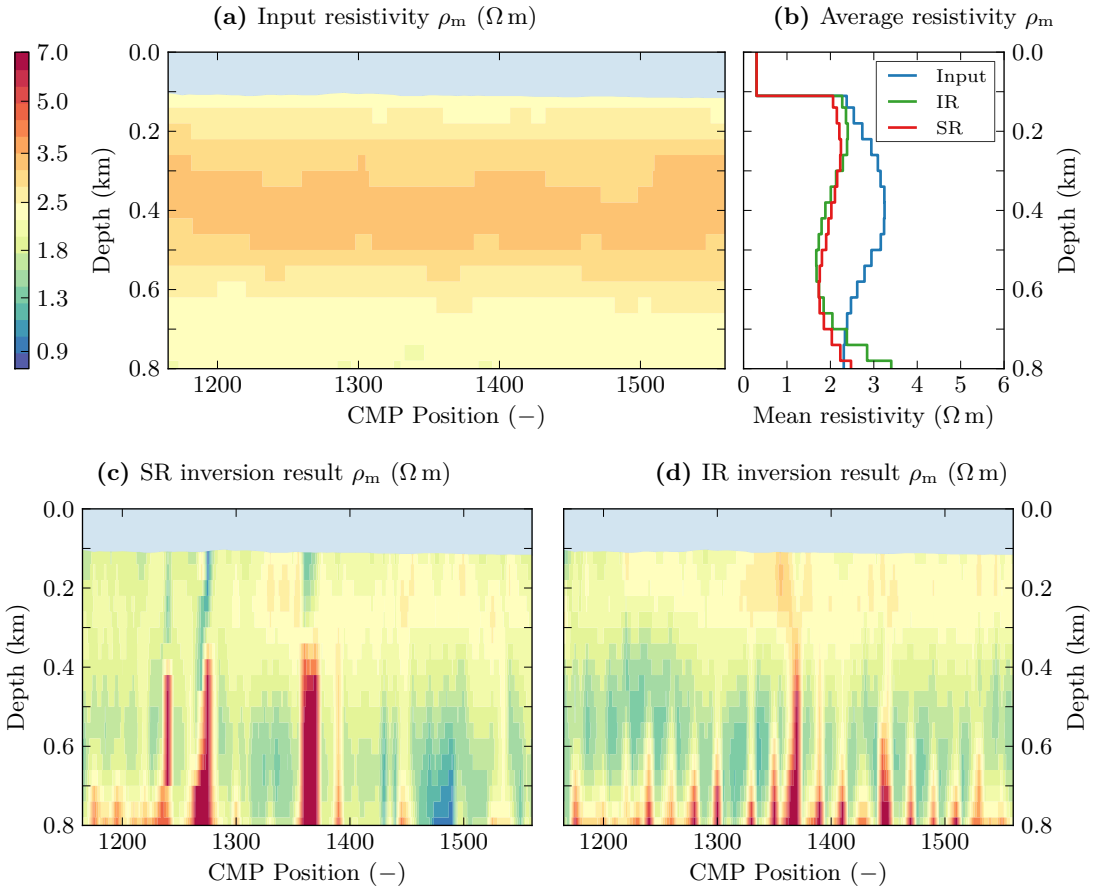


**Figure 6.17:** Near-surface 1D inversion result; (a) is the starting model, and (c) and (d) are the results of the step response and impulse response inversions, respectively. The colour bar applies to all plots. (b) shows the average mean resistivities across the whole profiles.

neglected resistivity values above 7 Ω m for this calculation, corresponding to the dark red areas in (d) and (c), for the reason mentioned above.

I use these average curves to update the background model for the 3D modelling in the next chapter. I combined the SR and IR inversion results for this, weighting the SR from 0 to 1 (top-down) and the IR 1 to 0, giving them weight where they are best. The update was applied to the top 720 m below sea surface. The horizontal resistivities of the updated background model are shown in Figure 6.18, and the differences can be seen by comparing them with Figure 5.11: the resistivities in the shallow part are lower, however, an anisotropy value of $\lambda = 1.5$ applies to the whole background.

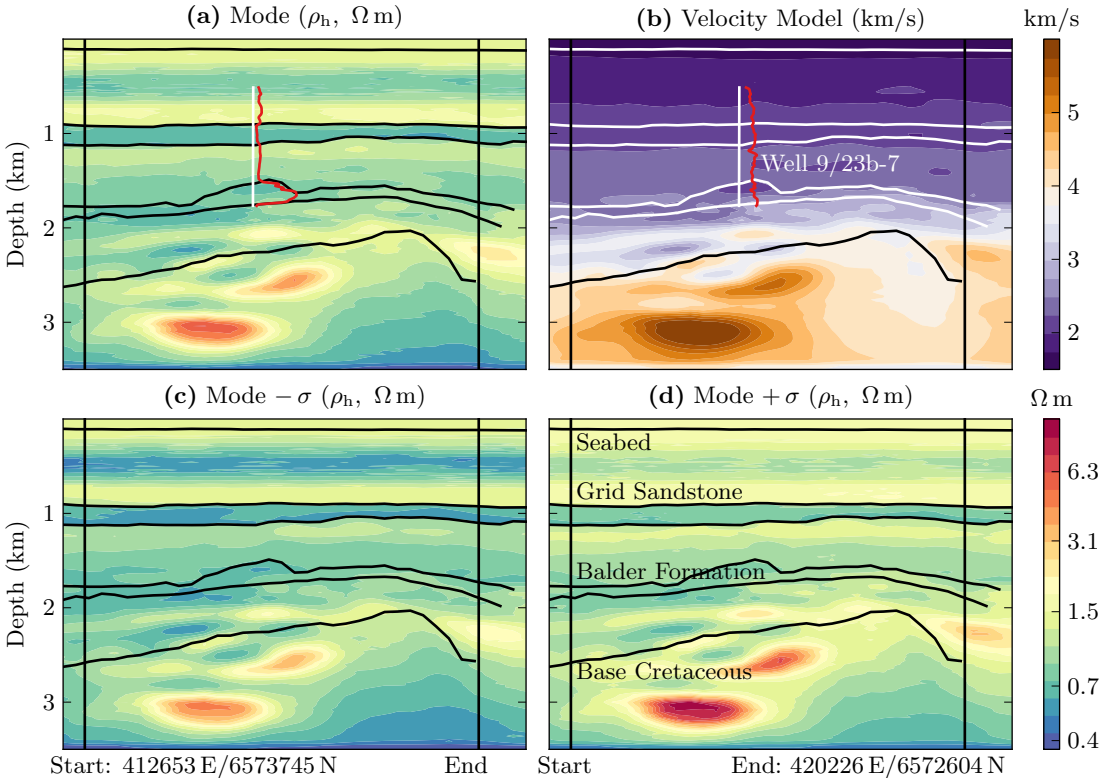


**Figure 6.18:** Updated horizontal resistivity background model from seismic velocities. The comparison to Figure 5.11 shows the lower horizontal resistivities in the shallow part. (a) is the mode of the background resistivity model, derived from the velocity model in (b), and updated as outlined in this chapter; Well 9/23b-7 and some major formations are annotated. (c) and (d) are the mode with minus and plus one standard deviation, respectively.

## 6.6 Deeper part

I estimate the anisotropy and improve the shallow resistivities in the previous two sections, which leaves the remaining unknown: the velocity-to-resistivity transform below well control. The deepest of the wells used for the calibration and verification reaches roughly 2.1 km depth below sea surface. The 1D assumption for this depth is no longer valid, and I cannot use the methodology used before for the shallow part. There is no way to check the validity of the resistivity of the deeper section. However, we can assume that rock properties stay more constant at this depth and pressure, as the rocks are consolidated. The transform might therefore be good for much more than the 2.1 km of well control. This was not the case in the shallow part, with the transition from unconsolidated sea sediments to actual sedimentary rocks.

However, the influence of this deep section is limited with the estimated anisotropy of $\lambda = 1.5$, as shown in Figure 6.19 with an idealised 1D model. The model has a

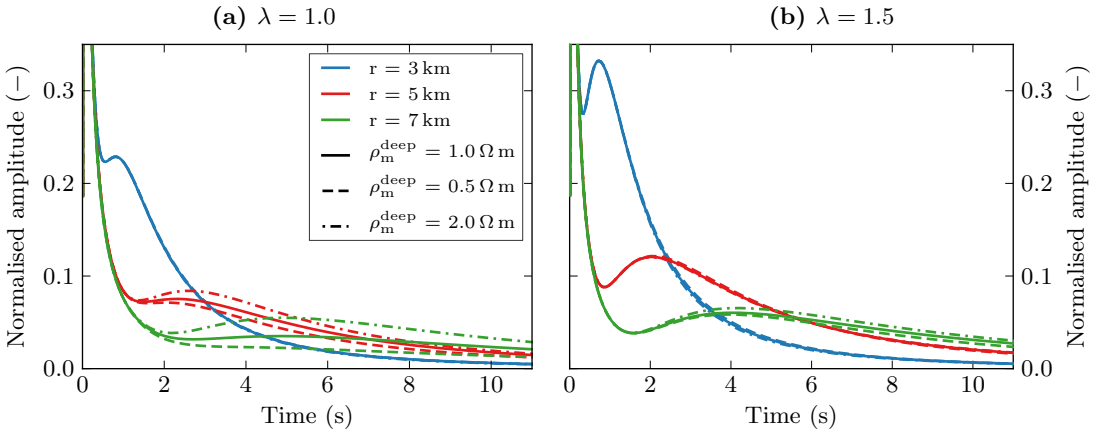


**Figure 6.19:** Sensitivity to deep resistivity, for (a) an isotropic and (b) an anisotropic. The model consists of a water layer of 110 m, and a 2090 m thick overburden with $\rho_m = 1\,\Omega\,m$. The mean resistivities below are given in the legend. The effect is significant in the isotropic case for larger offsets, but not relevant in the anisotropic case.

water depth of 110 m, with resistivity of 0.3 Ω m. Below the water layer is an overburden of 2090 m thickness, with mean resistivity $\rho_m = 1\,\Omega\,m$. The solid line shows the model which, below 2090 m, has the same resistivity as above, whereas the dashed and dash-dotted line are for mean resistivities of $\rho_m^{deep} = 0.5\,\Omega\,m$ and $2\,\Omega\,m$ below 2090 m, respectively. The changes are not ±10 %, as in the sensitivity tests at the beginning of the chapter, but ±50 %. The result for $\lambda = 1$ is shown in (a), and the influence of the deeper part is significant for larger offsets. The anisotropic case is shown in (b), and the effect on the response is minimal.

Although there is no way to improve the background model below well control, its influence on the responses is possibly small.

## Summary

1D modelling and inversion have advantages, such as speed and simplicity, but also severe limitations. The reality is not 1D. I carried out 1D anisotropic step response and impulse response inversions for a range of anisotropies to determine the best value of anisotropy for the shallow part of the section. Then I used this value of anisotropy $\lambda = 1.5$ to run 1D inversions of short-offset responses to improve the existing background resistivity model. I use this updated background resistivity model in the next chapter for 3D forward modelling and comparison to measured responses.

■

# 7

# Three-dimensional modelling

**The first principle is that you must not fool yourself,
and you are the easiest person to fool.**

*Richard Phillips Feynman (1918–1988)*
*Physicist*

I present 3D forward modelling results based on the resistivity model which I derived in the previous chapters, and compare them with acquired controlled-source electromagnetic (CSEM) data over the North Sea Harding field. The acquired responses are in very good agreement with the predicted responses based on the seismic data, and demonstrate that this methodology works. Most of the acquired earth impulse response peak amplitudes and about two-thirds of the peak arrival times are within plus and minus one standard deviation of the peak amplitudes and arrival times predicted from the resistivity background model. Limitations in this study are the vertical extent of the available well logs, the horizontal extent of the seismic velocity cube, and the estimate of electrical anisotropy. I start with a feasibility study for the Harding field, showing that it is at the limit of being a feasible CSEM target. It is therefore not possible to draw any conclusions from the joint interpretation of the predicted and the acquired impulse responses regarding a potential hydrocarbon reservoir. I then show some details regarding the bathymetry and modelling grid, and finally present the modelling results.

I submitted parts of this chapter to the SEG journal *Interpretation* for a special section on *Interpretation and integration of CSEM data* in the August 2014 issue.

## 7.1 Predicting CSEM responses

Seismic exploration is the main geophysical method in the search for hydrocarbons. The petroleum industry has a lot of experience in acquiring, processing, and interpreting seismic data. It also has confidence in the extracted physical properties and layer boundaries. This confidence in the resulting physical properties is due to the fact that it is possible to extract them directly from the data, as explained in Chapter 2; this is a unique advantage within geophysical methods. However, its low sensitivity to differences in pore fluids leaves a gap that can be filled with CSEM data. CSEM data are very sensitive to changes in resistivity, but they lack the resolution of seismic data, and there is no theory that allows resistivity to be extracted directly from CSEM data. Instead, a geophysicist estimates the resistivities and compares the resulting response from forward modelling with acquired impulse responses. This estimated model is then adjusted until it fits the data well enough, a process called inversion.

The equations of seismic wave propagation and electromagnetic propagation share no property of the medium. Rock physics is generally used to link the two data sets, usually via porosity, as I show in Chapter 3, where well logs can be used to calibrate these relations. But this link is not an exact link, and many of the parameters involved have an associated error. For this reason I use a Bayesian framework to estimate a resistivity model from seismic velocities in the form of probability density functions (pdfs), including the uncertainties of the rock-physics model, the rock-physics parameters, and the data. The resulting model, as presented in Chapter 5, yields our best estimate of the resistivities which are in agreement with our seismic data. But this model has two weaknesses which I address in Chapter 6: anisotropy and rock-physics transform outside well control. I use fast 1D inversions of short-offset CSEM data to get an estimate of anisotropy and improve the resistivity model of the top 700 m, where there is no well control. This is by no means ideal, and should be replaced if other data are available, such as velocity and resistivity well logs for the whole well extent, and good quality tri-axial resistivity logs to estimate anisotropy.

In this chapter I use this updated resistivity background model to forward model CSEM responses in 3D and compare them with the acquired data. As the background resistivity model is in the form of pdfs, I can calculate responses for different realisations of the background model. I generally calculate the responses for the mode of the resistivities, and plus and minus one standard deviation thereof. For a few responses I also calculate plus and minus two standard deviations.

Most of the peak amplitudes and about two-thirds of the peak arrival times of the acquired impulse responses lie within plus and minus one standard deviation of the

predicted peak amplitudes and peak arrival times. This is a remarkable result, and shows the power and possibilities of this method not just for CSEM feasibility studies and acquisition planning, but also for quality control (QC) during CSEM acquisition, and interpretation of the acquired data itself. There is an increasing mismatch with increasing offset, which is most likely due to the simplified approach to anisotropy, but also the decreasing signal-to-noise ratio with increasing offset. I use a detailed model for horizontal resistivity, and fix anisotropy at $\lambda = 1.5$. Ideally, one should seek to derive an equally detailed model for vertical resistivity, which in turn would yield a complex model of anisotropy. I suspect that the simplified approach to anisotropy is responsible for the mismatch in arrival time of the peak in some responses, as the arrival time of the peak is dominated by the vertical resistivity. Also, the resistivities in the deeper part, below well-control, might be over-estimated. A regional study with deeper wells could yield some additional calibration. Incorrect water resistivity also affects the peak at near offsets.

First I show results from a simple Harding feasibility study, followed by some notes regarding the bathymetry at Harding. Finally I present the results from the 3D background modelling and its comparison with acquired CSEM data (see Chapter 4 for more details regarding the acquisition).

### Modelling

For the forward modelling I use `PIE3D` from the Consortium for Electromagnetic Modeling and Inversion (licensed to PGS `http://www.cemi.utah.edu`). `PIE3D` is a 3D frequency-domain parallel electromagnetic (EM) forward modeller, based on the method of integral equations (e.g. Hursán and Zhdanov, 2002); see Appendix C for more details regarding the choice of forward modeller, the forward modeller itself, and its performance. The integral equations method embeds complex 3D structures in a 1D background. These complex structures can be used for instance to model a target or complex bathymetry. In my case, I use it to calculate the complex background model gained from seismic velocities including bathymetry.

I use a logarithmic fast Fourier transform (`FFTLog`) to calculate time-domain responses from frequency-domain responses, as described in Appendix A. I use 50 frequencies for the feasibility study, logarithmically distributed from $8.0 \times 10^{-4}$ Hz to $6.4 \times 10^{1}$ Hz with 10 frequencies per decade, and 21 frequencies for the background modelling, logarithmically distributed from $1.6 \times 10^{-3}$ Hz to $1.6 \times 10^{1}$ Hz with 5 frequencies per decade. This corresponds to times 0.025 s to 20 s and 0.1 s to 10 s, respectively, using `FFTLog` as described. The smaller frequency range was chosen to speed up the calculations;

tests have shown that five frequencies per decade are sufficient. Modelled source and receiver lengths are 1 m. (The acquired data are normalised by source length (400 m) and receiver length (200 m).)

## 7.2 Harding feasibility

The North Sea Harding field was chosen for a successful repeatability experiment, whose results are reported by Ziolkowski et al. (2010). A survey acquired data in 2008 which was able to reproduce data acquired in 2007. Harding was thought to be an easily detectable target, as isotropic 1D feasibility studies showed target responses that had amplitudes of two times or more the background amplitudes (PGS internal documents). I briefly reproduce the 1D feasibility study here, and use the Harding reservoir model from BP (January 2009) to carry out a simplified 3D feasibility study, where I use the background resistivities derived from seismic velocities for the background.

Figure 7.1 shows the detailed North Sea Harding Central reservoir model from BP, where the intensity of red represents the relative number of cells, the darker the colour the more cells it has at this particular location. The model is very detailed spatially, but it has actually only five distinct porosity values, three low porosity values (0.7 %, 6.3 %, 7.3 %) at the edges of the reservoir, and two high porosity values (30.0 %, 31.3 %) in the reservoir. It is therefore not as detailed as it looks from the cells. I re-gridded the reservoir into a coarser, regular grid for the forward modelling, and used Archie's second law (Archie, 1942) to calculate the resistivities of the cells,

$$\rho = \psi \rho_{\mathrm{f}} \phi^{-\zeta} S_{\mathrm{w}}^{-n} \ , \tag{7.1}$$

where $\psi$ is the tortuosity factor, $\rho_{\mathrm{f}}$ is brine resistivity, $\phi$ is porosity, $S_{\mathrm{w}}$ is water saturation, and $\zeta$, $n$ are the cementation and saturation exponents, respectively. Water saturation and porosity values are provided in the reservoir model. (I treat gas and oil as one entity, hydrocarbons.) I set the values for $\psi$, $\zeta$, and $n$ to 0.62, 2.15, and 2.0, respectively (following a BP internal petrophysical evaluation from July 2000). Furthermore, I limited the water saturation to $S_{\mathrm{w}} \geq 0.15$, and the total resistivity to $\rho \leq 1200\,\Omega\,\mathrm{m}$ (following Ziolkowski et al. (2010)); $\rho_{\mathrm{f}} = 0.18\,\Omega\,\mathrm{m}$, extracted from the background model derived from seismic data at reservoir level. See Chapter 3 for more details regarding rock-physics models. The resulting resistivities are shown in Figure 7.2: In (a) a plan view of the resistivities calculated for the original grid, and in (b) to (d) the resistivities calculated in the regular grid for the forward modelling. The locations of these slices of the reservoir model are indicated by the dashed lines in Figure 7.1. The visual difference between (a) and (b) comes from the upscaling. The averaging is done in 3D, (b)

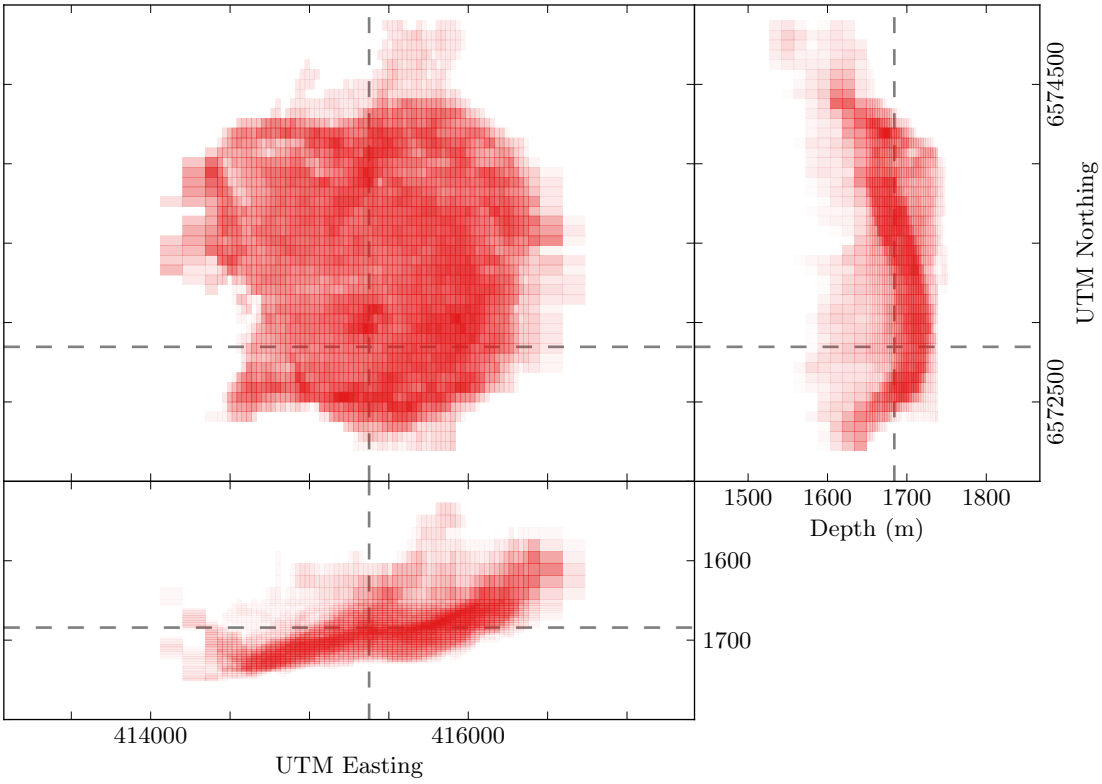


**Figure 7.1:** Harding reservoir model shown in plan view, with an aspect ratio of 1:1, and in Easting versus depth and Northing versus depth with a vertical exaggeration of 5. The intensity of red represents the number of cells: darker means more cells. The reservoir resembles a westward dipping bowl. The dashed lines indicate the locations of the sections in Figure 7.2.

is hence not only a representation of (a), but also of cells above and below it. The very high resistivities in (a) come from the low porosities, which result in high resistivities with Archie (Archie is basically not valid for low porosities). The total number of cells of the re-gridded model is 28 728, but only 4721 (about 16.4 %) represent the reservoir, the other cells are filled with the background resistivity.

For the feasibility I calculated both 1D and 3D models. The 3D modeller embeds the target in a 1D background. The only difference between 1D and 3D models is therefore the target. The background model used in all feasibility models is shown in Figure 7.3, the model discretization on the right, and the resistivity values on the left. Below a 110 m deep water layer of resistivity 0.3 Ω m are 10 layers of 20 m thickness, 10 layers of 40 m thickness, 8 layers of 80 m thickness, one thick layer of 480 m thickness within which the different reservoir models are located, 8 layers of 160 m, and finally a half-space. The horizontal resistivities of these background layers are taken from the average of the horizontal resistivity model derived from seismic velocities, our best estimate of the subsurface, with anisotropy of $\lambda = 1.5$. On the very left in Figure 7.3 is a cross-

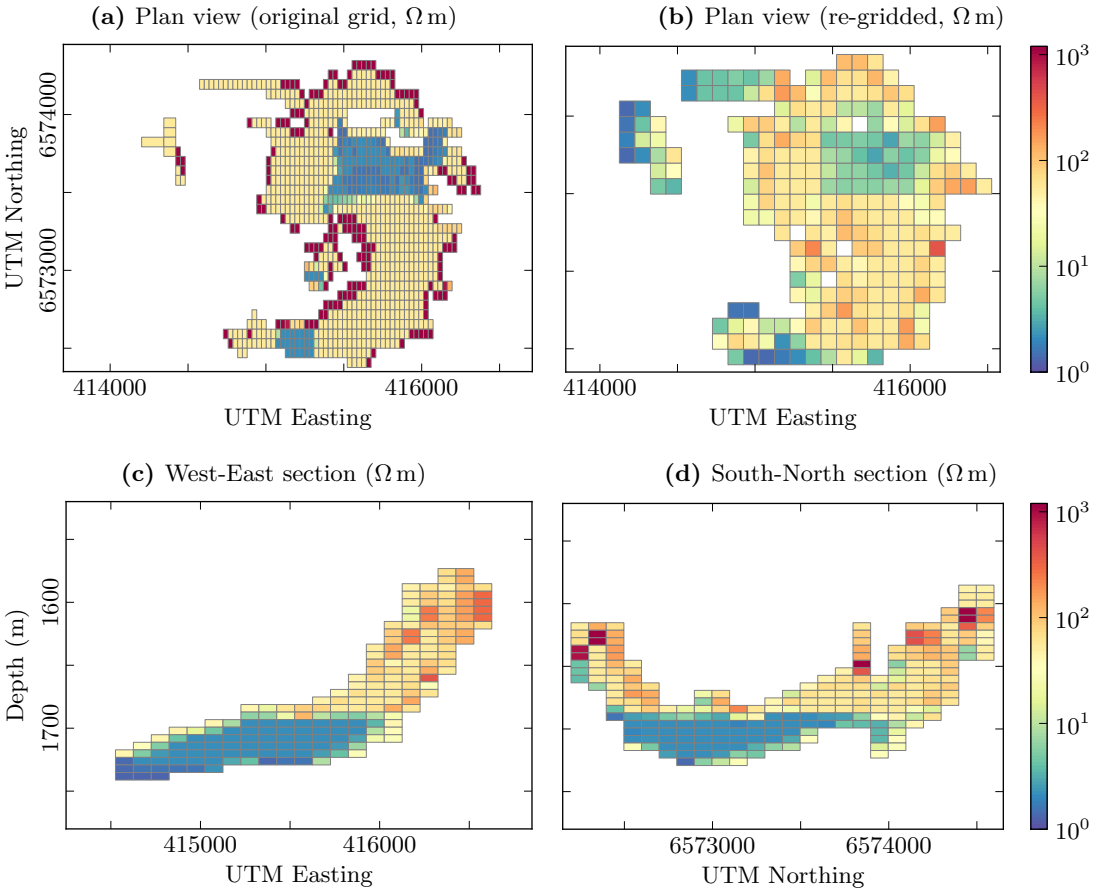


**Figure 7.2:** Harding reservoir model resistivities, original and re-gridded. (a) is a plan view of the original grid, and (b) is a plan view of the re-gridded reservoir. (c) and (d) are Easting and Northing vertical sections of the re-gridded reservoir. The locations of the sections are indicated by the dashed lines in Figure 7.1.

section of the background, overlain with the smoothed resistivity log from Well 9/23b-7. For the modelling I chose five offsets from 4 km to 8 km, all with common midpoint (CMP) location at zero; sources are 5 m and receivers are 2 m above the seabed, and their positions are indicated by the stars and the triangles, respectively. Offsets smaller than 4 km are not much affected by a target at 1.7 km depth, and responses from offsets larger than 8 km have a very small signal-to-noise ratio in real measurements.

I calculated responses for eight different feasibility models, two 1D models and six 3D models, as listed in Table 7.1. The corresponding largest normalised root mean square difference (NRMSD) is also listed, together with the corresponding offset. The 1D model consists of a 124 m thick target layer of resistivity of 1000 Ω m, as indicated by the blue dashed lines in Figure 7.3. This target model is derived from Well 9/23b-7, and closely follows the models used by PGS prior to the Harding acquisition, except

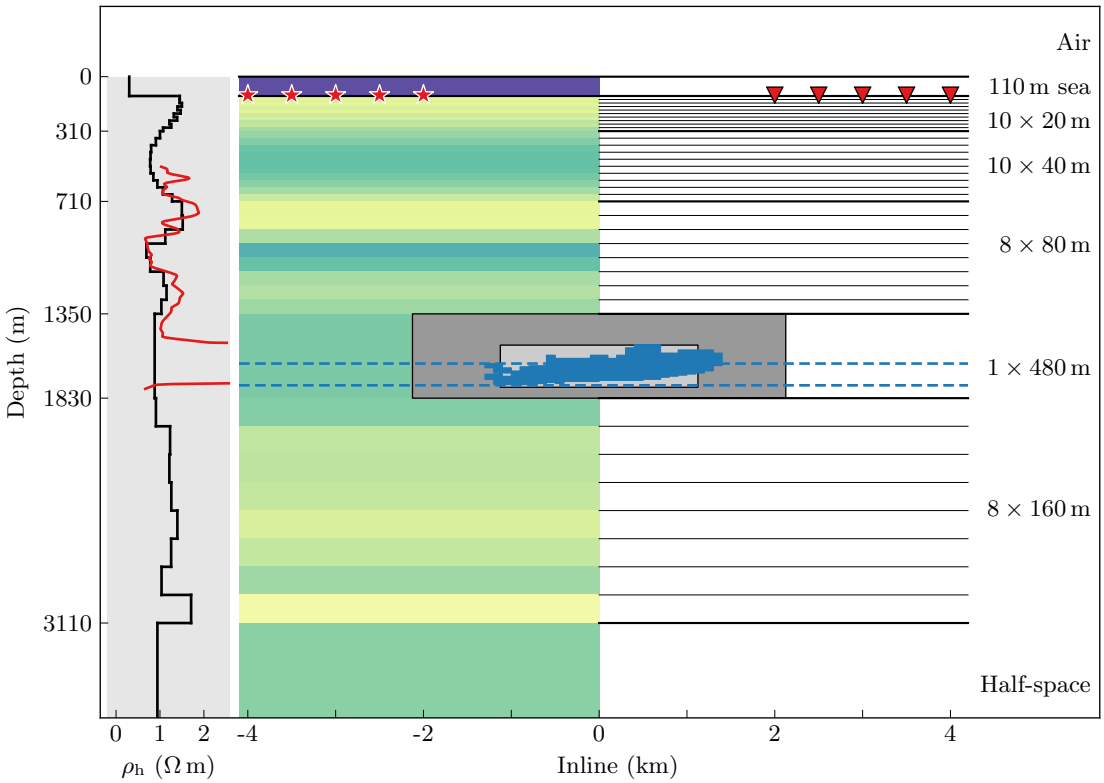


**Figure 7.3:** Harding feasibility model discretization, showing the 1D background layers used in all models, and the various reservoir models used in 1D (dashed blue lines) and 3D (blue reservoir and grey squares). Source and receiver locations are indicated by the red stars and triangles respectively. On the left is a cross-section of the background model, overlain by the smoothed resistivity log of Well 9/23b-7.

**Table 7.1:** Feasibility models with largest NRMSD and corresponding offset. The size of the Harding reservoir at this depth with the given background resistivities and anisotropy is at the edge of detectability.

| Case | Target shape | Resistivity $\rho_h$ Ω m | $\lambda$ – | NRMSD % | Offset km | Figure |
|---|---|---|---|---|---|---|
| 1D | 1D layer | 1000 | 1.0 | 88.3 | 8 | 7.4a |
| | | | 1.5 | 67.9 | 8 | 7.4b |
| 3D | Harding reservoir | $\rho_h$(Archie) | 1.0 | 4.6 | 4 | 7.5a |
| | | | 1.5 | 0.3 | 6 | |
| | | 1200 | 1.0 | 9.3 | 4 | 7.5b |
| | | | 1.5 | 0.7 | 6 | |
| | Small cube | 1200 | 1.5 | 1.6 | 6 | 7.5c |
| | Big cube | 1200 | 1.5 | 17.2 | 6 | 7.5d |

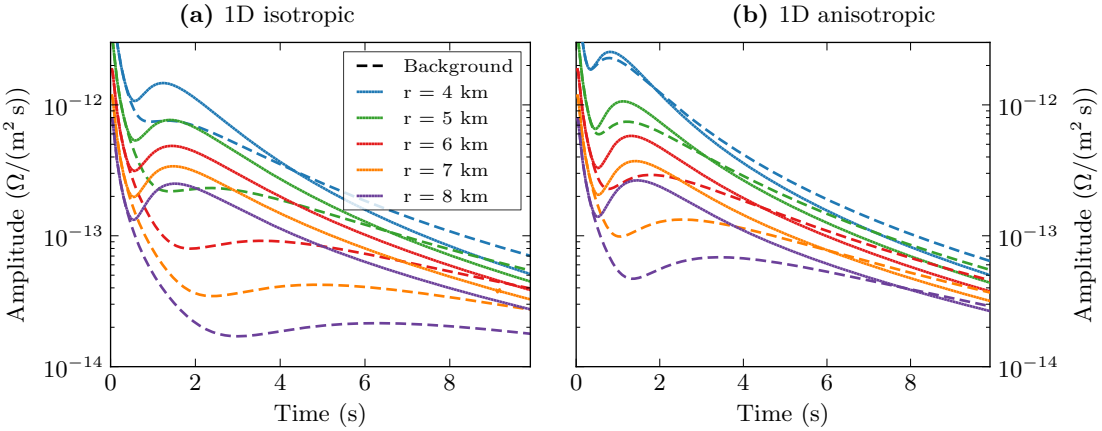


**Figure 7.4:** Harding 1D feasibility results, isotropic (a) and anisotropic (b). The Harding Central reservoir is a feasible target in 1D in both the isotropic and the anisotropic case. However, the anomaly is bigger in the isotropic case (see NRMSDs in Table 7.1).

for the anisotropy. The transverse resistance (124 m times 1000 Ω m) corresponds to the transverse resistance of the well log over the reservoir extent.

Figure 7.4 shows the responses from the 1D modelling, for an isotropic scenario in (a), and for an anisotropic scenario with $\lambda = 1.5$ in (b). All layers, except the water layer but including the target layer, are considered anisotropic in the anisotropic case. These responses show that the Harding reservoir is a very feasible model, both in the isotropic case and in the anisotropic case. However, including anisotropy (with the same horizontal resistivities) results in a smaller anomaly, as the NRMSDs values in Table 7.1 show.

The outline of the 3D Harding model is shown in blue in Figure 7.3. I used the reservoir for four different models, first with the resistivity derived by using Archie's law, isotropic and anisotropic, and second by assuming that each reservoir cell has a resistivity of $\rho_h$ of 1200 Ω m, isotropic and anisotropic. The reservoir model is from 2009, so after more than 10 years of oil production. The second case, however, fills every reservoir cell with hydrocarbon, and it can therefore be regarded as an upper limit. I calculated two additional models, a small and a big cube. The small cube has roughly the dimensions of the reservoir model outline, and the big cube is twice the dimension of the small cube in each direction. They are indicated in Figure 7.3 by the light grey and the dark grey squares, respectively. All reservoirs are centred at zero in both inline and crossline directions. The model sizes of these different reservoir models are listed in Table 7.2.

The feasibility results in 3D draw a very different picture from the results in 1D. Figure 7.5 shows the results from the 3D feasibility study. The responses from the

**Table 7.2:** Grid dimensions for the three different reservoir cases. The numbers represent the midpoint of the cells in the format start:end:step (# cells). In the detailed reservoir case, only 4721 cells have resistivities different from the background resistivity.

| | Reservoir (28 728) | Small cube (972) | Big cube (6936) |
|---|---|---|---|
| x | -1350:1350:100 (28) | -1000:1000:250 (9) | -2000:2000:250 (17) |
| y | -1300:1300:100 (27) | -1000:1000:250 (9) | -2000:2000:250 (17) |
| z | 1531:1753:6 (38) | 1538:1758:20 (12) | 1360:1820:20 (24) |

Harding reservoir are shown in (a) for the isotropic case, and in (b) for the anisotropic case. The red responses [$\rho$(Archie)] are the responses that result from the reservoir model as gained with the Archie equation. The blue responses (1200 Ω m) are the results from the reservoir model in which each reservoir cell is given the resistivity of 1200 Ω m. If the model is isotropic, it results in target responses which can clearly be distinguished from the background model. But if we take anisotropy into account, with the estimated anisotropy of $\lambda = 1.5$, the target responses can hardly be separated from the background responses.

The responses for the small cube model are shown in (c), and the responses for the big cube model (d). The small cube model does not differ significantly from the background. The big cube model, however, can be clearly differentiated from the background. Table 7.1 lists the highest NRMSDs for all models within the calculated offsets. The 1D isotropic model has a very high NRMSD of 88.3 %. The Archie model [$\rho$(Archie)] and 1200 model (1200 Ω m) show reasonable NRMSD in the isotropic case, but below 1 % in the anisotropic case.

A note regarding re-gridding and the calculation of resistivities: the correct way to upscale is a topic for discussion, especially when dealing with resistivities. But re-gridding it differently, or not limiting the resistivities to 1200 Ω m, would not significantly change the clear result in Figure 7.5, as the 1200 Ω m model shows that the target is hardly detectable even if we fill every cell with very high resistivity.

## 7.3 Bathymetry and source and receiver location

The bathymetry at Harding is relatively flat, so that we do not expect too much of an influence on the CSEM data. But we can include bathymetry in 3D modelling using the seabed horizon from seismic data. Figure 7.6 shows the resulting seabed model, where the cell size is 250 m by 500 m, and the water depth of the cells is the average of all the points of the seismic seabed horizon that fall within this square. The horizon is rotated and shifted, so that the CSEM survey line is at crossline y = 0, and all source and

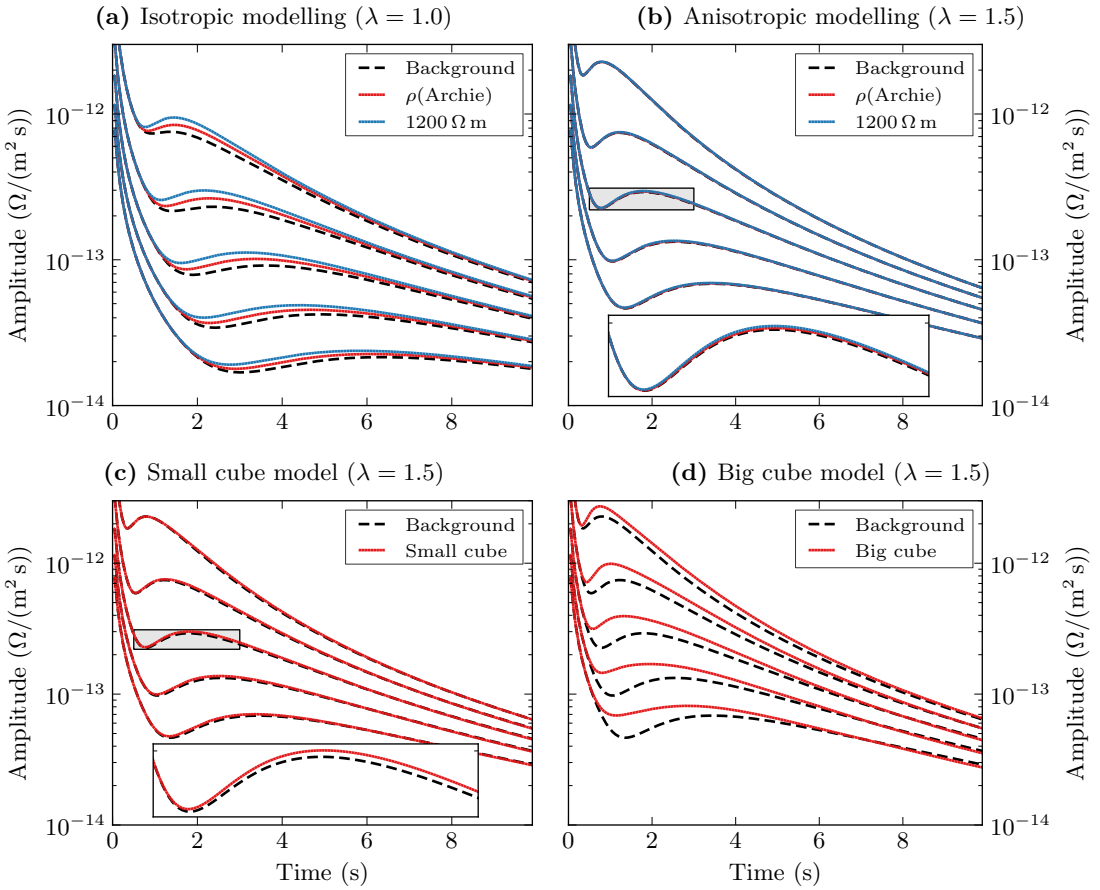


**Figure 7.5:** Harding 3D feasibility responses. The Harding reservoir is clearly distinguishable from the background in the isotropic case (a). But responses from the target are hardly different from the background responses if anisotropy is taken into account, (b). Not even the small cube in (c) produces a significant difference. However, the big cube (d) has reasonable NRMSD values (see Table 7.1) even with the expected anisotropy and the complex background model.

receiver positions are at positive inline locations. The inline extent of the bathymetry is limited by the seismic velocity cube. The crossline extent is set to plus and minus 3250 m. The minimum water depth within this area is 101 m and the maximum water depth is 118 m. Hence there is less than 20 m difference in a distance of more than 12 km (inline). The plots on the x-z-axis and y-z-axis show different sections through the original seismic seabed horizon, and the plot on the x-y-axis is a contour plot of the original seismic seabed horizon.

Figure 7.7 shows a plan view and an inline vertical section along the acquisition line, together with the source and receiver locations. The grey grid is the actual bathymetry modelling grid, the water depth outside the available modelling is set to 110 m. The source and receiver depths are taken from the acquisition data. However, the dashed

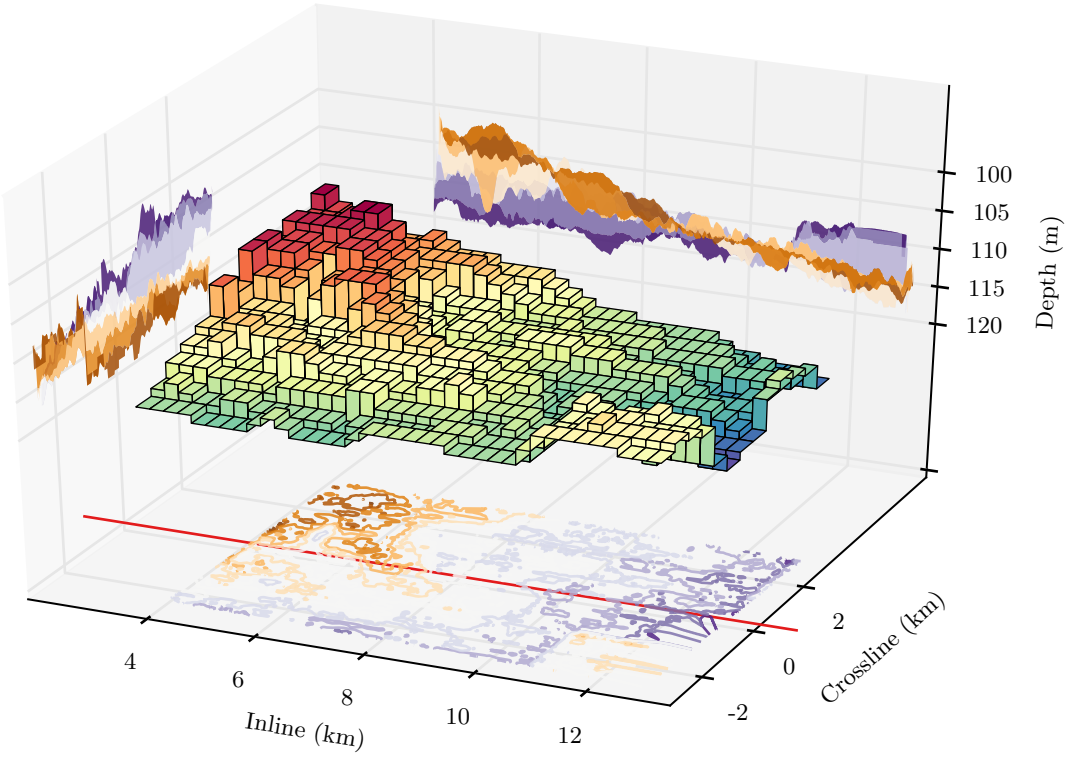


**Figure 7.6:** Bathymetry of Harding, gridded for 3D forward modelling. The contour plots on the axes are from the original seabed horizon, the used bathymetry depths are averages for cells of the size 250 m by 500 m. Note that the vertical exaggeration is more than 100. The coordinates are rotated as used for modelling, with the survey line along the x-axis (y = 0, indicated by the red line).

line marks the line two metres above the seabed. This line is set as the maximum depth for any source and receiver in the modelling. Note that in the plan view the exaggeration is more than 80; the source and receivers all lie within one grid row.

There is a problem with the source depth in the acquisition data. The second electrode has depths that are randomly up to 50 m higher or lower than the first electrode, which is not feasible given the bathymetry and the acquisition layout. I therefore used only the information from the first source electrode. Furthermore, a few sources had to be shifted by up to 10 metres in the inline direction, because they were located too close to a grid cell boundary, and one receiver was lifted an additional 0.8 metres, because it was directly on the 110 metre seabed. These adjustments were made because of limitations of the forward modelling code.

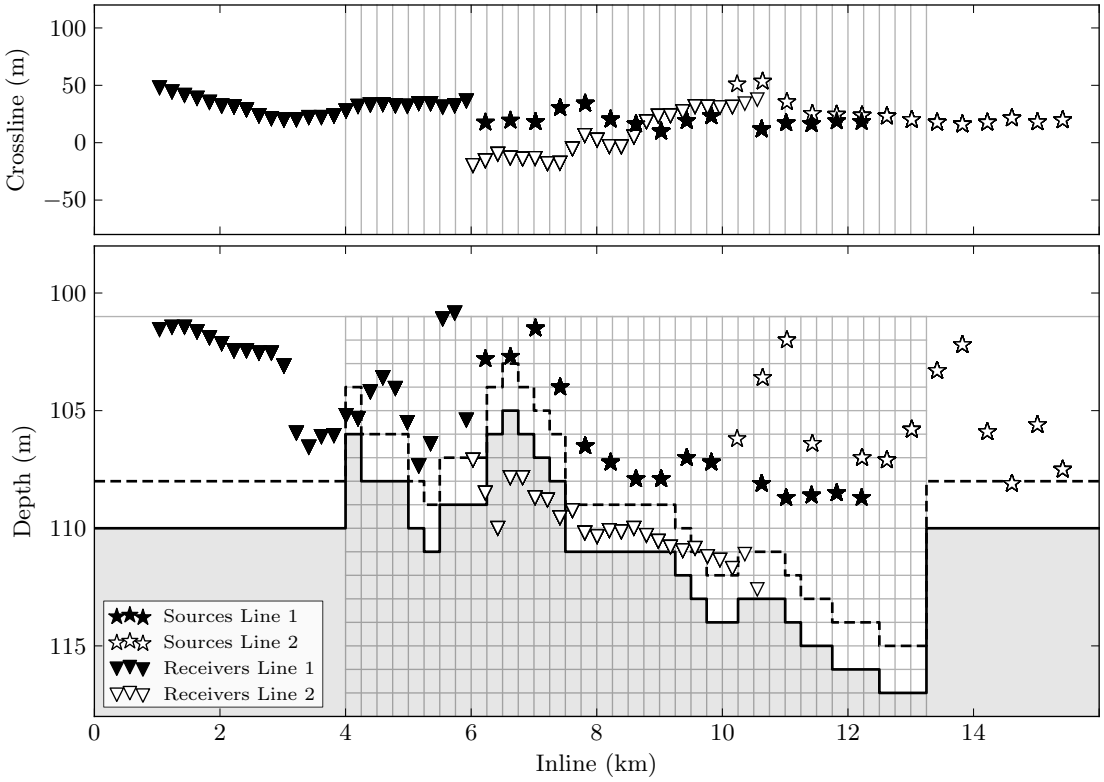


**Figure 7.7:** Source and receiver locations in plan view and as an inline-vertical section. The grey area is the subsurface, and the dashed line 2 m above the seabed marks the maximum modelling depth for any source and receiver. The detailed model does not cover the whole acquisition extent. Note the exaggerations in crossline and depth.

## 7.4 Modelling the Harding background resistivity

The seismic velocity cube, which I used to derive the background resistivity model, has a resolution of 250 m by 250 m horizontally, and 20 m vertically. This is the base of the 3D grid discretization. Figure 7.8 shows the Harding background discretization: in (a) is a plan view (aspect ratio is 1:1), where the black horizontal line marks the location of the survey line; (b) shows the background model, where the grey square indicates the location of the detailed grid; (c) and (d) are the x-z-discretization of the detailed grids, the grey horizontal lines indicate background layers. (The latter three plots are heavily vertically exaggerated.) The background model is the same as in the feasibility study, except that the thick reservoir in the feasibility study layer is split into two layers of 80 m thickness and two layers of 160 m thickness. The horizontal grid extent is the same as in the bathymetry, where inline cell size is 250 m and crossline cell size is 500 m. The grid cell thicknesses increase rapidly from 1 m to the maximum thickness of 20 m. Starting at 110 m, it consists of one layer each of 1 m, 2 m, 3 m, and 4 m, two layers each of 5 m and 10 m, followed by 168 layers of 20 m thicknesses. The top six layers change in the case

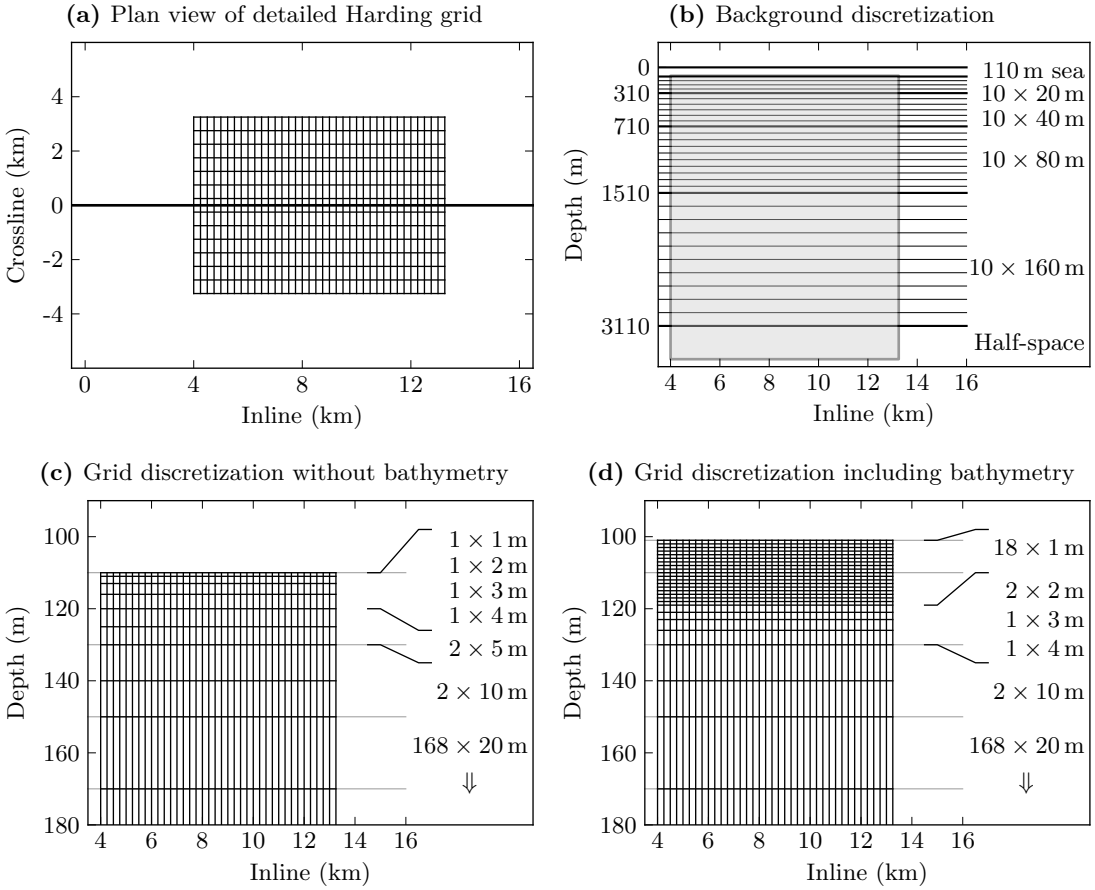


**Figure 7.8:** Harding background and grid discretization. The black line in the plan view (a) indicates the survey line. The 1D background is shown in (b), where the extent of the grid is given by the grey box. Inline vertical sections of the grid at y = 0 are shown in (c) and (d) for the grid without and with bathymetry, respectively.

where bathymetry is included, and the grid starts at depth 101 m, with 18 layers of 1 m (bathymetry model), two layers of 2 m, and one layer each of 3 m and 4 m thicknesses. (Background layer boundaries cannot cross grid boundaries.) The background layer resistivities are the average of the corresponding background resistivity model cells. The grid cells are the actual background resistivities. The resistivities of the complete model are shown in Figure 7.9, which includes bathymetry. However, the bathymetry is hardly visible, because the area is very flat.

Figure 7.10a shows the responses for an offset of 4079 m at CMP location 1330 (see Figure 7.11a). The original case (blue line) is calculated using the original resistivity model, the result of Chapter 5, with anisotropy of $\lambda = 1$. The updated model (red line) is calculated using the updated resistivity model, the result of Chapter 6, with anisotropy of $\lambda = 1.5$. Both cases are calculated without bathymetry. It shows nicely

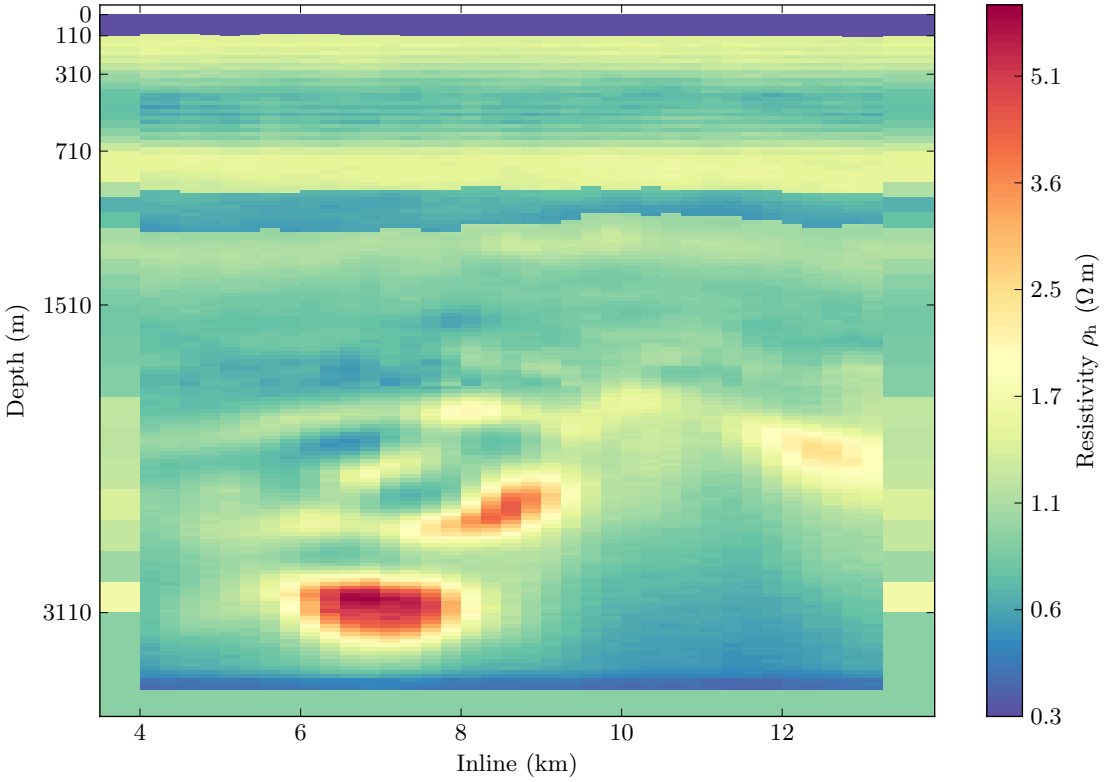


**Figure 7.9:** Harding background and grid resistivities for the 3D model including bathymetry; discretization details are given in Figure 7.8. The bathymetry is hardly visible, as the difference is less then 20 m.

that the isotropic model, based on well log resistivities which measure mainly horizontal resistivity, grossly underestimates the earth response, as the mean resistivities are much smaller than if anisotropy is taken into account. The airwave, however, seems to be better represented by the isotropic case in this example. The background case (green) uses the updated resistivity model, but uses only the averaged 1D background instead of the detailed grid. This shows the difference of 1D (red) to 3D (green) modelling. Figure 7.10b compares the responses when calculated with and without bathymetry in blue and red, respectively. The responses are very similar, but the bathymetry seems to have a significant effect on the airwave.

The resistivity models presented in Chapters 5 and 6 are based on a vertical section of the velocity cube along the CSEM survey line. It is for this section that I calculated the resistivities as pdfs. The original and updated responses with and without bathymetry in Figure 7.10 are calculated using the mode of these pdfs. For this, the detailed grid in Figure 7.8 repeats the resistivity values in the y-direction. So the detailed grid is in fact a 2D grid in a 1D background, yet still with a 3D bathymetry (and a 3D source). The full 3D case in Figure 7.10b shows the response for the resistivity model from the whole

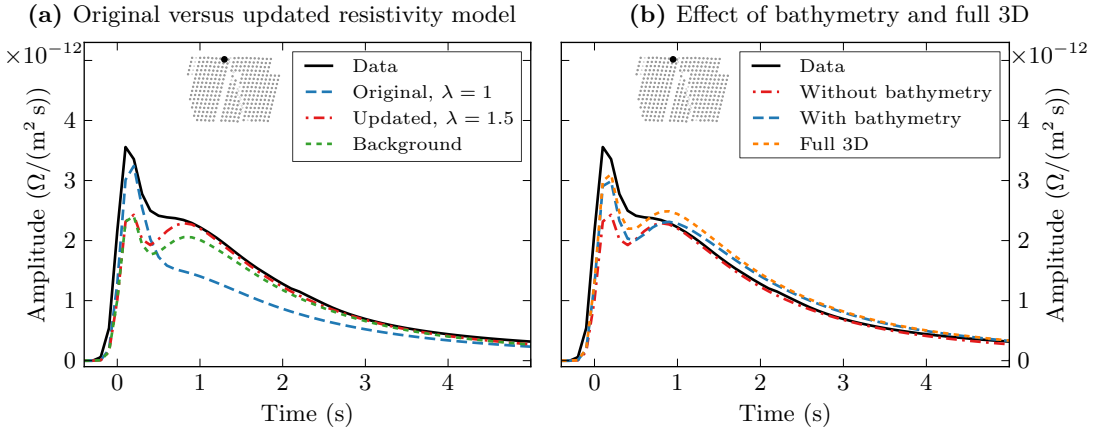


**Figure 7.10:** Comparison of different resistivity models and model discretizations. (a) shows the original model (blue), the updated model (red), and the response if only the averaged 1D background from the updated model is considered (green). (b) shows the updated model with (blue) and without (red) bathymetry, and the full 3D model (orange). For the rest of the chapter, the updated model with bathymetry is considered.

velocity cube, instead of a vertical section along the CSEM line. In this case, however, I calculated the deterministic value without the uncertainty analysis. The responses do differ, but the effect is not significant. This is not very surprising, considering the cell size in y-direction (500 m) and the flat depositional layers at Harding, which makes Harding close to a 2D model (even the Crawford ridge at Harding runs in a crossline direction, see Chapter 4). However, resistivity calculation of a full 3D model is important if the subsurface is more complex.

A remark regarding the different 3D models: The seismic velocity cube and the CSEM survey have an angle of $\approx 0.033$ rad. For the full 3D model, I rotated the resistivity model based on the seismic velocity cube geometry with the angle of the CSEM line. This results in a small error when moving away from the zero crossline. This error is negligible due to the small angle: the cells of the resistivity model never cross the cells of the modelling grid.

Figure 7.11a shows the coverage of the Harding acquisition and the responses considered. As 3D forward modelling is time-intensive, I focused on the offset range of interest from 4 km to 7 km. From about 4 km onwards we expect the responses to be sensitive to the reservoir, and at offsets larger than 7 km the quality of the data becomes poor due to the noise level. See Chapter 4 for more information regarding the Harding CSEM acquisition. The plot also shows the relation between CMP position and model grid inline coordinates. For every response I calculated the mode and plus and minus one standard deviation of the resistivity model, and also for plus and minus two standard deviations for a few responses. I removed a few responses in QC; either because

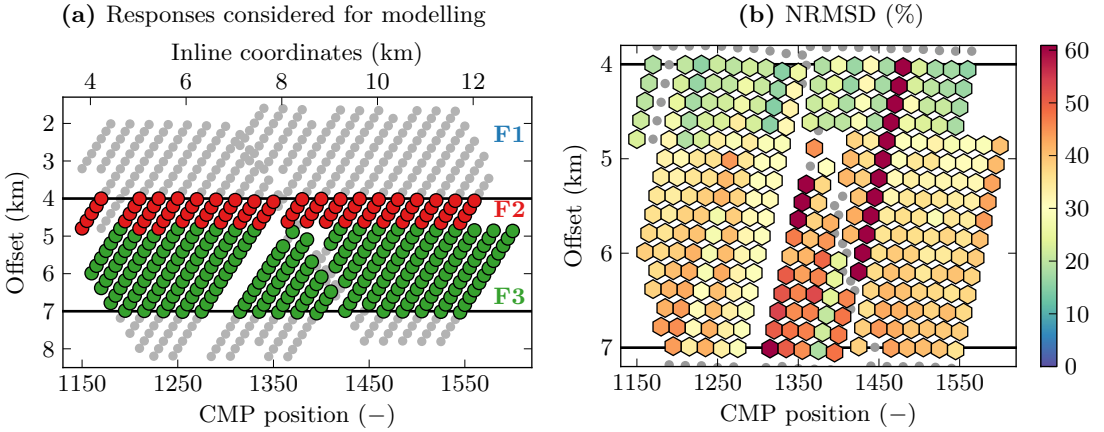


**Figure 7.11:** (a) offset range and source lines considered for 3D modelling. The two x-axis labels show the link between CMP position and modelling coordinates. (b) NRMSD between the acquired data and the responses calculated with the mode of the resistivity model.

the data quality is poor, or because the forward modelling was unstable. Figure 7.11b shows the NRMSD between the data and the responses calculated using the mode of the resistivity model. Remember that the resistivity model is in the form of pdfs. This means that the modelled responses are not thought to be the only true responses, they simply represent the most likely responses. The NRMSD therefore does not represent an error between data and model. But its distribution gives some insight into the model: The data seem to be generally closer to the modelled responses for short offsets (and frequency band F2) than for larger offset. The responses marked with an intense dark red have predicted amplitudes which are considerably higher than the acquired data. I suspect some issues with the forward modelling (perhaps source positioning).

Two more general quality checks of the modelling results are shown in Figure 7.12. Figure 7.12a is an earth response quality check. In this test I compare the peak of the earth impulse response of the acquired data with the peaks of the modelled data. The peak is a distinct feature in multi-transient electromagnetic (MTEM) impulse responses, and it contains the highest energy from the subsurface. Black hexagons indicate that the measured data has a higher peak amplitude than the response resulting from the plus one standard deviation model. Red hexagons indicate peaks that lie between the responses from the mode and the plus one standard deviation, blue hexagons indicate peaks that are between the responses from the mode and minus one standard deviation, finally white hexagons indicate if the peak amplitude is lower then the peak from the response resulting from the minus one standard deviation resistivity model. As can be seen in (a), most responses have a peak that falls between minus one standard deviation and plus one standard deviation. But there are some responses where the predicted amplitudes are higher than the acquired data. Interestingly, they are mostly

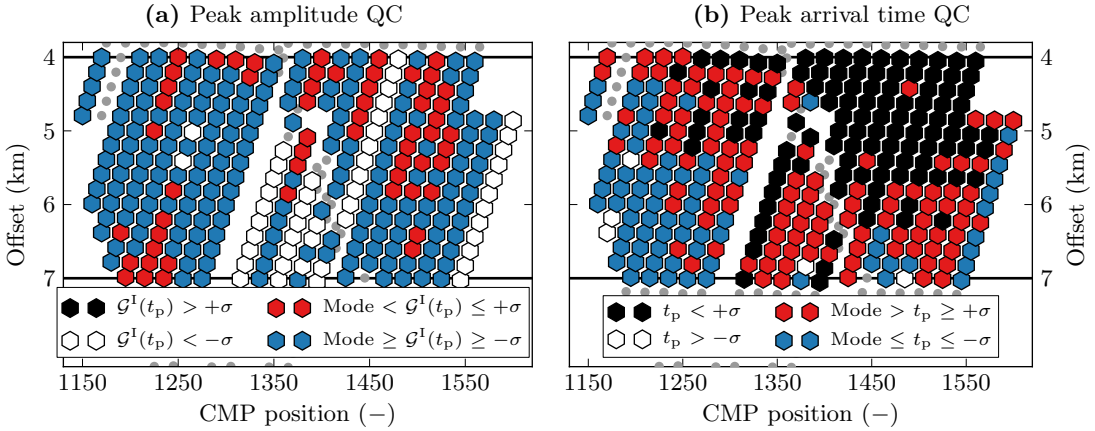


**Figure 7.12:** The peak amplitude quality check in (a) reveals that the peak of the earth response falls within one standard deviation in most case. However, some shot gathers have higher predicted amplitudes than one standard deviation. The peak arrival time quality check in (b) shows that roughly two-thirds of the arrival times fall within plus and minus one standard deviation.

for whole source gathers. Figure 7.12b shows a similar QC, but for the arrival time of the peak. Roughly two-thirds of the responses fall within plus and minus one standard deviation. However, peaks of responses from short offsets and higher CMPs seem to arrive earlier than predicted. In Chapter 6 I show that the arrival time of the peak is dominated by the vertical resistivity. This result shows that the simplified approach of having one single anisotropy value for the whole subsurface is not ideal.

Figure 7.13 shows example modelling results with the corresponding acquired data for offsets of (a) 4 km, (b) 5 km, (c) 6 km, and (d) 7 km for a source line with relatively low NRMSD in Figure 7.11b (roughly between 10 % and 35 %). In green is the response for the mode of the resistivity model, in orange and blue the responses for plus and minus one standard deviation, respectively, and in red and purple the responses for plus and minus two standard deviations. These results show three main points. First, the acquired data are generally well predicted by the modelling: the amplitudes fall very often not only between plus and minus two standard deviation, but even between plus and minus one standard deviation. Second, the airwave is underestimated, and increasingly so with increasing offset. Third, the amplitudes at later times are often overestimated.

Figure 7.14 shows the corresponding responses for a source line with a relatively large NRMSD in Figure 7.11b (roughly between 10 % and 55 %). It shows that the larger NRMSD comes from larger underestimation of the airwave, and from larger overestimation of the later part. However, this overestimation of the later part can partly be attributed to the data quality. This becomes clearer in the following two figures.

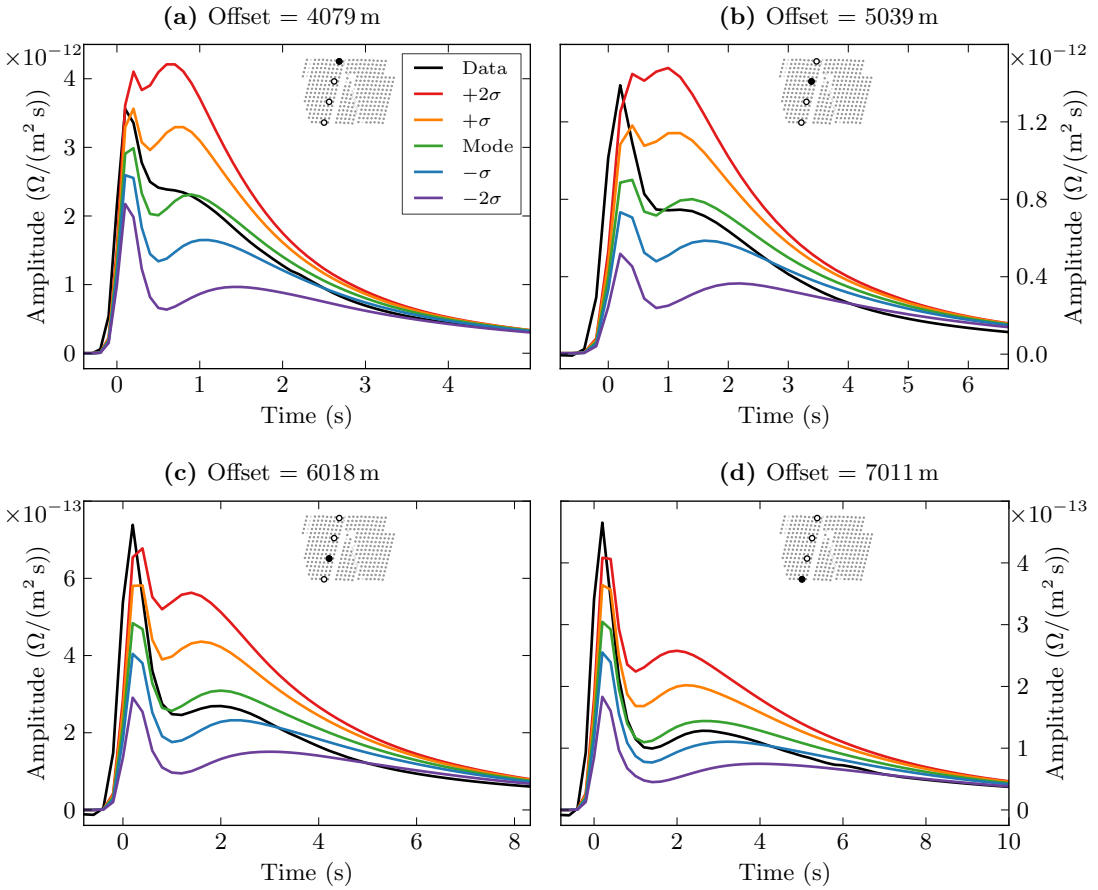


**Figure 7.13:** Results for a source gather with relatively small NRMSD. The earth responses lie well within the plus and minus one standard deviation models. However, the airwave is increasingly underestimated with increasing offset. The wide spread of the responses for plus and minus two standard deviations indicates that I could possibly be more conservative with the error estimates in my uncertainty analysis.

Figure 7.15 shows five responses overlapped at an offset of (a) 4.2 km, and of (b) 6.8 km; in green the responses from the mode, and in orange and blue the responses from plus and minus one standard deviation, respectively. The figure shows clearly how well the calculated responses predict the acquired data; with the exeption of the airwave and later times. The times where the main energy from the subsurface is recorded, the peak of the earth impulse response, are accurately predicted. Figure 7.15b also shows that some of the data have poor quality. The magnetotelluric (MT) noise removal that was applied to the data was able to eliminate a big part of the noise. However, it can only remove noise that is very well correlated. The amplitude drop-off of some responses is likely to be due to poor data quality. So the predicted responses might actually be more accurate than the recorded data.

Figure 7.16 shows six responses from one source gather, where the range from minus

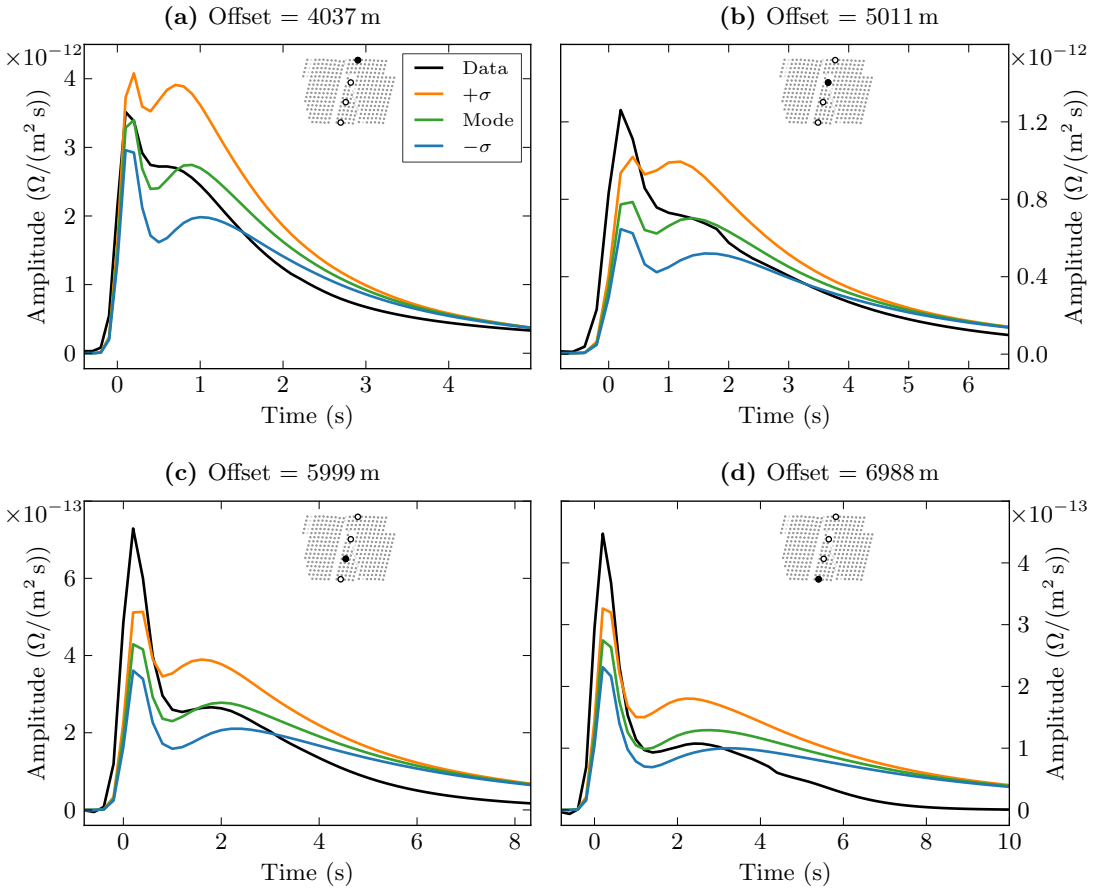


**Figure 7.14:** Results for a source gather with relatively big NRMSD. The peak of the earth response lies still well within plus and minus one standard deviation models. However, the airwave grossly underestimates for larger offsets. Furthermore, later times are overestimated, which also contributes to the high NRMSD. However, this is partly due to the data quality; see also Figure 7.15.

to plus one standard deviation is indicated with the filled areas, (a) on a linear scale, and (b) on a logarithmic scale. The first two responses are in the F2 acquisition band (10 Hz, 0.1 s time sampling), and the others in the F3 acquisition band (5 Hz, 0.2 s time sampling). The dashed lines are the responses from the F3 (first two) and F2 (others), respectively. It underpins the issue of data quality. Where the main energy arrives (peak), the responses from the two frequency bands are very similar, as expected. However, for lower amplitudes approaching the noise floor the data becomes random, and part of the NRMSD plotted in Figure 7.11b is therefore due to data quality.

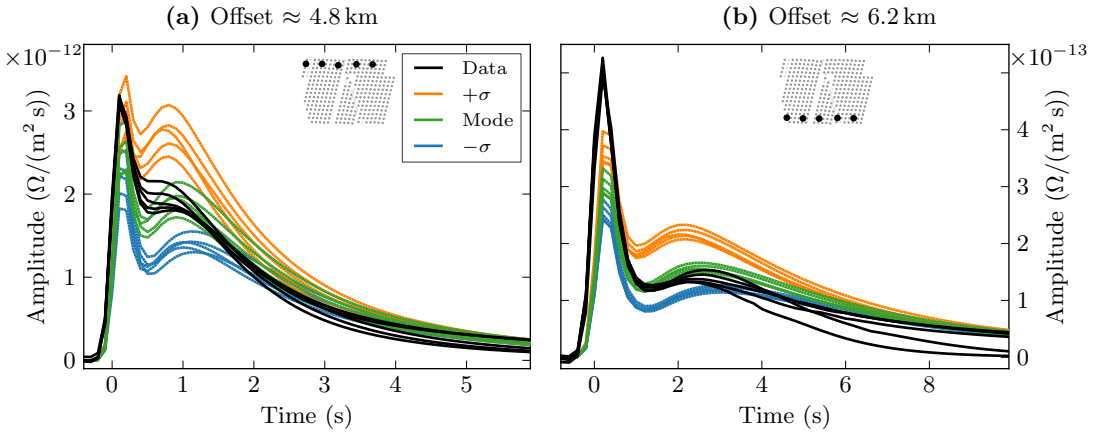


**Figure 7.15:** Collocation of results for offsets (a) 4.2 km and (b) 6.8 km. These plots repeat some of the findings from previous plots: The data agree very well with the calculated responses, but the airwave is underestimated for larger offsets. Specifically (b) shows that the NRMSD is also a function of data quality, as the quality is decreasing with increasing offset, where the amplitudes come closer to the noise level.

## 7.5 Discussion

The results presented in this chapter show that the methodology works. By methodology I mean the estimation of background resistivities from seismic velocities using rock physics, structural constraints, and depth trends, well logs to calibrate the transform, and Bayes to estimate the involved uncertainty from data, rock-physics parameters and rock-physics models. Furthermore, it includes short-offset 1D inversions to estimate the anisotropy and improve the shallow part of the resistivity model outside well control, and finally calculate the CSEM responses from this background resistivity model. In this way, I was able to predict the acquired data in the offset range from 4 km to 7 km.

The good result is that the amplitudes are predicted in the right magnitude, and the peaks of the acquired data are within plus and minus one standard deviation. This is achieved without any scaling, shifting, or fudge factors. In particular it is achieved without a *static shift* correction, a somewhat obscure "correction" frequently used in CSEM and MT methods to account for non-1D structures in a 1D interpretation.

There is scope for improvement. One of the limitations in this project is the horizontal extent of the available data, see Figure 7.7 and Chapter 4. The velocity model, and hence the detailed background resistivity model, and the bathymetry do not cover the whole extent of the CSEM survey. Another limitation is the vertical extent of the available data. Having velocity and resistivity well logs from the seabed to far below the target of interest would improve this approach. Another possibility would be to include

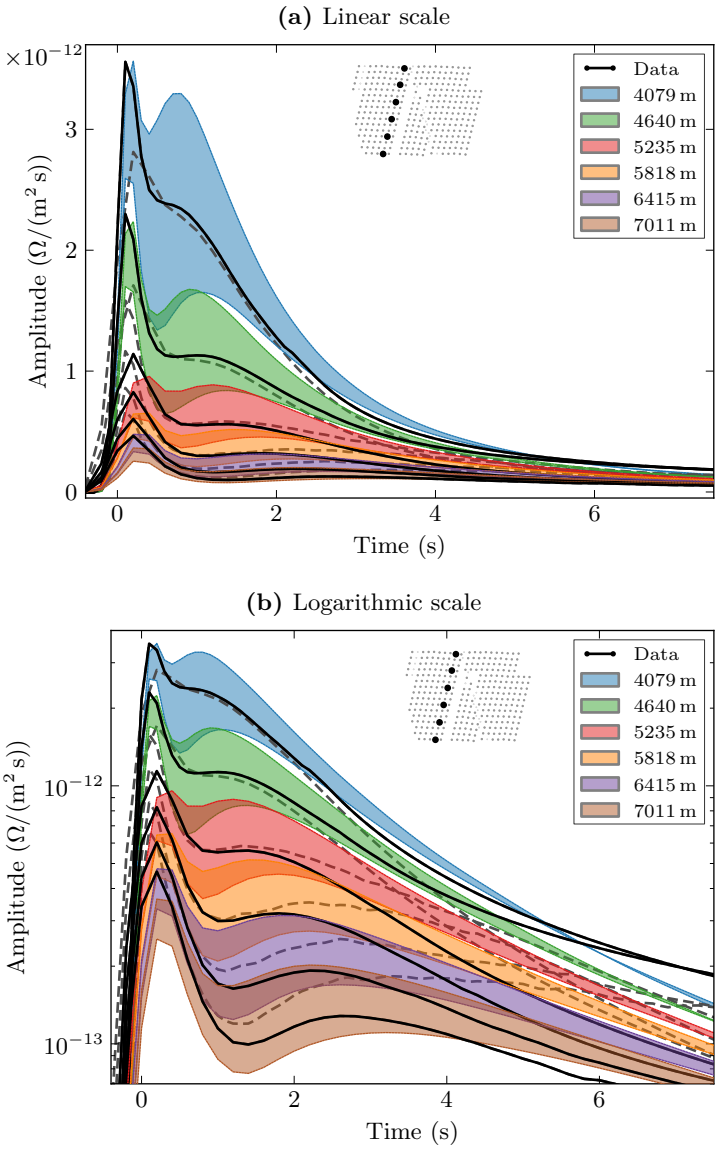


**Figure 7.16:** Detailed collocation for one source position on a linear scale (a) and on a logarithmic scale (b); the filled areas represent plus and minus one standard deviation. The two shorter offsets are in frequency band F2, the longer offsets in F3. The dashed lines are the acquired responses in the respective other frequency band. It shows that the earth peak impulse is robust, but for later times the data quality is not great. The prediction of the responses by the detailed resistivity model gained from seismic data is very good.

well logs from similar formations further away, in order to get a good calibration for the whole depth of interest.

However, I believe the biggest issue is anisotropy. The very detailed resistivity model in Chapter 5 is a model of horizontal resistivity. In reality, an equally complex model of the vertical resistivity is what we should aim for. The downside is that I had to use CSEM inversions of short offsets to estimate the anisotropy. Ideally, one should not have to use the CSEM data at all to get the resistivity model. For this we need another calibration, for instance better well coverage, and another method to estimate anisotropy, for instance tri-axial well logs. Furthermore, this approach resulted in a single value for anisotropy for the whole subsurface, which is not realistic. One possible improvement for the anisotropy is to use well logs that measure horizontal and vertical resistivities, and derive an anisotropy depth trend from it, or even better, two rock-physics transforms to calculate independently a horizontal and vertical resistivity model.

I expect a better handling of anisotropy to improve the match of the airwave. It should also have an effect on later times, as well as an improved calibration of the deeper part of the resistivity model, where I do not have any control of the accuracy of my transform. One problem could be the water resistivity. I show in Chapter 6 in Figure 6.2b that a 10 % change in the resistivity of the water has a significant effect on the amplitude of the peak of the airwave (not earth response). Throughout I assumed a water resistivity of 0.3 Ω m. This value might be in error by 10 %. Measurements of the sea water resistivity at Harding was not made, but it might have given a considerably improved result.

## Summary

The idea behind deriving a background resistivity model from seismic velocities is to enable CSEM responses to be modelled from these resistivities. The background resistivities can also be used as a starting model or for constraints in inversions. Modelled responses can be used for feasibility studies and interpretation, or even for QC during acquisition. If a potential reservoir has a significant effect on the CSEM responses, the acquired data will differ from the modelled data. The Harding reservoir is only at the edge of detectability for a single line and the present noise level, and no further conclusions can be drawn from comparing the predicted data with the acquired impulse responses. But the comparison shows that this workflow of deriving background resistivities from seismic velocities using rock physics, depth trends, estimate its uncertainty, and proper 3D modelling including bathymetry, is able to predict CSEM responses generally to within one standard deviation. This is achieved without any fudge factors such as static shift corrections.

■

# 8

# Discussion and conclusions

**Far better an approximate answer to the right question,**
**which is often vague,**
**than an exact answer to the wrong question,**
**which can always be made precise.**

*John Wilder Tukey (1915–2000)*
*Mathematician*

## 8.1 Findings

I present a workflow that is able to predict controlled-source electromagnetic (CSEM) responses based on seismic velocities. Seismic velocities are transformed to electrical resistivities using rock-physics models, which are calibrated with well-log measurements. The rock-physics models include depth trends and also vary with lithology; the lithology discrimination is based on well logs and seismic data. This workflow involves various levels of uncertainty. Rock-physics models are used to overcome the non-existent link in the theories of seismic wave propagation and electromagnetic diffusion. These models are therefore afflicted with uncertainty, as the link is empirical. They involve a variety of rock-physics parameters which have to be estimated and these estimates also have errors. The acquired data have errors too. Because of these uncertainties I use a Bayesian framework and Markov chain Monte Carlo (MCMC) modelling to predict the resistivities. This results in resistivities in the form of probability density functions (pdfs) instead of deterministic values. The predicted CSEM responses therefore span a range of amplitudes, rather than one response.

I apply this workflow to the North Sea Harding field, where I have seismic velocities and seismic horizons, a set of well logs and CSEM data. For the calibration I used a well log from the Harding South field, in order to show that a nearby well is sufficient for calibration, and test it on wells from Harding Central. The well logs are all nearly vertical, and the measured resistivities therefore represent mainly horizontal resistivity. I use short-offset 1D inversions of the CSEM data to estimate the anisotropy, and update the estimated resistivities for the shallow section where the well has not been logged. 3D forward modelling of this resistivity model is able to predict the responses in an offset range of 4 km to 7 km generally to within one standard deviation.

Figure 8.1 summarises the methodology presented in this thesis. An initial velocity model (a) is transformed into resistivities (b), where the resistivities are given as pdfs to account for the uncertainties. These resistivities are then used to predict CSEM responses (c), which are compared with the acquired responses.

## 8.2 Relevance

The importance of the topic can be seen in increased research interest since the start of this project. In the petroleum industry CSEM is acknowledged as a tool that can provide valuable information to complement seismic data, but its use is limited as a stand-alone tool. Various research groups and consortia around the globe are therefore

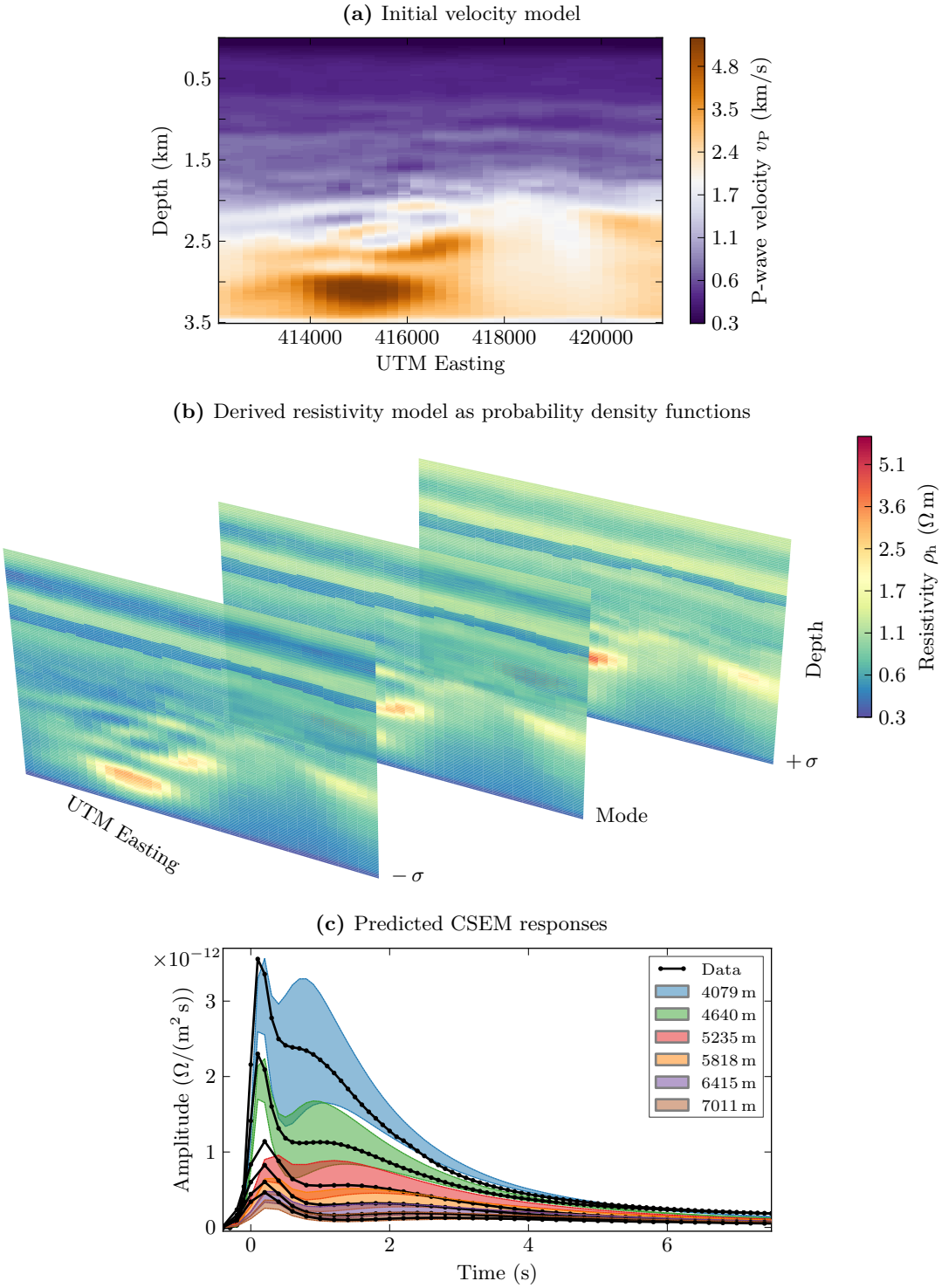


**Figure 8.1:** From velocities to CSEM responses. An initial velocity model is transformed into resistivities, given in the form of pdfs accounting for the uncertainties. The resistivities are then used to predict CSEM responses, which are compared with the acquired responses.

looking at ways of combining seismic and CSEM data in different ways. However, none of these approaches tries to predict CSEM responses to compare them to acquired data. In the following I first look at some projects and then go over some of the recent published work.

### Research projects and lectures

The research project Joint Inversion with Bayesian Analysis (JIBA) aimed to jointly invert diverse geophysical data sets, and applied a Bayesian framework to include the uncertainty. The three-year project (2008–2011) was hosted at Durham University (UK, Dr. Richard Hobbs) and at the IFM-GEOMAR in Kiel (DE, Dr. Marion Jegen) and backed by several oil companies. Some of the findings are published in Moorkamp et al. (2011), where they present a 3D framework for joint inversion of magnetotelluric (MT), gravity, and seismic refraction data. Marion Jegen also gave a Society of Exploration Geophysicists (SEG) Honorary Lecturer Europe tour in 2013, titled *Joint inversion: The way forward to a comprehensive Earth model*. In their inversion approach they merge all data in one joint objective function which has to be minimised, where they try both direct parameter coupling via rock physics and structural similarity via the cross-gradient method. Their conclusion is that it depends on the problem being tackled as to which one is better. If an accurate rock-physics model holds, this method yields better results, as the interaction is stronger. However, the cross-gradient method is better suited if the parameter coupling is not well understood. When Marion Jegen gave her SEG lecture in Edinburgh (4 March 2013), she told me that the two biggest unknowns, which can influence the inversion significantly, are the coupling of the two data sets and the relative weighting of the different data sets. These issues arise because of the non-existent physical link and the different resolution of the two methods.

Another SEG Honorary Lecturer Europe tour took place two years earlier in 2011, in which Lucy MacGregor from Rock Solid Images (RSI) presented a talk titled *Integrating well log, seismic, and CSEM data for reservoir characterization*. Her talk was later published in MacGregor (2012). The focus of the lecture was, as the title suggests, on reservoir properties such as porosity and hydrocarbon saturation.

The continuing interest in the topic is also shown by another project, Joint interpretation of seismic and EM (JoiSE) by SINTEF Petroleum Research (SINTEF, 2011), which was started in 2011 and should last for 3.5 years. The focus is also on structure-based joint inversion and rock physics driven joint inversion.

### Publications

Abubakar et al. (2012) present an approach in 2D similar to the above mentioned paper from the JIBA project (without the Bayesian aspect). They develop a joint inversion for CSEM and full waveform seismic data, where they can use (1) a rock-physics link and (2) a structural link; the structural link is done via the cross-gradient method. They set the inversion up to determine porosity and fluid saturations, where they include the two data sets in the same cost function which has to be minimised. They show synthetic results only, but claim that a joint inversion significantly improves the inversion result compared with single inversion of either data set. The same was done by Gao et al. (2012) for a synthetic crosswell example, albeit only for the rock-physics link, not for the structural link. Another crosswell study involving Bayes is presented by Dell'Aversana et al. (2011), which uses velocity, resistivity, and density measurements from well logs to estimate porosity, fluid saturations and permeability.

Two other publications consider CSEM and seismic amplitude variation with angle of incidence (AVA) data instead of the full waveform, always with the same conclusion that joint inversion improves the result compared with inversion of one data set only. Chen and Hoversten (2012) deploy in a synthetic $CO_2$ monitoring experiment a Bayesian inversion scheme in two steps: first they invert low frequency seismic data only, to obtain the structure; second they jointly invert high frequency seismic data and CSEM data. The really interesting bit in their results is the rock-physics link. They use correlation-based rock-physics relationships instead of rock-physics models. In other words, they statistically derive the relationship for each different lithology from well log data, instead of calibrating an existing model. Lien (2013) uses 2D inversions for fluid flow monitoring, for two types of coupling: (1) rock-physics coupling and (2) structural coupling. But for the structural coupling she uses an implicit representation of common parameter structure instead of the cross-gradient method. The assumption is the same, in that the magnitude of the different parameters change simultaneously.

A slightly different approach to the cross-gradient method is taken by Brown et al. (2012), who carry out synthetic and real 1D CSEM inversions and use regularization weights based on the gradient in the seismic velocity model; a process they termed "guided inversion". It is in this respect not a joint inversion, but a CSEM inversion in which seismic data are used for guidance, similar to using seismic layer boundaries as constraints in CSEM inversions.

Kwon and Snieder (2011) investigate uncertainty in the integration of seismic and CSEM data in a Bayesian framework, where they consider four sources of uncertainty: (1) seismic wave velocity, (2) electrical resistivity, (3) seismic data, and (4) CSEM data.

The uncertainty is observed by calculating porosity and water saturation, in the model space, for 1D models. They conclude that the uncertainty in seismic wave velocity and electrical resistivity is more significant than the uncertainty in seismic data and CSEM data, but that both are important. Interestingly, they did not consider the uncertainty in the rock-physics models themselves.

The need for a joint analysis of seismic and CSEM data also results in new rock-physics models. Han et al. (2011), for instance, derive a new three-phase effective medium model for shaley sandstones. The interest in updated rock-physics models is an interesting side-effect of the push for joint inversions. However, the more specialised a model is the more it is valid only for a very specific lithology. This might be useful in reservoir characterization, but more general models might be more appropriate when we try to gain resistivities from seismic velocities for the whole subsurface. In any case, calibration and the estimate and calculation of the resulting uncertainty is key.

The journal *First Break*, published by the European Association of Geoscientists & Engineers (EAGE), has published several papers in the last couple of years by commercial companies which are either acquiring CSEM data or using CSEM data for their services. The journal is more case-study focused, showing results rather than the methodology and the theory behind them. Both EMGS and partners and RSI and partners present several case studies where they jointly interpret seismic and CSEM data (Gabrielsen et al., 2013; Escalera Alcocer et al., 2013; MacGregor et al., 2012). They mainly show how the addition of CSEM data to seismic data can help to reduce uncertainty and help making decisions in hydrocarbon exploration. Ellis et al. (2012) discuss the importance of anisotropy in rock-physics modelling in integrated seismic and CSEM interpretation, based on well logs.

All these publications show how the inclusion of CSEM improves the understanding of the subsurface, where the focus is usually on the parameter space with porosity and fluid saturations. I have not found any research results where seismic data was used to actually predict CSEM responses, and validate in this way the applied rock-physics transform.

## 8.3 Implications

The implications of my results are manifold. I personally think the most important utilisation is for detailed feasibility studies prior to acquiring CSEM data. Unsuccessful acquisitions have a negative impact on the reputation of the CSEM technology in the petroleum industry, and proper feasibility studies should minimise failures. Once a

detailed feasibility study is carried out, the results can be used for survey planning and on-board quality control (QC) during acquisition. These three applications, feasibility studies, survey planning, and acquisition QC, are obviously possible only if the planned survey happens to be in an area where seismic data, and preferably well data, are available. They are not possible for frontier exploration surveys.

Once data have been acquired the method can be used for interpretation. If the reservoir is of reasonable size, one would expect the acquired data to show higher amplitudes over the reservoir than the predicted amplitudes and agree with predicted amplitudes everywhere else. A comparison of the acquired data with the predicted data will reveal patterns of higher or lower resistivities than predicted. These patterns can then be interpreted given the geological settings of the survey.

The calculated resistivity model can also be used in inversion, for instance as a starting model or as a background model. I assume that stochastic inversion schemes will be used more frequently in CSEM inversion in the future, given that computing power will increase over time. The calculated background model resistivities in the form of pdfs are ideally suited to serve as a complete background model, including the probability of the different resistivity values.

## 8.4 Further research

More effort should be invested in the shortcomings of this work. (1) The anisotropy determination: a better handling on anisotropy is crucial, and an investigation with modern well logs with tri-axial resistivity measurements would be ideal. (2) The calibration of the depth extent where there are no well logs: inclusion of regional data could help to further calibrate the velocity-to-resistivity transform. (3) The water resistivity: the results have shown that the airwave is often under-estimated. In the sensitivity analysis in Chapter 6 I show in Figure 6.2b that a difference of 10 % in the water resistivity has a huge influence on the airwave. I assumed a water resistivity of $0.3\,\Omega\,\mathrm{m}$, but this might well be incorrect by 10 %. A good estimate of the water resistivity could further improve the result.

In this project it was basically myself with a set of data trying to find out what can be achieved. This also means that a lot of time was spent on data handling and familiarising myself with methods and concepts. However, in a commercial setting these things are usually in place, as are the software to handle the acquired data, and the expert knowledge in the different fields. What could be achieved if the seismic team, the reservoir team, the CSEM team, and the geologists team work together and bring in

their full knowledge? One could aim for a good estimate of the rock-physics parameters, include more lithology discrimination, and try to lower the error bars on all the inputs in the transform. How well could we predict CSEM data? Where are the limits? I think it is a very exciting field of research, and I expect that we will read and see a lot more of joint seismic and CSEM interpretation and inversion methods in the near future.

■

# Appendices

# A

# Complementary theory

**It is impossible to speak in such a way**
**that you cannot be misunderstood.**

*Karl Raimund Popper (1902–1994)*
*Philosopher*

---

In this appendix I list additional theoretical information and comments regarding multi-transient electromagnetic (MTEM) data processing and uncertainty analysis. This information is not the main purpose of my thesis, but it is necessary to understand, follow, and most of all reproduce my results.

---

## A.1 MTEM Processing

### Pseudo-random binary sequence

The MTEM method uses a transient source signal, which is often a pseudo-random binary sequence (PRBS). A PRBS is a sequence with $N = 2^n - 1$ samples, where $n$ is called the order of sequence. It switches between plus and minus the source strength at pseudo-random multiples of the basic time interval $\Delta t$. The advantage of the PRBS is that it has a flat amplitude spectrum within the frequency interval

$$\frac{1}{N\Delta t} \leq f \leq \frac{1}{2\Delta t} \ , \tag{A.1}$$

where the data has to be sampled at a rate bigger or equal than $1/\Delta t$. Ziolkowski et al. (2011) compare the transient PRBS to the transient square-wave source signature. The square wave results in higher amplitudes at the fundamental frequency and its odd harmonics, where the PRBS has a flat spectrum. However, the deconvolution (see Chapter 4) compresses the energy from the PRBS into an impulse response, which results in a significant signal-to-noise gain. It also allows further time-domain processing, such as correlated noise removal, which increases the signal-to-noise ratio.

### Gaussian filter

A Gaussian zero-phase filter is applied in the processing of MTEM data (Ziolkowski et al., 2007, Appendix A), given by

$$\hat{h}(\omega) = \exp\left(-\left[\frac{\omega}{\omega_0}\right]^2\right) \ , \tag{A.2}$$

where $\omega$ is angular frequency, and $\omega_0$ is generally chosen to be half the angular Nyquist frequency,

$$\omega_0 = \frac{\pi}{2\Delta t} \ . \tag{A.3}$$

The Fourier transform $h(t)$ of $\hat{h}(\omega)$ in Equation A.2 is

$$h(t) = \sqrt{\pi}\omega_0 \exp\left(-[\pi\omega_0 t]^2\right) \ , \tag{A.4}$$

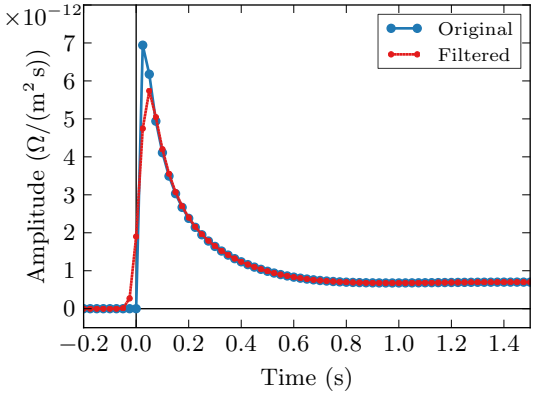


**Figure A.1:** The effect of the Gaussian filter. In blue is the causal modelled response. The Gaussian filter is applied on the red response, causing non-causal arrivals. The Gaussian filter only affects very early times, and therefore mainly the shape of the airwave.

which is a band-limited approximation to a delta function $\delta(t)$. It has the characteristics of the delta function with a peak at $t = 0\,\mathrm{s}$, and its integral is unity,

$$\int_{-\infty}^{\infty} h(t)\,\mathrm{d}t = 1\ . \tag{A.5}$$

This Gaussian filter is applied to all modelled data when compared to real data, in order to make a fair comparison with the MTEM responses. The effect of the Gaussian filter is shown in Figure A.1. The filter only affects very early times, therefore mainly the shape of the airwave. The modelled example is a 100 m water layer with resistivity of $0.3\,\Omega\,\mathrm{m}$ over an isotropic half-space of $1\,\Omega\,\mathrm{m}$ at offset of 4 km, calculated every 0.025 seconds (40 Hz).

### Logarithmic fast Fourier transform

Hamilton (2000, Appendix B) provides the theory for a logarithmic fast Fourier transform (giving credit to Talman (1978), who originally proposed it), and makes his code `FFTLog` (written in `Fortran`) available at `http://casa.colorado.edu/~ajsh/FFTLog`. He states that "*FFTLog can be regarded as a natural analogue to the standard FFT, in the sense that, just as the normal FFT gives the (to machine precision) Fourier transform of a linearly spaced periodic sequence, so also FFTLog gives the exact Fourier or Hankel transform, of arbitrary order $\mu$, of a logarithmically spaced periodic sequence. FFTLog shares with the normal FFT the problems of ringing (response to sudden steps) and aliasing (periodic folding of frequencies), but under appropriate circumstances FFTLog may approximate the results of a continuous Fourier or Hankel transform.*".

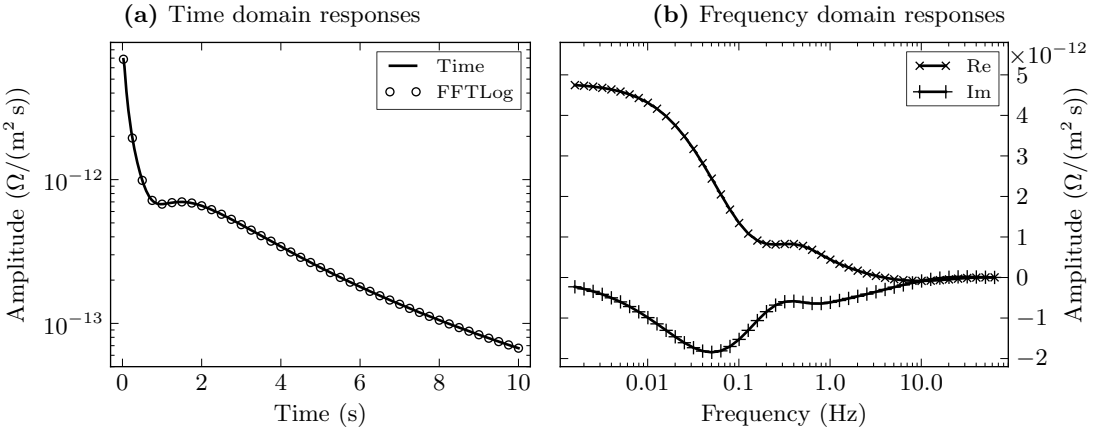


**Figure A.2:** Example of the `FFTLog`. The solid line in (a) shows the response calculated in the time domain, and the circles show the response calculated in the frequency domain, transformed to time domain with `FFTLog`. (b) shows the corresponding real and imaginary frequency amplitudes.

I use `FFTLog`, as implemented by PGS, to transform frequency responses from the forward modeller `PIE3D` (see Appendix C) into time responses. For this I used the `Python` wrapper `f2py` (`http://www.f2py.com`) to create a `Python` module from the `Fortran` code. An extra decade is added at each side of the timescale to ensure that the `FFTLog` in the desired time range is accurate (following the standard practice of PGS, where they extensively tested `FFTLog` for MTEM responses). Minimum ($f_{\text{min}}$) and maximum ($f_{\text{max}}$) frequencies are hence given by

$$f_{\text{min}} = \frac{0.1}{2\pi t_{\text{max}}} , \qquad f_{\text{max}} = \frac{10}{2\pi t_{\text{min}}} . \tag{A.6}$$

The number of logarithmically evenly spaced frequencies is therefore

$$N_f = \theta_{\text{dec}} \left( \log_{10} \left[ \frac{f_{\text{max}}}{f_{\text{min}}} \right] \right) + 1 , \tag{A.7}$$

where $\theta_{\text{dec}}$ is the number of frequencies per decade.

An example is shown in Figure A.2; the model is the same as in Figure A.1, without Gaussian filter. The solid line in (a) shows the response calculated in the time domain, the circles show the response calculated in frequency domain and subsequently transformed to time domain with `FFTLog`. Figure A.2b shows the corresponding logarithmically sampled real and imaginary frequency amplitudes. For the `FFTLog`, only the imaginary values are used, which start and end, theoretical, with zero amplitude. This is opposed to the real values, which end with zero amplitude, but are non-zero at 0 Hz, the direct current (DC) amplitude.

### Normalised root mean square difference (%)

I use the normalised root mean square difference (NRMSD) (e.g. Ziolkowski et al., 2010) to compare two time series $\mathbf{x}$ and $\mathbf{y}$, such as an MTEM response with a modelled response, which is given by

$$\mathrm{NRMSD}(\mathbf{x},\mathbf{y}) = 200\frac{\mathrm{NRMS}(\mathbf{x}-\mathbf{y})}{\mathrm{NRMS}(\mathbf{x})-\mathrm{NRMS}(\mathbf{y})}\ , \tag{A.8}$$

where

$$\mathrm{NRMS}(\mathbf{z}) = \sqrt{\frac{1}{N}\sum_{t=1}^{N} z_t^2}\ ; \tag{A.9}$$

$N$ is the number of time samples in the time series.

## A.2 Probability

### Kernel density estimation

Assuming a normal distribution (or another standard distribution) to describe a random parameter is often not very accurate, as probability density functions (pdfs) can have arbitrary shapes. This is where kernel density estimation (KDE) comes into place: KDE, sometimes also referred to as the Parzen-Rosenblatt window method (Rosenblatt, 1956; Parzen, 1962), is a way of estimating the pdf of a random variable, which is basically a smoothing problem. A KDE uses a probability distribution as a kernel. It then assigns every data point this distribution with a certain bandwidth, and sums up all the various distributions. The most common bandwidths are the Scott factor and the Silverman factor (Scott, 1979; Silverman, 1986).

To estimate the probability of a data point $p$, given the random dataset $\mathbf{x}$, the KDE is given by

$$f(p,\mathbf{x},\eta) = \frac{1}{\eta N}\sum_{n=1}^{N} K\left(\frac{p-x_n}{\eta}\right)\ , \tag{A.10}$$

where $K$ is the kernel, and $\eta$ the bandwidth. I use the default implementation in the scientific `Python SciPy` package, which uses by default a Gaussian kernel for $K$ (the normal distribution), and for the bandwidth the Scott factor, given by

$$\eta = N^{-\frac{1}{\theta+4}}\ , \tag{A.11}$$

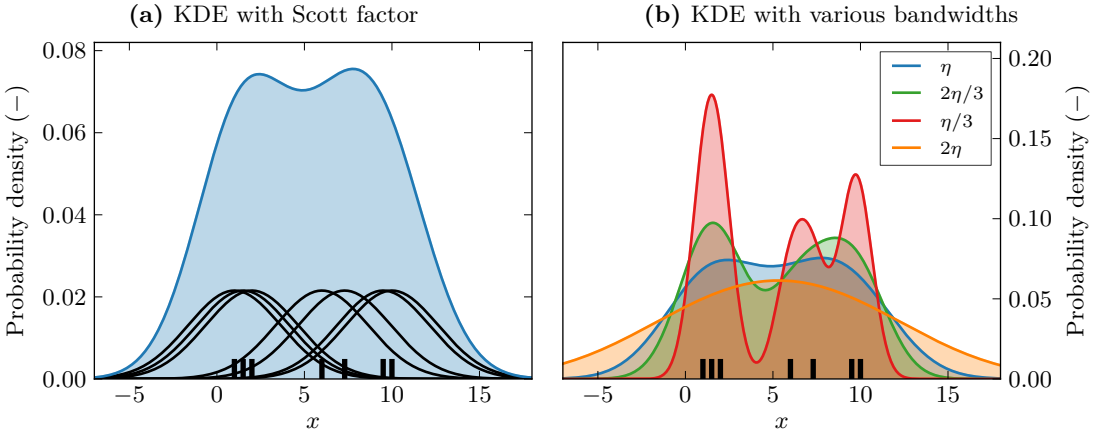


**Figure A.3:** KDE with a Gaussian kernel. (a) shows the KDE with the standard Scott bandwidth $\eta$, and the corresponding normal distributions for each data point. (b) shows the influence of the bandwidth, where the blue is the same as in (a), and green, red, and orange are two thirds of $\eta$, one third of $\eta$, and twice $\eta$, respectively.

where $N$ is the length of $\mathbf{x}$, and $\theta$ is the number of dimensions, which is 1 in all the cases in this thesis.

Figure A.3 demonstrates the method and shows the influence of the bandwidth. The seven data points are indicated by the rug plot (the black markers along the x-axis). In (a), the black Gaussian curves indicate the contribution of each data point, and the blue curve is the KDE with the standard Scott bandwidth $\eta$. The influence of the bandwidth is shown in (b) for $\eta$ (blue), $2\eta/3$ (green), $\eta/3$ (red), and $2\eta$ (green).

Using only seven sample data points for a KDE is good to show the method, but it makes the KDE very sensitive to the bandwidth. An example with 500 random draws from a standard normal distribution is shown in Figure A.4, with the same values for the bandwidth as before; the data are indicated by the rug plot. Choosing too narrow bandwidth yields a very wiggly plot, choosing it too wide smooths the data too much. The standard bandwidth does a good job in estimating the true pdf, which is plotted in black.

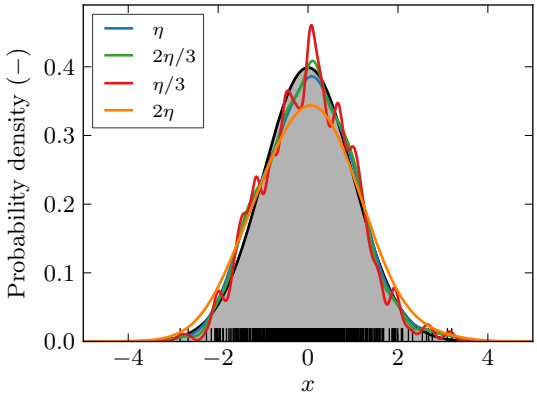


**Figure A.4:** KDEs for a set of 500 random draws from a standard normal distribution. In black is the true Gaussian, the rug plot shows the randomly drawn data. In blue, green, red, and orange are the KDEs for the Scott factor $\eta$, two third of $\eta$, one third of $\eta$, and twice $\eta$, respectively. It shows that the Scott factor does a good job in approximating the true distribution. Too narrow bandwidths yield a wiggly curve, too wide bandwidths smooth the data too much.

# B

# Extrema analysis

**A propensity to hope and joy is real riches:**
**One to fear and sorrow, real poverty.**

*David Hume (1711–1776)*
*Philosopher*

The electric field for an x-directed impulsive dipole source measured inline on the surface has a distinct feature, a peak, which arrival time can be calculated for an isotropic, homogeneous half-space. I extend this to the electric field measured anywhere in full-space. The x-component of the electric field has two extrema everywhere except inline, where there is only the mentioned maximum. The y-component (z-component) of the electric field has everywhere one extrema, except in the x-z- and y-z-planes (x-y and y-z), where the field vanishes. Tracking the extrema of the electromagnetic waveform could potentially be extended to an analogy to seismic ray-tracing.

## B.1 Motivation for ray-path analysis

Ray-tracing (Červený, 2001; Červený et al., 1974) is a powerful tool, or better a powerful approximation, in seismic data processing, mainly due to its low computational requirements compared to full-waveform modelling. Also, the idea of ray-tracing can be easily explained on a piece of paper and is easier understood than full-waveform theories. Multi-transient electromagnetic (MTEM) impulse responses are characterised by a maximum at any given time, the earth response. The question of interest is if it is possible to follow this maximum through space and time, and therefore create a ray path for it.

I start with the electric field in full-space for a step switch-on source. The source is always an x-directed dipole in this analysis, located at the origin. $\mathcal{G}^{\mathrm{S}}_{\mathrm{x}}$ and $\mathcal{G}^{\mathrm{I}}_{\mathrm{x}}$ denote the step and impulse responses for an x-directed receiver anywhere in full-space; accordingly also for the subscripts y and z.

## B.2 Electric field for an impulsive dipole source in full-space

The step response for times $t > 0\,\mathrm{s}$ for an x-directed dipole source in an isotropic, homogeneous full-space located at the origin and switched on at time $t = 0\,\mathrm{s}$ is derived by Ward and Hohmann (1988, Equation 2.50),

$$\mathcal{G}^{\mathrm{S}} = \frac{\rho}{4\pi r^3}\left\{ \left[\left(\frac{4}{\sqrt{\pi}}\theta^3 r^3 + \frac{6}{\sqrt{\pi}}\theta r\right)\exp\left(-\theta^2 r^2\right) + 3\,\mathrm{erfc}(\theta r)\right]\left[\frac{x^2}{r^2}\tilde{\mathbf{x}} + \frac{xy}{r^2}\tilde{\mathbf{y}} + \frac{xz}{r^2}\tilde{\mathbf{z}}\right] - \left[\left(\frac{4}{\sqrt{\pi}}\theta^3 r^3 + \frac{2}{\sqrt{\pi}}\theta r\right)\exp\left(-\theta^2 r^2\right) + \mathrm{erfc}(\theta r)\right]\tilde{\mathbf{x}}\right\} . \quad \text{(B.1)}$$

$\mathcal{G}^{\mathrm{S}}$ ($\Omega/\mathrm{m}^2$) is the electric field (V/m) to a step switch-on source, normalised by the source strength (A) and the dipole length (m); $\rho$ is the full-space resistivity ($\Omega\,\mathrm{m}$). The spatial coordinates are denoted by $x$, $y$ and $z$ (m) with the corresponding dimensionless unit vectors $\tilde{\mathbf{x}}$, $\tilde{\mathbf{y}}$ and $\tilde{\mathbf{z}}$, and time is denoted by $t$ (s). Furthermore, $\theta$ (1/m) and $r$ (m) are defined by

$$\theta = \sqrt{\frac{\mu_0}{4\rho t}} , \quad \text{(B.2)}$$

and

$$r = \sqrt{x^2 + y^2 + z^2} , \quad \text{(B.3)}$$

respectively, where $\mu_0$ is the magnetic permeability of free space, $4\pi \times 10^{-7}\,\mathrm{H/m}$; erfc is the complementary error function. See Symbols and Abbreviations for a detailed list of symbols and functions.

The electric field to an impulsive source is obtained by taking the time derivative of the step response. The time derivatives for terms containing $\theta$ are given by,

$$\frac{\partial}{\partial t}\theta^n = -\frac{n\theta^n}{2t}\ , \tag{B.4}$$

$$\frac{\partial}{\partial t}\exp\left(-\theta^2 r^2\right) = \frac{\theta^2 r^2}{t}\exp\left(-\theta^2 r^2\right)\ \text{, and} \tag{B.5}$$

$$\frac{\partial}{\partial t}\operatorname{erfc}(\theta r) = \frac{\theta r}{\sqrt{\pi}t}\exp\left(-\theta^2 r^2\right)\ . \tag{B.6}$$

The time derivative of Equation B.1 is then given by

$$\begin{aligned}\frac{\partial}{\partial t}\mathcal{G}^{\mathrm{S}} &= \frac{\rho}{4\pi r^3}\left\{\frac{4}{\sqrt{\pi}t}\theta^5 r^5\exp\left(-\theta^2 r^2\right)\left[\frac{x^2}{r^2}\tilde{\mathbf{x}}+\frac{xy}{r^2}\tilde{\mathbf{y}}+\frac{xz}{r^2}\tilde{\mathbf{z}}\right]\right.\\ &\qquad\left.-\left(\frac{4}{\sqrt{\pi}t}\theta^5 r^5-\frac{4}{\sqrt{\pi}t}\theta^3 r^3\right)\exp\left(-\theta^2 r^2\right)\tilde{\mathbf{x}}\right\}\\ &= \frac{\rho\theta^3}{\pi^{3/2}t}\left\{\left[\theta^2\left(x^2\tilde{\mathbf{x}}+xy\tilde{\mathbf{y}}+xz\tilde{\mathbf{z}}\right)-\left(\theta^2 r^2-1\right)\tilde{\mathbf{x}}\right]\exp\left(-\theta^2 r^2\right)\right\}\ ,\end{aligned} \tag{B.7}$$

or in other words

$$\mathcal{G}^{\mathrm{I}} = \frac{\rho\theta^3}{\pi^{3/2}t}\exp\left(-\theta^2 r^2\right)\left\{\left[1-\theta^2\left(y^2+z^2\right)\right]\tilde{\mathbf{x}}+\theta^2 x\left(y\tilde{\mathbf{y}}+z\tilde{\mathbf{z}}\right)\right\}\ , \tag{B.8}$$

where $\mathcal{G}^{\mathrm{I}}$ stands for the impulse response $(\Omega/(\mathrm{m}^2\,\mathrm{s}))$.

The following conclusions can be drawn from Equation B.8:

1. For $x = 0$ (y-z-plane) $\rightarrow$ $\mathcal{G}^{\mathrm{I}}_{\mathrm{z}} = \mathcal{G}^{\mathrm{I}}_{\mathrm{y}} = 0$
2. For $y = 0$ (x-z-plane) $\rightarrow$ $\mathcal{G}^{\mathrm{I}}_{\mathrm{y}} = 0$
3. For $z = 0$ (x-y-plane) $\rightarrow$ $\mathcal{G}^{\mathrm{I}}_{\mathrm{z}} = 0$
4. For $y^2 + z^2 = 1/\theta^2 = 4\rho t/\mu_0$ $\rightarrow$ $\mathcal{G}^{\mathrm{I}}_{\mathrm{x}} = 0$
5. $\mathcal{G}^{\mathrm{I}}_{\mathrm{x}}$ is symmetric about the x-axis and the y-z-plane.
6. $\mathcal{G}^{\mathrm{I}}_{\mathrm{y}}$ and $\mathcal{G}^{\mathrm{I}}_{\mathrm{z}}$ are symmetric about the origin.
7. $\mathcal{G}^{\mathrm{I}}_{\mathrm{y}} = \mathcal{G}^{\mathrm{I}}_{\mathrm{z}}$ rotated by $\pi/2$ around the x-axis.

First, I look into the extrema of the x-component in the x-z-plane, and then into the extrema of the z-component in the x-z-plane. These two define, with the above symmetry observations, the extrema anywhere in the complete full-space.

## B.3 Extrema of x-component in the x-z-plane

### Arrival time

The extrema of a function of time are found by taking the derivative with respect to time and setting the result equals zero. If we consider $\mathcal{G}^{\mathrm{I}}_{\mathrm{x}}$ solely and set $y = 0$, the time derivative of Equation B.8 is given by

$$\begin{aligned}\frac{\partial \mathcal{G}^{\mathrm{I}}_{\mathrm{x}}}{\partial t} &= \frac{\partial}{\partial t}\frac{\rho}{\pi^{3/2}}\exp\left(-\theta^2 r^2\right)\left[\frac{\theta^3}{t} - \frac{\theta^5}{t}z^2\right] \\ &= \frac{\rho}{\pi^{3/2}}\exp\left(-\theta^2 r^2\right)\left\{\frac{\theta^2}{t}r^2\left[\frac{\theta^3}{t} - \frac{\theta^5}{t}z^2\right] + \left[\frac{7\theta^5}{2t^2}z^2 - \frac{5\theta^3}{2t^2}\right]\right\} \\ &= \underbrace{\frac{\rho\theta^3}{2\pi^{3/2}t^2}\exp\left(-\theta^2 r^2\right)}_{K_1}\left[-5 + 2\theta^2 r^2 + 7\theta^2 z^2 - 2\theta^4 z^2 r^2\right] = 0 \ , \end{aligned} \tag{B.9}$$

using Equation B.5 and the following relation,

$$\frac{\partial}{\partial t}\frac{\theta^n}{t^p} = -\frac{(2p+n)\theta^n}{2t^{p+1}} \ . \tag{B.10}$$

$K_1 > 0$ for all times $t > 0$ in Equation B.9. The problem reduces therefore to

$$-5 + (2x^2 + 9z^2)\theta^2 - 2\theta^4 z^2(x^2 + z^2) = 0 \ , \tag{B.11}$$

which is a second order quadratic equation in $t$, with the solution

$$t^{\mathrm{x}}_{\mathrm{p}} = \frac{\mu_0}{40\rho}\left[2x^2 + 9z^2 \pm \sqrt{4x^4 - 4x^2z^2 + 41z^4}\right] \ , \tag{B.12}$$

where $t^{\mathrm{x}}_{\mathrm{p}}$ denotes the times of the peaks for the $\mathcal{G}^{\mathrm{I}}_{\mathrm{x}}$-field. For $z = 0$, Equation B.12 reduces to

$$t^{\mathrm{xx}}_{\mathrm{p}} = \frac{\mu_0}{40\rho}\left[2x^2 \pm 2x^2\right] \quad \overset{t>0}{\Longrightarrow} \quad t^{\mathrm{xx}}_{\mathrm{p}} = \frac{\mu_0 x^2}{10\rho}, \tag{B.13}$$

which agrees with the solution derived by Ziolkowski et al. (2007), who derived the solution for inline (hence $y = z = 0$) source and receiver at the surface of a half-space

below a non-conducting half-space. The solutions are the same in full-space and on the surface of a half-space below a non-conducting half-space for an inline source and receiver configuration for times $t > 0$. Similarly, for $x = 0$,

$$t_{\mathrm{p}}^{\mathrm{xz}} = \frac{\left(9 \pm \sqrt{41}\right) \mu_0 z^2}{40\rho} \quad \Longrightarrow \quad t_{\mathrm{p}+}^{\mathrm{xz}} \approx 3.85 \frac{\mu_0 z^2}{10\rho} \;,\; t_{\mathrm{p}-}^{\mathrm{xz}} \approx 0.65 \frac{\mu_0 z^2}{10\rho} \;. \tag{B.14}$$

Equations B.13 and B.14 show that in x-direction there is one and in z-direction there are two extrema of $\mathcal{G}_{\mathrm{x}}^{\mathrm{I}}$; one of them arriving earlier ($t_{\mathrm{p}-}^{\mathrm{xz}}$) and the other later ($t_{\mathrm{p}+}^{\mathrm{xz}}$) than the extreme in x-direction.

### Maximum or minimum

Equation B.12 gives all the times where an extreme of $\mathcal{G}_{\mathrm{x}}^{\mathrm{I}}$ occurs in the x-z-plane, but does not say whether it is a minimum or a maximum. To get this information we need the second derivative of $\mathcal{G}_{\mathrm{x}}^{\mathrm{I}}$ with respect to time,

$$\begin{aligned}
\frac{\partial^2 \mathcal{G}_{\mathrm{x}}^{\mathrm{I}}}{\partial t^2} &= \frac{\partial}{\partial t} \frac{\rho}{2\pi^{3/2}} \exp\left(-\theta^2 r^2\right) \left[ -\frac{5\theta^3}{t^2} + (2x^2 + 9z^2) \frac{\theta^5}{t^2} - (x^2 z^2 + z^4) \frac{2\theta^7}{t^2} \right] \\
&= \frac{\rho}{2\pi^{3/2}} \exp\left(-\theta^2 r^2\right) \left\{ \frac{\theta^2}{t} r^2 \left[ -\frac{5\theta^3}{t^2} + (2x^2 + 9z^2) \frac{\theta^5}{t^2} - (x^2 z^2 + z^4) \frac{2\theta^7}{t^2} \right] \right. \\
&\qquad \left. + \left[ \frac{35\theta^3}{2t^3} - (2x^2 + 9z^2) \frac{9\theta^5}{2t^3} + (x^2 z^2 + z^4) \frac{11\theta^7}{t^3} \right] \right\} \\
&= \overbrace{\frac{\rho\theta^3}{4\pi^{3/2} t^3} \exp\left(-\theta^2 r^2\right)}^{K_2} \left[ 35 - (28x^2 + 91z^2)\theta^2 + (4x^4 + 44x^2 z^2 + 40z^4)\theta^4 \right. \\
&\qquad \left. - (4x^4 z^2 + 8x^2 z^4 + 4z^6)\theta^6 \right] \;,
\end{aligned} \tag{B.15}$$

where $K_2 > 0$ for all times $t > 0$. For $z = 0$ and $t_{\mathrm{p}}^{\mathrm{xx}}$, Equation B.15 becomes

$$\frac{\partial^2}{\partial t^2} \mathcal{G}_{\mathrm{x}}^{\mathrm{I}}(x, z = 0, t_{\mathrm{p}}^{\mathrm{xx}}) = -10 K_2 \quad < \quad 0 \quad \rightarrow \quad \text{maximum} \;. \tag{B.16}$$

Similarly, for $x = 0$ and $t_{\mathrm{p}}^{\mathrm{xz}}$,

$$\frac{\partial^2}{\partial t^2} \mathcal{G}_{\mathrm{x}}^{\mathrm{I}}(x = 0, z, t_{\mathrm{p}}^{\mathrm{xz}}) \approx \begin{cases} -8.31 K_2 & < 0 \quad \text{for } t_{\mathrm{p}+}^{\mathrm{xz}} \quad \rightarrow \quad \text{maximum} \;, \\ 49.31 K_2 & > 0 \quad \text{for } t_{\mathrm{p}-}^{\mathrm{xz}} \quad \rightarrow \quad \text{minimum} \;. \end{cases} \tag{B.17}$$

### Absolute value

By inserting $t_{\mathrm{p}}^{\mathrm{x}}$ into Equation B.8, it can be seen that the minimum is bigger than the maximum at any depth $z_i$, and the maximum at $x_i = z_i$ is in-between,

$$\left|\mathcal{G}_{\mathrm{x}}^{\mathrm{I}}(x=0, z_i, t_{\mathrm{p}-}^{\mathrm{xz}})\right| > \left|\mathcal{G}_{\mathrm{x}}^{\mathrm{I}}(x_i, z=0, t_{\mathrm{p}}^{\mathrm{xx}})\right| > \left|\mathcal{G}_{\mathrm{x}}^{\mathrm{I}}(x=0, z_i, t_{\mathrm{p}+}^{\mathrm{xz}})\right| \ . \tag{B.18}$$

### Wavefront

The waves of the extrema are given by solving Equation B.12 for $x$,

$$|x| = \pm\sqrt{\frac{-5 + 9\theta^2 z^2 - 2\theta^4 z^4}{2\theta^2(\theta^2 z^2 - 1)}} \ , \quad \text{with} \quad \theta^2(\theta^2 z^2 - 1) \neq 0 \ , \tag{B.19}$$

which has real values within the limits

$$0 \ \leq \ |z| \ \leq \sqrt{\frac{10}{\left(9 + \sqrt{41}\right)\theta^2}} \qquad \text{maximum wave} \ , \tag{B.20}$$

$$\frac{1}{\theta} \ < \ |z| \ \leq \sqrt{\frac{10}{\left(9 - \sqrt{41}\right)\theta^2}} \qquad \text{minimum wave} \ . \tag{B.21}$$

The upper limits follow from Equation B.14, and the lower limits from Equation B.19.

### Figures for extrema of x-component in the x-z-plane

Figures B.1 to B.3 show some time-snapshots of the electric field. Full-space resistivity is $\rho = 20\,\Omega\,\mathrm{m}$. In these examples we look at the extrema at an offset of 1.5 km. The arrival time of $t_{\mathrm{p}-}^{\mathrm{xz}}$ at $z = 1.5\,\mathrm{km}$ is at $\approx 9.2 \times 10^{-3}\,\mathrm{s}$. The electric field for this time is shown in Figure B.1 in (a) on a logarithmic scale, and in (b) on a linear scale. The extrema wavefronts at this time are shown with the green lines. The arrival time of $t_{\mathrm{p}}^{\mathrm{xx}}$ at $x = 1.5\,\mathrm{km}$ is at $\approx 1.4 \times 10^{-2}\,\mathrm{s}$, and the fields are shown in Figure B.1 (c) and (d), the wavefronts are shown in black. The fields for $t_{\mathrm{p}+}^{\mathrm{xz}}$ ($\approx 5.4 \times 10^{-2}\,\mathrm{s}$) are given in Figure B.1 (e) and (f), and the wavefronts are shown in purple.

In Figure B.2, the extrema are plotted as a function of time, (a) and (c) in z-direction, (b) in $x$-direction. The big symbols correspond to the location indicated by the white symbols in Figure B.1 (b), (d), and (f); they show the maximum peak at an offset of 1.5 km. The line colour corresponds to the wavefronts in Figure B.1. Figure B.3 finally shows the maximum amplitude as a function of offset. The symbols and line colours correspond again to the symbols and wavefronts in Figure B.1.

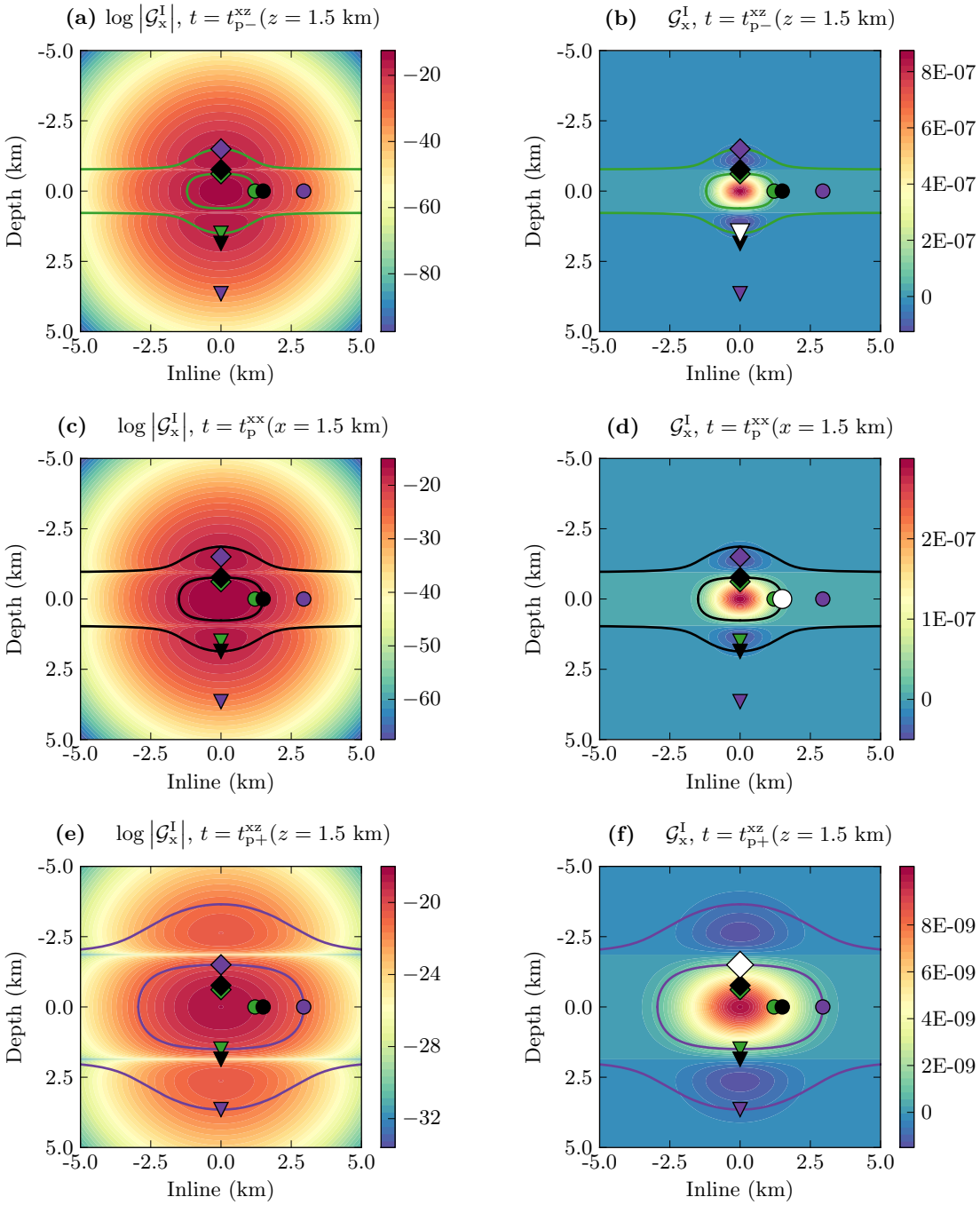


**Figure B.1:** $\mathcal{G}^{\mathrm{I}}_{\mathrm{x}}$-field ($\Omega/(\mathrm{m}^2\,\mathrm{s})$) in the x-z-plane on a logarithmic scale on the left, and on a linear scale on the right. (a) and (b) for time $t^{\mathrm{xz}}_{\mathrm{p}-}(z = 1.5\ \mathrm{km}) \approx 9.2 \times 10^{-3}$ s, (c) and (d) for time $t^{\mathrm{xx}}_{\mathrm{p}}(x = 1.5\ \mathrm{km}) \approx 1.4 \times 10^{-2}$ s, and (e) and (f) for time $t^{\mathrm{xz}}_{\mathrm{p}+}(z = 1.5\ \mathrm{km}) \approx 5.4 \times 10^{-2}$ s.

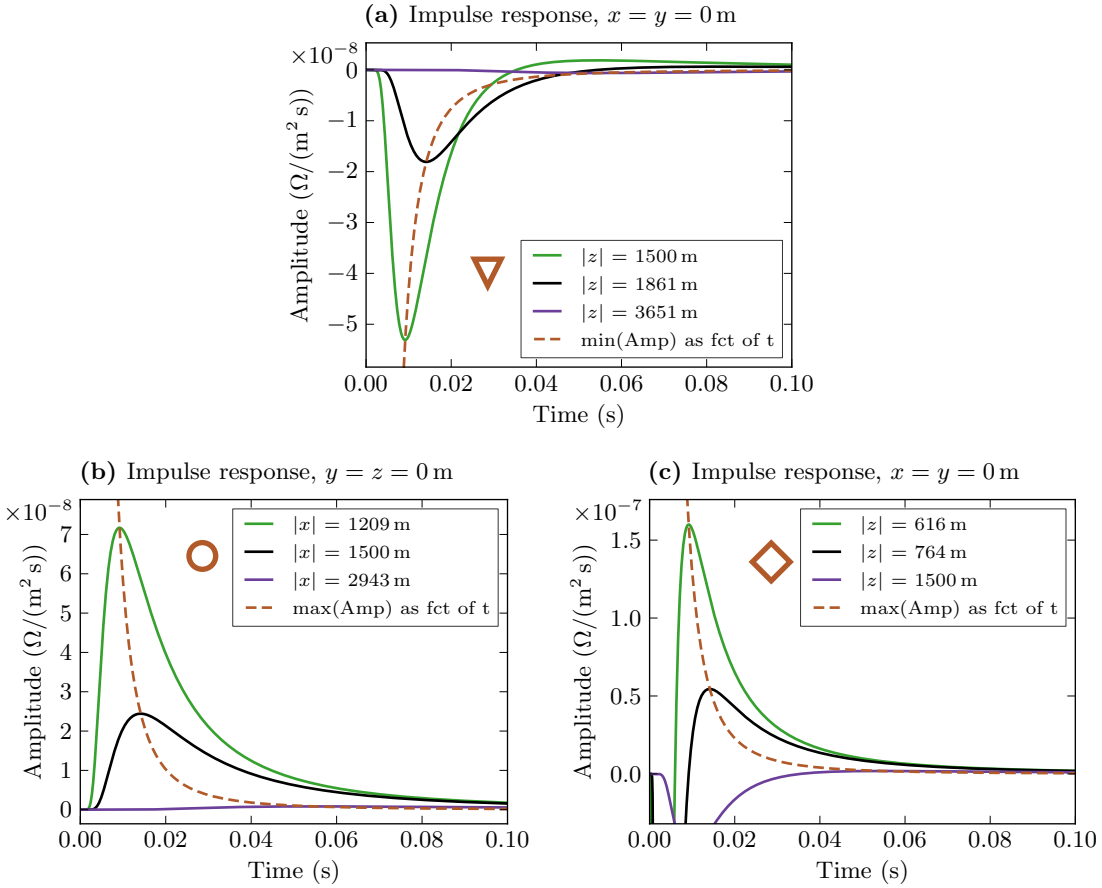


**Figure B.2:** Impulse responses for the locations marked with the corresponding symbols and colours in Figure B.1. Note that (a) and (c) show the same responses: In (a) are the complete responses to show the minima, whereas (c) zooms into the positive part to show the maxima. The dashed lines show the maxima and minima for the whole time-range.

## B.4 Extrema of z-component in the x-z-plane

### Arrival time

For $\mathcal{G}_z^{\mathrm{I}}$ solely and $y = 0$ the time derivative of Equation B.8 is given by

$$\frac{\partial \mathcal{G}_z^{\mathrm{I}}}{\partial t} = \frac{\partial}{\partial t}\frac{\rho\theta^5}{\pi^{3/2}t}\exp\left(-\theta^2 r^2\right)xz = \underbrace{\frac{\rho\theta^5}{2\pi^{3/2}t^2}\exp\left(-\theta^2 r^2\right)}_{K_3}\left[2\theta^2 r^2 - 7\right]xz = 0\ , \quad \text{(B.22)}$$

where $K_3 > 0$ for all times $t > 0$. The problem reduces therefore to

$$\left[2\theta^2\left(x^2 + z^2\right) - 7\right]xz = 0\ , \quad \text{(B.23)}$$

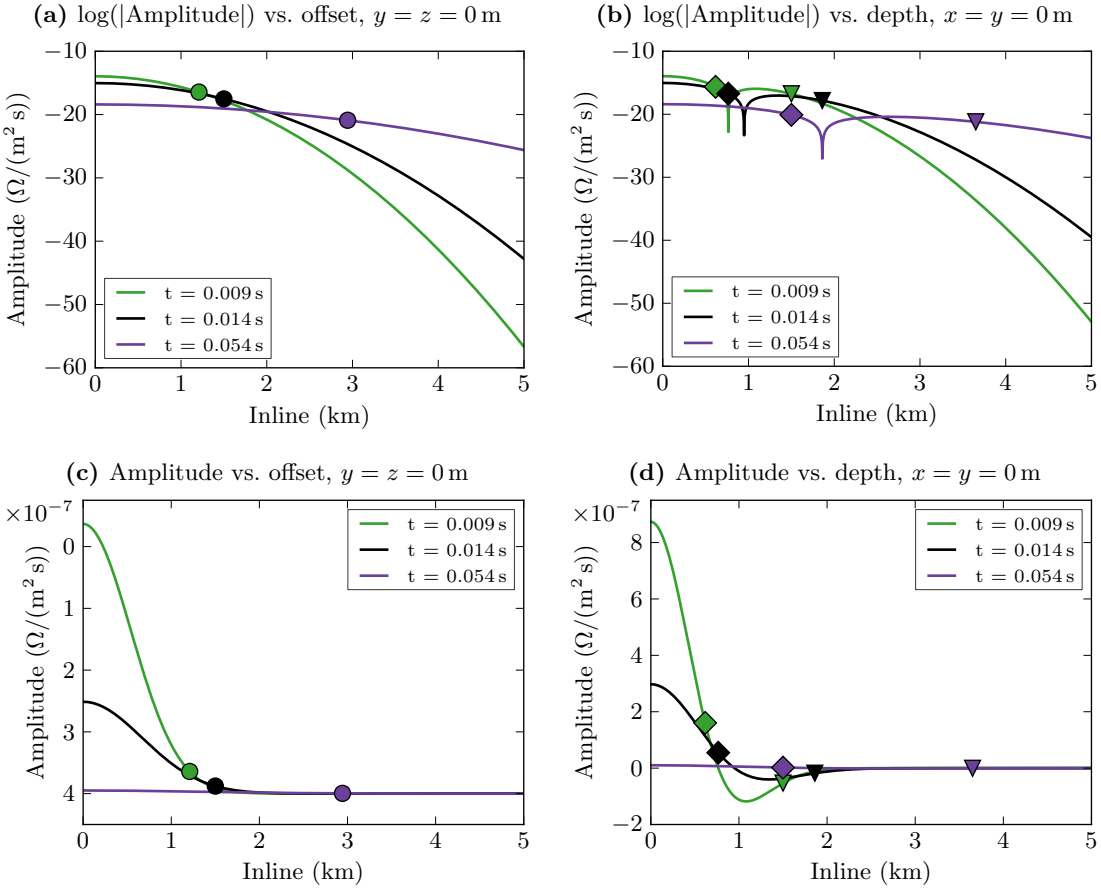


**Figure B.3:** Amplitude versus offset (left column) and versus depth (right column); on the top row with a logarithmic scale for the amplitude. The symbols correspond to the ones in Figure B.1.

with the solution

$$t_{\mathrm{p}}^{\mathrm{z}} = \frac{\mu_0 \left(x^2 + z^2\right)}{14\rho} \approx 0.71 \frac{\mu_0 \left(x^2 + z^2\right)}{10\rho} \ , \quad \text{with} \quad x, z \neq 0 \ , \tag{B.24}$$

where $t_{\mathrm{p}}^{\mathrm{z}}$ denotes the time of the peak for the $\mathcal{G}_{\mathrm{z}}^{\mathrm{I}}$-field. Equations B.24 shows that there is everywhere one extreme, except for $x = 0$ or $y = 0$, where the $\mathcal{G}_{\mathrm{z}}^{\mathrm{I}}$-field vanishes.

### Maximum or minimum

The second derivative of $\mathcal{G}_{\mathrm{z}}^{\mathrm{I}}$ with respect to time is given by

$$\begin{aligned}\frac{\partial^2 \mathcal{G}_{\mathrm{z}}^{\mathrm{I}}}{\partial t^2} &= \frac{\partial}{\partial t}\frac{\rho}{2\pi^{3/2}}\exp\left(-\theta^2 r^2\right)\left[\frac{2\theta^7 r^2}{t^2} - \frac{7\theta^5}{t^2}\right] xz \\ &= \underbrace{\frac{\rho\theta^5}{4\pi^{3/2}t^3}\exp\left(-\theta^2 r^2\right)}_{K_4}\left[4\theta^4\left(x^2+z^2\right)^2 - 36\theta^2\left(x^2+z^2\right) + 63\right] xz \ , \end{aligned} \tag{B.25}$$

where $K_4 > 0$ for all times $t > 0$. Inserting $t_{\mathrm{p}}^{\mathrm{z}}$, it follows that the extreme is a maximum in the quarters where $x$ and $z$ are either both positive or both negative, and a minimum in the other quarters,

$$\frac{\partial^2}{\partial t^2}\mathcal{G}_{\mathrm{z}}^{\mathrm{I}}(x,z,t_{\mathrm{p}}^{\mathrm{z}}) \approx -14K_4 xz \begin{cases} < 0 & \text{if} \quad xz > 0 \quad \rightarrow \quad \text{maximum} \ , \\ > 0 & \text{if} \quad xz < 0 \quad \rightarrow \quad \text{minimum} \ . \end{cases} \tag{B.26}$$

### Wavefront

The wave of the extreme is given by solving Equation B.24 for $x$,

$$|x| = \pm\sqrt{\frac{7}{2\theta^2} - z^2} \ , \quad \text{with} \quad x, z \neq 0 \ , \tag{B.27}$$

which has real values within the limits

$$0 \ < \ |z| \ \leq \sqrt{\frac{7}{2\theta^2} - x^2} \ . \tag{B.28}$$

The upper limit follows from Equation B.24, and the lower limit from Equation B.27.

### Figure for extrema of z-component in the x-z-plane

Figure B.4 shows in (a) and (b) the analogue to Figure B.1, in (c) the analogue to Figure B.2, and in (d) the analogue to Figure B.3 for the z-component in the x-z-plane. It can be seen in (b) that the z-component is symmetric about the origin, and the absolute value of the extreme (wavefront) is circular around the origin.

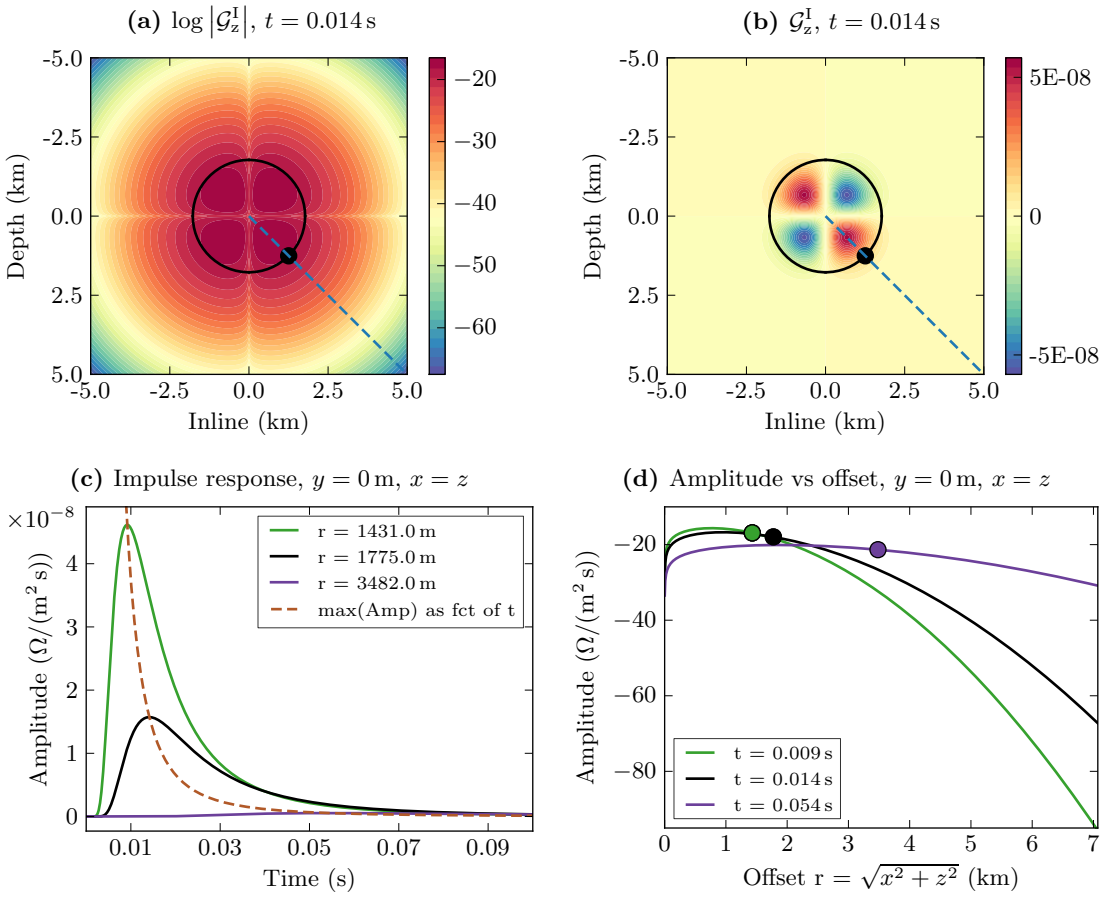


**Figure B.4:** (b) $\mathcal{G}_z^I$-field ($\Omega/(m^2\,s)$) in the x-z-plane in (a) on a logarithmic scale, and in (b) on a linear scale, for time $t = 0.014\,s$. Impulse responses and amplitude versus offset are shown in (c) and (d), respectively. The plotted times and the colours correspond to the ones in Figures B.2, B.1 (c) and (d), and B.3. The dashed line in (a) and (b) indicates the x-axis of (d).

## B.5 Extrema of the total field in the x-z-plane

The following figures show the relation between the extrema of $\mathcal{G}_x^I$ and $\mathcal{G}_z^I$ compared with the amplitude of the total field in the x-z-plane. Note that the amplitude of $\mathcal{G}^I$ is defined as $|\mathcal{G}^I| = \mathcal{G}^I = \sqrt{\mathcal{G}_x^{I\,2} + \mathcal{G}_z^{I\,2}}$, and has therefore only positive values, in contrary to $\mathcal{G}_x^I$ and $\mathcal{G}_z^I$.

The total field in the x-z-plane is shown in Figure B.5 and can be compared to the corresponding fields of $\mathcal{G}_x^I$ in Figures B.1 (c) and (d) and $\mathcal{G}_z^I$ in Figures B.4 (a) and (b). The waves of the maxima are indicated by the green ($t_{p-}^x$), orange ($t_p^z$), and blue ($t_{p+}^x$) lines. The figure shows the order of arrival of the maxima at a specific location: the extreme of $t_{p-}^x$ arrives first, followed by $t_p^z$, and finally $t_{p+}^x$. However, a prediction

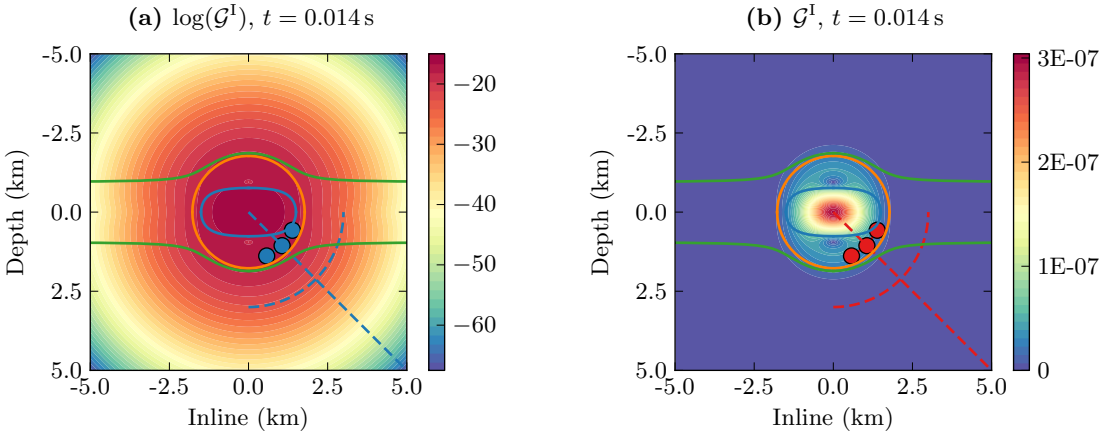


**Figure B.5:** $\mathcal{G}^{\mathrm{I}}$-field ($\Omega/(\mathrm{m}^2\,\mathrm{s})$) in the x-z-plane in (a) on a logarithmic scale, and in (b) on a linear scale, for time $t = 0.014\,\mathrm{s}$. The lines are: $t^{\mathrm{x}}_{\mathrm{p}-}$ (green), $t^{\mathrm{z}}_{\mathrm{p}}$ (orange) and $t^{\mathrm{x}}_{\mathrm{p}+}$ (blue). The dashed curved line outlines the x-axis of Figure B.6, the little circles are the locations of Figures B.7 (a) and (c), and the dashed straight line outlines the x-axis of Figure B.7d.

of the maxima of the total field is not possible. (The dashed lines and the little circles indicate locations of the following figures.)

Figure B.6 shows the maxima of $\mathcal{G}^{\mathrm{I}}_{\mathrm{x}}$ and $\mathcal{G}^{\mathrm{I}}_{\mathrm{z}}$ as a function of angle for constant radius $r = 3\,\mathrm{km}$, indicated by the curved dashed line in Figure B.5 (where $\varphi = 0$ is the positive x-axis, and $\varphi = \pi/2$ is the positive z-axis). The red line is the maxima of the total field. It shows not surprisingly that close to the z-axis $t^{\mathrm{x}}_{\mathrm{p}-}$ is the dominant peak, where close to the x-axis $t^{\mathrm{x}}_{\mathrm{p}+}$ is dominant. At around $\varphi = \sqrt{2}\pi/8$ the dominant peak is $t^{\mathrm{z}}_{\mathrm{p}}$, and everywhere in-between it is a combination of both, amplitudes as well as arrival times. (Note that this figure provides no information about arrival times.)

Inserting Equation B.24 into Equation B.8 for $\mathcal{G}^{\mathrm{I}}_{\mathrm{z}}$ yields the analytical solution for the maximum of $t^{\mathrm{z}}_{\mathrm{p}}$ as a function of radius and angle,

$$\max\left|\mathcal{G}^{\mathrm{I}}_{\mathrm{z}}(r,\varphi)\right| = \frac{\rho^2}{\pi^{3/2}\mu_0}\frac{343\sqrt{14}}{8}\frac{\sin(2\varphi)}{r^5}\exp(-7/2)\ , \tag{B.29}$$

which is the orange line in Figure B.6. Note that the shape is not changing with changing radius, only the amplitude decreases by a factor $1/r^5$. The equivalent for $\mathcal{G}^{\mathrm{I}}_{\mathrm{x}}$ results not in such a nice analytical formula, and is calculated numerically.

Figures B.7 (a) and (c) finally show the impulse responses for $\mathcal{G}^{\mathrm{I}}_{\mathrm{x}}$, $\mathcal{G}^{\mathrm{I}}_{\mathrm{z}}$, and $\mathcal{G}^{\mathrm{I}}$ for three different locations with radius $r = 1.5\,\mathrm{km}$, and angles $\varphi = \pi/8, \pi/4, 3\pi/8$ (the locations are marked by the little circles in Figure B.5). The equivalent figures for angles $\varphi = 0$, $\pi/2$ are shown in Figure B.2, as the z-component vanishes for $x = 0$ and $z = 0$. Figure B.7d plots radius versus amplitude for $\varphi = \pi/4$ at time $t = 0.014\,\mathrm{s}$. Note that

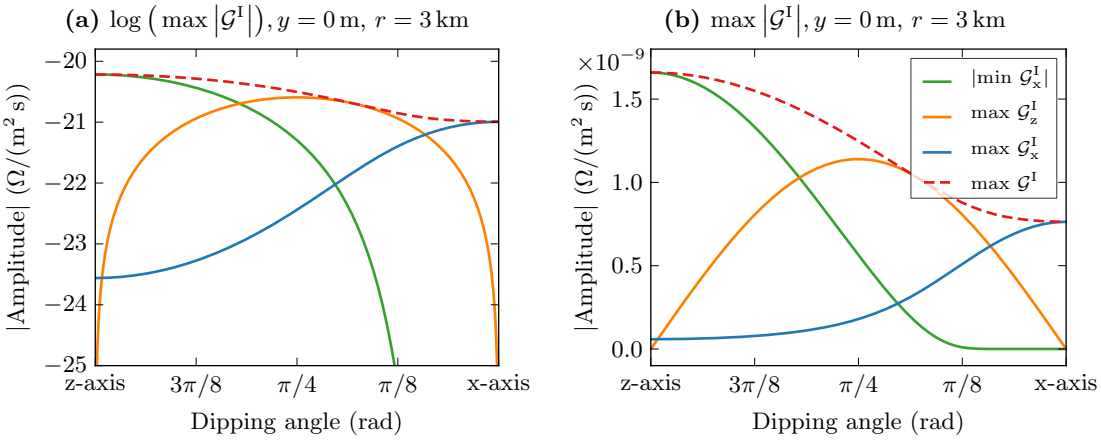


**Figure B.6:** Maxima of $\mathcal{G}^{\mathrm{I}}$, $|\mathcal{G}^{\mathrm{I}}_{\mathrm{x}}|$, and $\mathcal{G}^{\mathrm{I}}_{\mathrm{z}}$ ($\Omega/(\mathrm{m}^2\,\mathrm{s})$) as a function of dipping angle (rad) for constant radius $r = 3\,\mathrm{km}$ in the x-z-plane; absolute values in (b) and logarithmic values in (a). The x-axis is indicated in Figure B.5 by the dashed curved line. The figure provides no indication about the arrival times of these extrema.

the orange lines in Figures B.7 (b) and (d) are the same as the black lines in Figures B.4 (c) and (d), respectively.

## B.6 Final comments

The extrema analysis within this document is limited to the x-z-plane. However, Equation B.8 shows that $\mathcal{G}^{\mathrm{I}}$ is symmetric around the x-axis. This implies that $\mathcal{G}^{\mathrm{I}}_{\mathrm{x}}$ remains unchanged if one keeps the diameter $\eta = \sqrt{y^2 + z^2}$ constant for a given $x$. Hence $z$ can be replaced by $\eta = \sqrt{y^2 + z^2}$ in all derivations for $\mathcal{G}^{\mathrm{I}}_{\mathrm{x}}$. As an example, Equation B.14 becomes

$$t_{\mathrm{p}}^{\mathrm{xz}} = \frac{\left(9 \pm \sqrt{41}\right) \mu_0 z^2}{40\rho} \quad \Longrightarrow \quad t_{\mathrm{p}}^{\mathrm{x}\eta} = \frac{\left(9 \pm \sqrt{41}\right) \mu_0 \sqrt{y^2 + z^2}}{40\rho}\,, \tag{B.30}$$

which denotes the arrival times of the minimum and maximum waves of $\mathcal{G}^{\mathrm{I}}_{\mathrm{x}}$ anywhere in the y-z-plane ($x = 0$).

Similarly $\mathcal{G}^{\mathrm{I}}_{\mathrm{z}} = \mathcal{G}^{\mathrm{I}}_{\mathrm{y}} = \mathcal{G}^{\mathrm{I}}_{\eta}$ for, again, $\eta = \sqrt{z^2 + y^2}$ = constant, and $z$ can be replaced by $y$ or $\eta$ in all the derivations for $\mathcal{G}^{\mathrm{I}}_{\mathrm{z}}$. The solutions for the x-z-plane provide therefore the solutions for the extrema in the entire full-space.

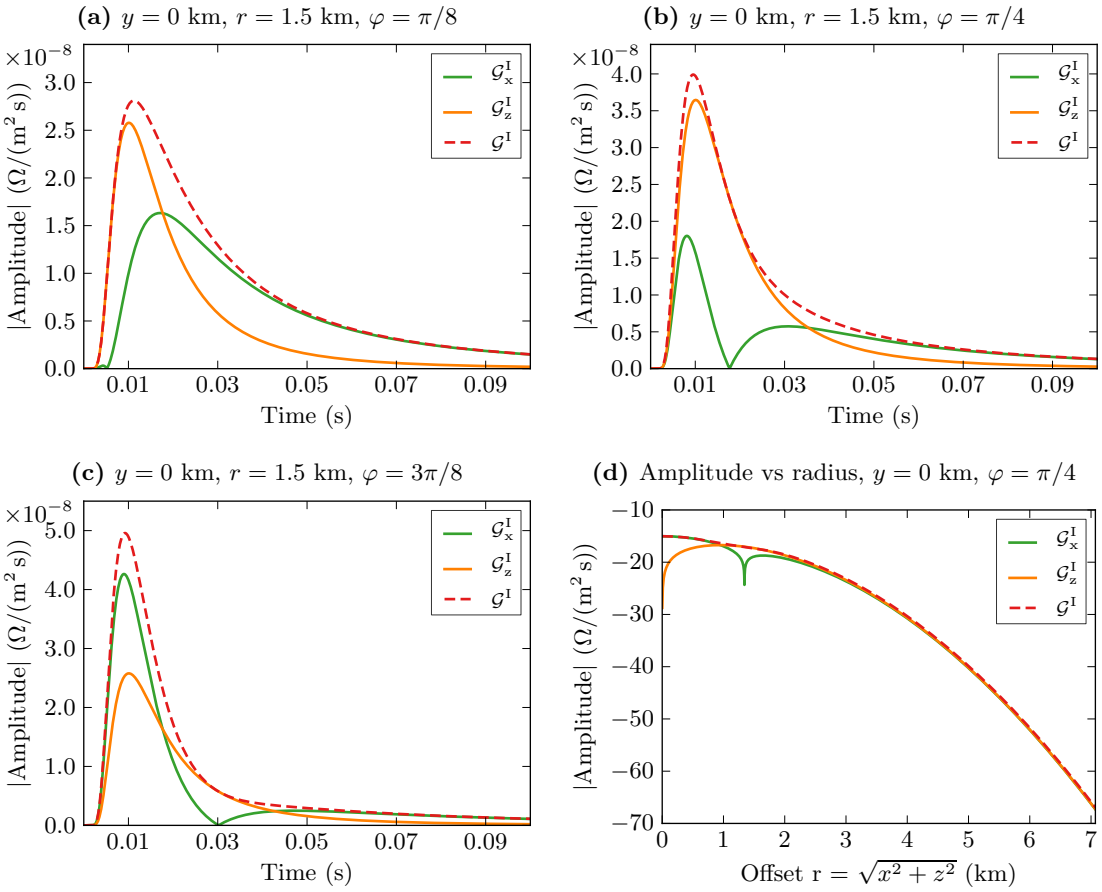


**Figure B.7:** (a), (b), and (c) show the impulse responses at locations $r = 1.5\,\mathrm{km}$ and $\varphi = \pi/8, \pi/4, 3\pi/8$, indicated by the little circles in Figure B.5. (d) amplitude versus offset for $\varphi = \pi/2$ at time $t = 0.014\,\mathrm{s}$, indicated by the dashed straight line in Figure B.5.

## Summary

The idea behind this extrema analysis is to draw an analogy to seismic ray tracing for MTEM impulse responses. In this full-space study, I derived the arrival times and the locations of the extrema, so it should be possible to calculate the velocity of these extrema waves as a function of space. But everything in this chapter is done in full-space. The question is what would happen if we try to calculate it for a half-space below air, and then for a multi-layer case? Are analytical solutions possible (unlikely) or does it have to be calculated numerically (likely)? If it can be done for a multi-layer case, then one could start with simple MTEM tomography. It remains an interesting research topic.

■

# C

# Reproducibility, data, and software

**Beware of bugs in the above code;**
**I have only proved it correct, not tried it.**

*Donald Ervin Knuth (1938–)*
*Computer Scientist*

---

Research has to be reproducible, otherwise it looses its credibility. I tried my best to make my results easily reproducible by using wherever possible open-source software and documenting my code extensively. Every result and every figure of my thesis can be reproduced with the provided codes. However, there are proprietary parts, both in software and in data. In this appendix I describe briefly my code, the data, and the software I used, point out the proprietary parts, and list alternatives.

---

## C.1 Reproducibility (enclosed CD-ROM)

"Reproducible research" is a term often attributed to Jon Claerbout, a professor in geophysics at Stanford University. His ideas are neatly summarised by Buckheit and Donoho (1995): *An article about computational science in a scientific publication is* not *the scholarship itself, it is merely* advertising *of the scholarship. The actual scholarship is the complete software development environment and the complete set of instructions which generated the figures.* The Journal *Computing in Science & Engineering* dedicated its first issue in 2009 to the topic of reproducible research, and its guest editor's introduction by Fomel and Claerbout (2009) is well worth reading.

This entire thesis is reproducible; the results, the figures, and the thesis itself (assuming the proprietary parts outlined below are at hand). Provided with this thesis is a CD-ROM, containing the `LaTeX` source files, the `Python` scripts, and an extensive manual for these scripts; the content of the CD-ROM is outlined in Figure C.1. The directory `data/` contains all non-proprietary data used for the thesis. The `LaTeX` source files are in the directory `Thesis/`, and all `Python` scripts are in `Python/`. In the top directory are three files (respectively soft-links to the corresponding files): `jsempy.html` and `jsempy.pdf` are the manual for the `Python` scripts as a `html` and a `pdf` version, respectively. And `Thesis.pdf` is this thesis as a `pdf`. The `pdf` version of the manual is good if you have to print out parts of it. However, the power comes with the `html` version of the manual. It has a very useful search facility, and most of all, you can switch between the documentation and the source code.

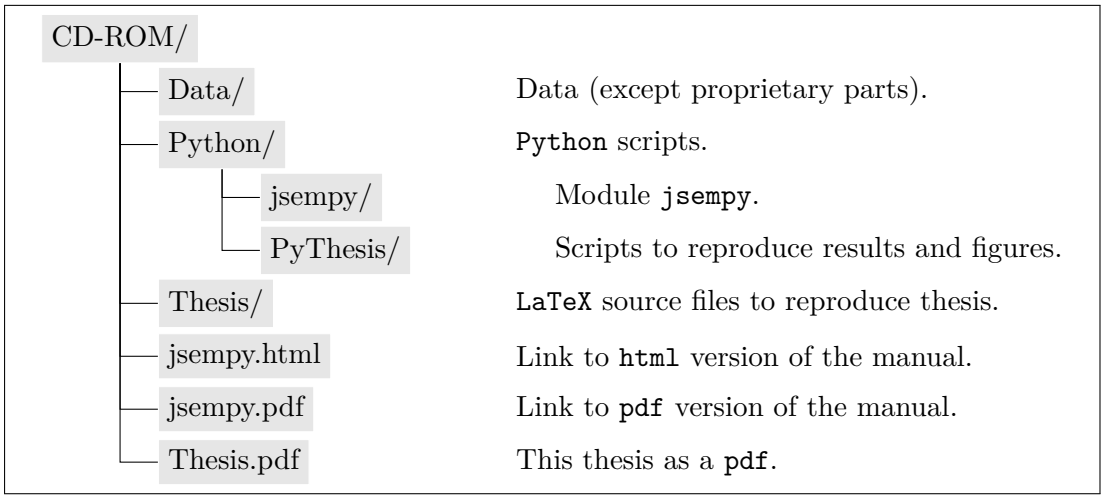


**Figure C.1:** Content of the accompanying CD-ROM. The CD-ROM contains everything to reproduce this entire thesis, apart from proprietary software and data.

To reproduce this thesis, just run `pdfTeX` and `BibTeX` within `Thesis`, several times if necessary.

The `Python` folder contains two subdirectories. The first is `jsempy`, which is a `Python` module which name I coined as an abbreviation for "Joint Seismic and EM PYthon module". It is extensively described in the provided manual. The module contains various subroutines: `jsempy.data` for data handling (seismic data, well logs, multi-transient electromagnetic (MTEM) data), `jsempy.modinv` for input file creation and output file handling of (iterative) forward modelling of MTEM data, `jsempy.rock` for rock physics and uncertainty calculations, and `jsempy.utils` for general utilities (signal processing, plotting routines, unit conversions). The manual for the `Python` module `jsempy` and the thesis scripts is itself data driven; it is mainly extracted from the comments of the source code using the "Python Documentation Generator" `Sphinx`. The necessary files for this are provided in `Python/jsempy/manual`. Running `make html` or `make latexpdf` in this directory will reproduce the provided manual. The documentation is extracted from the source code, which also means that you can access all documentation with your `Python` environment in the usual way, without the need of the manual.

The folder `Python/jsempy` has to be in a folder that is in your `Python PATH`, in order to use the scripts provided in `Python/PyThesis`. The folder `PyThesis` contains a sub-folder for each chapter of the thesis, and within these sub-folders are the scripts used to calculate the results and the figures. All figures are produced with `Python`, except for Figure C.1, which is produced directly by `LaTeX`. The figures are data driven; running `create_all_thesis_figures.py` in `Python/PyThesis` reproduces all figures in one go (takes less than 8 minutes on my laptop).

## C.2 Data

### Freely accessible data

The data from the U.S. exploration drilling success rates in Figure 1.1 are available at the U.S. Energy Information Administration, `http://www.eia.gov/dnav/pet/pet_crd_wellend_s1_m.htm`.

The topography data of Figure 4.1 are downloaded from the National Geophysical Data Center (`http://www.ngdc.noaa.gov`). The corresponding median line is available from the UK Department of Energy & Climate Change at `https://www.gov.uk/oil-and-gas-offshore-maps-and-gis-shapefiles`.

### Proprietary data

PGS provided the MTEM data for the Harding field.

BP provided the seismic velocity model, the seismic horizons, the well logs, the reservoir model, and also the water-oil contact shown in Figure 5.5 (all for the Harding field).

### Alternatives

The Netherlands, amongst other countries, do a good job in making exploration data openly and freely available, see `http://www.nlog.nl`. Well data and seismic surveys can be downloaded, amongst a lot of other useful information regarding the Dutch sector of the North Sea.

The open-source seismic interpretation system `OpendTect` (`http://www.opendtect.org`) is maintaining and actively expanding an *Open Seismic Repository* (`https://www.opendtect.org/osr`). The repository has, as of now, 2D and 3D seismic data, both pre- and poststack, and also well logs, seismic horizons and acoustic impedance data.

The Institute for Geophysics at University of Texas hosts an *Academic Seismic Portal* at `http://www.ig.utexas.edu/sdc`. The US National Geophysical Data Center also hosts some data, `http://www.ngdc.noaa.gov`. The Society of Exploration Geophysicists (SEG) hosts also a database of openly available seismic (and other) data, see `http://wiki.seg.org/index.php/Open_data`.

I am not aware of any MTEM data being openly available.

## C.3 Software

### Open-source software

I briefly list the used software and the latest version I used to generate the thesis. The operating system is Ubuntu 12.04 64-bit. The LaTeX version used to generate the thesis is pdfTeX and BibTeX from the TeX Live 2009 distribution. Furthermore, I used `Python` 2.7.3, and did most of my hacking in the excellent `IPython` environment (Pérez and Granger, 2007, `http://ipython.org`), version 0.13.2, with `SciPy` 0.9.0 (Jones et al., 2001, `http://www.scipy.org`) that comes with `matplotlib` 1.1.1rc (Hunter, 2007, `http://matplotlib.org`), and `NumPy` 1.6.1.

#### PyMC (Version 2.1alpha)

The uncertainty analysis was calculated using the PyMC module in Python, see Patil et al. (2010). PyMC is an open-source project under an Academic Free License with almost 10 years of development; the aim of the authors is to make Markov chain Monte Carlo (MCMC) "more accessible to non-statisticians". The source code can be found on github, https://github.com/pymc-devs/pymc, along with extensive documentation, in addition to the afore-referenced paper. I calculated 10 000 samples, without burn-in or thinning, for the simple example in Chapter 3, and 50 000 samples without burn-in and a thinning factor of 25 for the calculations in Chapter 5. The probability density functions shown were then estimated with a Gaussian kernel density estimation (KDE), see Appendix A.

By default, PyMC uses the Metropolis-Hastings algorithm. This can lead to a lot of rejections if sampling is in higher dimensions. To get better results, I used the thinning factor of 25 in the complex example. However, this takes 25 times longer to get the same amount of samples.

*Probabilistic Programming & Bayesian Methods for Hackers* is a book written by Davidson-Pilon (2013), using PyMC. It is written entirely as an IPython notebook, an interactive, web-based Python environment. This means that the whole book as such can be run and edited online or locally, to test and experiment with the code, which I highly recommend.

### Proprietary software

#### EX1D (Version EX1DV1.2a)

The 1D MTEM forward modelling code EX1D is proprietary software of PGS, written in Fortran 90. It is a front end for the 1D time-domain forward modeller MTEM1D, which is based upon code from R. N. Edwards, see Edwards (1997) (but also Edwards and Chave, 1986; Cheesman et al., 1987; Chave and Cox, 1982). This specific version of EX1D was developed to study the effects of anisotropy, see Werthmüller (2009).

#### MTEM1D_INV (Version MTEM1DINV_2_2_2a)

The MTEM inversion code MTEM1D_INV is proprietary software of PGS, written in Fortran 90. It is an Occam inversion (Constable et al., 1987) using EX1D as a forward modeller.

The inversion minimises the normalised misfit

$$\eta^2 = \frac{1}{N}\sum_{t=1}^{N}\left[\frac{x_t - \Xi_t(p)}{\epsilon_t}\right]^2 , \tag{C.1}$$

where $t$ is the time step, ranging from 1 to $N$, $x$ is the measured amplitude, $\Xi$ is the forward model of model $p$, and $\epsilon$ the error. This specific version of `MTEM1D_INV` was developed to study the effects of anisotropy, see Werthmüller (2009). The used stopping criteria in this thesis are either a misfit below $\eta^2 < 0.6$, or maximum of 15 iterations, or the misfit flattens out.

#### `PIE3D (VERSION 2012)`

The 3D electromagnetic (EM) forward modelling code `PIE3D` is proprietary software of the Consortium for Electromagnetic Modeling and Inversion (CEMI, University of Utah, Michael Zhdanov, `http://www.cemi.utah.edu`), licensed to PGS. `PIE3D` is a 3D frequency-domain parallel EM forward modeller, based on the method of integral equations (Hursán and Zhdanov, 2002; Zhdanov et al., 2006; Endo et al., 2008). It allows to model a 3D anomaly within a 1D background structure. It is written in `C`, `C++`, `Fortran`, and `MATLAB`. I used the code at the PGS office in Edinburgh, on a workstation running CentOS 5.8, with 12 CPUs and 15 GB of RAM (I run the code only on 10 CPUs).

`PIE3D` running time with regard to the models in Chapter 7: For 21 source-receiver pairs it took $100 - 120$ hours. However, performance is better if calculations are done with source gathers. Calculating 76 responses from seven sources took $40 - 47$ hours, 161 responses from 14 sources $64 - 79$ hours.

A note regarding the choice of 3D forward modeller: The PGS internal 3D EM forward modelling code is `PEMrad`, which is also based on the method of integral equations. However, as of now `PEMrad` is not able to calculate the low frequencies required to calculate time responses using `FFTLog`. I therefore used `PIE3D` for all my 3D calculations.

### Alternatives

The Scripps Marine EM Laboratory has 1D controlled-source electromagnetic (CSEM) forward modelling and inversion codes online, `http://marineemlab.ucsd.edu/`. Another 1D CSEM code is `DeliveryCSEM` by Gunning et al. (2010).

R. Nigel Edwards used to release his software to colleagues (according to http://www.physics.utoronto.ca/~edwards/). His colleagues at University of Toronto might continue to do so.

*OpenEM.org* promotes open source, open data, and open exchange in electromagnetic geophysics (http://www.openem.org). They have, amongst others, a software repository and a data repository. The platform is, however, stronger in the field of mining than in the field of hydrocarbon exploration.

I am not aware of any open or free CSEM modelling and inversion code in 2D or 3D. I personally think this is a disadvantage for the growth of CSEM. Open-source CSEM modelling tool would simplify and possibly increase academic research in the field, as students could easily get the code. The seismic community is much more advanced in this respect, for instance `Madagascar` (http://www.reproducibility.org) and `OpendTect` (http://www.opendtect.org). Much the same applies to the availability of CSEM data.

Lists and links to geophysical open-source software can be found on Wikipedia (http://en.wikipedia.org/wiki/List_of_free_geophysics_software) and also on the website of the SEG (http://software.seg.org/).

■

# References


Abubakar, A., G. Gao, T. M. Habashy, and J. Liu, 2012, Joint inversion approaches for geophysical electromagnetic and elastic full-waveform data: Inverse Problems, **28**, 055016; doi: 10.1088/0266-5611/28/5/055016. 149

Archie, G. E., 1942, The electrical resistivity log as an aid in determining some reservoir characteristics: Trans. AIME, 54–62; doi: 10.2118/942054-G. 54, 126

Bannister, P., 1968, Determination of the electrical conductivity of the sea bed in shallow waters: Geophysics, **33**, 995–1003; doi: 10.1190/1.1439993. 28

Bayes, T., and R. Price, 1763, An essay towards solving a problem in the doctrine of chances: Philosophical Transactions of the Royal Society of London, **53**, 370–418; doi: 10.1098/rstl.1763.0053. 57

Beckly, A. J., T. Nash, R. Pollard, C. Bruce, P. Freeman, and G. Page, 2003, The Harding Field, Block 9/23b, *in* United Kingdom oil and gas fields commemorative millennium volume: Geological Society Publishing House, Bath, volume **20** *of* Memoirs of the Geological Society of London, 283–290; ISBN: 1-86239-089-4. 66, 83, 92

Berryman, J. G., 1995, Mixture theory for rock properties, *in* Rock Physics & Phase Relations: A Handbook of Physical Constants: AGU, **3**, 205–228; doi: 10.1029/RF003. 51, 53, 54, 84

Bhattacharya, R. K., and H. P. Patra, 1968, Direct Current Electric Sounding: Elsevier Publishing Company, volume **9** *of* Methods in Geochemistry and Geophysics; ISBN: 978-0444569783. 103

Bolthausen, E., and M. V. Wüthrich, 2013, Bernoulli's law of large numbers: ASTIN Bulletin, **43**, no. 02, 73–79; doi: 10.1017/asb.2013.11. 59

BP, 2003, The Harding Field: BP Exploration, The UK Upstream Asset Portfolio; http://www.bp.com/liveassets/bp_internet/globalbp/STAGING/global_assets/downloads/U/uk_asset_harding.pdf, accessed 11 July 2013. 65

———, 2012, BP to sell package of Central North Sea assets to TAQA: http://www.bp.com/en/global/corporate/press/press-releases/bp-to-sell-package-of-central-north-sea-assets-to-taqa-for-1.1-billion.html, accessed 11 July 2013. 65

Brevik, I., P. T. Gabrielsen, and J. P. Morten, 2009, The role of EM rock physics and seismic data in integrated 3D CSEM data analysis: SEG Technical Program Expanded Abstracts, **28**, 835–839; doi: 10.1190/1.3255881. 44

Brown, V., K. Key, and S. Singh, 2012, Seismically regularized controlled-source electromagnetic inversion: Geophysics, **77**, E57–E65; doi: 10.1190/geo2011-0081.1. 149

Bruggeman, D. A. G., 1935, Berechnung verschiedener physikalischer Konstanten von heterogenen Substanzen. I. Dielektrizitätskonstanten und Leitfähigkeiten der Mischkörper aus isotropen Substanzen: Annalen der Physik, **416**, 636–664; doi: 10.1002/andp.19354160705. 86

Buckheit, J. B., and D. L. Donoho, 1995, Wavelab and reproducible research, *in* Wavelets and Statistics: Springer New York, volume **103** *of* Lecture Notes in Statistics, 55–81; doi: 10.1007/978-1-4612-2544-7_5. 178

Bussian, A. E., 1983, Electrical conductance in a porous medium: Geophysics, **48**, 1258–1268; doi: 10.1190/1.1441549. 87

Carcione, J. M., B. Ursin, and J. I. Nordskag, 2007, Cross-property relations between electrical conductivity and the seismic velocity of rocks: Geophysics, **72**, E193–E204; doi:

10.1190/1.2762224. 31, 48, 50, 51, 82, 83, 84, 85, 86

Castagna, J. P., M. L. Batzle, and R. L. Eastwood, 1985, Relationships between compressional-wave and shear-wave velocities in clastic silicate rocks: Geophysics, **50**, 571–581; doi: 10.1190/1.1441933. 52

Červený, V., 2001, Seismic ray theory: Cambridge University Press Cambridge; doi: 10.1017/CBO9780511529399. 164

Červený, V., J. Langer, and I. Pšenčík, 1974, Computation of geometric spreading of seismic body waves in laterally inhomogeneous media with curved interfaces: Geophysical Journal of the Royal Astronomical Society, **38**, 9–19; doi: 10.1111/j.1365-246X.1974.tb04105.x. 164

Chave, A. D., S. C. Constable, and R. N. Edwards, 1991, Electrical exploration methods for the seafloor, In Nabighian (1991), chapter 12, 931–966; doi: 10.1190/1.9781560802686. 28

Chave, A. D., and C. S. Cox, 1982, Controlled electromagnetic sources for measuring electrical conductivity beneath the oceans: 1. forward problem and model study: Journal of Geophysical Research, **87**, 5327–5338; doi: 10.1029/JB087iB07p05327. 28, 181

Cheesman, S., R. Edwards, and A. Chave, 1987, On the theory of sea-floor conductivity mapping using transient electromagnetic systems: Geophysics, **52**, 204–217; doi:10.1190/1.1442296 . 29, 181

Chemali, R., S. Gianzero, R. W. Strickland, and S. M. Tijani, 1983, The shoulder bed effect on the dual laterolog and its variation with the resistivity of the borehole fluid: SPWLA 24th Annual Logging Symposium; `http://www.onepetro.org/mslib/app/Preview.do?paperNumber=SPWLA-1983-UU&societyCode=SPWLA`. 32, 73

Chen, J., and T. A. Dickens, 2009, Effects of uncertainty in rock-physics models on reservoir parameter estimation using seismic amplitude variation with angle and controlled-source electromagnetics data: Geophysical Prospecting, **57**, 61–74; doi: 10.1111/j.1365-2478.2008.00721.x. 31, 32, 43, 58, 60, 83, 91

Chen, J., and G. M. Hoversten, 2012, Joint inversion of marine seismic AVA and CSEM data using statistical rock-physics models and Markov random fields: Geophysics, **77**, R65–R80; doi: 10.1190/geo2011-0219.1. 149

Chen, J., G. M. Hoversten, D. Vasco, Y. Rubin, and Z. Hou, 2007, A Bayesian model for gas saturation estimation using marine seismic AVA and CSEM data: Geophysics, **72**, WA85–WA95; doi: 10.1190/1.2435082. 43

Christian, R. P., N. Chopin, and J. Rousseau, 2009, Harold Jeffreys's theory of probability revisited: Statistical Science, **24**, 141–172; doi: 10.1214/09-STS284. 58

Clavier, C., G. Coates, and J. Dumanoir, 1984, Theoretical and experimental bases for the dual-water model for interpretation of shaly sands: Journal of Petroleum Technology, **24**, 153–168; doi: 10.2118/6859-PA. 83, 89

Constable, S., 2010, Ten years of marine CSEM for hydrocarbon exploration: Geophysics, **75**, 75A67–75A81; doi: 10.1190/1.3483451. 29

Constable, S., and L. J. Srnka, 2007, An introduction to marine controlled-source electromagnetic methods for hydrocarbon exploration: Geophysics, **72**, WA3–WA12; doi: 10.1190/1.2432483. 29, 83

Constable, S. C., R. L. Parker, and C. G. Constable, 1987, Occam's inversion: A practical algorithm for generating smooth models from electromagnetic sounding data: Geophysics, **52**, 289–300; doi: 10.1190/1.1442303. 82, 181

Cox, C. S., S. C. Constable, A. D. Chave, and S. C. Webb, 1986, Controlled-source electromagnetic sounding of the oceanic lithosphere: Nature, **320**, 52–54; doi: 10.1038/320052a0. 29

Davidson-Pilon, C., 2013, Probabilistic Programming & Bayesian Methods for Hackers: Online; `https://github.com/CamDavidsonPilon/Probabilistic-Programming-and-Bayesian-Methods-for-Hackers`. 181

Dell'Aversana, P., G. Bernasconi, F. Miotti, and D. Rovetta, 2011, Joint inversion of rock properties from sonic, resistivity and density well-log measurements: Geophysical Prospecting, **59**, 1144–1154; doi: 10.1111/j.1365-2478.2011.00996.x. 149

Dewan, J. T., 1983, Essentials of modern openhole log interpretation: Pennwell Corp; ISBN: 978-0878142330. 89

Duncan, P., A. Hwang, R. Edwards, R. Bailey, and G. Garland, 1980, The development and applications of a wide band electro-

magnetic sounding system using a pseudo-noise source: Geophysics, **45**, 1276–1296; doi: 10.1190/1.1441124. 28

Eaton, B. A., 1975, The equation for geopressure prediction from well logs: SPE of AIME Technical Program Expanded Abstracts, SPE 5544; doi: 10.2118/5544-MS. 90

Edwards, R., 1997, On the resource evaluation of marine gas hydrate deposits using sea-floor transient electric dipole-dipole methods: Geophysics, **62**, 63–74; doi: 10.1190/1.1444146. 181

Edwards, R., and A. Chave, 1986, A transient electric dipole-dipole method for mapping the conductivity of the sea floor: Geophysics, **51**, 984–987; doi: 10.1190/1.1442156. 29, 181

Edwards, R., D. Nobes, and E. Gómez-Treviño, 1984, Offshore electrical exploration of sedimentary basins: The effects of anisotropy in horizontally isotropic, layered media: Geophysics, **49**, 566–576; doi: 10.1190/1.1441691. 29, 103

Edwards, R. N., 2005, Marine controlled source electromagnetics: principles, methodologies, future commercial applications: Surveys in Geophysics, **26**, 675–700; doi: 10.1007/s10712-005-1830-3. 29

Eidesmo, T., S. Ellingsrud, L. M. MacGregor, S. Constable, M. C. Sinha, S. E. Johansen, F. N. Kong, and H. Westerdahl, 2013, Sea Bed Logging (SBL), a new method for remote and direct identification of hydrocarbon filled layers in deepwater areas: First Break, **20**, 144–152; doi: 10.1046/j.1365-2397.2002.00264.x. 29

Ellingsrud, S., T. Eidesmo, S. Johansen, M. Sinha, L. MacGregor, and S. Constable, 2002, Remote sensing of hydrocarbon layers by seabed logging (SBL): Results from a cruise offshore Angola: The Leading Edge, **21**, 972–982; doi: 10.1190/1.1518433. 29

Ellis, D. V., and J. M. Singer, 2007, Well Logging for Earth Scientists, 2 ed.: Springer; ISBN: 978-1-4020-3738-2. 74

Ellis, M., F. Ruiz, S. Nanduri, R. Keirstead, I. Azizov, M. Frenkel, and L. MacGregor, 2012, Importance of anisotropic rock physics modelling in integrated seismic and CSEM interpretation: First Break, **29**, 87–95; http://earthdoc.eage.org/detail.php?pubid=51279. 150

Ellis, M. H., M. C. Sinha, and R. Parr, 2009, Investigations into the discrepancies between electro-magnetic and borehole derived resistivities in overburden sediment: EAGE Technical Program Expanded Abstracts, X021; http://earthdoc.eage.org/detail.php?pubid=24181. 103, 117

Endo, M., M. Čuma, and M. S. Zhdanov, 2008, A multigrid integral equation method for large-scale models with inhomogeneous backgrounds: Journal of Geophysics and Engineering, **5**, 438; doi: 10.1088/1742-2132/5/4/007. 182

Engelmark, F., 2010, Velocity to resistivity transform via porosity: SEG Technical Program Expanded Abstracts, **29**, 2501–2505; doi: 10.1190/1.3513358. 31, 44, 53, 82, 83, 89, 95

Erratt, D., G. M. Thomas, N. R. Hartley, R. Musum, P. H. Nicholson, and Y. Spisto, 2010, North Sea hydrocarbon systems: some aspects of our evolving insights into a classic hydrocarbon province: Petroleum Geology Conference series, **7**, 27–56; doi: 10.1144/0070037. 66

Escalera Alcocer, J. A., M. V. García, H. S. Soto, D. Baltar, V. R. Paramo, P. T. Gabrielsen, and F. Roth, 2013, Reducing uncertainty by integrating 3D CSEM in the Mexican deep-water exploration workflow: First Break, **31**, 75–79; http://earthdoc.eage.org/detail.php?pubid=67468. 150

Evans, D., C. Graham, A. Armour, and P. Bathurst, eds., 2003, The Millennium Atlas: Petroleum Geology of the Central and Northern North Sea: Geological Society of London; ISBN: 978-1862391192. 66

Faust, L. Y., 1953, A velocity function including lithologic variation: Geophysics, **18**, 271–288; doi: 10.1190/1.1437869. 55

Fomel, S., and J. F. Claerbout, 2009, Guest Editor's Introduction: Reproducible Research: Computing in Science & Engineering, **11**, 5–7; doi: 10.1109/MCSE.2009.14. 33, 178

Gabrielsen, P. T., P. Abrahamson, M. Panzner, S. Fanavoll, and S. Ellingsrud, 2013, Exploring frontier areas using 2D seismic and 3D CSEM data, as exemplified by multi-client data over the Skrugard and Havis discoveries in the Barents Sea: First Break, **31**, 63–71; http://earthdoc.eage.org/detail.php?pubid=66023. 150

Gallardo, L. A., and M. A. Meju, 2007, Joint two-dimensional cross-gradient imaging of magnetotelluric and seismic traveltime data for structural and lithological classification: Geophysical Journal International, **169**, 1261–1272; doi: 10.1111/j.1365-246X.2007.03366.x. 31, 41, 82

Gao, G., A. Abubakar, and T. M. Habashy, 2012, Joint petrophysical inversion of electromagnetic and full-waveform seismic data: Geophysics, **77**, WA3–WA18; doi: 10.1190/geo2011-0157.1. 149

Gardner, G. H. F., L. W. Gardner, and A. R. Gregory, 1974, Formation velocity and density – the diagnostic basics for stratigraphic traps: Geophysics, **39**, 770–780; doi: 10.1190/1.1440465. 52

Gassmann, F., 1951, Über die Elastizität poröser Medien: Vier. der Natur. Gesellschaft Zürich, 1–23. 85

Glover, P. W. J., M. J. Hole, and J. Pous, 2000, A modified Archie's law for two conducting phases: Earth and Planetary Science Letters, **180**, 369–383; doi: 10.1016/S0012-821X(00)00168-0. 54

Griffiths, D. J., 1999, Introduction to electrodynamics, 3 ed.: Addison-Wesley; ISBN: 978-0139199608. 39

Gunning, J., M. E. Glinsky, and J. Hedditch, 2010, Resolution and uncertainty in 1D CSEM inversion: A Bayesian approach and open-source implementation: Geophysics, **75**, F151–F171; doi: 10.1190/1.3496902. 182

Hamilton, A. J. S., 2000, Uncorrelated modes of the non-linear power spectrum: Monthly Notices of the Royal Astronomical Society, **312**, 257–284; doi: 10.1046/j.1365-8711.2000.03071.x. 157

Han, D., A. Nur, and D. Morgan, 1986, Effects of porosity and clay content on wave velocities in sandstones: Geophysics, **51**, 2093–2107; doi: 10.1190/1.1442062. 52

Han, T., A. I. Best, L. M. MacGregor, J. Sothcott, and T. A. Minshull, 2011, Joint elastic-electrical effective medium models of reservoir sandstones: Geophysical Prospecting, **59**, 777–786; doi: 10.1111/j.1365-2478.2011.00956.x. 31, 150

Hanai, T., 1960, Theory of the dielectric dispersion due to the interfacial polarization and its application to emulsions: Colloid & Polymer Science, **171**, 23–31; doi: 10.1007/BF01520320. 86

Harris, P., Z. Du, L. MacGregor, W. Olsen, R. Shu, and R. Cooper, 2009, Joint interpretation of seismic and CSEM data using well log constraints: an example from the Luva Field: First Break, **27**, 73–81; http://earthdoc.eage.org/detail.php?pubid=28932. 44, 82

Hashin, Z., and S. Shtrikman, 1963, A variational approach to the theory of the elastic behaviour of multiphase materials: Journal of the Mechanics and Physics of Solids, **11**, 127–140; doi: 10.1016/0022-5096(63)90060-7. 53, 54

Hermance, J. F., 1979, The electrical conductivity of materials containing partial melt: A simple model from Archie's law: Geophysical Research Letters, **6**, 613–616; doi: 10.1029/GL006i007p00613. 54

Hobbs, B. A., and D. Werthmüller, 2010, Method for determining resistivity anisotropy from earth electromagnetic responses: US20100235100 A1, EP2230534 A1; http://www.google.com/patents/EP2230534A1. 110

———, 2011, Method for determining resistivity anisotropy from earth electromagnetic transient step response and electromagnetic transient peak impulse response: US20110012601 A1, EP2275838 A2; http://www.google.com/patents/EP2275838A2. 110

Hou, Z., Y. Rubin, G. M. Hoversten, D. Vasco, and J. Chen, 2006, Reservoir-parameter identification using minimum relative entropy-based Bayesian inversion of seismic AVA and marine CSEM data: Geophysics, **71**, O77–O88; doi: 10.1190/1.2348770. 43

Hoversten, G. M., F. Cassassuce, E. Gasperikova, G. A. Newman, J. Chen, Y. Rubin, Z. Hou, and D. Vasco, 2006, Direct reservoir parameter estimation using joint inversion of marine seismic AVA and CSEM data: Geophysics, **71**, C1–C13; doi: 10.1190/1.2194510. 31, 43

Hoversten, G. M., R. Gritto, J. Washbourne, and T. Daley, 2003, Pressure and fluid saturation prediction in a multicomponent reservoir using combined seismic and electromagnetic imaging: Geophysics, **68**, 1580–1591; doi: 10.1190/1.1620632. 45

Hu, W., A. Abubakar, and T. M. Habashy, 2009, Joint electromagnetic and seis-

mic inversion using structural constraints: Geophysics, **74**, R99–R109; doi: 10.1190/1.3246586. 31, 42, 82

Hunter, J. D., 2007, Matplotlib: A 2D graphics environment: Computing in Science & Engineering, **9**, 90–95; doi: 10.1109/MCSE.2007.55. 180

Hursán, G., and M. S. Zhdanov, 2002, Contraction integral equation method in three-dimensional electromagnetic modeling: Radio Science, **37**, 1–1–1–13; doi: 10.1029/2001RS002513. 125, 182

Issler, D. R., 1992, A new approach to shale compaction and stratigraphic restoration, Beaufort-Mackenzie Basin and Mackenzie Corridor, Northern Canada: American Association of Petroleum Geologists Bulletin, **76**, 1170–1189. 53

Jeffreys, H., 1983, Theory of probability, 3rd ed.: Oxford University Press; ISBN: 0-19-853193-1. 58

Jegen, M. D., R. W. Hobbs, P. Tarits, and A. Chave, 2009, Joint inversion of marine magnetotelluric and gravity data incorporating seismic constraints: preliminary results of sub-basalt imaging off the Faroe Shelf: Earth and Planetary Science Letters, 47–55; doi: 10.1016/j.epsl.2009.02.018. 41

Jones, E., T. Oliphant, P. Peterson, et al., 2001, SciPy: Open source scientific tools for Python; http://www.scipy.org/. 180

Kaufmann, A. A., and G. V. Keller, 1983, Frequency and transient soundings: Elsevier Publishing Company, volume **16** *of* Methods in Geochemistry and Geophysics; ISBN 978-0-444-42032-9. 108

Krief, M., J. Garat, J. Stellingwerff, and J. Ventre, 1990, A petrophysical interpretation using the velocities of P and S waves (full-waveform sonic): The Log Analyst, **31**, 355–369; `http://www.onepetro.org/mslib/app/Preview.do?paperNumber=SPWLA-1990-v31n6a2&societyCode=SPWLA`. 85

Kwon, M. J., and R. Snieder, 2011, Uncertainty analysis for the integration of seismic and controlled source electro-magnetic data: Geophysical Prospecting, **59**, 609–626; doi: 10.1111/j.1365-2478.2010.00937.x. 83, 91, 149

Laplace, P.-S., 1774, Mémoire sur la probabilité des causes par les événements: L'académie des sciences, volume **8** *of* Œuvres complètes de Laplace. 57

Lelièvre, P. G., C. G. Farquharson, and C. A. Hurich, 2012, Joint inversion of seismic traveltimes and gravity data on unstructured grids with application to mineral exploration: Geophysics, **77**, K1–K15; doi: 10.1190/geo2011-0154.1. 30

Lien, M., 2013, Simultaneous joint inversion of amplitude-versus-offset and controlled-source electromagnetic data by implicit representation of common parameter structure: Geophysics, **78**, ID15–ID27; doi: 10.1190/geo2012-0188.1. 149

Linfoot, J., B. Hobbs, G. Li, and C. Clarke, 2007, Treatment of "static shifts" in Multi-Transient ElectroMagnetic (MTEM) data: 544–548; doi: 10.1190/1.2792480. 37

Løseth, L., H. Pedersen, B. Ursin, L. Amundsen, and S. Ellingsrud, 2006, Low-frequency electromagnetic fields in applied geophysics: Waves or diffusion?: Geophysics, **71**, W29–W40; doi: 10.1190/1.2208275. 29, 40

MacGregor, L., 2012, Integrating seismic, CSEM, and well-log data for reservoir characterization: The Leading Edge, **31**, 268–277; `http://www.seg.org/documents/10161/5407316/3103_SA_MacGregor.pdf`. 148

MacGregor, L., S. Bouchrara, J. Tomlinson, U. Strecker, J. Fan, X. Ran, and G. Yu, 2012, Integrated analysis of CSEM, seismic and well log data for prospect appraisal: a case study from West Africa: First Break, **30**, 77–82; `http://earthdoc.eage.org/detail.php?pubid=57978`. 150

Maillet, R., 1947, The fundamental equations of electrical prospecting: Geophysics, **12**, 529–556; doi: 10.1190/1.1437342. 103

Mavko, G., T. Mukerji, and J. Dvorkin, 2009, The Rock Physics Handbook: Cambridge University Press Cambridge; ISBN: 978-0521861366. 52, 84

McGrayne, S. B., 2011, The theory that would not die: Yale University Press; ISBN: 978-0-300-16969-0. 57

Meju, M. A., L. A. Gallardo, and A. K. Mohamed, 2003, Evidence for correlation of electrical resistivity and seismic velocity in heterogeneous near-surface materials: Geophysical Research Letters, **30**, 26–1–26–4; doi: 10.1029/2002GL016048. 41

Moorkamp, M., B. Heincke, M. Jegen, A. W. Roberts, and R. W. Hobbs, 2011, A framework for 3-D joint inversion of MT, grav-

ity and seismic refraction data: Geophysical Journal International, **184**, 477–493; doi: 10.1111/j.1365-246X.2010.04856.x. 148

Nabighian, M., 1984, Foreword and introduction: Geophysics, **49**, 849–853; doi: 10.1190/1.1441730. 28

Nabighian, M. N., ed., 1988, Electromagnetic methods in applied geophysics vol. 1: SEG. Investigations in Geophysics, No. 3; doi: 10.1190/1.9781560802631. 28, 191

Nabighian, M. N., ed., 1991, Electromagnetic methods in applied geophysics vol. 2: SEG. Investigations in Geophysics, No. 3; doi: 10.1190/1.9781560802686. 28, 186

Negi, J. G., and P. D. Saraf, 1989, Anisotropy in Geoelectromagnetism: Elsevier Publishing Company, volume **28** *of* Methods in Geochemistry and Geophysics; ISBN: 978-0444874955. 103

Nekut, A. G., and B. R. Spies, 1989, Petroleum exploration using controlled-source electromagnetic methods: Proceedings of the IEEE, **77**, 338–362; doi: 10.1109/5.18630. 28

Newman, G. A., and M. Commer, 2010, Joint electromagnetic-seismic inverse modeling for matched data resolution: EGM 2010 International Workshop; http://earthdoc.eage.org/detail.php?pubid=41122. 45

Norman, T., H. Alnes, O. Christensen, J. J. Zach, O. Eien, and E. Tjåland, 2008, Planning time-lapse CSEM-surveys for joint seismic-EM monitoring of geological carbon dioxide injection: EAGE Technical Program Expanded Abstracts, A11; http://earthdoc.eage.org/detail.php?pubid=15269. 44

Olver, F. W. J., D. W. Lozier, R. F. Boisvert, and C. W. Clark, 2010a, NIST Digital Library of Mathematical Functions: http://dlmf.nist.gov/, Release 1.0.6 of 2013-05-06; Online companion to Olver et al. (2010b). 58, 190

———, 2010b, NIST Handbook of Mathematical Functions: Cambridge University Press; Print companion to Olver et al. (2010a), ISBN: 978-0521192255. 190

Oristaglio, M., and B. Spies, eds., 1999, Three-dimensional electromagnetics: SEG. Geophysical Developments, No. 7; doi: 10.1190/1.9781560802154. 30, 105

Parzen, E., 1962, On estimation of a probability density function and mode: The Annals of Mathematical Statistics, **3**, 1065–1076; doi: 10.1214/aoms/1177704472. 159

Patil, A., D. Huard, and C. J. Fonnesbeck, 2010, PyMC: Bayesian stochastic modelling in python: Journal of Statistical Software, **35**, 1–81; http://www.jstatsoft.org/v35/i04. 59, 181

Pérez, F., and B. E. Granger, 2007, IPython: a System for Interactive Scientific Computing: Computing in Science & Engineering, **9**, 21–29; doi: 10.1109/MCSE.2007.53. 180

Raiga-Clemenceau, J., J. P. Martin, and S. Nicoletis, 1988, The concept of acoustic formation factor for more accurate porosity determination from sonic transit time data: The Log Analyst, **29**, 54–60; http://www.onepetro.org/mslib/app/Preview.do?paperNumber=SPWLA-1988-v29n1a4. 53

Raymer, L. L., E. R. Hunt, and J. S. Gardner, 1980, An improved sonic transit time-to-porosity transform: Presented at the SPWLA 21st Annual Logging Symposium, SPWLA; http://www.onepetro.org/mslib/app/Preview.do?paperNumber=SPWLA-1980-P&societyCode=SPWLA. 52

Riley, K. F., M. P. Hobson, and S. J. Bence, 2006, Mathematical Methods for Physics and Engineering, 3 ed.: Cambridge University Press; ISBN: 9780521679718. 38

Rosenblatt, M., 1956, Remarks on some nonparametric estimates of a density function: The Annals of Mathematical Statistics, **3**, 832–837; doi: 10.1214/aoms/1177728190. 159

Schön, J. H., 1996, Physical properties of rocks: Fundamentals and principles of petrophysics: Pergamon Press; ISBN: 978-0080410081. 54

Scott, D. W., 1979, On optimal and data-based histograms: Biometrika, **66**, 605–610; doi: 10.1093/biomet/66.3.605. 159

Sen, M., and P. L. Stoffa, 1995, Global optimization methods in geophysical inversion: Elsevier Publishing Company, volume **4** *of* Advances in Exploration Geophysics; ISBN: 978-0444817679. 58

Sen, P. N., and P. A. Goode, 1992, Influence of temperature on electrical conductivity on shaly sands: Geophysics, **57**, 89–96; doi: 10.1190/1.1443191. 89

Sen, P. N., C. Scala, and M. H. Cohen, 1981, A self-similar model for sedimentary-rocks

with application to the dielectric constant of fused glass-beads: Geophysics, **46**, 781–795; doi: 10.1190/1.1441215. 86, 87

Sheriff, R. E., 2002, Encyclopedic Dictionary of Applied Geophysics, 4 ed.: SEG. Geophysical References Series, No. 13; doi: 10.1190/1.9781560802969. 42

Shin, C., and Y. H. Cha, 2009, Waveform inversion in the Laplace–Fourier domain: Geophysical Journal International, **177**, 1067–1079; doi: j.1365-246X.2009.04102.x. 45

Silverman, B. W., 1986, Density estimation for statistics and data analysis: Chapman and Hall, volume **26** *of* Monographs on Statistics and Applied Probability; ISBN: 978-0412246203. 159

SINTEF, 2011, JoiSE – Joint Interpretation of Seismic and EM: `http://www.sintef.no/upload/Petroleumsforskning/Brosjyrer/JoiSE.pdf`, accessed 24 July 2013. 148

Srnka, L. J., J. J. Carazzone, M. S. Ephron, and E. A. Eriksen, 2006, Remote reservoir resistivity mapping: The Leading Edge, **25**, 972–975; doi: 10.1190/1.2335169. 29, 31, 44

Statham, L., 1936, Electric earth transients in geophysical prospecting: Geophysics, **1**, 271–277; doi: 10.1190/1.1437105. 28

Talman, J. D., 1978, Numerical Fourier and Bessel transforms in logarithmic variables: Journal of Computational Physics, **29**, 35 – 48; doi: 10.1016/0021-9991(78)90107-9. 157

TAQA, 2013, TAQA completes acquisition of BP assets: `http://www.taqaglobal.com/media-centre/press-releases/2013/01-06-2013.aspx?sc_lang=en`, accessed 11 July 2013. 65

Tarantola, A., 2006, Popper, Bayes and the inverse problem: Nature Physics, **2**, 492–494; doi: 10.1038/nphys375. 58

Ursin, B., C. Bauer, H. Zhao, and C. Fichler, 2003, Combined seismic inversion and gravity modeling of a shallow anomaly in the southern Barents Sea: Geophysics, **68**, 1140–1149; doi: 10.1190/1.1598106. 30

Viriglio, M., M. D. Stefano, S. Re, F. G. Andreasi, and F. F. C. Snyder, 2010, Simultaneous joint inversion of seismic and magnetotelluric data for complex sub-salt depth imaging in Gulf of Mexico: PIERS Proceedings, 617–620. 42

Walls, J., and R. Shu, 2008, Seismic and EM rock physics and modeling, Norwegian Sea: SEG Technical Program Expanded Abstracts, 657–661; doi: 10.1190/1.3063736. 44

Ward, S. H., and G. W. Hohmann, 1988, Electromagnetic theory for geophysical applications, In Nabighian (1988), chapter 4, 130–311; doi: 10.1190/1.9781560802631. 164

Waxman, M. H., and E. C. Thomas, 1974, Electrical conductivities in shaly sands – I. The relation between hydrocarbon saturation and resistivity index; II. The temperature coefficient of electrical conductivity: Journal of Petroleum Technology, **26**, 213–225; doi: 10.2118/4094-PA. 89

Weir, G. J., 1980, Transient electromagnetic fields about an infinitesimally long grounded horizontal electric dipole on the surface of a uniform half-space: Geophysical Journal of the Royal Astronomical Society, **61**, 41–56; doi: 10.1111/j.1365-246X.1980.tb04302.x. 108

Werthmüller, D., 2009, Inversion of multi-transient EM data from anisotropic media: M.Sc. Thesis, TU Delft, ETH Zürich, RWTH Aachen; UUID: f4b071c1-8e55-4ec5-86c6-a2d54c3eda5a. 89, 103, 108, 181, 182

Werthmüller, D., A. Ziolkowski, and D. Wright, 2012a, Background resistivity model from seismic velocities: SEG Technical Program Expanded Abstracts, **31**; doi: 10.1190/segam2012-0696.1. 34

———, 2012b, Uncertainty analysis of velocity to resistivity transforms for near field exploration: EAGE Technical Program Expanded Abstracts, A014; `http://earthdoc.eage.org/detail.php?pubid=59219`. 34

———, 2013a, Background resistivity model from seismic velocities: Geophysics, **78**, E213–E223; doi: 10.1190/geo2012-0445.1. 33, 34, 81

———, 2013b, Modelling electromagnetic responses from seismic data: EGU Geophysical Research Abstracts, **15**; `http://meetingorganizer.copernicus.org/EGU2013/EGU2013-7802.pdf`. 34

Wilson, A. J. S., 1997, The equivalent wavefield concept in multichannel transient electromagnetic surveying: Ph.D. Thesis, University Of Edinburgh; `http://hdl.handle.net/1842/7101`. 108

Wilt, M., and D. Alumbaugh, 1998, Electromagnetic methods for development and production: State of the art: The Leading Edge,

**17**, 487–492; doi: 10.1190/1.1437997. 48

Wright, D., A. Ziolkowski, and B. Hobbs, 2002, Hydrocarbon detection and monitoring with a multicomponent transient electromagnetic (MTEM) survey: The Leading Edge, **21**, 852–864; doi: 10.1190/1.1508954. 29, 69

———, 2005, Detection of subsurface resistivity contrasts with application to location of fluids: U.S. Patent 6 914 433; http://www.google.com/patents/US6914433. 69

Wyllie, M. R. J., A. R. Gregory, and L. W. Gardner, 1956, Elastic wave velocities in heterogeneous and porous media: Geophysics, **21**, 41–70; doi: 10.1190/1.1438217. 52, 84

Yilmaz, Ö., 2001, *in* Seismic Data Analysis Volume 1 & 2, 2nd ed.: SEG, Investigations in Geophysics, No. 10; ISBN: 978-1560800941. 36

Zhdanov, M., S. Lee, and K. Yoshioka, 2006, Integral equation method for 3D modeling of electromagnetic fields in complex structures with inhomogeneous background conductivity: Geophysics, **71**, G333–G345; doi: 10.1190/1.2358403. 182

Ziolkowski, A., and F. Engelmark, 2009, Use of seismic and EM data for exploration, appraisal and reservoir characterization: CSPG CSEG SWLS Joint Convention Expanded Abstracts, CSEG, 424–427; http://www.geoconvention.org/archives/2009abstracts/177.pdf. 30, 44, 82

Ziolkowski, A., B. Hobbs, and D. Wright, 2007, Multitransient electromagnetic demonstration survey in france: Geophysics, **72**, F197–F209; doi: 10.1190/1.2735802. 29, 69, 92, 110, 156, 166

Ziolkowski, A., R. Parr, D. Wright, V. Nockles, C. Limond, E. Morris, and J. Linfoot, 2010, Multi-transient electromagnetic repeatability experiment over the North Sea Harding field: Geophysical Prospecting, **58**, 1159–1176; doi: 10.1111/j.1365-2478.2010.00882.x. 68, 83, 92, 106, 126, 159

Ziolkowski, A., and D. Wright, 2008, Method for attenuating correlated noise in controlled source electromagnetic survey data: US Patent Application 12/231,118; http://www.google.com/patents/US20100057366. 70

———, 2012, The potential of the controlled source electromagnetic method: A powerful tool for hydrocarbon exploration, appraisal, and reservoir characterization: Signal Processing Magazine, IEEE, **29**, 36–52; doi: 10.1109/MSP.2012.2192529. 29, 69, 82

Ziolkowski, A., D. Wright, and J. Mattsson, 2011, Comparison of pseudo-random binary sequence and square-wave transient controlled-source electromagnetic data over the Peon gas discovery, Norway: Geophysical Prospecting, **59**, 1114–1131; doi: 10.1111/j.1365-2478.2011.01006.x. 28, 70, 156